

Experimental and theoretical investigation of saturated flow boiling of R410A refrigerant and nanoparticle laden lubricant mixtures in a smooth tube.

by

Pratik S. Deokar

A dissertation submitted to the Graduate Faculty of
Auburn University
in partial fulfillment of the
requirements for the Degree of
Doctor of Philosophy

Auburn, Alabama
August 3, 2019

Keywords: nanofluid; nanorefrigerant; nanolubricant; two-phase flow boiling

Copyright 2019 by Pratik S. Deokar

Approved by

Dr. Lorenzo Cremaschi, Chair, Associate Professor of Mechanical Engineering
Dr. Sushil Bhavnani, Professor and Associate Department Chair of Mechanical Engineering
Dr. Robert Jackson, Professor of Mechanical Engineering
Dr. Stephen Nichols, Assistant Professor of Aerospace Engineering
Dr. Hans-Werner van Wyk, Assistant Professor of Mathematics and Statistics

Abstract

In air conditioning systems, a small amount of lubricating oil inevitably leaves the compressor and circulates through the other components. This lubricant acts as a contaminant affecting heat transfer and pressure losses in the heat exchangers. Mixtures of refrigerant and nanolubricants, that is, nanoparticles dispersed in the lubricant oils, have shown potential to augment heat transfer in the refrigerant evaporators. However, the mechanisms of heat transfer enhancement due to the nanolubricants are still not well explained. Two-phase flow boiling heat transfer coefficient superposition models, available in the literature, used Dittus-Boelter or Gnielinski correlations to predict convective heat transfer, and Forster-Zuber or Cooper correlations to estimate the nucleate boiling heat transfer. These correlations do not account for the presence of nanoparticles in the flow and are not able to predict the heat transfer enhancements, or sometimes the degradation, observed during flow boiling experiments of refrigerant and nanoparticle laden lubricant mixtures. A new comprehensive model was developed by modifying and integrating existing convective heat transfer models originally developed for nanofluids and pool boiling models for nanolubricants. The new model accounted for the mass conservation of nanoparticles during their migration from the laminar sublayer near the wall to the adjacent turbulent layer near the gas core, and for the effect of nanoparticle concentration on two-phase convective heat transfer multiplier.

A new test apparatus was constructed and the newly developed model was experimentally verified with heat transfer data of the single-phase convective heat transfer processes and saturated

two-phase flow boiling heat transfer processes of refrigerant R410A with two nanolubricants in a 9.5 mm I.D. smooth copper tube. The selected nanolubricants had non-spherical ZnO nanoparticles and spherical γ -Al₂O₃ nanoparticles dispersed in Polyolester (POE) lubricant. In the smooth tube, R410A-nanolubricant mixtures, which had higher thermal conductivity and kinematic viscosity than R410A-POE lubricant mixture, showed some degradation in heat transfer coefficient compared to R410A-POE case; but they also had lower pressure drops. The model explained this by accounting for the effect of increased laminar sublayer thickness and reduced thermal conductivity in laminar sublayer due to diffusion of nanoparticles towards the turbulent layer. These phenomena were responsible for the observed two-phase flow boiling heat transfer coefficient degradation when using the present R410A-nanolubricant mixtures

Al₂O₃ nanolubricant shared similar thermal conductivity in the wet state as that of ZnO nanolubricant. However, both data and simulations showed that Al₂O₃ nanolubricant had about 15% higher heat transfer coefficient than ZnO nanolubricant. The ZnO nanoparticles, with their large aspect ratio, were predicted to diffuse slowly under Brownian motion than Al₂O₃ nanoparticles. Experiments also showed that long-term flow boiling testing of R410A-nanolubricant mixtures resulted in a continuous and gradual increase of the heat transfer coefficient. A possible explanation was that the nanoparticle deposition on the tube inner wall and its near wall interaction led to small but incremental enhancements in the nucleate boiling phenomena. Finally, if nanoparticles were to be constrained in the laminar sublayer and near the wall of the tube, the predicted heat transfer coefficients from the simulations were higher than that of R410A- POE mixture. The analysis of this case revealed that the nucleate boiling contribution was significantly augmented for such scenario.

Acknowledgments

I am thankful to Dr. Lorenzo Cremaschi for his guidance, encouragement, and support throughout my research at Oklahoma State University and Auburn University. I would also like to thank all my course Professors and my Ph.D. Committee. I thank ASHRAE for supporting this work through the ASHRAE Innovative Research Grant (IRG0021).

A special acknowledge and thanks to Dr. Andrea Bigi for directing the research and coding thermophysical properties correlations and heat transfer models in our in-house program, Thiam Wong and Gennaro Criscuolo for assisting in collecting the micro-fin and smooth tube experimental data, Ellyn Harges for taking care of the lab equipment purchase, Burak Adanur for assisting with tube calorimeter construction and DAQ wire installation, and Ford Gibbes for plumbing, insulating the test apparatus components, and grooving copper blocks. My appreciation also goes to all unmentioned lab members of the BETSRG and HPS-BEST lab. I would like to express my deep gratitude to my friend Kedar Pai who helped and encouraged me during my Ph.D.

I wish to express my deep gratitude and would dedicate by work to my wife Nishigandha and my parents Shashikant and Anuprita Deokar who have always helped and supported me in making decisions throughout my Ph.D. journey, without whom the degree would have been impossible.

Table of Contents

Abstract.....	ii
Acknowledgments.....	iv
List of Tables	x
List of Figures.....	xii
List of Abbreviations and Nomenclature.....	xvi
1. Introduction.....	1
1.1 Motivation of research	1
1.2 Objectives of research	8
1.3 Approach taken to achieve the objectives.....	8
1.4 Organization of this PhD dissertation	10
2. Literature Review.....	12
2.1 Pool boiling of nanofluids.....	13
2.1.1 Nanoparticles deposition on heater’s surface	13
2.1.2 Nanoparticles influence on heater’s surface wetting characteristics	19
2.1.3 Nanoparticles influence in the microlayer under a growing bubble	20
2.2 Flow Boiling of nanofluids	26

2.3	Pressure Drop	34
2.4	Dispersants and Surfactants used with nanofluids and nanolubricants.....	35
2.5	Nanoparticle mass transfer.....	37
2.6	System Performance.....	38
2.7	Heat transfer Models for Nanofluids.....	40
2.8	Kedzierski flow and nucleate pool boiling research	46
2.9	Bigi flow boiling research	52
2.10	Main lessons learnt from the literature review	54
3.	Experimental Setup.....	58
3.1.	Components of the Experimental Test Facility.....	62
	<i>Test Section</i>	62
	<i>Preheater</i>	68
	<i>Postheater</i>	69
	<i>Subcooler</i>	69
	<i>Lubricant Syringe Pump</i>	70
	<i>Oil Separator</i>	71
	<i>Sight Glass tube</i>	73
	<i>Low Temperature Refrigeration Chiller Facility</i>	74
	<i>Data Acquisition System (DAQ) and Controls</i>	77
	<i>Nanoparticle Sizer</i>	79

<i>Ultrasonicator</i>	80
<i>Borescope-type CCD camera</i>	81
3.2. Test Conditions	85
3.3. Data Reduction.....	88
3.4. Heat Balance at Test Section.....	106
3.5. Uncertainty Analysis	109
3.6. Estimation of oil mass fraction at the test section.....	111
4. Results and Discussion	118
4.1. Flow patterns of R410A, R410A-POE, and R410A-nanolubricant mixtures.....	118
4.2. Heat Transfer Factor and Pressure Drop Factor.....	125
4.3. Effect of nanoparticle deposition on heat transfer	133
4.4. Effect of nanoparticle agglomeration and concentration on heat transfer	142
5. Heat transfer and pressure drop models.....	148
5.1. Thermophysical properties of nanolubricants	149
5.2. Application of existing two-phase flow boiling pressure drop correlations	152
5.3. Application of existing two-phase flow boiling heat transfer correlations	156
5.4. Heat transfer modeling for nanolubricants.....	161
5.4.1 Forced flow convection of nanofluids	161
5.4.2 Diffusion of non-spherical nanoparticles.....	162
5.4.3 Definition for the dimensionless laminar sublayer thickness	167

5.4.4 Mass balance of nanoparticles in laminar sublayer and turbulent core	167
5.4.5 Annular film thickness and laminar sublayer thickness	174
5.4.6 Modified Buongiorno model predictions of experimental results	176
5.4.7 Pool boiling of the refrigerant and nanolubricant mixture.....	185
5.4.8 Superposition model for saturated flow boiling.....	188
5.4.9 Correlation for two-phase convective multiplier	189
5.4.10 Superposition model sample calculation and effect of non-spherical nanoparticles on heat transfer.....	191
5.4.11 Prediction of Superposition model for saturated flow boiling.....	198
6. Conclusions.....	206
7. Recommendations for Future Work.....	210
References.....	212
Appendix-A.....	223
Literature Review Summary.....	223
Appendix-B.....	231
LabVIEW Front Panel and Block Diagram	231
Appendix-C.....	244
Two-Phase Flow Experimental Data Set	244
Appendix-D.....	249
Single-Phase Flow Experimental Data Set	249

Appendix-E.....	251
Data Reduction in EES	251
Appendix-F	269
Uncertainty Calculation in EES	269
Appendix-G.....	271
Modified Buongiorno Model Script in C++	271
Appendix-H.....	283
Two-Phase Flow Model Prediction Data	283

List of Tables

Table 1: Specification of the Components.....	82
Table 2: Sample data reduction calculations for two-phase flow boiling of R410A at $x_{avg}=0.5$, $q=15 \text{ kW/m}^2$, $m=165 \text{ kg/m}^2\text{-s}$, $OMF=N.A.$, $NPconc=N.A.$, and flow pattern type=Annular.	96
Table 3: Sample data reduction calculations for two-phase flow boiling of R410A-POE at $x_{avg}=0.5$, $q=15 \text{ kW/m}^2$, $m=165 \text{ kg/m}^2\text{-s}$, $OMF=2.4 \text{ wt.}\%$, $NPconc=N.A.$, and flow pattern type=Annular.	98
Table 4: Sample data reduction calculations for two-phase flow boiling of R410A-ZnO NL at $x_{avg}=0.5$, $q=15 \text{ kW/m}^2$, $m=165 \text{ kg/m}^2\text{-s}$, $OMF=2.4 \text{ wt.}\%$, $NPconc=20 \text{ wt.}\%$, and flow pattern type=Annular.	101
Table 5: Sample data reduction calculations for two-phase flow boiling of R410A-Al ₂ O ₃ NL at $x_{avg}=0.5$, $q=15 \text{ kW/m}^2$, $m=165 \text{ kg/m}^2\text{-s}$, $OMF=2.4 \text{ wt.}\%$, $NPconc=20 \text{ wt.}\%$, and flow pattern type=Annular.	103
Table 6: Single-phase test data for heat balance at test section.	108
Table 7: Experimental uncertainties and repeatability.....	110
Table 8: Images of two-phase flow of R410A at $T_{sat}=6.1^\circ\text{C}$, $m=165 \text{ kg/m}^2\text{-s}$, and $q=0 \text{ kW/m}^2$ at different refrigerant vapor qualities through a sight glass tube.	120
Table 9: Images of two-phase flow of R410A-POE mixture at 2.4 wt.% OMF , $T_{sat}=6.1^\circ\text{C}$ and $m=165 \text{ kg/m}^2\text{-s}$ at different refrigerant vapor qualities through a sight glass tube.	123
Table 10: Images of two-phase flow of R410A-ZnO NL mixture at 20 wt.% $NPconc$, 2.4 wt.% OMF , $T_{sat}=6.1^\circ\text{C}$, $m=165 \text{ kg/m}^2\text{-s}$, and $q=0 \text{ kW/m}^2$ at different refrigerant vapor qualities through a sight glass tube.	124
Table 11: Literature pressure drop correlations.	154
Table 12: Mean absolute deviation between correlations prediction and experimental ΔPL	155
Table 13: Literature two-phase flow boiling heat transfer correlations.....	158
Table 14: Mean absolute deviation between correlations prediction and experimental HTC	160

Table 15. Diffusion time of nanoparticles under the influence of different slip mechanisms.... 166

Table 16: Sample superposition model calculations for two-phase flow boiling of R410A, R410A-POE, R410A-ZnO NL, and R410A-Al₂O₃ NL at $x_{avg}=0.5$, $q=15$ kW/m², and $m=165$ kg/m²-s. 194

List of Figures

Figure 1: Nanoparticle deposition on the heated surface: (a) Nanoparticle are small enough to clog the cavity, (b) Agglomerated nanoparticles clog and split the cavity to have new nucleation sites, and (c) Large agglomerated nanoparticles clog the cavity and create a new porous layer. (reproduced from Vafaei (2015))	17
Figure 2: Regions of bubble growth on a heated surface; (a) boiling of pure liquid, and (b) boiling of nanofluid in the presence of nanoparticles.	22
Figure 3: Change the radius of the bubble, microlayer, triple-contact line during bubble growth (reproduced from Jung and Kim (2014)).	23
Figure 4: Schematic of the test apparatus.	60
Figure 5: P-h diagrams of a two-phase flow test in the test apparatus.	60
Figure 6: Image of the refrigerant flow circuitry through the test section, the postheater, and the oil separator.	61
Figure 7: (a) Two-phase annular flow during boiling of refrigerant and nanolubricant mixture in a smooth tube, and (b) Schematic of the tube calorimeter (test section) with the location of thermocouples and heaters.	63
Figure 8: Exploded view of the test section with plate heater and welded thermocouples' locations on the copper blocks and refrigerant copper tube.	64
Figure 9: Cross section of refrigerant tube placed in the groove of copper blocks.	65
Figure 10: Tube calorimeter (test section) before insulation.	65
Figure 11: Inline thermocouple and absolute pressure transducer at the inlet of the test section.	66
Figure 12: Assembly of differential pressure transducers.	67
Figure 13: Plate heaters on the copper block.	68
Figure 14: Lubricant syringe pump setup with lubricant injection line connected to refrigerant line of the test system.	71
Figure 15: Oil separator with tape heater.	73

Figure 16: Outlet sight glass tube with high-speed CCD camera.....	74
Figure 17: (a) Pump module and low temperature cryogenic chiller installed side by side, (b) cryogenic refrigeration module, and (c) water/ethylene-glycol pump module at the facility.	75
Figure 18: Schematic of the tube calorimeter facility for refrigerants heat transfer and pressure drop research at research facility.	76
Figure 19: National Instruments data acquisition controller and hardware.....	77
Figure 20: Control station for conducting experiments.	78
Figure 21: Monitors and LabVIEW graphic user interface of the test facility.	78
Figure 22: Nano zetasizer for measuring nanoparticle size of the present work.	79
Figure 23: Ultrasonicator probe (top photos) and controller (bottom photo) used in present work.	80
Figure 24: Borescope-type CCD camera used in present work.	81
Figure 25: Calibration of the test section by measuring the heat gain to the refrigerant in the copper pipeline installed from the preheater outlet to the test section inlet.....	89
Figure 26: Tube calorimeter (test section) after insulation.....	106
Figure 27: Heat balance between the refrigerant side and electric heaters side in the test section estimated by using equation (28).	107
Figure 28: Prediction of smooth tube two-phase flow total pressure drop using (a) (Zürcher et al. 1998) correlation and (b) (Zürcher et al. 1998) correlation prediction with modified exponent n	113
Figure 29: (a) System volume simulation to determine OMF in the test section, and (b) (Zürcher et al. 1998) correlation prediction of two-phase flow total pressure drop with modified exponent n and OMF determined from the simulation.	115
Figure 30: Total pressure drop for R410A-POE oil injection-extraction tests and oil circulation tests at $x=0.60$	116
Figure 31: Field of view of camera images of two-phase flows at the sight glass tube.	119
Figure 32: (a) Flow pattern map for R410A two-phase flow in 9.5 mm I.D. smooth horizontal tube (generated with Wojtan et al. (2005) model for $T_{sat}=6.1^{\circ}\text{C}$ and $q=15\text{ kW/m}^2$, assuming a fixed value of $m=165\text{ kg/m}^2\text{-s}$), and (b) Flow pattern images of two-phase flow of R410A, R410A-POE, and R410A-ZnO NL mixtures at $m=165\text{ kg/m}^2\text{-s}$, and $q=0\text{ kW/m}^2$, and $x=0.43$	121

Figure 33: (a) Heat Transfer Factor (<i>HTF</i>) and (b) Pressure Drop Factor (<i>PDF</i>) of R410A-POE and R410A-ZnO NL mixtures. $T_{sat}=6.1^{\circ}\text{C}$, $q=15\text{ kW/m}^2$, $OMF=2.4\text{ wt.}\%$	126
Figure 34: (a) Heat Transfer Factor (<i>HTF</i>) and (b) Pressure Drop Factor (<i>PDF</i>) of R410A-POE and R410A-Al ₂ O ₃ NL mixtures. $T_{sat}=6.1^{\circ}\text{C}$, $q=15\text{ kW/m}^2$, $OMF=2.4\text{ wt.}\%$	129
Figure 35: (a) ZnO deposition and (b) Al ₂ O ₃ deposition, on the inner wall of the tube calorimeter.	134
Figure 36: (a) <i>HTF_{fouling}</i> and (b) <i>PDF_{fouled}</i> , of R410A in absence of lubricant. (Two-phase flow tests were conducted at $T_{sat}=6.1^{\circ}\text{C}$, $x=0.49$, and $q=15\text{ kW/m}^2$, while the single-phase flow tests were conducted at $T_{ref}=9.6^{\circ}\text{C}$ and $q=8.7\text{ kW/m}^2$)	136
Figure 37: (a) <i>HTC</i> and (b) Pressure drop data for repeated tests of R410A-ZnO NL mixture and R410A-Al ₂ O ₃ NL mixture over several days in a smooth copper tube at $x=0.48$ and 15 kW/m^2	139
Figure 38: (a) Number-weighted diameter of ZnO nanoparticles with DLS instrument and (b) corresponding settling characteristics of ZnO nanoparticles in the extracted nanolubricant sample after tests.	143
Figure 39: (a) Number-weighted diameter of Al ₂ O ₃ nanoparticles with DLS instrument and (b) corresponding settling characteristics of Al ₂ O ₃ nanoparticles in the extracted nanolubricant sample after tests.	144
Figure 40: (a) ZnO nanoparticles settling in sight glass, and (b) Al ₂ O ₃ nanoparticles settling in sight glass.	146
Figure 41: Prediction of smooth tube total pressure drop using literature correlations for (a) R410A, (b) R410A-POE, (c) R410A-ZnO NL, and (d) R410A-Al ₂ O ₃ NL mixtures. ..	153
Figure 42: Prediction of smooth tube <i>HTC</i> using literature correlations for (a) R410A, (b) R410A-POE, (c) R410A-ZnO NL, and (d) R410A-Al ₂ O ₃ NL mixtures.	157
Figure 43: Influence of <i>NBT</i> on nanoparticle distribution in the laminar sublayer.	171
Figure 44: Nanoparticle distribution in the laminar sublayer and turbulent layer in two-phase flow.	173
Figure 45: Experimental and modified Buongiorno model predicted <i>HTF</i> for (a) Single-phase flow <i>HTF</i> at same mass flux of $m=207\text{ kg/m}^2\text{-s}$ and (b) single-phase <i>HTF</i> at same Reynolds number of $Re=13900$, for R410A-POE, R410A-Al ₂ O ₃ NL ($NP_{conc}=20\text{ wt.}\%$), and R410A-ZnO NL ($NP_{conc}=14\text{ wt.}\%$) mixtures. ($q=8.7\text{ kW/m}^2$, $OMF=3\text{ wt.}\%$)	178
Figure 46: Experimental <i>HTC_{exp}</i> , modified Buongiorno model predicted <i>HTC_{cht}</i> , and Gnielinski correlation predicted <i>HTC_{cht}</i> , <i>Gnielinski</i> for (a) Single-phase flow <i>HTC</i> at same mass flux of $m=207\text{ kg/m}^2\text{-s}$ and (b) single-phase <i>HTC</i> at same Reynolds number	

of $Re=13900$ for R410A ($OMF=0$ wt.%), R410A-POE, R410A- Al_2O_3 NL ($NPconc=20$ wt.%, $OMF=3$ wt.%), and R410A-ZnO NL ($NPconc=14$ wt.%, $OMF=3$ wt.%) mixtures. ($q=8.7$ kW/m ²).....	180
Figure 47: Local inner wall surface temperatures along the length of tube for R410A test at $m=207$ kg/m ² -s, $q=8.7$ kW/m ² , and $OMF=0$ wt.%.	183
Figure 48: Experimental and present model predicted HTF for (a) Single-phase flow HTF at same mass flux of $m=207$ kg/m ² -s and (b) single-phase HTF at same Reynolds number of $Re=13900$, for R410A-POE, R410A- Al_2O_3 NL ($NPconc=20$ wt.%), and R410A-ZnO NL ($NPconc=14$ wt.%) mixtures. ($q=8.7$ kW/m ² , $OMF=3$ wt.%, R410A-lubricant predicted by modified Buongiorno model, and the baseline R410A was predicted using Gnielinski correlation)	184
Figure 49: Lubricant excess layer, laminar sublayer, and annular film thickness for the two-phase flow experimental tests of (a) R410A-POE, (b) R410A-ZnO NL, and (c) R410A- Al_2O_3 NL	187
Figure 50: Correlation development for the two-phase convective multiplier, F	190
Figure 51: (a) Superposition model HTC prediction deviation of all in-tube flow boiling experimental data of R410A, R410A-POE, R410A-ZnO NL, and R410A- Al_2O_3 NL mixtures, and (b) Experimental and predicted HTC of tests at 165 kg/m ² -s.	199
Figure 52: (a) Experimental and (b) predicted HTC of R410A flow boiling tests.	200
Figure 53: (a) Experimental and (b) predicted HTC of R410A-POE flow boiling tests.	200
Figure 54: (a) Experimental and (b) predicted HTC of R410A-ZnO NL flow boiling tests.	201
Figure 55: (a) Experimental and (b) predicted HTC of R410A- Al_2O_3 NL flow boiling tests... ..	201
Figure 56: Superposition model HTC prediction of R410A-ZnO NL mixture at $m=165$ kg/m ² -s and at refrigerant vapor qualities of (a) $x_{avg}=0.2$, (b) $x_{avg}=0.5$, and (c) $x_{avg}=0.72$, at different nanoparticle mass concentration in the laminar sublayer ($NPconc=20$ wt.%).....	203
Figure 57: Superposition model HTC prediction of R410A-ZnO NL mixture at different relative roughness of the tube ($q=15$ kW/m ² , $m=165$ kg/m ² -s, and $x=0.5$)	205
Figure 58: LabVIEW Front Panel with schematic of test apparatus showing process variables.	232
Figure 59: LabVIEW Front Panel with plots of process variables.	233
Figure 60: LabVIEW Block Diagram with coded VIs (virtual instruments).....	243

List of Abbreviations and Nomenclature

English symbols

a	aspect ratio [-]
a	polynomial in refrigerant saturation temperature correlation
A	constants in refrigerant saturation temperature correlation
A_s	surface area [m ²]
AFM	Atomic force microscopy
b	polynomial in refrigerant saturation temperature correlation
Bo	boiling number
c_p	specific heat [J/kg-K]
C	variable in Hu et al. (2008) and Kattan et al. (1998) <i>HTC</i> correlations
C_{F1}, C_{F2}	variables in Friedel (1979) correlation
CCD	Charged Coupled Device
CHF	critical heat flux [W/m ²]
Co	convection number
d	diameter or minor axis of a nanoparticle [m]
D	diffusivity [m ² /s]
D	diameter [m]
dz	infinitesimal length [m]
DLS	dynamic light scattering

$E1, E2$	variables in Gungor and Winterton (1987) correlation
EDS	Energy dispersive spectrometer
EES	Engineering Equation Solver
ETW	water/ethylene-glycol mixture
f	Darcy friction factor
f_F	Fanning friction factor
F	two-phase convective multiplier
\bar{F}	desired two-phase convective multiplier
Fr	Froude number
F_S	variable in Shah (1982) correlation
FESEM	Field Emission scanning electron microscope
g	acceleration due to gravity [m/s^2]
h	enthalpy [kJ/kg]
h_{fg}	latent heat of vaporization [kJ/kg]
HTC	heat transfer coefficient [$\text{kW/m}^2\text{-K}$]
HTF	heat transfer factor [%]
k	thermal conductivity [W/m-K]
k_B	Boltzmann's constant
L	length, total pressure drop length of the test section [m]
La	length in the axial direction of the refrigerant copper tube [m]
L_r	length between the thermocouples at different levels on copper block [m]
L_{HT}	heat transfer length of the test section [m]

$L_{TC,Top}$	length between level3 thermocouples on top copper block and the refrigerant copper tube [m]
$L_{TC,Bottom}$	length between level4 thermocouples on bottom copper block and refrigerant copper tube [m]
$L_{\Delta P}$	total pressure drop length of the test section [m]
\bar{l}	locations along the length of the test section tube
l_e	thickness of lubricant excess layer [m]
m	mass [kg]
m_1	variable in Hu et al. (2008) and Kattan et al. (1998) <i>HTC</i> correlation
\dot{m}	mass flow rate [kg/s]
\ddot{m}	mass flux [kg/m ² -s]
\bar{m}	locations on the top, side, and bottom of the inner wall of the test section tube
M	molecular weight [g/mol]
n	exponent
N_{BT}	ratio of Brownian and thermophoretic diffusivities
NL	nanolubricant
NP_{conc}	nanoparticle mass concentration [wt.%]
Nu	Nusselt number
OMF	oil mass fraction [wt.%]
P	pressure [Pa]
Pr	Prandtl number
PDF	pressure drop factor [%]
\dot{q}	heat flow rate [W]

\ddot{q}	heat flux [W/m ²]
r	radial distance from the center of the tube [m]
r_b	bubble departure radius [m]
R	resistance to heat transfer [°C/W]
Re	Reynolds number
S	suppression factor
$S1, S2$	variables in Gungor and Winterton (1987) correlation
SEM	Scanning electron microscope
t	wall thickness of refrigerant copper tube [m]
T	temperature [°C, K]
TEM	Transmission electron microscope
u, V	velocity [m/s]
V_i	interface velocity between laminar sublayer and turbulent layer [m/s]
V_*	friction velocity [m/s]
We	Weber number
x	refrigerant vapor quality [-]
X_{tt}	Martinelli parameter
y	radial distance away from the wall and towards the center of the tube [m]
z	coordinate along the axis of the tube [m]
$z1 \dots 4$	variables in Shah (1982) correlation

Greek symbols

α	void fraction
----------	---------------

β	proportionality factor
δ_f	annular liquid film thickness [m]
δ_v	laminar sublayer thickness [m]
δ_v^+	dimensionless laminar sublayer thickness [-]
Δ, d	difference
ε	tube roughness [m]
θ	contact angle [°]
θ_{dry}	circumferential dry angle in tube [radian]
λ	thermal boundary layer parameter
μ	dynamic viscosity [Pa-s]
ν	kinematic viscosity [m ² /s]
$\Pi(H)$	structural disjoining pressure
ρ	density [kg/m ³]
σ	surface tension [N/m]
σ	standard deviation
τ	shear stress [Pa]
ϕ	nanoparticle volume concentration in liquid refrigerant and oil mixture [m ³ /m ³]
ϕ_l^2	liquid two-phase frictional multiplier
ϕ_g^2	vapor two-phase frictional multiplier
ω	local oil mass fraction [kg/kg]

Subscripts

amb ambient

<i>avg</i>	average
<i>b</i>	bulk, turbulent layer
<i>B</i>	Brownian motion
<i>Bottom</i>	bottom side of refrigerant copper tube
<i>bab</i>	saturated bubble temperature
<i>bv</i>	properties evaluated at nanoparticle volume concentration, ϕ , in refrigerant-POE mixture which is charged into the system
<i>cb</i>	convective boiling
<i>CBD</i>	convective boiling dominant in Kandlikar (1990) correlation
<i>cht</i>	convective heat transfer
<i>conc</i>	concentration
<i>Cooper</i>	Cooper correlation prediction
<i>corr_div</i>	correlation deviation
<i>crit</i>	critical
<i>Cu</i>	copper
<i>Dittus – Boelter</i>	Dittus-Boelter correlation prediction
<i>exp</i>	experimental
<i>evaporate</i>	evaporation of refrigerant from boiling surface
<i>ETW</i>	water/ethylene-glycol mixture
<i>f</i>	liquid
<i>f</i>	liquid refrigerant
<i>f</i>	liquid refrigerant-oil-nanoparticles mixture
<i>fo</i>	liquid only

Forster – Zuber Forster-Zuber ittus-Boelter correlation prediction

fouling fouling of tube wall

frict frictional pressure drop

g gas

Gain energy gain [W]

Gnielinski Gnielinski correlation prediction

h hydraulic

HT heat transfer

i interface of turbulent layer and laminar sublayer

ifg interface of annular liquid film and gas core

in inlet, inlet of the test section if no additional description given in the subscript

inline inline thermocouple

j locations on inner tube wall of test section

l liquid

L pure lubricant without nanoparticles

level locations on thermocouples on copper blocks and slab/blocks of copper

lv liquid-vapor interface

mom momentum or acceleration

nb nucleate boiling

NBD nucleate boiling dominant in Kandlikar (1990) correlation

np nanoparticle

0 baseline

oil pure lubricant without nanoparticles

<i>out</i>	outlet of the test section
<i>p</i>	prediction
<i>pL</i>	refrigerant-POE mixture used in Kedzierski (2003a, 2003b) model
<i>PipeLine</i>	copper tubing in between the preheater outlet and test section inlet
<i>preheater</i>	preheater of test apparatus
<i>quench</i>	quenching of boiling surface after bubble departure
<i>ref</i>	refrigerant only
<i>ref + L</i>	refrigerant-POE mixture or refrigerant-nanolubricant mixture
<i>s</i>	inner wall surface of tube
<i>sat</i>	saturated
<i>Side</i>	side surface of refrigerant copper tube
<i>sl</i>	solid-liquid interface
<i>sv</i>	solid-vapor interface
<i>T</i>	thermophoretic motion
<i>Top</i>	top side of refrigerant copper tube
<i>v</i>	laminar sublayer
<i>go</i>	gas/vapor only
<i>w</i>	inner wall of the tube, or heater's surface
<i>wet</i>	circumferential wetting in tube
ΔP	pressure drop
1 – <i>phase</i>	single-phase flow
2 – <i>phase</i>	two-phase flow, saturated two-phase conditions

1. Introduction

1.1 Motivation of research

Flow boiling of refrigerants is a primary mode of heat transfer in air conditioning and refrigeration. Researchers are focused on improving the flow boiling in heat exchangers to achieve high heat transfer coefficient, HTC , which correlated to the high energy efficiency of the AC systems. An unavoidable small portion of the compressor lubricating oil circulates with the refrigerant throughout the system components. This circulating oil can form a fairly homogeneous mixture with the liquid refrigerant but, depending on the oil concentration, the heat exchanger geometry, and the operational conditions, it may penalize the heat transfer coefficient, HTC , and increases the pressure drop: both effects are highly undesired but yet unavoidable (Cremaschi et al. 2005). In evaporators, the lubricant accumulates on the heater's surface via preferential boiling of the high vapor pressure refrigerant from the bulk refrigerant-lubricant mixture. As a result, lubricant excess layer resides on the heater's surface and it affects the heat transfer performance by controlling the bubble departure diameter and the site density, giving either an enhancement or degradation (Kedzierski 2003a). R134a-POE refrigerant-oil mixtures had degraded nucleate pool boiling heat transfer with respect to R134a because of lubricant excess layer at the boiling surface (Kedzierski 2011; Kedzierski and Gong 2009). However, the R134a-POE refrigerant-oil mixtures had enhanced flow boiling heat transfer, where the lubricant excess layer had a cloud of micro-bubbles that acted like a porous surface in providing more active nucleation sites (Kedzierski and Kaul 1998). Wei et al. (2007) observed the mineral oil enhanced the heat transfer of R22 by up to

15% below vapor qualities of 0.65. In other study (Peng et al. 2010), the presence of VG68 oil reduced the nucleate boiling of R113 refrigerant, and the boiling performance decreased with increase in the lubricant mass fraction. The increase in mixture viscosity and surface tension in presence of lubricant promotes the early annular flow formation Shen and Groll (2005) and thus causing the lubricant excess layer to cover the entire heating surface of a tube (Cremaschi 2012). Negative effects of lubricants on the flow boiling heat transfer in heat exchangers were also experimentally observed (Zhao et al. 2002).

Nanofluid is a new class of heat transfer fluid first reported by Choi and Eastman (1995), where the size of the nanoparticles varied from 1 to 100 nm. The enhanced thermal property of nanofluid, like its higher effective thermal conductivity than the base fluid, made nanoparticles an important subject under study to aid in augmentation of heat transfer of refrigerants in the presence of oil. Sanukrishna et al. (2018) provide a comprehensive review of the nanorefrigerants' experimental studies. Nanoparticles dispersed in oil are termed as nanolubricant. Once the nanolubricant are charged in the system along with a refrigerant, the nanoparticles suspend in the liquid phase of the refrigerant and oil mixture, this mixture is a classification of a nanorefrigerant. The nanofluid flow boiling studies are sporadic, with only few studies using refrigerants as a base fluid. The number of studies carried out with refrigerant and nanolubricant mixtures in two-phase flow boiling are even less frequent, and basically absent from the open domain literature. Kedzierski (2013) suggests a need for a constant research, to understand the use of nanofluids in refrigeration systems and their interaction with system components; this will lead to a development of compatible and stable nanofluids for long-term use. This will eventually result in cost effective, reliable, and high efficiency refrigeration systems.

The pool boiling tests with R134A-POE in the presence of Al₂O₃ and CuO nanoparticles

showed the heat transfer enhancements up to 275% and these enhancements decreased with increase in the oil concentration and thickness of the lubricant excess layer (Kedzierski 2011; Kedzierski and Gong 2009). The lubricant excess layer had higher nanoparticle concentration, thus had higher effective thermal conductivity than the rest of the bulk fluid. Kedzierski and Gong found that the increased effective thermal conductivity of the nanolubricant was responsible for 20% of the heat transfer enhancement if the lubricant excess layer has nanoparticles accumulated up to a 9 vol.%. Kedzierski (2011) developed a semi-empirical pool-boiling model to predict the heat transfer enhancement caused by the transfer of momentum from the nanoparticles to the bubbles. Experiments with refrigerant-nanolubricant mixtures have shown the potential of enhancing the *HTC*; for example, the two-phase flow boiling of refrigerant with spherical CuO and Al₂O₃ based refrigerant-nanolubricant mixtures in horizontal smooth and micro-fin tubes have shown enhancements and sometimes no significant change in the *HTC* compared to refrigerant-lubricant mixture (Cremaschi et al. 2017; Deokar et al. 2016; Henderson et al. 2010). The pressure drop of nanorefrigerants increased above 20% in the absence of lubricants (Alawi et al. 2015; Mahbubul et al. 2013; Peng et al. 2009b). However, the observed pressure drop for refrigerants in presence of nanolubricants mixture was negligible among other researchers (Cremaschi et al. 2017; Deokar et al. 2016; Henderson et al. 2010). The proposed mechanism of pressure drop rise was the increase in the viscosity of the base fluid in the presence of nanoparticles.

Researchers have proposed diverse and sometimes contradictory mechanisms of heat transfer under the presence of nanoparticles to explain the apparent inconsistency among their experimental findings. Several reasons and mechanisms were proposed explaining the nanofluid boiling *HTC* enhancement. Nanoparticles increased the effective thermal conductivity of the

nanofluids that helped to increase the heat transfer. Later, several researchers postulated that the magnitude of the heat transfer enhancement was much higher than the gain in the liquid thermal conductivity (Bartelt et al. 2008; Y. Ding et al. 2007a; Kedzierski and Gong 2009; White et al. 2010). The deposition of nanoparticles on the heater surface modified the wettability and cavity dimensions. The deposition created porous layer and new micro-cavities, increased surface roughness, and effected bubble departure diameter and the bubble departure frequency (Bartelt et al. 2008; Cieśliński and Kaczmarczyk 2015; Kedzierski 2003a; Kedzierski and Gong 2009; S. J. Kim et al. 2010, 2007; Patra et al. 2019; Nikulin, Khliyeva, et al. 2019). Nanoparticles transferred their momentum to the bubbles by collision (Kedzierski 2011). Nanoparticle movements created a thermal mixing and decreased the boundary layer thickness, and formation of molecular adsorption layer on the nanoparticle surface might occur. A decrease in the boundary layer thickness was due to higher Reynolds number for refrigerant-nanolubricant mixture than base fluid and thus had steeper temperature gradient at the wall (Baqeri et al. 2014; Nikulin, Moita, et al. 2019; Peng et al. 2009a). The evaporation of liquid microlayer formed beneath a vapor bubble created a high nanoparticle concentrated nanofluid in the microlayer with a high effective thermal conductivity that increased the heat dissipation from the heated surface (Li et al. 2015). Decrease in bubble departure diameter and increase in the liquid film evaporation under a growing bubble due to decreased triple-contact line radius by the structural disjoining pressure caused by the structuring of nanoparticles in the vapor bubble microlayer (Vafaei 2015; Wasan and Nikolov 2003; Wen 2008; Xu and Xu 2012). The diffusion of the nanoparticles within the refrigerant/oil liquid layers and possessing relative (slip) velocities promoted an increase in Nusselt number (Buongiorno 2006; Cremaschi 2012; Savithiri et al. 2011; Wen and Ding 2005).

On the contrary, limited mechanisms were proposed to explain the nanofluid boiling heat

transfer degradation. Nanoparticle agglomerates or nanoparticles filled the surface cavities that reduced the surface roughness and the nucleation site density (Kathiravan et al. 2009; Kedzierski 2003a; Liu and Yang 2007; Shoghl et al. 2017; Vafaei 2015; Abedini et al. 2017). Kedzierski (2011) later suggested the heat transfer degradation due to the filling of cavities was small compared to the enhancements due to the nanoparticles dispersed in the lubricant excess layer. Increase in viscosity of the fluid with nanoparticle addition counteracted the enhancement effect due to the increased effective thermal conductivity of the nanofluids (Williams et al. 2008). Suppression of bubble nucleation and transport by the suspended nanoparticles in the base fluid counteracted the enhancement effect of pool boiling on a roughened surface with nanoparticle coating. (White et al. 2010). Deposition of nanoparticles provided thermal resistance to heat transfer even at higher nanoparticle concentration in base fluid (Henderson et al. 2010; Patra et al. 2019). The decrease in the effective thermal conductivity of the nanofluid with the aggregation and loss of nanoparticles led to a decrease in heat transfer (Baqeri et al. 2014; Henderson et al. 2010).

Nanofluids research and their application to actual systems are still in infancy in the refrigeration industry. The fundamental mechanisms of heat transfer enhancement due to nanoparticle laden lubricants are not well understood because actual data that isolate and quantifies the effect of the nanoparticles concentration, dimensions, and shape within the based lubricant are basically missing in the open domain literature. Previous work (Bigi 2018; Bigi et al. 2017; Deokar et al. 2016; Wong 2015) had shown enhancement in heat transfers for refrigerant R-410A and nanolubricant mixture in micro-fin tube. However, the enhancement mechanism were not well understood. Therefore, this work presents an experimental study of refrigerant R-410A and nanolubricant mixture, undergoing in-tube two-phase flow boiling and single-phase forced

convective heat transfer in a smooth horizontal tube, to isolate and understand the fundamental mechanisms responsible for heat transfer enhancement or degradation. The goals of this work are to investigate the influence non-spherical ZnO nanoparticles in contrast to spherical Al₂O₃ nanoparticles on two-phase flow boiling heat transfer and pressure drop in the stratified-wavy and the annular flow regimes, and to understand the influence of agglomeration and deposited nanoparticles on the refrigerant flow heat transfer.

The superposition models for two-phase boiling available in the literature (John C. Chen 1966; Gungor and Winterton 1987, 1987; Haitao Hu, Ding, and Wang 2008; Kandlikar 1990; N. Kattan et al. 1998; Sawant 2012; Shah 1982) have used Dittus-Boelter or Gnielinski correlations to model the convective heat transfer component of the two-phase flow. A simple approach for nanofluids modeling was to assume homogeneous flow, where the nanoparticles moved with the same velocity as the base fluid and were in the local thermal equilibrium. These nanofluids homogeneous models extended the use of pure-fluid heat transfer correlations and superposition models by using the nanofluid mixture's thermophysical properties. However, these models did not explain the significance of mechanisms that involved nanoparticles, basefluid, and nanoparticle-heated surface interaction. A comprehensive review of nanofluid flow and heat transfer models is beyond the scope of this work, a summary of the models based on semi-analytical and numerical methods can be found in the review paper by Sheikholeslami and Ganji (2016).

Buongiorno (2006) provided a two-component, four-equation, non-homogeneous equilibrium model that accounted for the distribution and relative velocities of nanoparticles within the base fluid during single-phase forced convective flow. The model calculated diffusion of nanoparticles from laminar sublayer towards turbulent layer under the influence of Brownian

diffusion and thermophoresis. For spherical shaped nanoparticles, with diameters smaller than 100 nm, at nanoparticle volumetric concentrations, ϕ , of 1 vol.% and 3 vol.%, the model predicted enhancement in the convective heat transfer due to thinning of laminar (or viscous) sublayer near the wall due to the reduction in the viscosity of the fluid inside the laminar sublayer. Buongiorno model could be used to model the convective heat transfer component in the two-phase flow superposition models for refrigerant and nanolubricant mixtures, but needs experimental verification. The single-phase flow experimental results of this work were used to verify the Buongiorno model predictions. Finally, the two-phase experimental data is used to develop a new superposition model, which implements the validated Buongiorno (2006) convective heat transfer model.

1.2 Objectives of research

The specific objectives of the PhD dissertation are as follows:

- Investigation of the influence of nanoparticles on the turbulent single-phase flow convective heat transfer of the refrigerant and nanolubricant mixtures.
- Investigation of the influence of nanoparticle shape, diameter, local concentration, agglomeration, and deposition on two-phase flow boiling heat transfer and pressure drop of the refrigerant and nanolubricant mixtures.
- Advancement of the fundamental understanding of the mechanisms responsible for the heat transfer enhancement or degradation of the refrigerant and nanolubricant mixtures.
- Modification of the existing Buongiorno (2006) model to account for the mass balance of nanoparticles while evaluating distribution of nanoparticles in the laminar sublayer and the turbulent layer of the single-phase flow and annular liquid film of the two-phase flow.
- Development of a new comprehensive model by modifying and integrating existing convective heat transfer model originally developed for nanofluids and pool boiling model developed for nanolubricants.

1.3 Approach taken to achieve the objectives

Experimental work and theoretical modeling work was conducted on refrigerant and nanolubricants two-phase flow boiling. The approach taken to achieve the above-mentioned objectives consists of the following steps:

- Heat transfer coefficients were experimentally measured for the single-phase flow convective heat transfer of R410A with two nanolubricants in a horizontal smooth copper tube: a ZnO nanoparticle laden lubricant and a γ -Al₂O₃ nanoparticle laden lubricant. The tests were

performed at same mass flux and Reynolds number to verify the nanofluid behavior of R410A-nanolubricant mixtures as per Buongiorno (2006) model.

- Heat transfer coefficients and pressure drops were experimentally measured for the saturated two-phase flow boiling of R410A with two nanolubricants in a horizontal smooth copper tube: an elongated ZnO nanoparticle laden lubricant and a spherical γ -Al₂O₃ nanoparticle laden lubricant. The two-phase flow tests were performed at different mass fluxes and refrigerant vapor quality to study nanoparticle influence in stratified-wavy and annular flow regimes. The effect of nanoparticle deposition was studied by recording the flow boiling measurements at same conditions but over extended time.
- Extensive literature review was performed to identify the heat transfer enhancement and degradation mechanisms in nanofluids. The experimental heat transfer and pressure drop results of this work helped to recognize the mechanisms for R410A-nanolubricant mixtures in the presence of ZnO and AL₂O₃ nanoparticles.
- Buongiorno model was modified to account for the mass balance of nanoparticles while evaluating distribution of nanoparticles in the laminar sublayer and the turbulent core. The new modified model was validated for the R410A-nanolubricant mixtures using single-phase flow heat transfer experimental data.
- A new superposition model was developed that implemented Kedzierski (2011) pool boiling model for the microconvective mechanism of heat transfer and Buongiorno (2006) convective heat transfer model for the macroconvective mechanism of heat transfer. The newly developed model accounted for the increased in the heat transfer by transfer of momentum from the nanoparticles to the bubbles, the nanoparticle distribution due to slip velocity effects at the interface between the nanoparticles and the base fluid, and the decrease in the heat transfer due

to the increased laminar sublayer thickness. Experimental heat transfer data of the two-phase flow boiling of R410A-nanolubricant mixtures were used to validate the new superposition model.

In addition, I contributed measuring the data on internally-enhanced fin copper tubes, which were presented in Bigi (2018) PhD dissertation for Bigi model validation. These data on finned copper tubes served as preliminary findings that motivated the present work. Because the goal of this PhD research was to advance the fundamental understanding of the effects of the nanoparticles in the two-phase flow of refrigerant and nanolubricant mixtures, this document work intentionally considers only the data that was measured on smooth copper tubes. By eliminating the internal fins, it was able to decouple their influence on the nanoparticles migration and lubricant flow near the inner walls of the tube. This approach allowed to isolate and quantify the macroscopic effect on the two-phase flow heat transfer coefficient due to the nanoparticles' Brownian motion and thermophoresis.

1.4 Organization of this PhD dissertation

This thesis consists of mainly 7 chapters and large amount of information is reported in the appendices. The background information, motivations, and objectives of the thesis were discussed in the previous chapter. Next, chapter 3 presents the test setup that was developed as part of this PhD work and describes the test methodology. The data measured on smooth copper tube are presented in chapter 4, while the modeling efforts are summarized in chapter 5. Finally, the conclusions from this work and potential suggestions for follow-up research and additional work on this topic based on the experience and lessons learnt are provided.

For convenience, a summary of the relevant literature review findings are included in tabulated format in Appendix-A. To avoid being too verbose in the body text of this thesis, the

data acquisition system program that was directly developed in LabVIEW during this PhD are included in Appendix-B. The full set of experimental data are reported in Appendix-C and Appendix-D. The data reduction and error analysis was conducted by using Engineering Equations Solver (EES) program and the full set of equations that were coded in EES are given in Appendix-E. The model of refrigerants and nanolubricants mixtures heat transfer, which was extended and improved with respect to the one originally developed by Bigi (2018), was written in C++ language and the code is provided in Appendix-G. Finally, the detailed statistical analysis of the deviation between the simulation results and the data is given in Appendix-H.

2. Literature Review

Researchers (Ahuja 1975; K. V. Liu et al. 1988) realized that fluids with suspended micron-sized particles (0.05 mm to 3.2 mm) had higher thermal conductivities than their base fluids, augmented heat transport during single-phase flows, and had little to no change in pressure drops at moderate particle concentration. However, such large-sized particles caused problems like abrasion and clogging and were thus not suitable for modern compact heat exchangers. Choi and Eastman (1995) first reported nanofluid was a new class of heat transfer fluid, where the size of the suspended nanoparticles varied from 1 to 100 nm, which overcame the disadvantages of micron-sized particles. Today improved techniques for the production of the nanofluids, and for making indefinite suspension of the nanoparticles, have made the nanofluids inexpensive and have made their application successful in inks, paints, and suntan lotion products. Industrial and transportation application also find the use of lubricants with nanoparticles additives to reduce energy loss due to friction and wear and reduce fuel consumption by 5% to 7.5% (Erdemir 2013). Heat transfer in the presence of nanofluids has found potential in the industrial sectors of air conditioning, refrigeration, thermal and nuclear power plants, electronics cooling, and rocket engine nozzle cooling. Nanofluids though successful in various other industries, their study and use are still in infancy in the HVAC&R sector.

The available literature shows the nanoparticles used in the heat transfer research were mostly aluminum oxide, copper oxide, and titanium dioxide, while other studies were with zinc oxide, silicon dioxide, silicon carbide, aluminum nitride, magnetite, zirconium dioxide, gold,

aluminum, copper, carbon nanotubes and diamond nanoparticles. Water, ethylene-glycol, mineral oil, polyol esters, and refrigerants were used as the base fluids for the synthesis of the nanofluids. The nanofluid boiling research includes about 70% pool boiling, 20% flow boiling, and 10% heat pipes and jet impingement boiling studies.

2.1 Pool boiling of nanofluids

Several authors (Vafaei & Borca-Tasciuc, 2014; Vafaei, 2015; Ciloglu & Bolukbasi, 2015; Fang et al., 2016) presented the review of nanofluids' experimental pool boiling studies. In the pool boiling experimental studies in the literature, 53.6% of studies showed enhancement, 39.3% of studies showed degradation, and rest showed unchanged results for heat transfer coefficient (*HTC*) and critical heat flux (*CHF*). The *HTC* and *CHF* enhancements were inconsistent among various researchers using different nanoparticle type, size, and concentration. A study with 50 nm (0.1 vol. %) Al₂O₃ – water nanofluid pool boiling showed a highest *HTC* enhancement of 200% and degradation of 40%. A study with (0.3 g/liter) graphene oxide – water nanofluid pool boiling showed a maximum *CHF* enhancement of 145 to 245%, and a study with 10 nm CuO nanoparticle suspension in the water showed a maximum *CHF* degradation of 75%. The authors studying and reviewing the nanofluid pool boiling made several observations, which are presented further.

2.1.1 Nanoparticles deposition on heater's surface

The enhancement and degradation of *HTC* and *CHF* strongly depended on the nanoparticles and boiling surface interaction. The nanoparticles continuously deposited on the boiling surface during nucleate pool boiling, and it changed the microstructure of this heated surface. The rewetting of the surface with high concentrated nanofluid with the bubble departure, along with the Van der Waals force between the nanoparticles and heating surface caused the

nanoparticle disposition and surface modification (Wen et al. 2011). The surface modification by nanoparticle deposition would occur every time during boiling, and was an inherent feature even for stable nanofluids. The nanoparticles deposition increased the heat transfer surface and created new nucleation sites, or it split the existing nucleation cavity into smaller cavities, thus enhancing the *HTC*. At low deposition concentration, the effect of higher effective thermal conductivity of the nanofluid could cause enhancement in *HTC*, however as the deposition concentration increased the thermal conductivity was no longer be a dominant factor causing a decrease in the *HTC*. As the deposition concentration on the boiling surface increased, the thick layer of nanoparticles reduced the nucleation sites and provided extra thermal resistance, this could have decreased the *HTC* for some studies, but other studies showed the thermal resistance effect to have a negligible effect on *HTC*. The *HTC* and *CHF* increased with increase in the nanoparticle suspension concentration in the base fluid. The *HTC* showed degradation, once the nanoparticles concentration reached an optimum value, while the *CHF* remained constant.

Excess bubbles at the heating surface coalesced together and prevented the liquid from reaching the surface, leading to a departure from nucleate boiling and reaching *CHF*. The nanoparticle deposition on the boiling surface favored the *CHF* enhancement by improving the surface characterizes; like surface wettability, roughness, and capillary wicking (Bang and Kim 2010; S. J. Kim et al. 2007). Kim et al. (2007) was first to understand and relate the mechanisms of *CHF* enhancement in nanofluids (the macrolayer dryout theory, the hot/dry spot theory, and the bubble interaction theory) due to change in wettability changes caused by nanoparticle deposition on the heated surface. Kim et al. (2007) suggested discarding the use of hydrodynamic instability theory for nanofluid *CHF*, as it did not account for surface effects like roughness and wettability. Kamatchi et al. (2015), who observed highest *CHF* enhancement of 145 to 245% for graphene

oxide suspension in the water on the heated thin Ni-Cr wire, suggested that the deposited graphene oxide formed a porous layer at the heating surface, resulting in lower static contact angle of the liquid on the heating surface, or wettability enhancement. This porous layer held the liquid and helped in capillary wicking flow towards the dry area below the growing bubble. The availability of liquid below the bubble growing on the heated surface delayed the local dryout and cooled the dry spot. (H. D. Kim and Kim 2007; Sarafraz, Kiani, et al. 2016; Sarafraz, Hormozi, et al. 2016) presented similar findings for deposition of TiO₂, SiO₂, Al₂O₃, CNT (from water-based nanofluids), and ZrO₂ (from zirconium oxide-water ethylene glycol nanofluid) on the heating surface. Kamatchi et al. (2015) suggested the macrolayer dryout model (Haramura and Katto 1983) supported the mechanism of *CHF* enhancement.

The pool boiling *HTC* increased with the density of active nucleation sites. The dependency of the activated cavity size range on wall superheat was given by Hsu (1962). At low heat flux, the effect of concentration of nanoparticles on the pool boiling heat transfer coefficient was negligible, since only large cavities were active at low heat fluxes. As the heat flux was increased, the active cavity size range increased, thus smaller cavities were active as well. At higher heat fluxes, when smaller cavities were active, the *HTC* of nanofluids decreased as the concentration of nanoparticles increased, this might be due to the filling of the smaller cavities by the deposited nanoparticles, and an effective reduction of the nucleation site density (Kathiravan et al. 2009; Vafaei 2015). At elevated heat fluxes, the pressure fluctuations inside a pores (nucleation cavities) increases, which may help in unclogging the pores to make them into an active nucleation sites (Cieśliński and Kaczmarczyk 2015). The increase in the nanoparticle concentration promoted nanoparticle collision, agglomeration, and deposition on the heating surface forming a porous layer. The heating surface coated with porous matrix layer shows enhancement of *HTC* in nanofluids. Cieśliński and

Kaczmarczyk (2015) explains the mechanism called as suction-evaporation, where the pressure inside the porous layer drops during the bubble growth period, and with the departure of the bubble, the surrounding liquid along with nanoparticles gets sucked inside the pores. The bubble growth and departure in presence of loosely packed porous deposition of nanoparticles on the heated surface created convection currents and disturbance within the porous layer, which helped the nanoparticles to overcome the adhesive force from neighboring particles and re-suspend in the base fluid (Lin et al. 2019).

If deposited nanoparticles would be small but not too small compared to surface roughness, then deposited nanoparticles sit into the cavities, clog, and make the pores inactive, or split the cavities, and increase nucleation site density. The deposited nanoparticle size increased with the concentration of the nanoparticles in the nanofluid. If deposited nanoparticles would be bigger than surface roughness, then nucleation site density might change differently (Vafaei 2015). The roughness of the heated surface decreased, because of clogged cavities, when the size of the deposited nanoparticles was one or two orders of magnitude smaller than the surface roughness, that is, smaller than the size of the cavities (shown Figure 1 (a)). Some agglomerated nanoparticles when inside the cavities, split them into multiple nucleation sites, thus increasing the nucleation site density (shown in Figure 1 (b)). Large agglomerated nanoparticles which had a size in the same order of magnitude as the surface roughness, or cavity, decreased the nucleation site density on the heated surface. These large deposited agglomerated nanoparticles could form a porous layer and further create new cavities (shown Figure 1 (c)). Surface roughness was slightly increased by deposited nanoparticles, as the concentration of alumina nanofluid increased to 0.001 vol. %. However, as the concentration of nanofluid increased further, the surface roughness decreased (Vafaei and Borca-Tasciuc 2014). Liu and Yang (2007) observed that Au nanoparticles helped to

increase the pool boiling heat transfer of R141b refrigerant. The nanoparticles degraded the heat transfer by depositing inside the nucleation cavities over a period of time. The authors observed the test tube roughness decrease from $0.317\ \mu\text{m}$ to $0.162\ \mu\text{m}$ and the nanoparticles aggregated from $3\ \mu\text{m}$ before test to $110\ \mu\text{m}$ after test.

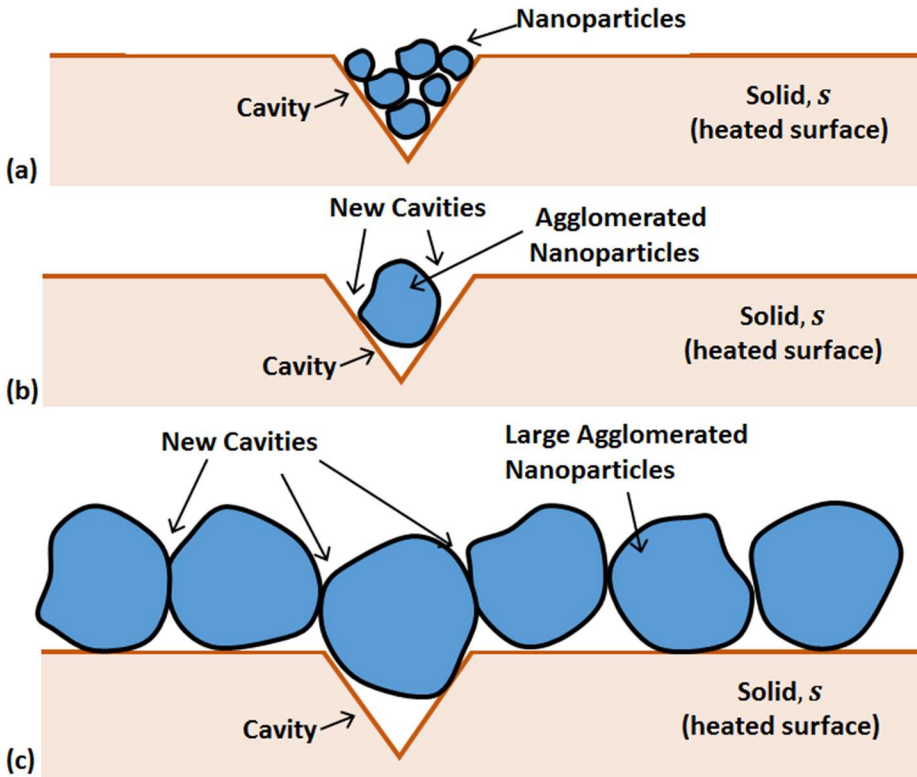


Figure 1: Nanoparticle deposition on the heated surface: (a) Nanoparticle are small enough to clog the cavity, (b) Agglomerated nanoparticles clog and split the cavity to have new nucleation sites, and (c) Large agglomerated nanoparticles clog the cavity and create a new porous layer. (reproduced from Vafaei (2015))

During the nucleate pool boiling, the superheats of pure water and ZnO-water nanofluid while boiling on ZnO nanoparticle coated surface, and the superheats of pure water and $\alpha\text{-Al}_2\text{O}_3$ -water nanofluid while boiling on $\alpha\text{-Al}_2\text{O}_3$ nanoparticle coated surface were about higher than of water boiling on clean heater surface (Shoghl et al. 2017). This was observed on the Nukiyama

plot with curves shifting to higher superheats. The α -Al₂O₃ nanoparticle coated surface performed better than the ZnO coated surface. Water boiling on the coated surface showed the number of nucleation sites and bubble frequency to decrease. The deposition of α -Al₂O₃ and ZnO nanoparticles, which were smaller than the surface roughness of the clean heated surface, decreased the surface roughness. The surface roughness decreased, or surface became smoother, with an increase in the nanoparticle concentration in the nanofluid. Tests suggested that α -Al₂O₃ and ZnO nanofluid improved the pool boiling performance in the absence of surface modification conditions due to their improved thermophysical properties, where the α -Al₂O₃ nanofluid performed better than ZnO nanofluid. However the nucleate pool boiling superheats of pure water and CNT-water-SDS boiling on CNT nanoparticle coated surface were much lower than of water boiling on clean heater surface, this was seen as curves shifted to lower superheat on Nukiyama plot. The surface roughness increased in case of CNT (treated with SDS) deposition, as the size of CNTs were larger than the clean heater surface roughness, as well as the number of nucleation sites and bubble frequency increased.

White et al. (2010) tested alternate pool boiling of water and 40 nm ZnO-water nanofluids (2.3 vol.%) and allowed gradual deposition of nanoparticles on the boiling surface, with aim to study the contribution of nanoparticle layering on the boiling surface roughness, and distinguish it from effects of suppression of bubble nucleation and motion of suspended particles. The water boiling performance enhanced consequently with each successive nanoparticle coating cycle and increased by 62% after four cycles of boiling. The author suggested that the increased surface roughness, from 0.06 μ m to 0.44 μ m, of the heated surface with nanoparticle deposition, helped to enhance the boiling performance of water. While the ZnO-water nanofluid showed 24% *HTC* enhancement over *HTC* of water when boiled on a clean un-roughened surface in the first cycle,

the author attributed it to the improved thermal properties of the nanofluids and disruption of the thermal boundary layer by the suspended nanoparticles. ZnO-water nanofluid *HTC* reduced in the second test cycle by about 7% to 20% and stayed nearly constant for each additional cycle of nanofluid boiling on the nanoparticle-coated surface. However, the performance of ZnO-water compared to *HTC* of water continued to reduce in later test cycles when boiled. The author attributed the possibility of suppression of bubble nucleation and transport by the suspended particles resulted in decreased in the boiling performance in case of ZnO-water nanofluids.

2.1.2 Nanoparticles influence on heater's surface wetting characteristics

There was a decrease of static contact angle of Al₂O₃-water nanofluids at 0.01 vol.% from 73° on clean steel surface to 23° on nanoparticle deposited surface, and decrease of static contact angle of water from 79° on clean steel surface to 22-30° on Al₂O₃ nanoparticle deposited surface (Kim et al., 2007). There was a decrease of static contact angle of ZnO-water nanofluids at 0.01 vol.% from 87.2° on a clean copper surface to 38.5° on a ZnO nanoparticle deposited surface. However, the ZnO-water nanofluids continued spreading on the nanoparticle deposited surface until it covered the entire surface (Bang and Kim 2010). [note: water had an average static contact angle of 82° on a clean copper surface (Bang and Kim 2010)]. The suspended nanoparticles in the nanofluid have minimal change in surface tension over basefluid, but adhesion tension of water increase from about 10 mN/m on stainless steel to about 60 mN/m on alumina deposited surface. Hence, suspended nanoparticles do not have much effect on wettability in the bulk fluid. As per modified Young's equation, the deposition of the nanoparticles on the heated surface enhances wettability due to increase in the adhesion force of the liquid with the solid surface and increase in the surface roughness (S. Kim et al. 2006; S. J. Kim et al. 2007; Wenzel 1949). Kim et al. (2007) observed that 5 min of nanofluid nucleate boiling increased the roughness by 20 times and surface

area by 5 times. No nanoparticle deposition layer was observed for single-phase convective heat transfer, only nucleate boiling showed deposition at the rate of $0.02 \mu\text{m/s}$ at $0.001 \text{ vol.}\%$ nanofluid concentration. Deposition of nanoparticle porous-layer during nucleate boiling, which improved wettability, had a significant enhancement in *CHF* at nanoparticle concentrations less than $0.1 \text{ vol.}\%$. Observed *CHF* enhancements were 52% for alumina nanofluids, 75% for zirconia nanofluids, and 80% for silica nanofluids.

The newly formed cavities due to deposited nanoparticles, or the existing cavities, will act as new nucleation sites if they were not flooded with the liquid, and had the availability of a nucleating vapor. The chance of liquid to fill the cavities and make them inactive nucleation sites increased with wettability. Hence, the increase in wettability could reduce the nucleation site density. Kim et al. (2007) reported a reduction in *HTC* for pool boiling of Al_2O_3 -water, ZrO_2 -water, and SiO_2 -water nanofluids. During the nucleate pool boiling, the superheats of all the nanofluids were about 10°C higher than of water, which was seen as curves of nanofluids shifted to the right on Nukiyama plot. Kim et al. (2007) suggested the reduction in *HTC* could be due to the thermal resistance of deposited nanoparticle porous layer on the heated surface, and due to the reduction of nucleation site density with a decrease in wettability. Kedzierski and Gong (2009) too during the pool boiling observed the superheats for the R134a-POE-CuO nanorefrigerant (at *OMFs* of 1 and 2%) to be about 3°C more than the pool boiling of pure R134a refrigerant, suggesting a heat transfer degradation with respect to pure R134a pool boiling.

2.1.3 Nanoparticles influence in the microlayer under a growing bubble

Four forces are acting on a bubble: buoyancy, drag, inertia, and surface tension force. The buoyancy and drag force causes the bubble departure from the heating surface, while the inertia and surface tension force prevents the bubble from departing the heating surface. There are three

regions of heat transfer under a growing bubble on a heated surface: heat transfer to dry spot area between the heated surface and vapor (I), conduction through thin microlayer and evaporation of liquid at liquid-vapor interface (II and IV), and heat transfer area to the bulk liquid (III), as shown in Figure 2. Jung and Kim (2014) estimated that, during a complete growth of a single bubble and neglecting condensation at the upper side of the bubble, the heat transfer through the liquid microlayer was 17% and the heat transfer from the superheated bulk liquid surrounding the bubble was 83%.

A liquid microlayer formed beneath a vapor bubble after it nucleated at a cavity, shown region-II in Figure 2 (a), had annular geometry with a triangular cross-section. The thickness this liquid microlayer grew outwards starting from zero at the inner annulus radius (the triple-contact line radius) and had a maximum thickness at the outer annulus radius (microlayer radius). The outer edge of the microlayer, at microlayer radius, was at the interface of region-II and region-III in Figure 2 (a), or at the interface of region-IV and region-III in Figure 2 (b). The slope of the triangular profile is the same as the contact angle formed between the liquid-vapor and liquid-solid interface. In the region-III of bulk liquid, the slope of the liquid-vapor interface increased rapidly starting at the outer edge of the microlayer.

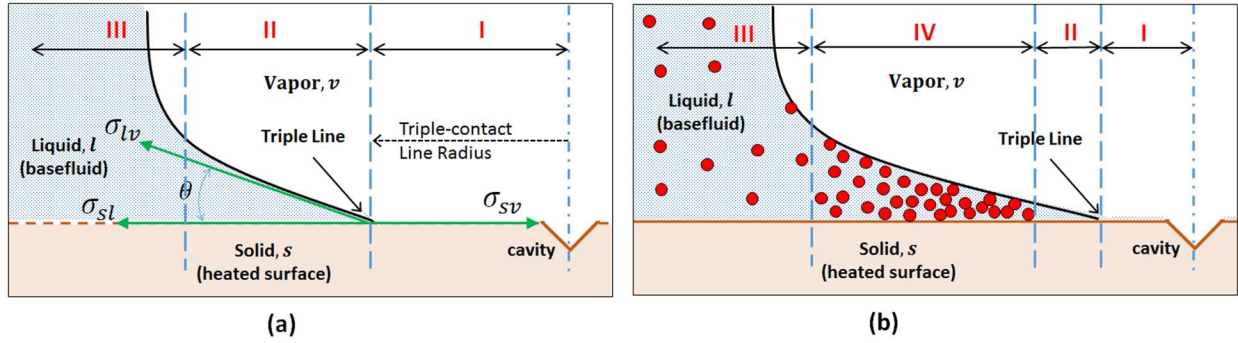


Figure 2: Regions of bubble growth on a heated surface; (a) boiling of pure liquid, and (b) boiling of nanofluid in the presence of nanoparticles.

Theoretical models predicting the microlayer diameters are absent, observed experimental results by Jung and Kim (2014) for nucleate pool boiling of water are shown in Figure 3. As the bubble size increased in stage 1, both the microlayer radius and the triple-contact line radius expanded outwards, this resulted in an enlarged microlayer-area in contact with the heated surface. As time progressed, the microlayer radius reaches its maximum. In stage 2, the microlayer radius began to shrink and the triple-contact line radius kept increasing that led to a decrease of the microlayer-area. At the end of stage 2, the triple-contact line radius increased until the edge of microlayer, and the microlayer dried up. In the following stage 3, as the drag and buoyant force on the bubble started dominating the triple-contact line radius decreased, and the bubble shape changed from spherical to ellipsoidal. This ellipsoidal bubble was elongated in vertical direction under the influence of buoyancy. Furthermore, the bubble then departed once the triple-contact line reached the cavity. The pool boiling experimental results and analysis by Jung and Kim (2014) were presented in the literature review section to show the influence of nanoparticles on the growing bubble dimension, however this data was not used during the experimental data analysis and model development of this dissertation work.

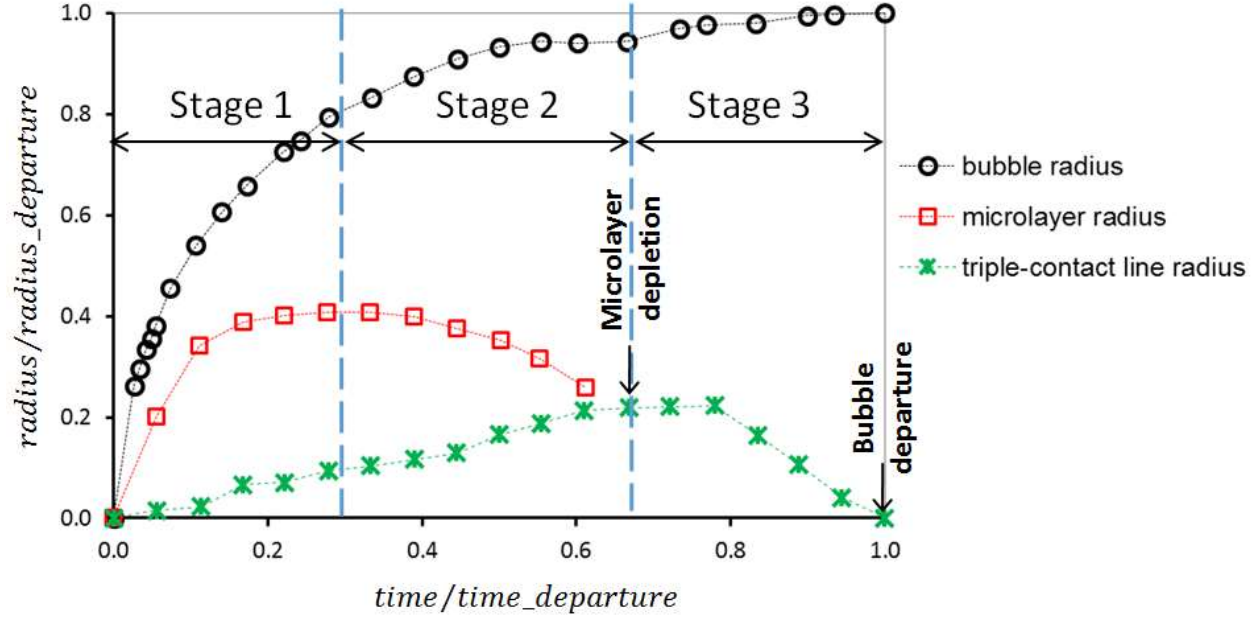


Figure 3: Change the radius of the bubble, microlayer, triple-contact line during bubble growth (reproduced from Jung and Kim (2014)).

The suspended and deposited nanoparticle during nanofluid boiling changes the force balance at the vapor-liquid-solid interface, due to change in the surface tensions; thus it modifies the behavior of triple-contact line and bubble dynamics like bubble growth and departure frequency. Wen (2008) and Xu and Xu (2012) presented a force balance, equation (1), on a growing bubble on a heated surface, supplied with constant heat flux, and in the presence of nanoparticles.

$$P_f - P_g = - \left(\sigma \left(\frac{d^2 H}{dy^2} \right) / \left[1 + \left(\frac{dH}{dy} \right)^2 \right]^{\frac{3}{2}} \right) - \Pi(H) + \Delta \rho g H + \frac{\dot{q}^2}{2 \rho_g h_{fg}^2} \quad (1)$$

where, H was the microlayer film thickness of the meniscus close to the triple line. H was measured from the solid surface and is of the order of a nanoparticle diameter. P was the pressure, y was a horizontal coordinate parallel to the surface, \dot{q} was the heat flux. The first term on the right was the capillary contribution, the second term on the right, $\Pi(H)$ was the structural disjoining

pressure, the third term was the gravitational contribution, and the fourth term was caused by the heating effect contribution to the pressure difference. There was a presence of a new region (IV), where the boiling of microlayer occurred in the presence of nanoparticles, as shown in Figure 2 (b). The new region (IV) had the structural disjoining pressure or excess pressure in the microlayer film relative to bulk fluid due to structuring of nanoparticles in the microlayer's wedge film that enhanced the spreading of nanofluids on a solid surface (Wasan and Nikolov 2003). Thus, the structural disjoining pressure pushed the triple-contact line towards the vapor side that reduced the dry area of heat transfer between the heated surface and vapor (I). The amount of reduction of the region (I) increased with increase in the nanoparticle volume concentration in the bulk fluid. The influence area of the structural disjoining pressure ranged from the interface of the region (II) and region (IV), where the film thickness was of the order of one nanoparticle diameter, to a distance where the film thickness was of the order of about five nanoparticles diameter. The pushing of the triple-contact line, or the liquid-vapor meniscus, towards the vapor side was similar to enhancement of the wettability of liquid, or the reduction of the apparent contact angle, which could reduce the nucleation site density and thus reduce heat transfer. However, the reduction of the region (I) and increase of region (IV) would enhance the heat transfer.

The surface tension at the liquid-vapor interface, σ_{lv} , for alumina-water nanofluid was same as water, with a value of 0.072 N/m (Xu and Xu 2012; Vafaei 2015). As per simple explanation by Vafaei (2015), the surface tension at the solid-liquid interface, σ_{sl} , for alumina-water nanofluid was less than that of the water, due to alumina-water nanofluids' higher contact angle, θ , than water. The force balance between surface tension at the solid-vapor interface, σ_{sv} , and relatively lower σ_{sl} caused the bubble triple-contact line radius to be less in the case of alumina-water nanofluid, as shown in Figure 2 (b). Xu and Xu (2012) observed elongated bubble

flow patterns for pure water flow in microchannels, and the nanofluid tests showed fewer chances of elongated bubbles and more of miniature bubbles flow pattern. They suggested that the structural disjoining pressure in the presence of nanoparticles decreased the surface tension acting on the bubbles, which resulted in small bubbles before the bubble departure. The elongated bubbles blocked microchannels resulting in an increased upstream pressure, this increased pressured further unblocked the channels resulting in oscillation flow instability. The miniature bubbles in nanofluids did not block the flow, and had stable flow and heat transfer. Xu and Xu (2012) did not observed nanoparticle deposition on the heater surface, and attributed it to the use of low Al₂O₃-water nanofluid concentration of 0.2 wt.% or 0.052 vol.% (no dispersants were used).

During nucleate boiling, the average nanoparticle concentration inside the microlayer, which is beneath the growing bubble, increases exponentially (Li et al. 2015) as the liquid from the microlayer evaporates. The microlayer average nanoparticle concentration is much higher than the bulk-fluid nanoparticle concentration, hence has enhanced effective thermal conductivity associated with the Brownian motion of nanoparticles. At the same time, the nanoparticles in the evaporating microlayer deposited on the heated surface to form a porous layer (Kim et al., 2007). Li et al. (2015) model showed the lower bulk-fluid concentrations of less than 0.01 vol.% caused an insignificant increase in the microlayer average nanoparticle concentration. However, the bulk-fluid concentrations of greater than 0.1 vol.% caused a significant increase of the microlayer average nanoparticle concentration, and thus increased microlayer's effective thermal conductivity as large as 0.2 W/m-K), which could not be neglected. At higher nanoparticle concentration and smaller nanoparticle size in the microlayer, the effective thermal conductivity of the nanofluid dramatically improved due to Brownian motion; thus the heat dissipation from a heated surface due to Brownian motion becomes significant. Following this theory, Li et al. (2015) proposed a

new heat flux partitioning model for the nucleate boiling, where an additional heat transfer component by nanoparticle Brownian motion in the microlayer was considered in addition to convection, evaporation, and quenching. The model predicted a strong dependence of heat transfer by nanoparticle Brownian motion on heat flux. Higher heat flux led to an increase in the heated surface superheat, thus increase in active nucleation sites. Higher nucleation sites led to an increased number of microlayers where heat transfer due to Brownian motion existed. The numerical solution of the model showed the heat transfer by nanoparticle Brownian motion was considerably high at elevated heat fluxes.

2.2 Flow Boiling of nanofluids

A review of nanofluids' experimental flow boiling studies was presented by (Fang et al., 2015; Fang et al., 2016). In the flow boiling experimental work, 66.7% of studies showed enhancement and 33.3% of studies showed degradation results for *HTC*. Similar to pool boiling studies, the *HTC* enhancements were inconsistent among various researchers using similar nanoparticle types, sizes, and concentrations. A study with (0.05 vol.%) Al₂O₃ - ethanol nanofluid flow boiling showed a highest *HTC* enhancement of 400%, while a study with (0.05-0.5 vol.%) R134a-SiO₂ nanofluid flow boiling showed a maximum *HTC* degradation of 55%. The nanofluid boiling research includes 20% flow boiling studies, with only 5% of the studies using refrigerants as base fluid (Fang et al., 2016), and the number of studies performed with refrigerant and nanolubricant boiling are even less. The reviewers suggested that the nanoparticle deposition, which increased with time of operation and nanoparticle concentration in the nanofluid, was responsible for inconsistent and contradictory *HTC* results. In a refrigeration cycle, with continuous alternating evaporation and condensation, the nanoparticle deposition caused the

concentration of TiO₂ in R141b-NM56 refrigerant-oil mixture to decrease by 72% after 20 cycles (Lin et al. 2017).

Researchers have proposed diverse and even contradictory mechanisms of heat transfer under the presence of nanoparticles to explain their inconsistent *HTC* results. Several proposed mechanisms explained the nanofluid flow boiling *HTC* enhancement. Few are as follows: increase in the effective thermal conductivity of the nanofluids, deposition of nanoparticles on the heater surface, decrease in the boundary layer thickness due to disturbance of nanoparticles, formation of molecular adsorption layer on the nanoparticle surface, or increase in the liquid film evaporation due to decrease in heated surface dryout by the structural disjoining pressure. Available studies on flow pattern and bubble dynamics are limited. The explanation of mechanisms of *CHF* enhancement included; improvement in wettability due to deposition of nanoparticles on the heated surface, and motion of suspended nanoparticle in the nanofluid.

Faulkner et al. (2003) were one of the first researchers to experiment flow boiling of nanofluids to cool microwave electronics, in order to study effects on boiling heat transfer and flow distribution in the presence of nanoparticles suspension. Subcooled and saturated forced flow boiling of nanofluids, made of Al₂O₃ and AlN nanoparticles suspension in water, was observed in a parallel microchannel heat sink. For different operating condition and nanofluid types, there was both improvement and degradation in heat transfer, significant improvement in heat transfer was seen when channel size was reduced from 1mm to 0.5 mm. Suspended nanoparticles caused uniformity of bubbles and improved flow distribution in the microchannels. As channel size decreases, the sensitivity of the flow boiling heat transfer to the deposited nanoparticles increases (Vafaei and Borca-Tasciuc 2014).

Bartelt et al. (2008) and Henderson et al. (2010) experimented two-phase flow boiling of R134a-POE-CuO refrigerant-nanolubricant mixture in a smooth horizontal tube at low refrigerant qualities of $x < 0.073$. The *HTC* enhancements improved with the increase in nanolubricant *OMF* and nanorefrigerant flow rate. Moreover, the presence of nanolubricants had an insignificant effect on the flow boiling pressure drop, as the viscosity change was insignificant at low nanoparticle concentration. At 1% and 2% *OMF* (or nanoparticle volume fraction of 0.04% and 0.08%), the *HTC* had enhancements between (42% and 82%) and (50% and 101%), respectively, for R134a-POE-CuO above R134a-POE. The observed saturation temperatures of the nanorefrigerant increased with increasing nanolubricant *OMF*. Bartelt et al. (2008) and Henderson et al. (2010) for flow boiling and Kedzierski and Gong (2009) for pool boiling of R134a-POE-CuO nanorefrigerant provided similar reasoning for their observed heat transfer enhancements. The mechanism responsible for *HTC* enhancement was not just an improvement in the effective thermal conductivity of the nanolubricant, but there was also a possibility of nanoparticles inducing secondary nucleation sites at the heated surface or CuO nanoparticle movement creating a thermal mixing.

The flow boiling of R134a-SiO₂ at a nanoparticle volume fraction of 0.05 vol.% and 0.5 vol.% showed the *HTC* for the nanofluids to decrease by about 55% below the baseline R134a *HTC*, due to unstable nanoparticle suspension. After tests, SiO₂ particle aggregates were observed to be deposited on the tube walls. Henderson et al. (2010) suggest the degradation of the R134a-SiO₂ *HTC* could be due to thermal resistance caused by the deposited nanoparticles and decrease in the effective thermal conductivity of the nanofluid with the aggregation and loss of SiO₂ nanoparticles. The R134a baseline was repeatable after cleaning the test section, as the deposition of hydrophobic-coated SiO₂ was not permanent on the boiling surface. However, after cleaning

the test section after the R134a-POE-CuO flow boiling tests, the repeated 1% *OMF* R134a-POE test showed more than 50% *HTC* enhancement above the original 1% *OMF* R134a-POE baseline test, as the boiling surface was permanently modified with the CuO nanoparticles deposition that could not be cleaned.

Peng et al. (2009a) studied two-phase flow boiling of R113-CuO nanorefrigerant, at different nanoparticle mass fractions, in a smooth tube. The refrigerant R113, even though a CFC, was chosen as the base fluid because; the R113 stayed in a liquid phase at ambient temperature and pressure and eased the dispersion of nanoparticles in the base fluid R113. Besides, the physical properties of R113 were close to other refrigerants (like R410A, R134a, and R22); hence the heat transfer characteristics of R113-based nanofluid could reflect those of other refrigerant-based nanofluids. The *HTC* for pure R113 refrigerant and all R113-CuO nanofluids increased with an increase in quality or increase in mass flux. For each mass flux, the *HTC* enhancement or impact factor, which is the ratio of *HTC* of nanofluid and *HTC* of pure refrigerant, increased with increase in the nanoparticle mass fraction. However, the amount of the *HTC* enhancement decreased with increase in mass flux, which the author suggested could be due to higher mass fluxes concealing the influence of nanoparticles on heat transfer. The measurements showed the highest *HTC* enhancement of 29.7% for the lowest mass flux and lowest nanoparticle mass fractions. The author suggested the *HT* enhancement in nanofluids were due to a reduction in the boundary layer height caused by disturbance of nanoparticles and formation of molecular adsorption layer (of liquid molecules) on the surface of nanoparticles moving in the fluid.

Kim et al. (2010), during the subcooled flow boiling experimentation, showed the *HTC* to increase with the increase in mass flux and heat flux, for deionized water as well as Al₂O₃, ZnO, and diamond nanofluids. *CHF* enhancement increased with the mass flux and nanoparticle

concentration. The maximum *CHF* enhancements were 53%, 53%, and 38% for alumina, zinc oxide, and diamond nanofluids, respectively. Nanofluids and water *HTC* were within $\pm 20\%$ for similar test conditions. The confocal microscopy showed nanoparticle deposition on the boiling surface during nanofluid boiling, which changed the number of micro-cavities on the surface and the surface wettability. Within mass flux of 1500 and 2000 $\text{kg/m}^2\text{-s}$, the water *HTC* was higher (but not significantly higher) than that of the alumina nanofluids. As the testing time progressed, for mass fluxes above 2000 $\text{kg/m}^2\text{-s}$ the alumina nanofluids performed better than water. Kim et al. (2010) attributed the Al_2O_3 nanofluid performance improvement to nanoparticle deposition on the boiling surface that modified the surface characteristics, like nucleation site density. The ZnO nanofluid had similar observations, but not for the diamond nanofluid. Kim et al. (2010) using the sessile droplet method and confocal microscopy measured the roughness factor (r) and apparent contact angle (θ_a), and calculated the intrinsic contact angle (θ_i) using the modified Young's equation, $\cos \theta_a = (\sigma_{sv} - \sigma_{sl}/\sigma_{lv})r = r \cdot \cos \theta_i$, for water on stainless steel, Al_2O_3 , ZnO, and diamond coated surfaces as $\theta_i = 86.5^\circ$, 61.0° , 60.8° , and 94.5° , respectively. The confocal microscopy also gave the number of micro-cavities (m'') on the test section surface. The nucleation site density ($n'' \propto m''(1 - \cos \theta_i)$) calculated as per Wang and Dhir (1993) model showed nucleation site density enhancement for Al_2O_3 and diamond nanofluids, and deterioration for ZnO nanofluids. The nucleation site density ratio for Al_2O_3 -nanofluid and ZnO-nanofluid boiling on Al_2O_3 and ZnO coated surface, respectively, with the micro-cavity diameter range of 1-10 μm was $n''_{\text{Al}_2\text{O}_3}/n''_{\text{ZnO}}=1.82$, and with the micro-cavity diameter range of 2.2-10 μm was $n''_{\text{Al}_2\text{O}_3}/n''_{\text{ZnO}}=2$. The nucleation site density ratio for Al_2O_3 and diamond coated surface ($n''_{\text{Al}_2\text{O}_3}/n''_{\text{diamond}}$) varied within 1.03 to 1.38, and showed increase in the ratio with an increase in micro-cavity depth from 3 μm to 7 μm (refer Table 1 in the reference paper). Kim et al., (2007)

pointed out that the decrease of the contact angle would tend to decrease the active nucleation site density (n'') by flooding the cavities, and thus decrease the heat transfer coefficient. However, this effect could be countered by the higher number of micro-cavities (m'') created by the porous layer of nanoparticle deposition. Even with the presence of enhancement or deterioration of nucleation site density for different nanofluids, Kim et al. (2010) found no correlation between the nucleation site density and the *HTC*, suggesting that the nanoparticles must affect the *HTC* by some other mechanisms, like the bubble departure diameter and the bubble departure frequency.

Sarafraz and Hormozi (2014) and Sarafraz et al. (2014) tested upward subcooled flow boiling of (0.5, 1.0, and 1.5 wt.%) Al₂O₃-water nanofluid and CuO-water/ethylene glycol nanofluid in an annular test section. The *HTC* increased with increase in heat flux and mass flux, while with an increase in nanoparticle concentration the forced convective *HTC* increased and nucleate boiling decreased. The *HTC* decreased with time due to the sedimentation of nanoparticles on the heating surface. The authors suggested that the sedimentation of nanoparticle scales on the heating surface increased the fouling resistance, and modified nucleation sites and wettability. The increase in surface wettability increased both the bubble departure diameter and bubble departure time, which lead the bubbles to accumulate near the heating surface and preventing liquid from reaching the surface and thus decrease heat transfer. However, Xu and Xu (2012) for flow boiling of Al₂O₃-water nanofluid in a single microchannel of 0.1 mm x 0.25 mm observed increase in *HTC* compared to the base fluid water. They suggested that in the presence of nanofluid both the bubble departure diameter and time decreased, this prevented blockage of the channel and disturbed the boundary layer by intensified intermixing of hot and cold fluids, thus had a stable flow and increased microconvection heat transfer.

Patra et al. (2019) experimentally investigated subcooled flow boiling of water-Al₂O₃ and water-SiO₂ nanofluids (at 0.001 to 0.01 vol.%) in a vertical annular tube at subcooling of 20° and 40°C. The authors observed a smaller departure bubble size in case of nanofluids that delayed the development of dry patch on the heater surface and aided to have a smaller amplitude of flow oscillation. The *HTC* decreased at higher nanoparticle concentration, which the authors believed was due to thermal resistance caused by excess deposition of nanoparticles on the heater wall and their interaction with nucleation sites.

Abedini et al. (2017) experimentally investigated single-phase heat transfer and subcooled flow boiling of water-based nanofluids containing oxide nanoparticles (TiO₂, Al₂O₃, CuO). During single-phase heat transfer, the *HTC* increase with nanoparticle concentration, while the heat transfer degraded during subcooled flow boiling with the increase in nanoparticle concentration, and the degradation was irrespective of the nanoparticle type and was lower than the base fluid water. The nanoparticle size had more effect on *HTC* variation. The thermal conductivity of the nanofluid did not appear to affect the heat transfer during the flow boiling; however, the degradation was due to the interaction of nanoparticles with the nucleation sites.

Zangeneh et al. (2016) studied the effect of nanofluids, prepared using four different types of ZnO-nanoparticles having different morphologies, on the single-phase forced convective and partial subcooled flow boiling performance. The tests showed the nanofluids had delayed the onset of nucleate boiling (ONB) than water due to their higher ability to transport heat from the surface. The ratio of *HTC* of ZnO (type I, II, III and IV) nanofluids at 0.02 vol.% with respect to *HTC* of water was 5.14%, 8.14%, 5.75% and -6.75%, respectively. ZnO (type I, II, and III) performance increased with increase in the volume concentration, while ZnO (type IV) performance decreased with concentration rise. ZnO (type IV) nanofluid had lower flow boiling *HTC* than flow boiling of

water. The author attributed this to the higher binding probability of finer ZnO (type IV) nanoparticles to the heater surface and its higher probability to fill cavities affecting the boiling performance. The cylindrical shaped ZnO (type II, and III) nanoparticles showed better heat transfer performance than other spherical ZnO nanoparticles. ZnO-water nanofluid's potential application in nuclear reactors as a coolant and corrosion preventer, made Rana et al. (2013, 2014) to study the flow visualization of subcooled annular-flow boiling of ZnO–water nanofluids in the absence of a surfactant. The SEM images showed nanoparticles deposited during boiling, where the deposition suppressed nucleation of bubbles and thus helped to have a low void fraction, which was beneficial for the safety of the nuclear reactor. Bang and Kim (2010) showed that the deposition of ZnO and SiC from its water-based nanofluid would act as a healing coating and help increase the *CHF* to contribute towards the safety of nuclear systems.

Baqeri et al. (2014) experimentally investigated the flow boiling of a mixture of isobutane R600a, POE RL68H, and CuO nanoparticles (NP_{conc} of 0.5 to 5 wt.%) at vapor quality less than 0.25 in an 8.26 mm ID smooth horizontal tube. The authors observed that at same mass flux there was a decrease in the boundary layer thickness due to higher Reynolds number for refrigerant-nanolubricant mixture than base fluid, thus had higher temperature gradient at the wall that enhanced the heat transfer. They too observed the degradation of *HTC* by 7.94% for CuO concentration of 5 wt.%, which they attributed to nanoparticle aggregation and settling.

Yang et al. (2017) studied two-phase flow boiling of R141b nanorefrigerants in a smooth tube and internally threaded tube, with Cu, CuO, Al, and Al₂O₃ nanoparticles at 0.1, 0.2, and 0.3 wt.%, at various mass fluxes. The heat transfer enhancements were always higher for internally threaded tube in comparison to the smooth tube. At higher mass flow rates, the heat transfer enhancement due to internal threaded tube was no better than the smooth tube. Metal nanoparticles

showed improved performance at lower vapor qualities, while the metal oxide nanoparticles performed better at higher qualities.

Y. Wang et al. (2017) experimentally investigated flow boiling heat transfer of water-based nanofluids with AlN and Al₂O₃ nanoparticles (0.1–0.5 Vol.%) in a vertical tube for a wide range of heat fluxes and mass fluxes. The author presented a new correlation with a dimensionless parameter to capture the experimental data. The author presented TEM images of nanoparticle sizes before and after the tests, but their work did not clearly mention the physics responsible for the change in heat transfer observed because of the presence of the nanoparticles.

2.3 Pressure Drop

The pressure drop characteristics of nanofluid flow is an essential aspect and should be studied alongside heat transfer characteristics. It determines the amount of energy consumed at the pump, which in turn determine the efficiency of heat transfer equipment in the presence of nanofluid. Choi and Eastman (1995), based on the past studies on slurry flow pressure drop, suggested that nanofluids with particle concentration of less than 20 vol.% should have little or no pressure drops as compared with the basefluids at similar flow rates. Hence, nanofluid, below 20% volume fractions, could be reasonably assumed as single-phase while modeling for pressure drops. There were more cases of increase in pressure drop for nanofluids (Fang et al. 2015). The proposed mechanism of pressure drop rise was the increase in the viscosity of the base fluid in the presence of nanoparticles. At same Reynolds number, the increase of Al₂O₃ nanoparticles mass fraction in isopropanol increased the *HTC* and pressure drop. The increased nanofluids viscosity lead to the increased in the single-phase pressure drop in laminar and turbulent flow, while the dependence of friction factor on Reynolds number was found to be same for both nanofluid and pure isopropanol. At same mass flux, the Al₂O₃ nanoparticles deteriorated the *HTC* in turbulent flow

and was attributed to a reduction in the degree of turbulence due to nanoparticles. The pressure drop of nanorefrigerants increased above 20% in the absence of lubricants in few studies (Alawi et al. 2015; Mahbubul et al. 2013; Peng et al. 2009b). However, the observed pressure drop for refrigerants in presence of nanolubricants mixture was negligible among other researchers (Cremaschi et al. 2017; Deokar et al. 2016; Henderson et al. 2010), no reason was provided for the unchanged pressure drops.

2.4 Dispersants and Surfactants used with nanofluids and nanolubricants

The following section discusses the role of dispersant and surfactant in preparation of stable nanofluids, their effect on effective thermal conductivity of nanofluid, and their effect on nucleate boiling heat transfer.

Dispersants, added to suspensions, prevent aggregation and settling, and improve even separation of nanoparticles in the base fluids. The dispersant can also have additional effects on boiling bubble parameters and surface wettability that could change the boiling performance. A dispersant consists typically of one or more surfactants. Surfactants modify the interfacial tension either between the base fluid and nanoparticles or between the basefluid and the boiling surface. The commonly used dispersants were thiols, oleic acid, laurate salts, and sodium dodecyl sulfate (SDS) (Bang and Kim 2010; Xuan and Li 2000). Viscosity and pH level of the basefluid, properties of the dispersants, and dispersion technique, like ultrasonic vibration, were important parameters that determined the characteristics, like stable stability and low aggregation, of the nanoparticles suspension in the basefluids. Xuan & Li (2000) presented a procedure for preparing nanofluid and showed that the selection of the dispersant for a type of nanoparticle material was basefluid specific. About 22 wt.% of the oleic acid per weight of (100 nm sized) Cu nanoparticles was required to keep the suspension stable for 1 week in the transformer-oil basefluid, while minimum

of 9 wt.% of laurate salt per weight of Cu nanoparticles maintained the suspension stability of 5 vol.% of Cu nanoparticles in the de-ionized water

Li et al. (2010) explained a method to prepare hydrophobic silver nanoparticle, which could be dispersed in nonpolar basefluids like n-hexane, chloroform, and kerosene to form stable nanofluids. Their studies showed that the preparation temperature controlled the size distribution, and pH value controlled the morphology of the nanoparticles. A multilayered hydrophobic oleic acid coating on the surface of the silver nanoparticles acted as a surfactant, which helped in the nanoparticles' dispersion in oil and prevented their agglomeration. The oleic acid molecules either formed a bond through the carboxylic functional groups with the silver atoms at the surface of the nanoparticle with their hydrophobic carbon tails in an outward direction from the nanoparticle or were simply absorbed on the outside layer without coming in contact with the silver. This oleic acid due to its oily nature, increased the hydrophobicity of silver nanoparticle, increasing its water contact angle from 70° to 113°C . These oleic molecules started stripping from the nanoparticle surface, due to decomposition, at elevated temperatures; this reduced the nanofluid stability with an increase in temperature leading to agglomeration and precipitation, thus suggesting us an existence of an operational temperature limit for the use of nanofluids. Li et al. (2010) also observed the ratio of effective thermal conductivity of nanofluids to the thermal conductivity of the base fluid to increase significantly above 40°C . The authors attributed the increase in the thermal conductivity ratios to the improvement in the heat transfer due to the reduction of oleic acid surfactant layers on the nanoparticles' surface to bring the nanoparticles' silver core and base fluid closer and increase in Brownian motion at high temperatures.

Surfactants reduce the surface tension at the nanofluid-solid interface, which reduced the bubble triple-contact line radius, which affects the rate of bubble nucleation and increases departure

frequency. Thus, surfactants improved the *HTC* due to improvement in bubble transport and lowering in *CHF* (Fang et al., 2015; Fang et al., 2016). Oleic acid surfactant molecules along with TiO₂ nanoparticles have shown to change the bubble nucleation, growth, and departure conditions during pool boiling of R11 along with mineral oil (Nikulin, Khliyeva, et al. 2019). In the absence of nanoparticles, the surfactant decreased the *HTC* as the heat flux increased, *HTC* decrease by 7% when heat flux was increased from 5 to 60 kW/m². The surfactant along with nanoparticles did not appear to significantly contribute to the change the *HTC*. Contrary, in other study (Peng et al. 2011) the surfactants Sodium Dodecyl Sulfate (SDS), Cetyltrimethyl Ammonium Bromide (CTAB) and Sorbitan Monooleate (Span-80) enhanced the nucleate pool boiling of a R113-Cu nanofluid.

2.5 Nanoparticle mass transfer

Ding et al. (2009) experimentally studied the migration of nanoparticle from the liquid phase out to the vapor phase at the free surface during pool boiling of nanoparticles-refrigerant-oil mixtures. The condensed vapor of alumina nanofluid boiling showed the presence of nanoparticle under TEM, thus Vafaei (2015) confirmed that nanoparticles escaped the liquid phase and flew with the vapor phase. Two mechanisms by Ding et al. (2009); ‘individual escaping way’ and ‘bubble adhesion way’ resulted in the nanoparticle migration. In the individual escaping way, the nanoparticles have sufficient velocity due to Brownian motion that they overcome the surface tension of the liquid phase and migrate to the vapor phase. In the bubble adhesion way, the nanoparticles adhered to the rising bubbles during boiling and escaped to the vapor phase when the bubble break to the free surface. The migration ratio was the ratio of mass of migrated nanoparticles out of the boiling fluid to the original mass of nanoparticles in the fluid before boiling. The migration ratio of nanoparticles during pool boiling of R113-RB68EP-CuO mixture

was more than that during pool boiling of R113-CuO mixture. The observed migration ratios were 5.25%, 3.55%, and 0.93% for nanoparticle volume fractions of 0.0912 vol.%, 0.183 vol.%, and 1.536 vol.%, respectively, during the pool boiling of R113-RB68EP-CuO nanorefrigerant mixture. Thus, the migration ratio of nanoparticles decreases with the increase of the volume fraction of nanoparticles. The average migrated mass of CuO nanoparticles in the R113-CuO mixture was 17.5% larger than that in the R113-RB68EP-CuO mixture. The measured migrated mass of CuO nanoparticles was 0.0095 g when the original mass of CuO nanoparticles was 0.5000 g in the R113-RB68EP-CuO mixture. Ding et al. (2009) also developed a nanoparticle immigration model based on mechanisms of ‘individual escaping way’ and ‘bubble adhesion way’. The model was sensitive to the calculations of the mass fraction of the oil and more for the average velocity of a bubble, and predicted the experimental data within an average deviation of 7.7% to 38.4% for the R113-RB68EP-CuO mixtures.

2.6 System Performance

The available literature on the use of nanoparticles in refrigeration systems is limited. Most of the authors describe the improvement in the system performance with the introduction of nanoparticles. However, none of them have tested or commented on prolonged use of nanoparticles in the refrigeration system and its effects of system components. Following is a summary of a few selected research that has used nanoparticles in the refrigeration system.

Sharif et al. (2018) present a literature review of use nanoparticles and nanolubricants in the refrigeration system. The introduction of nanoparticles in the system showed enhancement of heat transfer coefficients from 12 to 101%, reduction in compressor work by 11%, and the enhancement of COP by 24%. Few authors claimed improvement in solubility and miscibility characteristics of the refrigerant-oil mixture with nanoparticles, while others reported unchanged

results. The nanolubricants showed better tribology characteristics with a 32% reduction in friction coefficient and a 13% reduction in wear rate. Kumar and Elansezhian (2012) investigated the use of AL₂O₃-PAG (poly alkaline glycol) nanolubricant, at 0.2 vol.%, in an R134a refrigeration system, the usage resulted in energy consumption reduction of 10.32%.

Bi et al. (2008) through experimental investigation showed the R134a domestic refrigerator to have around 20.8% to 26.1% less energy consumption when tested with mineral oil and (TiO₂ or Al₂O₃) nanoparticles mixtures as the lubricant instead of the POE oil. The use of mineral oil, instead of POE, resulted in a reduction of energy consumption of about 16.6%, the suspended nanoparticles in mineral oil achieved the rest energy saving. The measurements showed the use of nanoparticles resulted in a reduction of the compressor discharge and suction pressures, and reduction of the evaporation temperatures. The author reasoned the nanoparticles to enhance the heat transfer characteristics of the refrigerant and improve the friction characteristics of the lubricant in the compressor. The nanoparticles also increased the solubility of the mineral oil in the R134a refrigerant, and this helped to increase the amount of oil returned to the compressor. The oil return ratio of the compressor was only 84% for the use of mineral oil compared to 92% for the mineral oil and nanoparticles mixture. At 0.06 wt.%, the TiO₂ and the Al₂O₃ (mineral oil based) nanolubricants had energy savings of 21.2% and 23.24%, respectively. While at 0.1 wt.%, the TiO₂ and the Al₂O₃ (mineral oil based) nanolubricants had energy savings of 26.13% and 20.86%, respectively. The refrigerator showed same energy consumption after 50 days of operation, of about 0.8 kWh/day for 0.1 wt.%, the TiO₂-mineral oil nanolubricant, indicating the potential use of nanofluids for refrigerators for a longer time of operation. Bi et al. (2011) observed similar reduced energy consumption results for domestic refrigerator using TiO₂ nanoparticles with R600a refrigerant. The measurements showed energy savings of 5.94% and 9.6% for R600a-

TiO₂ nanofluids at nanoparticle concentrations of 0.1 g/L and 0.5 g/L, respectively, as compared to pure R600a.

2.7 Heat transfer Models for Nanofluids

A comprehensive review of nanofluid flow and heat transfer models is beyond the scope of this work. The following section discusses the different approach used by researchers in modeling heat transfer in the presence of nanofluids.

A simple approach for nanofluids modeling, for nano-sized particles in basefluid at very low concentration, was to assume that the nanoparticles move with the same velocity as the base fluid, and both these components were in local thermal equilibrium. Hence, the nanoparticle and base fluid mixture were considered as a single component nanofluid for the homogeneous models. These nanofluids homogeneous models extended the use of pure fluid heat transfer and pressure drop correlations, or equations of change (continuity, momentum, and energy), by using the nanofluids' mixture thermophysical properties. Many researchers have used this approach successfully with their analytical and numerical models for prediction of their nanofluid experimental data. However, the use of nanofluid thermophysical properties with the convective heat transfer correlation for fully developed turbulent flow, like Dittus-Boelter or Gnielinski correlation, did not explain the significance of mechanisms that involved nanoparticles, basefluid, and nanoparticle - heated surface interaction. Many available empirical correlations, which covers a wide range of fluid types and flow conditions, are attractive for solving industrial and practical application problems as they are in terms of simple expressions. Such correlations, based on experimental data, includes several adjustable coefficients that do not capture the fundamental physical phenomena, and thus they fail to recognize parameters that could be modeled independently for the presence of nanoparticles.

Ding et al. (2007), during the review of past work, observed a decrease in the convective heat transfer with an increase in the concentration of nanoparticles. The Nusselt number was inversely dependent on viscosity and directly dependent on the effective thermal conductivity of the nanofluid. The experimental decrease in value of Nusselt number was significantly higher than the theoretically measured value for nanofluids with increased viscosity and effective thermal conductivity. This suggested the presence of other mechanisms, which needed identification. Xuan & Li (2000) provided a modified single-phase heat transfer model based on the dispersed model for nanofluids flowing inside a tube. The dispersed model handled diffusion problems and accounted for the random movement of the nanoparticles in the main flow. The model considered the coexistence of Brownian diffusion, sedimentation, and dispersion due to Brownian force, gravity, and nanoparticle-fluid interface friction. The model considered non-zero slip velocity between the nanoparticles and the basefluid. Buongiorno (2006) describes the presence of seven relative (slip) velocities between the nanoparticle and base fluid while considering the convective heat transfer within nanofluids. The slip mechanisms: inertia, Magnus effect, diffusiophoresis, fluid drainage, and gravity were negligible as per the analysis. Brownian diffusion and thermophoresis were the important slip mechanisms considered while developing a two-component nonhomogeneous model that accounted for mass, momentum, and energy transfer. The model found its application in numerical Lagrangian-Eulerian based models and mixture models (Alvariño et al. 2013; Malvandi et al. 2014; Wen et al. 2009).

Buongiorno (2006) model for single-phase turbulent flow showed the energy transfer by nanoparticle dispersion and their motion under the influence of turbulence was negligible due to the size and homogeneity of nanoparticles within the base fluid. The enhancement in the heat transfer was due to thinning of laminar sublayer due to the reduction in the viscosity due to

diffusion, and significant change in the nanofluid properties under the influence of thermophoresis. Further, Williams et al. (2008), involving Buongiorno, experimentally tested alumina-water (0.9, 1.8, and 3.6 vol.%) and zirconia-water (0.2, 0.5, and 0.9 vol.%) nanofluids in a 9.4 mm ID heated horizontal tube at various flow conditions. They showed that the Nusselt number and pressure loss behavior of the nanofluids tested in single-phase fully developed turbulent flow could be predicted utilizing the traditional Dittus–Boelter correlation and Darcy–Weisbach equation within $\pm 10\%$ and $\pm 20\%$, respectively, when nanofluids mixture properties were used for the calculations. As per the authors, no other heat transfer enhancing mechanism other than increased thermal conductivity and increased viscosity of nanofluids were responsible for the change in the heat transfer behavior. The alumina-water and zirconia-water nanofluids due to increased viscosity had a higher ratio of heat transfer rate to pumping power than for water.

The existing pure refrigerants' HTC correlations; Shah correlation, Gungor–Winterton correlation, Kandlikar correlation, Liu–Winterton correlation, and Wattelet correlation underestimated the measured data of two-phase flow boiling of R113-CuO nanorefrigerant by an average of 9.4%, 9.9%, 10.2%, 12.9%, and 11.2%, respectively (Peng et al. 2009a). Whereas, Sarafraz and Hormozi (2014) and Sarafraz et al. (2014) showed that the Chen correlation better predicted their Al₂O₃-water nanofluid and CuO-water/ethylene glycol nanofluid experimental data when compared to the Gungor-Winterton and the Rohsenow correlations. Peng et al. (2009a) proposed a correlation to predict the heat transfer coefficient for refrigerant-based nanofluid flow boiling inside a smooth tube, HTC_{np+} . The correlation accounted for the thermophysical properties of the nanoparticle and the refrigerant, volume fraction of the nanoparticle in the refrigerant, mass flux, and the refrigerant vapor quality. The correlation also needed an HTC calculated from any existing pure

refrigerant correlations. This new correlation, equation (2), along with Wattleet correlation (HTC_{ref}), predicted 93% of the measured experimental data within a deviation of $\pm 20\%$.

$$HTC_{np+ref} = exp \left\{ \phi \left[0.8 \frac{k_{np}}{k_{r,L}} - 39.94 \frac{(\rho c_p)_{np}}{(\rho c_p)_{ref}} - 0.028 \dot{m} - 733.26x(1-x) \right] \right\} HTC_{ref} \quad (2)$$

where, k_{np} and k_{ref} are the thermal conductivities of nanoparticle and pure liquid refrigerant, respectively; ρ_{np} and ρ_{ref} are the densities of nanoparticle and liquid pure refrigerant, respectively; $c_{p,np}$ and $c_{p,ref}$ are the isobaric specific heats of nanoparticle and liquid pure refrigerant, respectively; ϕ is the volume fraction of nanoparticles in the liquid refrigerant based nanofluid, and \dot{m} is the mass flux of the flow.

Zhou et al. (2017) tested saturated flow boiling of Al₂O₃-water nanofluids in minichannels. The addition of nanoparticles resulted in enhancement of heat transfer. The averaged HTC enhancements were 11.2%, 15.4% and 18.7%, for 0.2 wt.%, 0.5 wt.% and 1.0 wt.% Al₂O₃-water nanofluids, respectively. The HTC enhancements increased with reduced channel hydraulic diameter because of increased capillary effects. Zhou et al. (2017) also proposed a saturated flow boiling HTC correlation, as a summation of convective heat transfer due to nanoparticle motion, convective heat transfer due to fluid motion, and nucleate boiling heat transfer. The nanoparticle convection accounted for nanoparticle distribution in the fluid that satisfied the fractal distribution theory. The nucleate boiling heat transfer considered the probability distribution density of bubbles random growth in a minichannel. The correlation predicted 94.2% of their experimental data within $\pm 20\%$. Zhou et al. (2017) correlation/model showed good predictability, but the theory of fractal distribution of nanoparticles did not look convincing as the references mentioned in Zhou et al. (2017) paper used the fractal distribution theory for completely different application.

A summary of the models based on semi-analytical and numerical methods can be found in the review paper by Sheikholeslami and Ganji (2016). Modeling includes use of Runge-Kutta method, finite difference, finite element, finite volume, control volume based finite element method, and Lattice Boltzmann method. The review paper also lists the various nanofluids thermophysical property models used by researchers for their simulation work. Other numerical mixture models for subcooled flow boiling of a single component nanofluid are available in the literature (Abedini et al. 2013) that account for turbulence, nucleate boiling at the wall, but no nanoparticle slip condition is considered. The numerical models used two-component, nanoparticle and basefluid, to better describe the nanofluid flow and heat transfer models, as it was necessary to consider relative slip velocities between particles and base fluids which had an important role on the nanofluids' enhanced convective heat transfer performance.

The heat flux partitioning model, for the local near-wall heat flux, by Kurul & Podowski (1990) considered the total heat flux at the wall to be made of three components, as shown in equation (3)

$$\ddot{q}_{wall} = \ddot{q}_{1-phase} + \ddot{q}_{quench} + \ddot{q}_{evaporate} \quad (3)$$

The first term, $\ddot{q}_{1-phase}$ is the flux of single-phase convective heat transfer at the non-boiling section of the heated wall due to the temperature difference between the wall and the bulk fluid. The second term, \ddot{q}_{que} is the quenching heat flux from the wall to the fresh bulk fluid approaching the wall after the bubble departure. The third term, $\ddot{q}_{evaporate}$ is the evaporation flux to convert the liquid into vapor at the heated wall. However, the quenching and evaporation heat fluxes terms required several phenomenological laws to achieve model closure. Podowski (2012) presented a mechanistic modeling concept, where the quenching and evaporation heat fluxes terms were replaced by a new term called boiling heat flux, $\ddot{q}_{boiling}$. Podowski (2012) model based on

theoretical first-principle concepts captured the underlying physical phenomena along with the use of minimal empirically determined coefficients. The heat flux partitioning model along with thermophysical property correlation of nanofluids found use as a boundary condition in the computational fluid dynamics modeling of nanofluids pool boiling and forced-convection boiling. X. Li et al. (2015) proposed a new heat flux partitioning model for the nucleate boiling, where an additional heat transfer component by nanoparticle Brownian motion in the microlayer was considered in addition to convection, evaporation, and quenching in the Kurul & Podowski (1990) model.

Buongiorno (2006) two-component, four-equation, non-homogeneous equilibrium model, which accounted for the distribution and slip of nanoparticles within the liquid during forced convection flow, found its application in numerical Lagrangian-Eulerian based models and mixture models (Alvariño et al. 2013; Malvandi et al. 2014; Wen et al. 2009). However, these models do not account for flow boiling phenomenon. A solver in OpenFOAM was developed by Meng (2017) to simulate the natural and forced convection of the nanofluid, its heat transfer, and nanoparticles sedimentation. Lagrangian method was the most straightforward method, but simulations under Eulerian-mixture approach were more efficient and required less computational resource. The solver development did not consider boiling of nanofluid; also, this solver is not yet available on open source platform of OpenFOAM.

2.8 Kedzierski flow and nucleate pool boiling research

Dr. Mark A. Kedzierski refrigerant boiling research has been a basis of the current work, hence the details of the refrigerant, refrigerant-lubricant, and refrigerant-nanolubricant boiling work by Kedzierski is summarized in this section.

Kedzierski and Kaul (1998) investigated flow boiling of R12, R134a, and R134a-POE oil mixtures in a 9 mm ID roughened quartz tube. The quartz tube was heated at the bottom with a 3 mm wide brass strip heater to have heat fluxes of 15 to 30 kW/m². The flow was stratified at low flow velocity and low vapor quality of about 0.01. A high speed camera was used to measure bubble density at the core of the tube for pure refrigerants, while it was impossible to measure nucleate site density and bubble frequency at the tube wall due to congested bubble activity. It was also not possible to measure the bubble density at the core for R134a-lubricant mixtures, as the bubbles had a smaller size with large density. Kedzierski and Kaul (1998) observed a flow-boiling enhancement of R134a in the presence of neopentyl POE oil. The average enhancements, at all heat transfer conditions, at 0.9 wt.% *OMF* were 13% higher and at 2.3 wt.% *OMF* were 15% higher compared to that of pure R134a. On the other hand, the authors observe R134a in the presence of another proprietary POE oil at 1.7 wt.% *OMF* showed average enhancement of only 4% higher compared to that of pure R134a. The R134a - proprietary POE oil had enhancements in pool boiling conditions, but resulted in *HTC* degradation from 3% to 8% compared to pure R134a, at higher liquid Reynolds number above 8000. Visual observation for R134a- neopentyle POE oil mixtures showed that the averaged bubble size decreased from 0.3 mm to 0.2 mm when the *OMF* increased from 0.9 wt.% to 2.3 wt.%, whereas the R134a- proprietary POE oil mixture had the smallest bubble size no larger than 10 μm. Pure R134a had averaged bubble size of 0.5 mm. Kedzierski and Kaul (1998) attributed the increased nucleate site density as the reason for the

enhancements of flow boiling HTC of R134a in presence of neopentyle POE oil, while R134a-proprietary POE oil mixture had enhanced nucleate site density, the significantly smaller bubble size led to their lower enhancements in HTC . The proprietary POE had higher viscosity than the neopentyl POE oil, and the authors suggested that the reduction in bubble size was due to increase in the viscosity, and was the primary reason for R134a- proprietary POE mixture to have lower enhancements. In presence of the lubricant excess layer, the force holding the bubbles to the heater wall are smaller for refrigerant-oil mixture than for pure refrigerant, thus the much bubbles are released from the surface into the lubricant excess layer to form a cloud of micro-bubbles. The cloud of micro-bubbles acted like a porous surface in providing more active nucleation sites. The Fritz equation estimated increase in the bubble diameter with addition of lubricant to the refrigerant, to predict the experimental data Kedzierski and Kaul (1998) had to increase the input contact angle from 34° for pure refrigerant to 40° for the refrigerant-lubricant mixture. Estimations for R134a- neopentyle POE oil mixtures showed that the bubble density in the core of the tube increased with increase in the OMF , and were 190/cm, 500/cm, and 2000/cm for OMF of 0 wt.%, 0.9 wt.%, and 2.3 wt.% respectively.

Kedzierski and Gong (2009), during the pool boiling on a rough and flat copper plate, observed the superheats for the R134a-POE refrigerant-oil mixtures (at OMF s of 0.5, 1 and 2 wt.%) to be about 3°C more than the pool boiling of pure R134a refrigerant (OMF of 0 wt.%), suggesting a heat transfer degradation with respect to R134a. The increasing superheat ($T_{wall} - T_{sat}$) values for all the refrigerant-oil mixture pool boiling were within 1°C of each other for the heat fluxes between 30 and 90 kW/m^2 . The reduction in the bubble size, thus reduction of vapor generated per bubble, due to an increase in the oil-lubricant mass fractions was the reason suggested for the degradation of heat transfer. This lubricant effect was more pronounced at higher

heat fluxes. Kedzierski (2011) measured similar degradation, the author observed the superheats for the R134a-POE refrigerant-oil mixtures (at *OMF*s of 0.5, 1 and 2 wt.%) to be about 0.1°C to 1.8°C more than the pool boiling of pure R134a refrigerant (*OMF* of 0 wt.%), and superheats for all mixtures were within 1.2°C of each other for entire tested heat flux range. Kedzierski and Gong (2009) observation showed the heat transfer to degrade as the lubricant mass fraction increased from *OMF* of 0.5 wt.% to 1 wt.%. Interestingly, the heat transfer performance (which was still a degradation with respect to pure R134a boiling) at 2 wt.% *OMF*, for heat fluxes above 90 kW/m², did not follow the above-mentioned trend and showed an increase in the performance compared to 1 wt.% *OMF*. Kedzierski (2011) for similar repeated tests observed the heat transfer performance of the 1 wt.% *OMF* mixture to be better than that of the 0.5 wt.% *OMF* mixture, and the heat transfer performance of the 2 wt.% *OMF* mixture to be worse than that of the 0.5 wt.% *OMF* mixture. The above two studies by Kedzierski and Gong (2009) and Kedzierski (2011) showed inconsistent results, yet the boiling performances of the 0.5 wt.% *OMF* and 1 wt.% *OMF* mixtures were similar or very close. The results for pool boiling of pure R134a was also inconsistency for both the studies, where the aging of the boiling surface over time caused an improvement of the heat transfer performance of the pure R134a refrigerant.

Kedzierski and Gong (2009) tests for pool boiling at 0.5 wt.% *OMF* showed the heat transfer enhancements between 50% and 275% for CuO-POE-R134a nanorefrigerant mixture with respect to the tests with POE-R134a. The pool boiling tests at 1 wt.% *OMF* showed smaller heat transfer enhancements on an average of 19% for CuO-POE-R134a nanorefrigerant mixture with respect to the tests with POE-R134a. Moreover, the pool boiling tests at 2 wt.% *OMF* showed still smaller heat transfer enhancements of about 12% for CuO-POE-R134a nanorefrigerant mixture with respect to the tests with POE-R134a.

Kedzierski (2011) tested pool boiling at 0.5, 1, and 2 wt.% *OMF* and at heat fluxes below 40 kW/m², and showed the heat transfer enhancements for Al₂O₃-POE-R134a nanorefrigerant mixtures with respect to the tests with pure R134a and much more than POE-R134a mixture. Also, below 40 kW/m² the mean pool boiling curves (superheat values) for all Al₂O₃-POE-R134a nanorefrigerant mixtures were within 1.4°C. For the heat flux range of 40 kW/m² and 100 kW/m², the superheat values of adjacent pool boiling curves differed by 0.5°C. The heat transfer performance degraded when the nanolubricant mass fraction increases from 0.5 wt.% *OMF* to 1 wt.% *OMF*, and the heat transfer performance improved when the nanolubricant mass fraction increases from 1 wt.% *OMF* to 2 wt.% *OMF*.

Thus, the amount of heat transfer enhancements decreased with increase in the nanolubricant concentration. After experimentation, a darker high nanoparticle concentration lubricant accumulated near the boiling surface, this supported the claim of the presence of lubricant excess layer on the heat transfer surface. The lubricant excess layer had higher nanoparticle concentration, thus had higher effective thermal conductivity than the rest of the bulk fluid. The pool boiling model by Kedzierski (2003a), which considered the effect of increased lubricant thermal conductivity on the boiling heat transfer, predicted that the increased effective thermal conductivity of the nanolubricant was responsible for only a small portion, about 20% of the heat transfer enhancement if the lubricant excess layer has nanoparticles accumulated up to a 9 vol.%. The authors suggested the remaining heat transfer enhancements due to the possibility of nanoparticles inducing secondary nucleation sites at the heated surface and on bubble, or CuO nanoparticle movement creating a thermal mixing. The degradation in the heat transfer was attributed to the nanoparticles filling the surface cavities.

Kedzierski (2003a) explained the formation of a thin lubricant excess layer on the heated surface of pool boiling. The lubricant mass fraction in the refrigerant-lubricant mixture layer increased due to its proximity to the boiling surface causing preferential evaporation of the refrigerant, as the refrigerant had high vapor pressure than the lubricant. The high lubricant concentration in the layer influences the boiling performance, by controlling the bubble departure diameter and the site density, causing either an enhancement or degradation in heat transfer. The increased lubricant mass fraction in the lubricant excess layer caused the departure bubble diameter to become smaller, reducing heat transfer. A semi-theoretical model by Kedzierski (2003a) predicts the pool boiling heat transfer for refrigerant (R123)-lubricant (York-C) mixtures (not pure refrigerants) on a rough horizontal flat surface. The model consists of a dimensionless excess layer parameter and a thermal boundary layer parameter that were fitted to excess surface density and heat transfer measurements. The model had three main assumptions; the lubricant lifted from the lubricant excess layer as lubricant caps on bubbles was a dominant mass lubricant mass transfer, the lubricant excess layer had linear temperature profile in its thermal boundary layer and was exponential on the outside of the thermal boundary layer, and the lubricant excess layer consisted entirely lubricant. For lubricant mass fractions in order of 0.1 wt.%, the thin excess layer at the wall acts a surfactant to reduce the surface energy, giving higher heat transfer coefficient than no lubricant condition. As the lubricant mass fractions increased above 0.1 wt.%, the model predicted a decrease in the heat transfer coefficient. The model also predicted increased pool boiling heat transfer with increased in lubricant viscosity for the same saturation temperature and the same refrigerant/lubricant critical solution temperature. The model predicted that the lubricant viscosity and miscibility were influential in determining the magnitude of the *HTC*. Kedzierski (2003b)

provided an improved wall superheat dependent thermal boundary layer parameter that enables the model to predict the full range of wall superheats for the R134a-lubricant mixtures.

Kedzierski (2011) developed a semi-empirical model to predict the heat transfer enhancement caused by the transfer of momentum from the nanoparticles to the bubbles. For the tests with 0.5 wt.% *OMF* of Al₂O₃-POE-R134a nanorefrigerant pool boiling, the model underpredicted heat transfer performance. The author suggested that due to the very small mass fraction of nanolubricant, the average size of the Al₂O₃ nanoparticles in the fluid was skewed to a smaller diameter than 10 nm. (Understanding that the probability for the average size of the nanoparticles in the nanolubricant to be 10 nm would increase with an increase in the volume or *OMF* of the nanolubricant). The Kedzierski (2011) model successfully calculated the increase in boiling performance if the input nanoparticle diameter was reduced below 10 nm. This model was only valid for the limited range of parameters investigated in the paper, but suggested that small particle size, with large nanoparticle volume fraction, and large nanolubricant mass fraction improved boiling heat transfer enhancement. The model had hidden bubble departure frequency and nucleation site density in an empirical constant, and failed to account for the possible reduction of heat transfer due to the filling of cavities by nanoparticles. The author suggested this heat transfer degradation due to the filling of cavities be small compared to the enhancements observed, as the nanoparticles were well dispersed in the lubricant excess layer, and the excess layer acted to stabilize the nanoparticles and minimize nanoparticle deposition on the boiling surface.

The work of Kedzierski (2003a), Kedzierski and Gong (2009), and Kedzierski (2011) suggested that enhancement and degradation in pool boiling heat transfer performance was depended on the concentration and size of nanoparticles in the nanolubricant. The improvement in thermal conductivity in the lubricant excess layer was not the governing factor in determining the

magnitude of the enhancement. A good dispersion of nanoparticles within the lubricant excess layer was necessary to have an enhancement via nanoparticle and bubble interaction.

2.9 Bigi flow boiling research

Bigi's experimental flow boiling research work on micro-fin tubes was phase-1 of the current research work (Bigi 2018), and is summarized in this section.

Previous work by Bigi (2018) investigated the thermophysical properties and thermal performances of mixtures of R410A refrigerant and nanolubricants, during two-phase flow boiling inside a micro-fin tube with hydraulic diameter of 5.45 mm. The study focused on the use of nanoparticles of Al₂O₃ with a 40 nm to 60 nm nominal diameter and spherical shape. The nanoparticles were dispersed at different mass concentrations (0 wt.%, 10 wt.%, and 20 wt.%) in a common ester oil (POE) with density of 0.981 g/ml at 20°C and kinematic viscosity of 31.2 cSt and 5.6 cSt, respectively at 40°C and 100°C. The base fluid was refrigerant R410A and oil concentration ranged between 0 wt.% and 3 wt.%. Different operational conditions were chosen for two-phase flow boiling tests, where mass flux was varied between 180 kg/m²s to 425 kg/m²s, heat flux was 12 kW/m², and refrigerant saturation temperature was 3.5°C ± 0.9°C.

The work by Bigi showed that the addition of POE based nanolubricants to refrigerant R410A during two phase flow boiling affected the heat transfer coefficient for a horizontal 9.5 mm O.D. micro-fin tube, and the effects were measurable. The effects on the two-phase flow pressure drop were less evident. It was observed that Al₂O₃ based nanolubricants provided an enhancement of the heat transfer coefficients with a non-measurable penalization of the two-phase flow pressure drop. When charging nanoparticles in the POE oil at 20 wt.% mass concentration and with oil concentration of 3 wt.% in the two-phase flow, the heat transfer coefficient increased by 15% and up to 40%. Bigi suggested that the spherical shaped Al₂O₃ nanoparticles created a

preferential path for heat transfer exchange across the liquid phase of the mixture but did not add any additional resistance to the flow of refrigerant and lubricant mixture inside the micro-fin tube.

Bigi and Cremaschi (2019) analyzed the slip mechanisms that nanoparticles can be affected by when dispersed in the liquid phase of a high-viscosity refrigerant-oil mixture undergoing evaporation inside a horizontal tube. Their study focused on annular flow pattern of refrigerant R410A and POE based nanolubricants with Al₂O₃ nanoparticles. Among ten different slip mechanisms considered (i.e., particles rotation, translation, inertia, Brownian diffusion, thermophoresis, diffusiophoresis, Magnus effect, gravity, drainage, and wall lubrication effects), Bigi and Cremaschi (2019) concluded that nanoparticles were dominated by eddies in the turbulent flow region, making any of those slip mechanisms basically ineffective. In laminar regime, of all the slip mechanisms analyzed, three were considered to have potential to affect the distribution of nanoparticles within the laminar sublayer: Brownian motion, thermophoresis, and gravity. However, the diffusion time of the gravity effect was quite high for Al₂O₃ nanoparticles in a high viscosity liquid, and, Bigi and Cremaschi neglected the gravity effects during two-phase flow boiling process in horizontal smooth tubes.

Bigi (2018) also developed a superposition model to describe the evaporative two-phase flow of a refrigerant-nanolubricant mixture. In his approach, he combined the Buongiorno (2006) correlation for nanofluid convective heat transfer with the Kedzierski (2012) correlation for pool boiling of refrigerant-nanolubricant mixtures on rectangular finned heat transfer surface. He conducted an initial experimental validation of his model for internally finned copper tubes and the simulation predictions had about $\pm 50\%$ deviation with respect to the experimental data.

One of the reason given in Bigi PhD dissertation for the deviation was the assumption of constant nanoparticles concentration in the turbulent layer. The concentration of nanoparticles in

the turbulent layer did not increase when they diffused from laminar sublayer towards the turbulent layer. Another limitation of the model originally developed by Bigi was the assumption of the two-phase convective multiplier, F , in the superposition model to be independent of the nanoparticle concentration. These two limitations were addressed in the present work, as it will be discussed later in chapter 5 of the present PhD dissertation. Current work also updated the Brownian diffusivity equations in order to extend Bigi's original model to non-spherical nanoparticles, such as ZnO nanoparticles. Finally, following a similar approach presented in Bigi and Cremaschi (2019) paper, the slip mechanisms effects for non-spherical nanoparticles were theoretically investigated. As it will pointed out later in this document, in comparison with the spherical nanoparticle case, the non-spherical nanoparticles diffuse slowly under Brownian motion to uniformly disperse in the base refrigerant-lubricant mixture.

2.10 Main lessons learnt from the literature review

Nanolubricants have been of great interest in recent years because the lubricant with nanoparticles could be optimized to enhance the heat transfer while also improving lubrication properties. Literature showed that using nanoparticles in compressor lubricants does not interfere with the compressor operation and nanolubricants have the potential to increase the system energy savings by over 20%. However, the mechanisms responsible for these energy savings were not well understood and the results were dependent on the type of the nanoparticles that were dispersed in the base fluid, as well as the adoption of specific surfactants required to achieve stable nanoparticles dispersions in lubricant and refrigerant liquid mixtures. From this point of view, this PhD work used the same surfactant that was successfully tested by Bigi (2018) in the study that was preliminary to the current work. The proprietary polymeric surfactant stabilized the Al₂O₃ and ZnO nanoparticles in POE oil and in refrigerant R410A and POE mixture. The details of the

testing of the surfactants were reported in Bigi et al. (2017) and Bigi (2018) and will not be repeated in here. However, it is worth to highlight in here that agglomeration and sedimentation of nanoparticles were not observed in POE oil for a period of 20 weeks of testing with still and undisturbed nanolubricant. In current heat transfer testing with moving nanolubricant inside the test section, as it will be described later in this document, some level of nanoparticle agglomeration was measured at the end of the heat transfer tests with refrigerant R410A and ZnO nanolubricant mixtures. While, significantly less agglomeration was observed when Al₂O₃ nanoparticles were tested.

For the heat exchangers of air conditioning systems, the lubricant is an undesired (yet unavoidable!) contaminant. Nanoparticles have been introduced in the lubricant in order to augment heat transfer exchange effectiveness of evaporators and condensers. Previous researchers have proposed different, and sometimes contradictory, mechanisms of heat transfer under the presence of nanoparticles to explain the apparent inconsistency among their experimental findings. Surface modification due to nanoparticle deposition, rewetting of the surface due to high concentrated nanofluid after bubble departure, and Van der Waals force between the nanoparticles and heating surface were some of the mechanisms recently investigated in the literature. However, these mechanism were mainly postulated and the models experimental validation was limited due to a lack of suitable data that isolated and quantified the effects from each mechanism.

Several studies on pool boiling can be found in the literature for nanofluids. Relevant for the present research work, is the experimental and modeling work of Kedzierski (2011) who used similar refrigerants and nanolubricants (and more important, same type of surfactants!) as the ones used in the present work. For this reason, Kedzierski (2011) pool boiling model was the basis of the present superposition model for nucleate boiling component of heat transfer. In Kedzierski

research work, the main contribution of the nanoparticles was the transfer of momentum from the nanoparticles to the bubbles in the lubricant excess layer close to the heat transfer surface.

Experimental work was conducted in two-phase flow boiling of refrigerant and nanolubricants mixtures. The two-phase flow boiling heat transfer coefficient with spherical CuO and Al₂O₃ based nanolubricants, were generally augmented in micro-fin tubes and the associated increase of two-phase flow pressure drop was negligible across several of the papers reported in the literature review section (Cremaschi et al. 2017; Deokar et al. 2016; Henderson et al. 2010). A common outcome reported in the literature was that the magnitude of the heat transfer enhancements were much higher than the gain in the effective thermal conductivity due to the nanoparticles dispersed in the liquid phase of the mixture (Bartelt et al. 2008; Y. Ding et al. 2007a; Kedzierski and Gong 2009; White et al. 2010).

The diffusion of the nanoparticles within the refrigerant-oil liquid layers and possessing relative (slip) velocities promoted an increase in Nusselt number (Buongiorno 2006; Cremaschi 2012; Savithiri et al. 2011; Wen and Ding 2005). Cremaschi (2012) developed a first-principle model for the slip mechanisms of the nanoparticles in refrigerant and nanolubricants two-phase flow processes. Bigi and Cremaschi (2019) showed that Brownian motion and thermophoresis were the main mechanisms that contributed to the slip mechanisms of the nanoparticles in the refrigerant-oil laminar sublayer. Bigi (2018) also developed a superposition model to describe the evaporative two-phase flow of a refrigerant-nanolubricant mixture. In his approach, Bigi combined the Buongiorno (2006) model for nanofluid convective heat transfer with the Kedzierski (2012) model for pool boiling of refrigerant-nanolubricant mixtures on finned heated surface. The present work model, which was built on Bigi's original model, addressed several limitations that were observed when applying Bigi's original model. With the additional experimental data measured in

the present work, Bigi's original model was improved and extended to Al₂O₃ and ZnO nanoparticles laden lubricants and refrigerant R410A saturated two-phase flow boiling in horizontal smooth copper tubes. It is worth to note here that an internally smooth copper tube was intentionally selected for the model experimental validation in the present work in order to isolate and quantify the effect of the nanoparticles in well-defined two-phase flow conditions. Because the internal fins were absent, the uncertainty associated with local boundary layers around the fins was practically eliminated. This allowed to investigate the nanoparticles local concentration in laminar sublayers regions for stratified-wavy and annular flow regimes.

Finally Appendix-A provides a summary of the water and refrigerant based pool and flow boiling experimental studies from the literature. For each studies, detailed information of the nanofluid(s), experimental test condition(s), test section geometry, heat transfer result(s), pressure drop result(s), and correlations information, if any were developed and reported in the literature.

3. Experimental Setup

This chapter presents the details of the experimental test apparatus that was designed, built, and instrumented as part of this PhD work and the description of main lab equipment and facility components that were used during the testing campaign for nanolubricants. Two-phase and single-phase tested conditions for refrigerant R410-lubricant mixtures are also presented in this chapter. Data reduction, uncertainty analysis, and important details for the estimation of the actual oil mass fraction in the mixture during the heat transfer tests are presented at the end of this chapter.

Figure 4 shows the experimental test apparatus of the present work. The test apparatus was a refrigerant pumped loop consisting of a test section with an evaporator tube. This tube is also referred as to “tube calorimeter” throughout this thesis. This test facility had only horizontal sections and vertical downward sections in the parts of the loop in which the refrigerant and oil mixtures were in the two phase region. This feature was important because it effectively eliminated any oil traps or potential pockets in which the nanoparticles can be get stuck from one test to the other. The tube calorimeter facility has only one riser, completely in the subcooled liquid region right at the outlet of the pump. And, since POE is completely miscible with refrigerant R410A in this section of the loop, no oil was retained in the pipelines of the test facility. It is worth noticing in here that this design of the pipeline of the test apparatus loop allowed to achieve good repeatability of the experimental results at various time intervals during the experimental test campaign.

The gear pump in Figure 4 increases the pressure of the subcooled liquid refrigerant from point (a) to (b), as shown in thermodynamic p-h diagram of refrigerant R410A of Figure 5. At the point (b), the refrigerant was significantly subcooled and the absolute pressure and temperature were measured to determine the enthalpy, $h_{preheater,in}$, of the refrigerant before it enters the preheater. The refrigerant was brought within the saturation region by the pre-heater, from point (b) to (c), with a vapor quality, x_{in} , between 0.14 and 0.68 at the inlet of the test section. The change in the vapor quality inside the test section, that is, from point (c) to point (d) in Figure 5, was typically less than 0.2. The refrigerant enters the postheater where it was further evaporated at the point (e). This was required in order to control and maintain the saturated pressure and temperature of the pumped-boiler loop system when varying the mass flux and inlet refrigerant quality to the test section. The refrigerant circulates through the subcooler from (e) to (a), where it was brought back to subcooled liquid before reentering the gear pump. The refrigerant mass flux was measured by a Coriolis type mass flow meter, from the manufacturer Micromotion, at the inlet of the preheater, and the speed of the gear pump, from Micropump Inc., which was controlled by a variable frequency drive, set the mass flux in the test section. The recording of the tests were started after steady state conditions were achieved during testing. Each test measurement was recorded for 30 minute at a sample rate of every 2 seconds.

Figure 6 shows the refrigerant flow circuitry involving the test section, the postheater, and the oil separator. The figure also shows location of shut-off valves installed on the system, whose purpose was to bypass the oil separator for ‘oil circulation tests’ and to isolate system in different sections to perform preliminary leak checks. The ‘oil circulation tests’ are discussed later in the document.

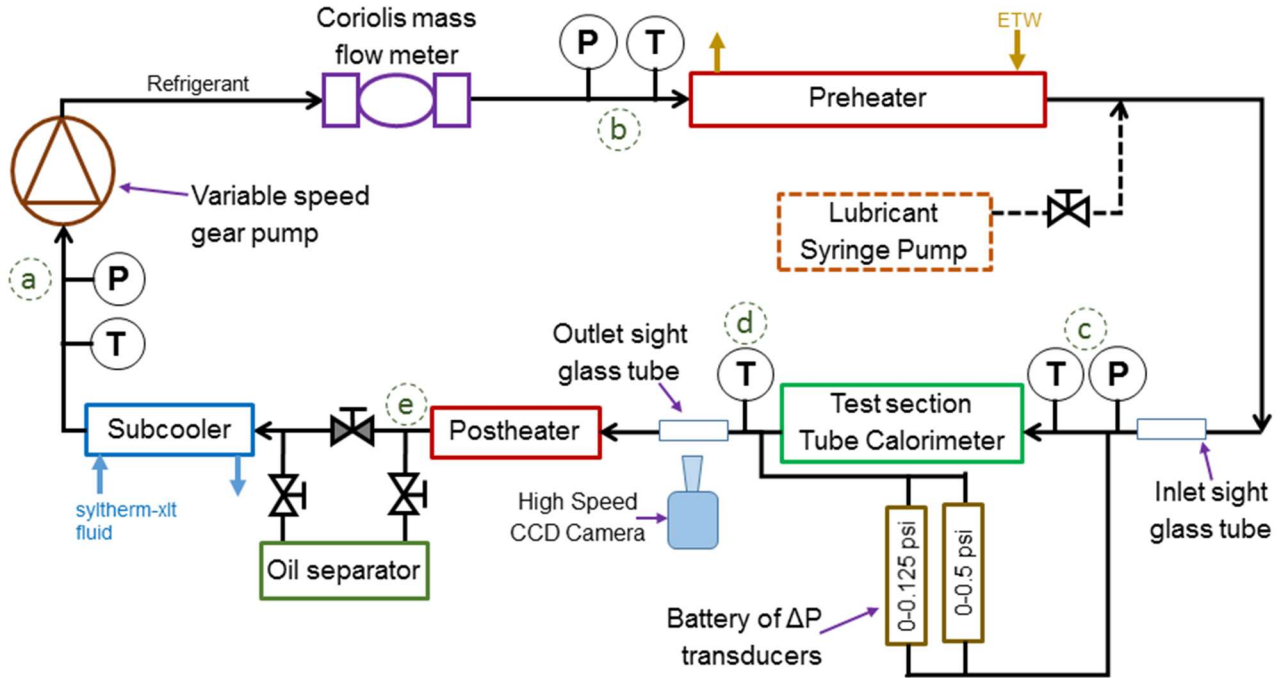


Figure 4: Schematic of the test apparatus.

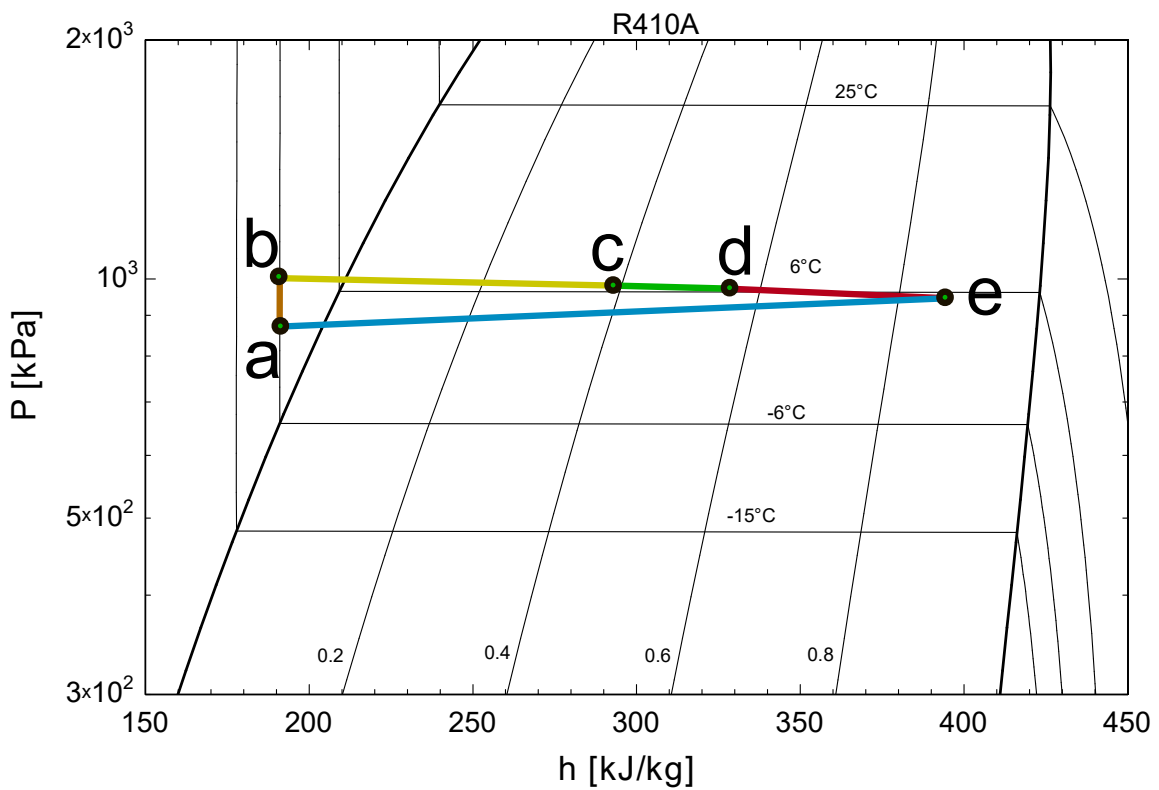


Figure 5: P-h diagrams of a two-phase flow test in the test apparatus.

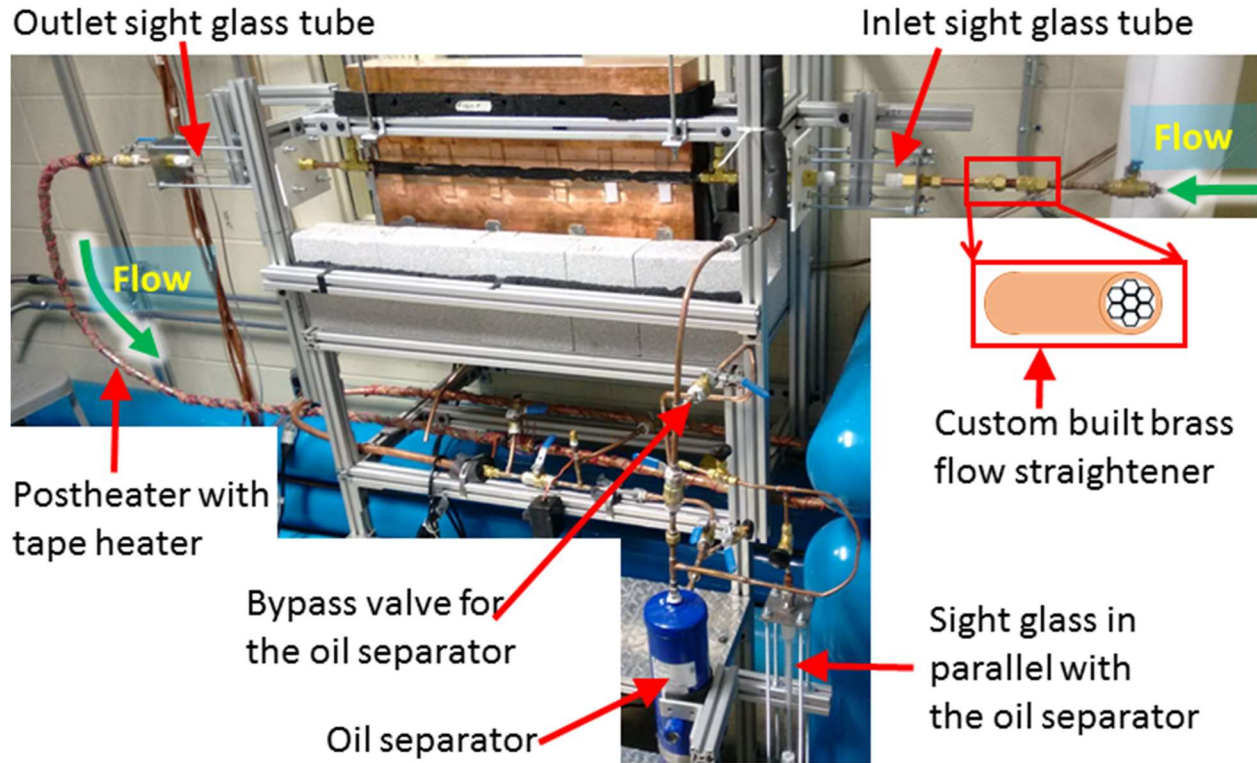


Figure 6: Image of the refrigerant flow circuitry through the test section, the postheater, and the oil separator.

Figure 6 also shows the cross section of the flow straightener installed upstream of the test section, the purpose of the flow straightener was to eliminate rotation in the flow before it entered the test section. A length of $30 \times D_h = 0.3$ m (11 inch) of 9.5 mm inner diameter tube was maintained after the flow straightener to allow a fully developed flow to enter the test section. Sight glasses were installed at the inlet and the outlet of the test section to provide optical access to the two-phase flow pattern. The details of the components and instrumentation of the test apparatus are further discussed in details

3.1. Components of the Experimental Test Facility

Test Section

A unique test section (tube calorimeter) was designed and constructed for the tests, as shown in Figure 4 and Figure 7. Copper blocks were used to direct heat from the top and bottom plate heaters to the refrigerant copper tube. Figure 7 (a) shows the liquid refrigerant and lubricant mixture with suspended nanoparticles accumulate on the inner wall of the smooth horizontal tube. The copper tube had a thick wall of $t=1.65$ mm and an inner hydraulic diameter (I.D.) of $D_h=9.5$ mm, and was placed in circular-grooves cut in the copper blocks, this allowed for uniform application of heat flux along the circumference and length of the copper tube.

Thirty T-type thermocouples were placed in 1.6 mm (1/16 inch) diameter holes drilled to the center of the 25.4 mm (1 inch) thick copper blocks to calculate the local heat fluxes ($\dot{q}_{\bar{i}m}$) and local inner wall temperatures ($T_{s,\bar{i}m}$) along the length of the tube. Figure 8 and Figure 9 shows the detailed location of the thermocouples attached on the copper blocks and outside the refrigerant copper tube. The locations on copper blocks were termed as level1 to level6 as shown in figures. Figure 8 shows the dimensions of the copper blocks, as well as the arrangement of copper blocks on top and bottom side of the refrigerant tube. Figure 8 gives clear distinction between the naming of the copper blocks; the top slab/block of copper had level1 and level2 thermocouples, the top copper block had level3 thermocouples, the bottom copper block had level4 thermocouples, and the bottom slab/block of copper had level5 and level6 thermocouples. The copper blocks were made of C110 copper and the refrigerant copper tube was made of C122 copper.

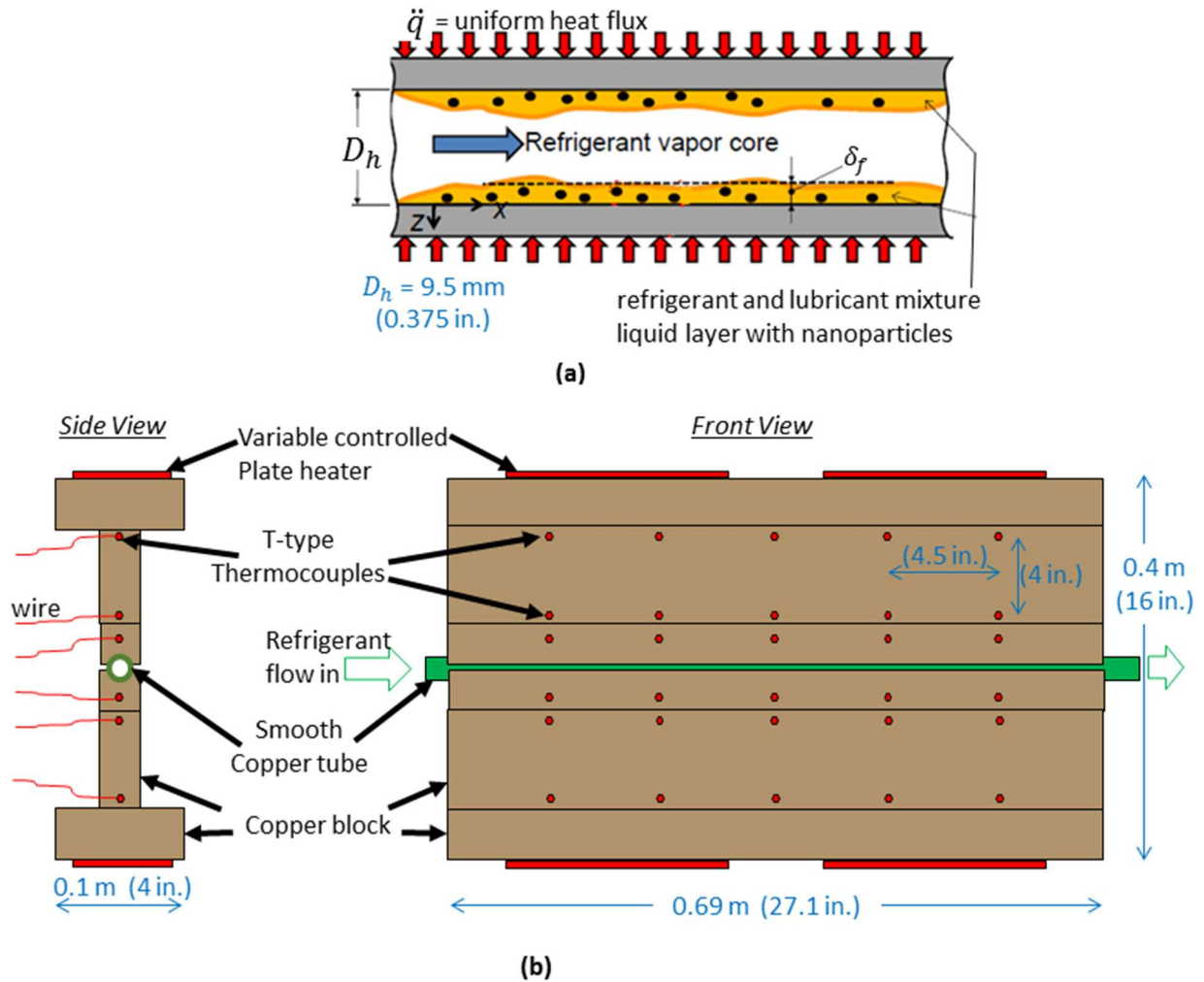


Figure 7: (a) Two-phase annular flow during boiling of refrigerant and nanolubricant mixture in a smooth tube, and (b) Schematic of the tube calorimeter (test section) with the location of thermocouples and heaters.

Figure 9 shows the refrigerant copper tube, of outer diameter (O.D.) of 12.8 mm, was placed in a 0.69 m long circular-groove cut in the top and bottom copper blocks. The circular-grooves were cut 1.59 mm deep in the copper blocks using a ball end mill of 12.8 mm (0.5 inch) diameter. A thermal paste (Arctic Silver[®] 5, High-Density Polysynthetic Silver Thermal Compound) was used in thermocouple holes and in between the mating copper blocks and refrigerant copper tube in order to eliminate the microscopic air gaps and maximize the heat

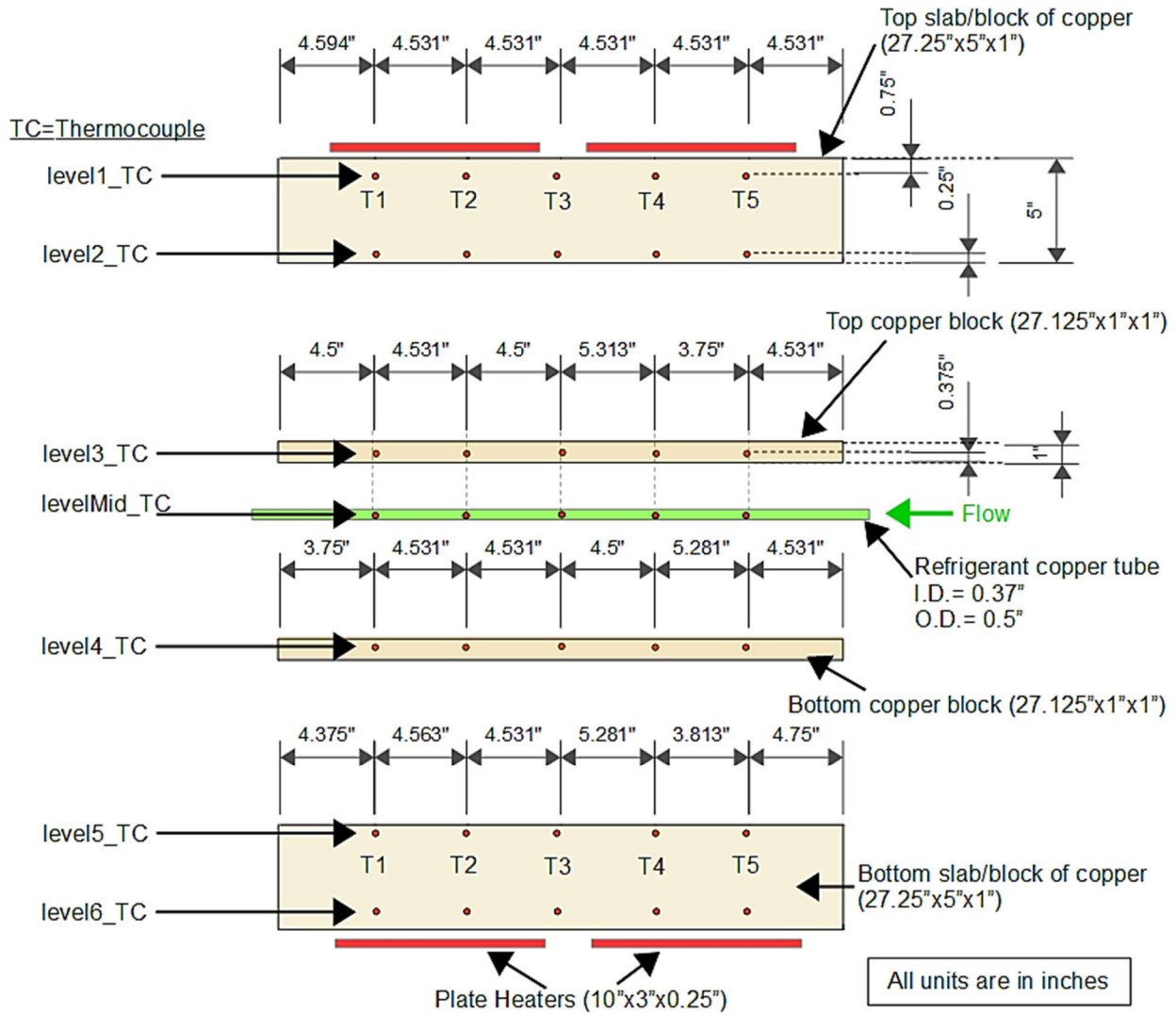


Figure 8: Exploded view of the test section with plate heater and welded thermocouples' locations on the copper blocks and refrigerant copper tube.

transfer. As shown Figure 9, the refrigerant copper tube surface in contact with top copper slab was called as top surface ($\bar{m}=1$), the refrigerant copper tube surface not in contact with any copper slab was called as side surface ($\bar{m}=2$), and the refrigerant copper tube surface in contact with bottom copper slab was called as bottom surface ($\bar{m}=3$). \bar{m} was the locations on the top, side, and bottom of the inner wall of the test section tube. \bar{l} was the locations along the length of the test

section tube. Figure 10 shows the image of the assembled components of the tube calorimeter (test section) before insulation.

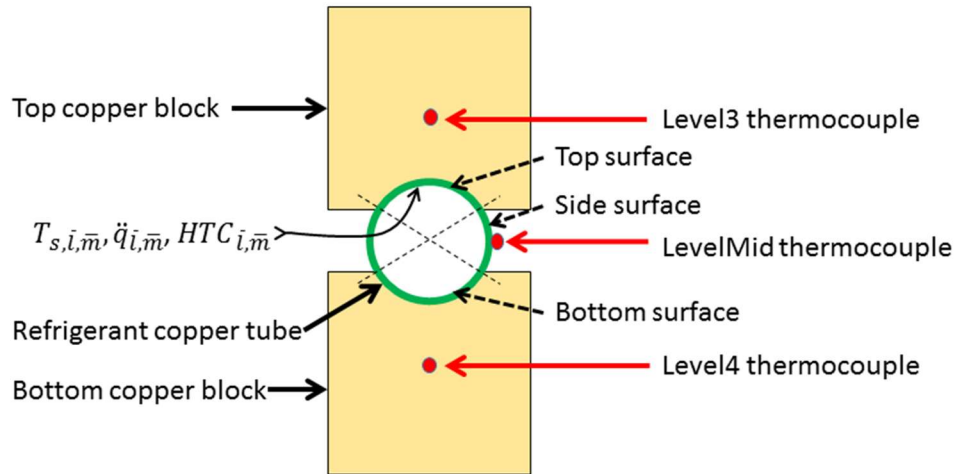


Figure 9: Cross section of refrigerant tube placed in the groove of copper blocks.

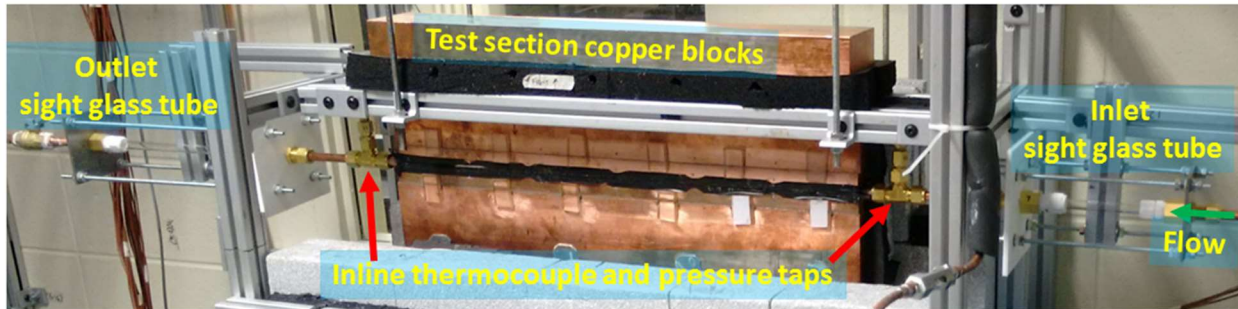


Figure 10: Tube calorimeter (test section) before insulation.

Figure 11 shows the arrangement of an inline thermocouple and the pressure line to the absolute pressure and differential transducers at the inlet of the test section. The inline thermocouples measured temperatures at the inlet, $T_{ref,in}$, and outlet, $T_{ref,out}$, of the test section. The inline thermocouple had a probe diameter of 1.6 mm and was inserted inside the refrigerant tube through a 6 mm hole drilled on the top side of the refrigerant copper tube. This arrangement allowed to have reduced flow disturbances at the location of intrusive temperature measurement.

The absolute pressure, $P_{ref,in}$, was measured at the inlet of the test section and two differential pressure transducers, with 0-0.86 kPa (0-0.125 psi) and 0-3.45 kPa (0-0.5 psi) ranges, were installed in parallel in order to measure the pressure drop, ΔP , across the test section. Depending on the actual pressure drop during an experiment, one of the two pressure transducers that had suitable full scale, was opened with help of valves to the test section inlet and outlet for measuring the refrigerant pressure drop. The pressure drop were measured over the test section copper tube length of $L_{\Delta P}=0.84$ m, and this length was further used to calculate the pressure gradient along the test section, $\Delta P/L$. The actual heat transfer length of the test section was $L_{HT}=0.69$ m. Figure 12 shows the image of the installed differential pressure transducer used to measure the pressure drop across the test section. Figure 12 shows three installed differential pressure transducer, however, only two were used for experiments.

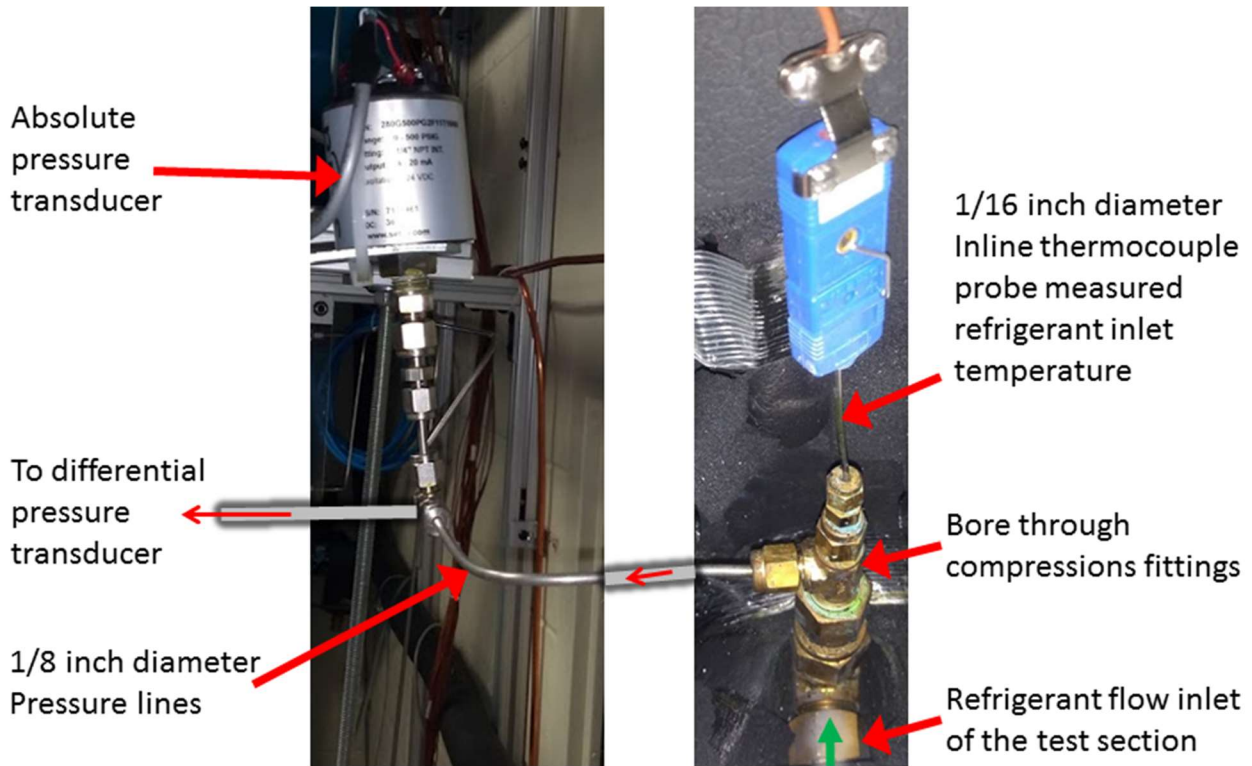


Figure 11: Inline thermocouple and absolute pressure transducer at the inlet of the test section.

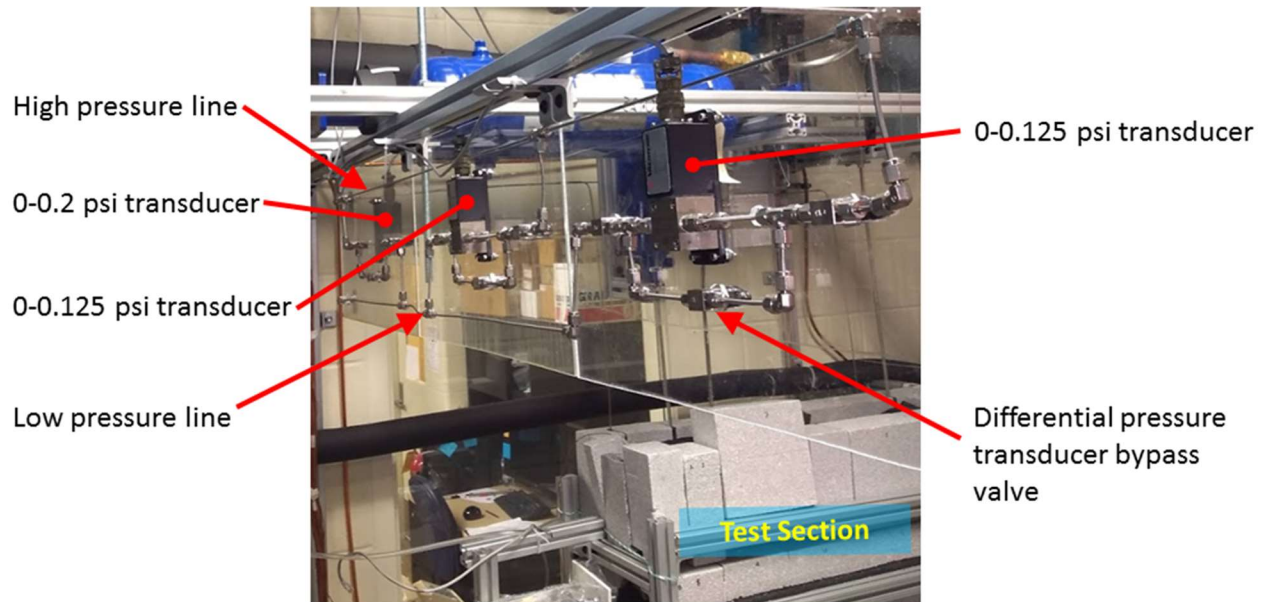


Figure 12: Assembly of differential pressure transducers.

Figure 13 shows plate heaters attached to the top of the copper block, and in the same configuration as explained in Figure 7 (b) and Figure 8. The variable transformers shown in the figure were used to control the plate heaters' supply voltage from a remote location. The figure also shows the use of high temperature limit switch to safely disrupt the power to the heaters in case of excess heating of copper.

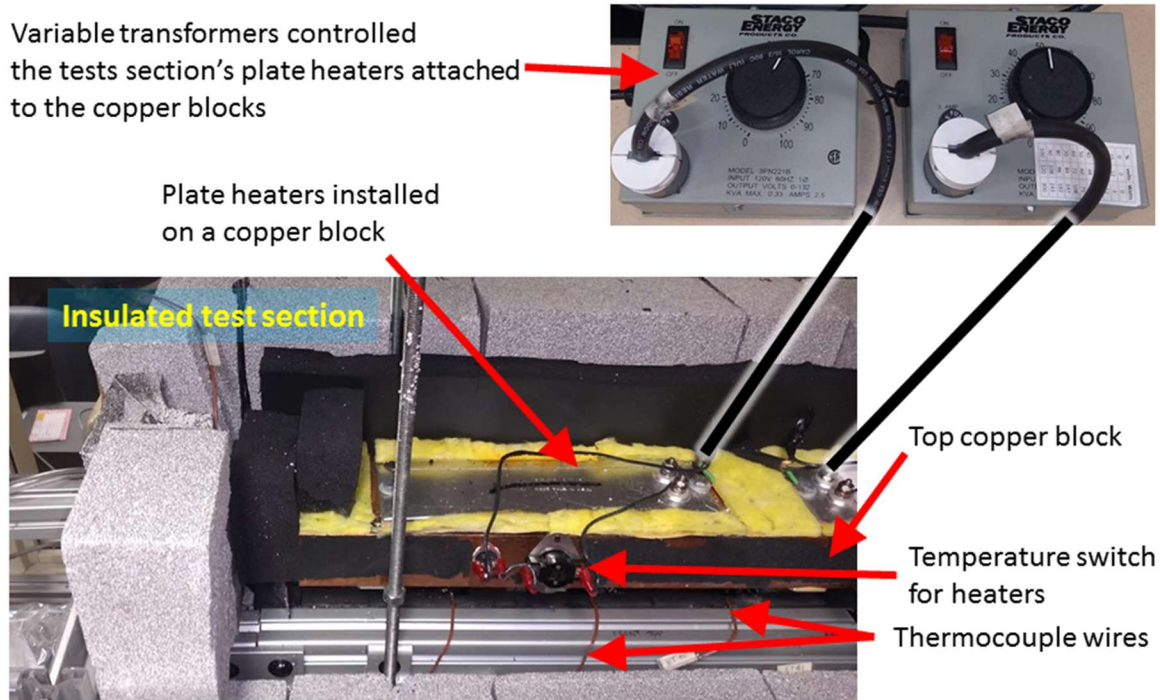


Figure 13: Plate heaters on the copper block.

Preheater

The preheater in Figure 4 controlled the refrigerant vapor quality at the inlet of the test section. The preheater was a counter flow tube in tube heat exchanger made of stainless steel. The refrigerant flowed in the inner tube of 9.5 mm I.D., while the 65%/35% mixture of water/ethylene-glycol (ETW) flowed inside the annulus. The outer tube had 25.4 mm I.D. and was covered with a 8 cm thick rigid polyurethane foam pipe insulation. The total length of the preheater was 5.5 m, and was a combination of two heat exchangers in series. The heat transfer from ETW mixture to the refrigerant in the preheater within 0.3 kW to 1.4 kW, and the corresponding change of the refrigerant enthalpy at the inlet of the test section, was controlled by varying the temperature of the ETW mixture within 12°C and 32°C. This allowed to achieve the desired refrigerant vapor quality of the fluid entering the test section. The temperatures entering and exiting the ETW lines to the preheater were measured using inline thermocouples, and these measurements ever used to

calculate the heat transferred to the refrigerant. An inline thermocouple and an absolute pressure transducer on the refrigerant line at the inlet of the preheater were used to evaluate the enthalpy, $h_{ref,preheater,in}$, of the subcooled refrigerant entering the preheater. In-house and in-situ calibrated inline T-type thermocouples were installed at several location in the test apparatus loop to measure refrigerant-lubricant mixture temperatures.

Postheater

The postheater in Figure 4 was installed to control and maintain the saturated pressure and temperature of the pumped-boiler loop system when varying the mass flux and inlet refrigerant quality to the test section. It was also used to bring the refrigerant and oil mixture to the superheat vapor region before entering the oil separator in order to effectively separate the lubricant from the refrigerant vapor. This operation was done in between the series of tests when cleaning and purging of the lubricant (or nanolubricant) from the test section was required. The postheater was made of a copper tube of 19 mm I.D., the total length of the postheater was 4.5 m, and had two variable controlled 576 W tape heaters surrounding the tube. The heat transfer from the tape heaters to the refrigerant was controlled within 0 kW to 1.1 kW. When the heat input to the refrigerant at the preheater was low at low refrigerant vapor quality tests, the postheater balanced the remaining heat input to the refrigerant to maintain uniform refrigerant superheat at the inlet of the subcooler.

Subcooler

The subcooler in Figure 4 controlled the refrigerant subcooling at the inlet of the variable speed gear pump. The subcooler was a counter flow tube in tube heat exchanger made of stainless steel. The refrigerant flowed in the inner tube of 9.5 mm I.D., while the syltherm-xlt fluid flowed inside the annulus. The outer tube had 25.4 mm I.D. and was covered with a 8 cm thick rigid polyurethane foam pipe insulation. The total length of the subcooler was 2.5 m. The heat transfer

from the refrigerant to the syltherm-xlt was controlled within 3 kW to 6.5 kW by varying the temperature of the syltherm-xlt fluid within -17°C and -31°C. This allowed to achieve 4°C to 20°C of subcooling of the refrigerant at the inlet of the variable speed gear pump.

Lubricant Syringe Pump

A precision syringe pump, model 1000D from Telydyne ISCO, in Figure 4 and Figure 14 allowed for slow and gradually metered lubricant injection before the test section at a flow rate of 0.03 g/s. The lubricant was injected after the preheater and at a length of 4.3 m before the test section to ensure the liquid refrigerant and lubricant are well mixed before entering the test section. The mass of the refrigerant, m_{ref} , charged in the refrigerant loop of the test apparatus was measured, and the masses of injected POE oil, m_{oil} , or nanolubricants (NL), $m_{np} + m_{oil}$, were calculated based on the desired specific oil mass fraction, $OMF = m_{np}/m_{ref}$ or $OMF = (m_{np} + m_{oil})/m_{ref}$, that had to be achieved during the experiments.

Figure 14 shows the lubricant syringe pump along with the fluid lines and valves used to inject lubricant in the refrigerant line in between the preheater and the test section. The control panel of the syringe pump was used to maintain the pressure and flow rate of the injected lubricant.

Liquid sampling, as per ASHRAE Standard 41.4-1994, was tried to measure the OMF in the liquid samples withdrawn from the flow circuit, but was inconvenient for the current setup as it disrupted the steady-state testing conditions and also because the error was excessive in the little extracted mass of oil. Oil concentrations were estimated using the subcooled refrigerant-oil mixture density measurements from the Coriolis mass flow meter using the method described by Thome (2010); however, the OMF calculated with this method had too much error due to considerable uncertainty in the density measured. Hence, the OMF was determined by measuring the masses of the refrigerant and oil charged into the system.

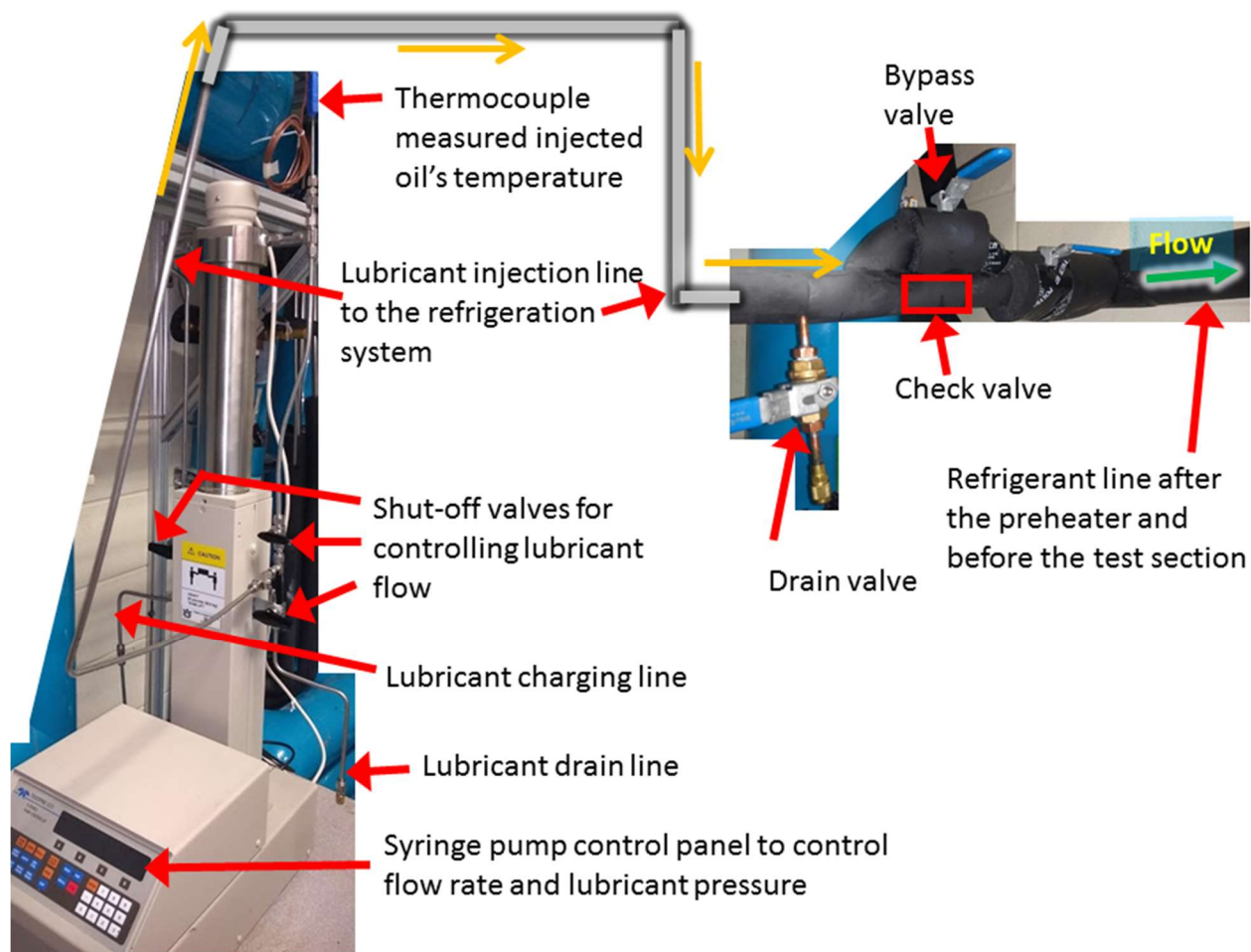


Figure 14: Lubricant syringe pump setup with lubricant injection line connected to refrigerant line of the test system.

Oil Separator

The oil separator, in Figure 4, placed after the test section and postheater could be isolated using shut-off valves to allow the refrigerant and lubricant mixture to circulate through the entire system, these tests were termed as ‘oil circulation tests’ in this work. Mostly horizontal pipelines and absence of any reservoir or pockets in the test apparatus’ loop prevented trapping of the lubricant and ensured consistent *OMF* at the test section throughout the testing duration. The oil

separator was engaged inline with the system to perform a set of tests termed as ‘oil injection-extraction tests’, in which the injected oil before the test section was collected after the test section using the oil separator and thus preventing the oil to circulate through the rest of the test setup. The oil separator also allowed to extract the lubricant from the system once the oil circulation tests were conducted. The extracted lubricant samples were further used to study sedimentation characteristics and size of the nanoparticles after the flow boiling tests. Several purging ports and shut off valves, not shown in Figure 4 for clarity, were installed before and after the components of the refrigerant loop in order to clean the components and remove lubricant and nanolubricant residuals at the end of the experiments. Cleaning operations were carried out at the end each R410A-lubricant and R410A-nanolubricant (NL) test series. These cleaning operations involved allowing the refrigerant and lubricant mixtures, at refrigerant vapor qualities of above 0.85, to flow through the oil separator for a duration of more than 24 hours to ensure all lubricant and nanoparticles were removed from the system. The postheater helped to achieve high refrigerant vapor qualities at the inlet of the oil separator. The oil separator was heated with a tape heater to help evaporate refrigerant from the mixture, to prevent accumulation of liquid R410A inside the oil separator.

Figure 15 shows the image of the helical oil separator along with the installed tape heater. The tape heater was used to provide heat and evaporate the refrigerant inside the oil separator to prevent flooding of the oil separator during the ‘oil injection-extraction tests’ and cleaning operation. The ‘oil injection-extraction tests’ and cleaning operation are explained in previous paragraph. No internal float valve was present inside the oil separator to help remove maximum extracted oil from the oil separator once the tests or cleaning operations were completed.

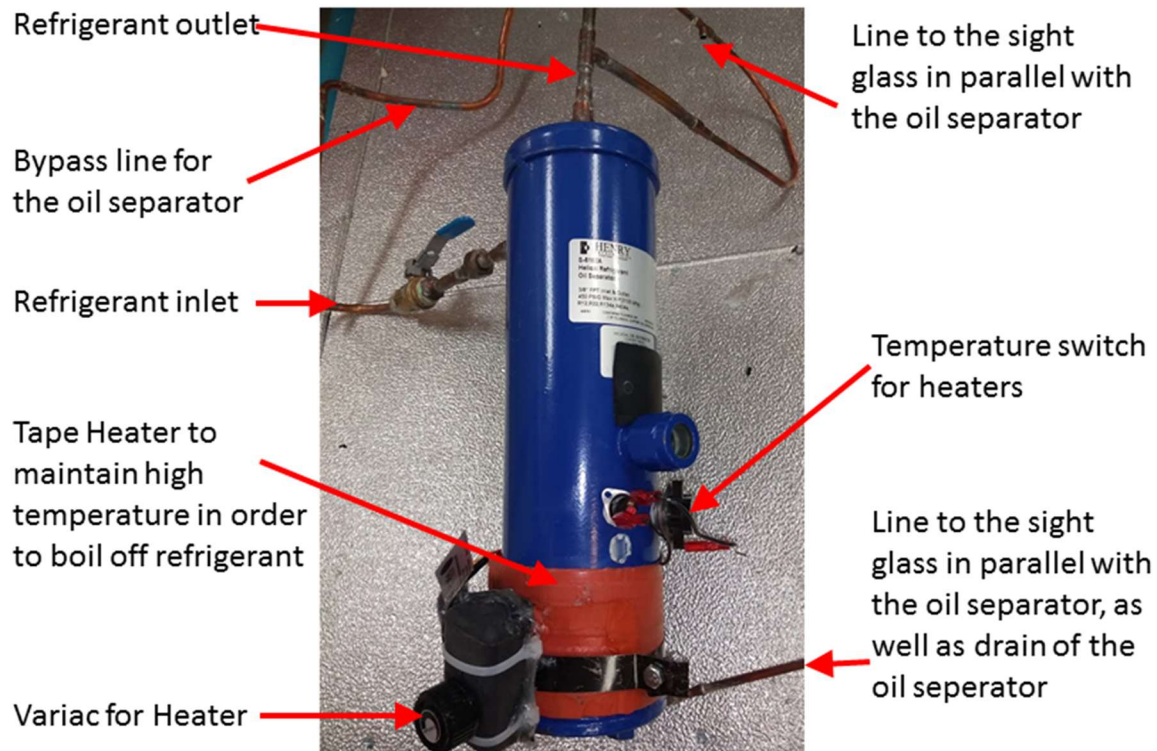


Figure 15: Oil separator with tape heater

Sight Glass tube

The sight glass tubes at the inlet and outlet of the test section are visible in Figure 6 and Figure 10. A compressed air displacement technique was used to clear the sight glass from external condensation and fogging as the refrigerant saturation temperatures inside the tube was below the dew point temperature. Figure 16 shows the sight glass at the exit of the test section covered with a transparent thin plastic film, where a flow of compressed air was supplied in between the plastic film and sight glass tube to limit any water vapor condensation on the outside of the glass tube. The sight glass tubes had same inner diameter as the test section copper tube to avoid disturbance in the flow pattern. A high-resolution high-speed CCD camera, Model MiniAX from Photron, with zoom magnifying lens optic was used to observe the flow pattern and nature of the liquid-vapor

interface at the test section's outlet sight glass tube, as shown in Figure 16. The camera captured flow pattern images and videos with a resolution of 768 x 769 pixels at 4000 fps.

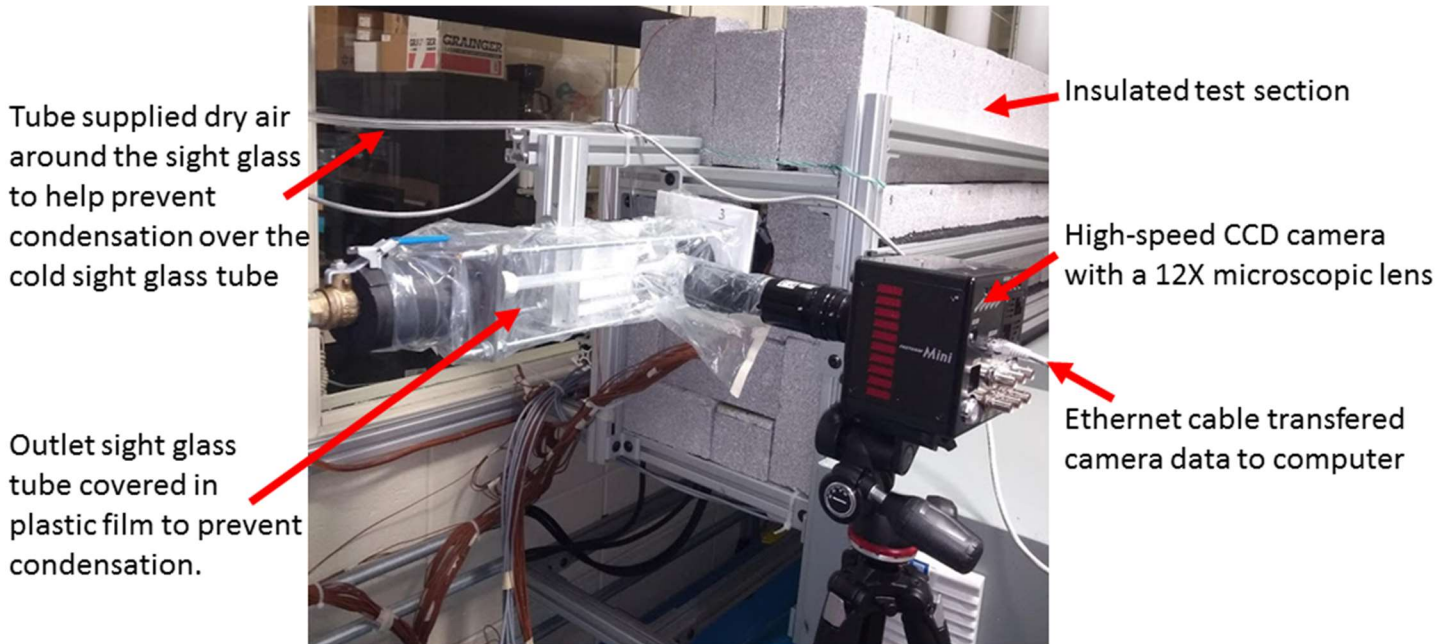


Figure 16: Outlet sight glass tube with high-speed CCD camera

Low Temperature Refrigeration Chiller Facility

Figure 17 shows the low temperature refrigeration chiller facility at Auburn University. This equipment was a low temperature refrigeration chiller with cooling capacity of 7 tons (25 kW) and temperature range from -40°C and $+30^{\circ}\text{C}$. The chiller had temperature control of $\pm 0.3^{\circ}\text{C}$ and process fluid flow rate ranging from 10 to 40 gpm.

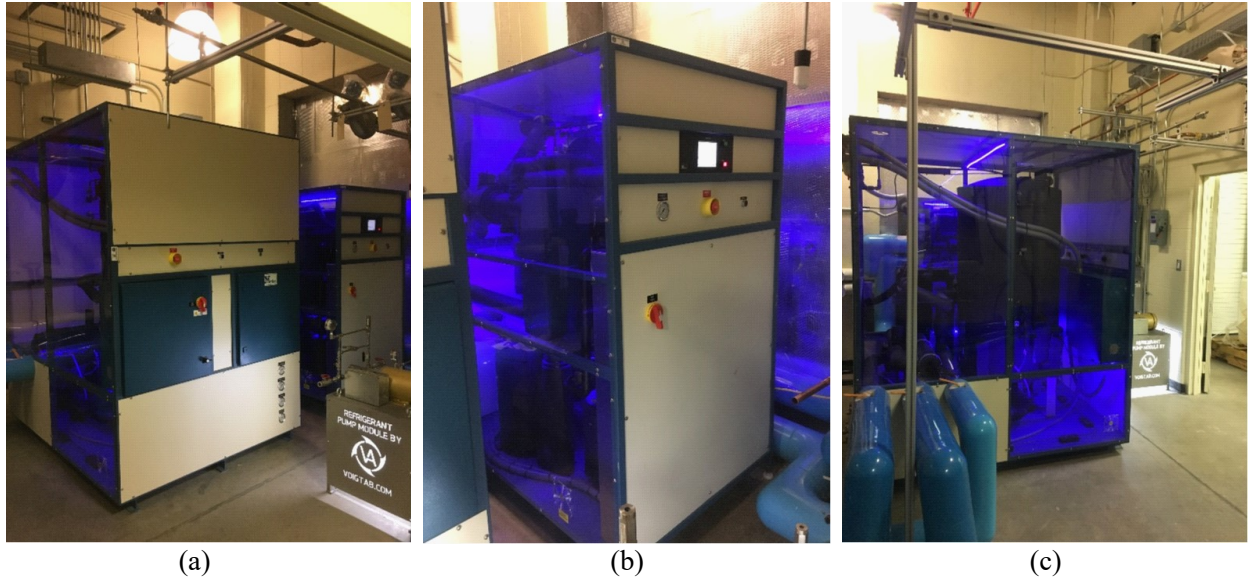


Figure 17: (a) Pump module and low temperature cryogenic chiller installed side by side, (b) cryogenic refrigeration module, and (c) water/ethylene-glycol pump module at the facility.

Figure 18 shows the piping diagram at the Auburn University research laboratory with all the control valves, pumps, and auxiliary heaters of the facility. During this PhD work, the refrigerant flow loop used for nanolubricant heat transfer testing was designed, built, and instrumented, which is shown in orange color lines. The water/ethylene-glycol ETW flow lines from pump module to the preheater is shown in green color lines, and the syltherm-xlt fluid lines from cryogenic chiller module to the subcooler is shown in yellow color lines. These lines were instrumented for measurement and control and were connected to the DAQ systems in order to perform the tests.

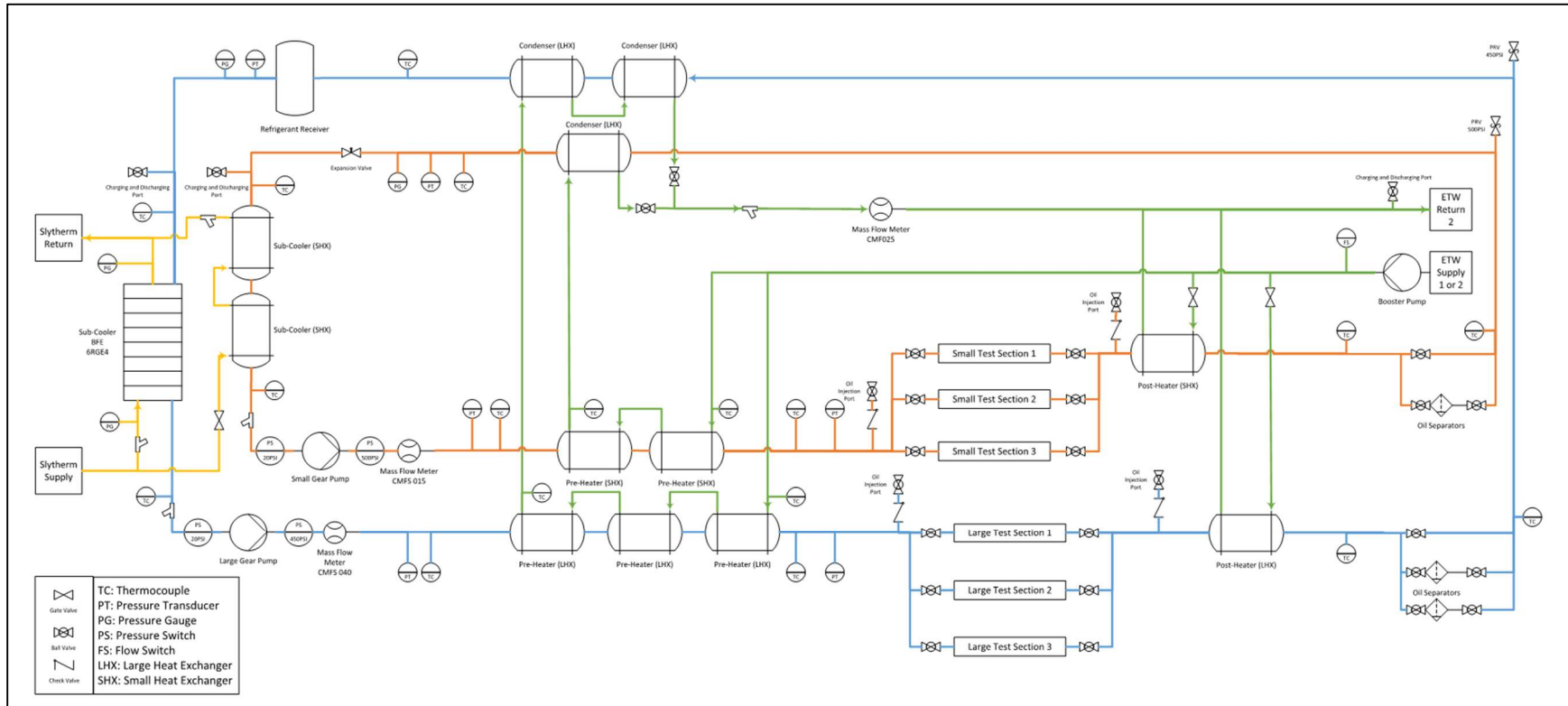


Figure 18: Schematic of the tube calorimeter facility for refrigerants heat transfer and pressure drop research at research facility.

Data Acquisition System (DAQ) and Controls

National Instruments controller and hardware was installed, as shown in Figure 19, and VIs (virtual instruments) were coded in LabVIEW program to communicate with the controller to record thermocouple, pressure, and flow rates measurements and also to transmit analog, digital, and serial communication signals to control the operations of the system components. The National Instruments controller was a NI cDAQ-9137 Controller, Atom 1.91 GHz, 32GB, 8-Slot, Linux RTPXI and performs all computations essential to operate the test facility, while a host computer was used as the graphical user interface, which displayed the sensor readings and their corresponding plots.

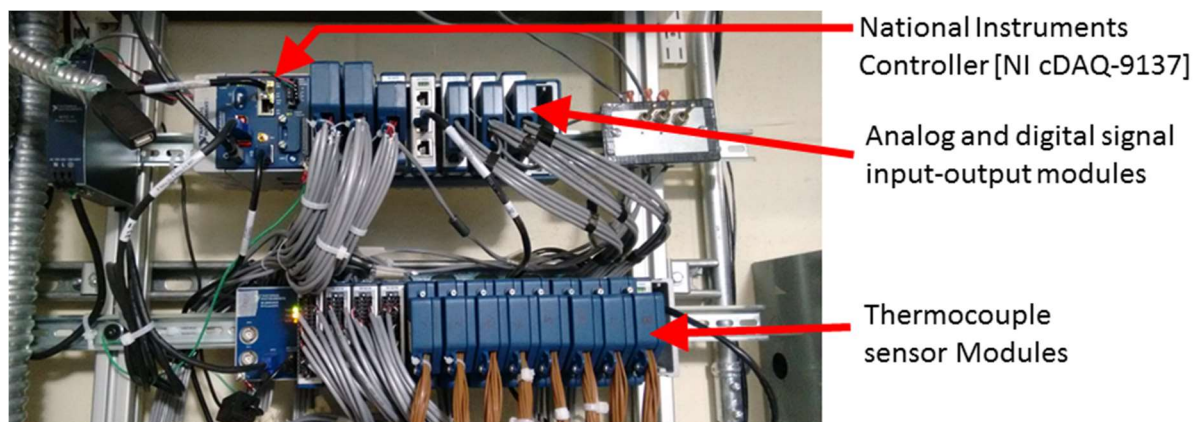


Figure 19: National Instruments data acquisition controller and hardware.

Figure 20 and Figure 21 shows control station for conducting experiments, the LabVIEW front panel on the monitor was used to observe live process variables to make adjustments to the system conditions, while the variable transformers in the figure were used to control the plate heaters attached to the copper blocks of the test section. The controlled system components through LabVIEW program were VFD frequency of refrigerant gear pump, the Cryogenic Chiller Module fluid's (syltherm xlt fluid) temperature that was used to condense the R410A refrigerant in the subcooler, and the water/ethylene-glycol Pump Module to pre-boil the refrigerant in the preheater

to achieve desired quality at the inlet of the tube calorimeter. Appendix-B shows the front panels (Figure 58 and Figure 59) created in LabVIEW program to observe the process variables on test system schematic while conducting experiments and coded VIs (Figure 60) to evaluate and plot the process variables.

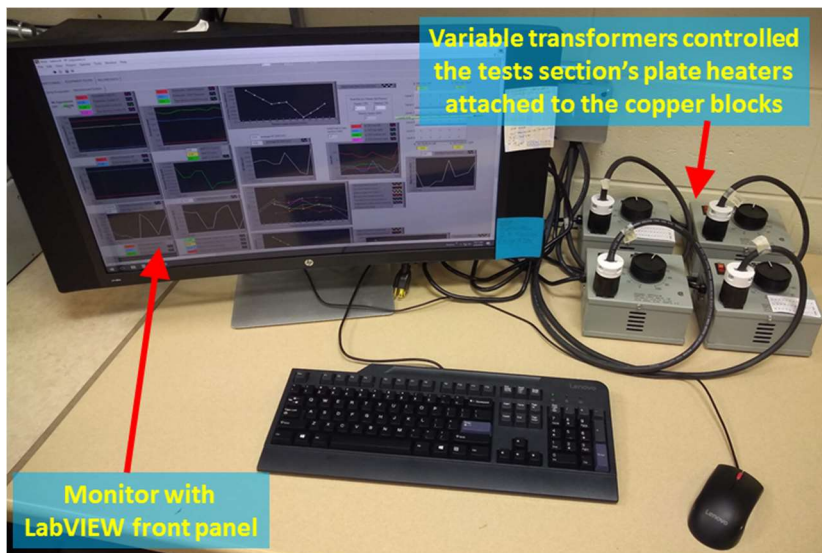


Figure 20: Control station for conducting experiments.



Figure 21: Monitors and LabVIEW graphic user interface of the test facility.

Nanoparticle Sizer

A Nano zetasizer analyzer, shown in Figure 22, was used to measure the nanoparticle sizes when dispersed in the base lubricant. The model of the Nano Zetasizer Analyzer was ZEN3600, and was manufactured by Malvern Instrument. The device was capable of measuring particle sizes ranging from 4 nm to 10 μm diameter. The instrument included application software and a user-friendly interface for measurement control and data analysis. It worked on the principal of dynamic light scattering (DLS) to measure the particle size and provided number weighted based average equivalent diameters of nanoparticles. The DLS instrument implemented an electrophoretic light scattering technique with a He-Ne laser of 633 nm wavelength. The interface software of the instrument analyzed the measurements on-line and correlate the back scattering reflection intensity of the laser to the mean particle sizes of the sample. The tested nanolubricant samples were diluted with POE oil to concentration of less than 1 wt.% before measuring the particle size in order to improve the reliability and accuracy of the particle size measurements. No zeta potential of nanofluid was measured in this work.



Figure 22: Nano zetasizer for measuring nanoparticle size of the present work.

Ultrasonicator

An ultrasonic liquid processor was used to homogenize the nanoparticle dispersion in the base lubricant and to potentially de-agglomerate the nanoparticle clusters before the heat transfer experiments. The equipment was a Vibra-Cell Ultrasonic Liquid Processor Model VC-750 with a 1 inch high efficiency solid full wave probe and booster amplifier manufactured by Sonics&Materials, Inc. A 750 watts, 20 kHz microprocessor-controlled timer controlled the energy delivered to the liquid to break the particle agglomerate. The Vibra-Cell instrument included a display monitor and controller in a compact design.



Figure 23: Ultrasonicator probe (top photos) and controller (bottom photo) used in present work.

Borescope-type CCD camera

A high definition borescope CCD camera, shown in Figure, was used to capture the images inside the test section tube to see nanoparticle deposition on the wall of the tubes. The camera was manufactured by Olympus America, Inc.; the IV9000N IPLEX NX base housed the image processor, controller, and touchscreen, and the IV9435N IPLEX NX SCOPE had the magnifying optical probe with embed CCD camera and high intensity lights in fiber optic bundle.



Figure 24: Borescope-type CCD camera used in present work.

Table 1 provides the specification of the components used in the experimental test apparatus. The table also includes the model number, accuracy, range, and location of the thermocouples, pressure transducers, and Coriolis mass flow meter used for testing.

Table 1: Specification of the Components

Components	Manufacturer [Model] {range} (Accuracy) location and use <signal>
Coriolis mass flow meter	Micro Motion Inc. [CMFS015M319N2BAECZZ] {used within 0.4 to 0.9 kg/min} ($\pm 0.04\%$) refrigerant flow in tests section <self excitation, 4-20 mA output signal> Micro Motion Inc. [CMFS040M319N2BAEKZZ] {used within 0.8 to 4.5 kg/min} ($\pm 0.02\%$) water/ethylene-glycol ETW flow in preheater <self excitation, 4-20 mA output signal>
Differential pressure transducers	Validyne Engineering [P55 E-1-E-4-20-W-5-B] {0 to 0.125 psid} ($\pm 0.1\%$ FS) [P55 E-1-E-4-26-W-5-B] {0 to 0.5 psid} ($\pm 0.1\%$ FS) [P55 E-1-E-4-30-W-5-B] {0 to 1.25 psid} ($\pm 0.1\%$ FS) <9-55 VDC excitation, 4-20 mA output signal>
Pressure transducers	Setra [280E] {0 to 500 psig} ($\pm 0.073\%$ FS) Preheater inlet <15-32 VDC excitation, 0.03-5.03 VDC output signal> Setra [280G500PG2F11T19NN] {0 to 500 psig} ($\pm 0.073\%$ FS) Test section inlet <24 VDC excitation, 4-20 mA output signal> Setra [2051500PG2F2B25WNN] {0 to 500 psig} ($\pm 0.11\%$ FS) Gear pump inlet <18-30 VDC excitation, 0-5 VDC output signal>

Components	Manufacturer [Model] {range} (Accuracy) location and use <signal>
Thermocouples	Omega Engineering, Inc. All thermocouples were T-type {in situ calibration from -40 to 54°C for all} [TMQSS-125G-6] inline in system {3.2 mm (1/8 inch) thick probe} (± 0.1°C) [TMQSS-062G-6] inline at inlet and outlet of test section {1.6 mm (1/16 inch) thick probe} (± 0.1°C) [TT-T-24-SLE-1000] welded and used on test section copper blocks {welded bead diameter less than 1.5 mm} (± 0.2°C)
Data acquisition and system control	National Instruments Controller [NI cDAQ-9137, Atom 1.91 GHz, 32GB, 8-Slot, Linux RTPXI] Analog input [NI 9207, NI 9208] signal from pressure sensors and flow meters Analog output [NI 9265] control pump VFDs and heater PIDs Digital output [NI 9475] start/stop pumps and heaters Thermocouple input [NI 9214]
High speed CCD camera	Photron [Mini-AX100] {1024 x 1024 pixels resolution at 4,000fps and a maximum frame rate of 540,000fps, while it was used at 768 x 769 pixels at 4000 fps, Internal memory 16GB, 36-bit color} sight glass tube, along with 12X zoom lens attachment
Refrigerant gear pump	Micropump [GC-M25.JF5S.E] Baldor [ACB530-U1-04A1-4] VFD for gear pump <4-20 mA control signal corresponding to 0-60 Hz>
Lubricant syringe pump	Teledyne ISCO [1000D] {0.001 to 340 ml/min} (± 0.5% of flow rate)
Test section plate heater	McMaster-Carr [3619K841] {120V, 0 to 300 W, plate size 25.4 cm x 7.6 cm} copper blocks of test section
Tape heater	BriskHeat [BSAT101008] {120V, 0 to 576 W, size 25 mm x 2.4 m} postheater
Tape heater	BriskHeat [SRMU100309P] {120V, 0 to 270 W, size 7.6 cm x 22.8 cm} oil separator
Variable transformer	Staco Energy Products Co. [3PN221B] control test section plate heaters {120 V, 2.5 Amps max}
Variable transformer	Staco Energy Products Co. [3PN1010B] oil separator tape heaters {120 V, 10 Amps max}
Helical oil separator	Henry Technologies Inc. [S-5182A]

Components	Manufacturer [Model] {range} (Accuracy) location and use <signal>
Sight glass tube	McMaster-Carr [8729K37] 12.7 mm O.D. and 9.7 mm I.D. tube at inlet and outlet of test section
Nanoparticle sizer, DLS	Malvern [ZEN3600 Zetasizer Nano ZS] {0.3 nm to 10 μ m particle size}
Ultrasonicator	Sonics&Materials, Inc. [Vibra-Cell Ultrasonic Liquid Processor Model VC-750] {1 inch high efficiency solid full wave probe, 750 watts, 20 kHz microprocessor-controlled timer, liquid processing volume capacity of up to 1 liter} homogenize the nanoparticle dispersion in the base lubricant
HD Borescope-type CCD camera	Olympus America, Inc. [IV9000N IPLEX NX base and IV9435N IPLEX NX scope] {base has 8.4" touchscreen, PulsarPic image processor and the controller, while the scope had 4 mm diameter and 3.5 m long probe with measurement tip, and stereo tip adapter and check tool} capture images inside the test section tube after tests

3.2. Test Conditions

In two-phase flow tests, the refrigerant bubble temperature, T_{bub} , was controlled to $6.1\pm 1^\circ\text{C}$, the test section inlet refrigerant absolute saturation pressure, $P_{ref,in}$, was controlled to 975 kPa, and the heat flux, \dot{q} , was $15\pm 0.5\text{ kW/m}^2$. The mass flux, \dot{m} , was incrementally varied from 100 to 200 $\text{kg/m}^2\text{-s}$ to study the nanoparticle influence in stratified-wavy and annular flow regimes. The averaged refrigerant vapor quality, x_{avg} , of the tube was varied from 0.25 and 0.75, and the change in the quality along the length of the tube varied from 0.1 for high mass fluxes to 0.22 for very low mass fluxes. The inlet refrigerant vapor quality, x_{in} , of the test section tube was varied from 0.14 and 0.68. The POE oil or the nanolubricant circulated through the tests section an *OMF* of 2.4 wt.% during the two-phase flow boiling tests. The *OMF* is defined in equation (4).

In the single-phase flow tests, the refrigerant temperature, T_{ref} , was controlled to $9.6\pm 1.1^\circ\text{C}$ and the heat flux was $8.6\pm 0.4\text{ kW/m}^2$. The inlet single-phase refrigerant absolute pressure, $P_{ref,in}$, of the test section tube was within 1400 kPa and 1740 kPa during tests, while the test section inlet subcooled temperatures were within 9°C and 17°C . The mass flux of the refrigerant-lubricant mixture was varied between 198 to 240 $\text{kg/m}^2\text{-s}$ to maintain constant Reynolds number during the tests. The *OMF* of the lubricant or nanolubricant in the refrigerant was 3 wt.%.

The tested conditions for the two-phase flow and single phase flow tests are reported in Appendix-C and Appendix-D, respectively.

Nanoparticles selected for the present paper were spherical shaped alumina ($\gamma\text{-Al}_2\text{O}_3$, termed as Al_2O_3 in this document) nanoparticles and elongated ZnO nanoparticle that had an aspect ratio of up to 3. The spherical Al_2O_3 and non-spherical ZnO nanoparticles had surface

weighted diameters of 40 nm and 20-40 nm, respectively, after their manufacturing. The number weighted based average equivalent diameters, measured using Dynamic Light Scattering, DLS, nanoparticle sizer instrument for the Al₂O₃ and the ZnO nanoparticles were 68 nm and 125 nm, respectively. The chosen nanoparticles had a different aspect ratio, but share similar thermal conductivity when dispersed in the RL32-3MAF polyolester (POE) lubricant at nanoparticle mass concentration, NP_{conc} , of 20 wt.% (Bigi et al. 2017). The NP_{conc} in oil was also called as mass fraction in work by Bigi et al. (2017), and was evaluated as in equation (5). While, Bigi et al. (2017) defined the nanoparticle volume fraction, ϕ , in refrigerant and lubricant as shown in equation (6). ZnO having a significantly different shape than Al₂O₃ nanoparticles made them excellent candidates to investigate the effects of particle aspect ratio on the fluid flow induced motion. The POE lubricant had a density of 0.981 g/ml at 20°C and kinematic viscosity of 31.2 cSt and 5.6 cSt at 40°C and 100°C, respectively. The nanoparticles were dispersed in POE to form nanolubricant (NL) with an aid of a proprietary polymeric surfactant. Bigi et al. (2017) studied sedimentation characteristics of Al₂O₃ nanoparticles coated with three different surfactants, the results showed the proprietary polymeric surfactant, which is used in current work, prevented agglomeration and sedimentation of nanoparticles for total tested period of 20 weeks. In current work, the surfactant was present in the refrigerant-nanolubricant mixture during the tests with R410A-Al₂O₃ NL and R410A-ZnO NL mixtures, while the surfactant was absent during tests with R410A and R410A-POE mixture.

$$OMF = \frac{m_{oil}}{m_{ref}} 100, NP_{conc} = 0 \quad (4)$$

$$OMF = \frac{m_{np} + m_{oil}}{m_{ref}} 100, NP_{conc} > 0$$

$$NP_{conc} = \frac{m_{np}}{m_{np} + m_{oil}} 100 \quad (5)$$

$$\phi = \frac{NP_{conc}}{NP_{conc} + (1 - NP_{conc}) \rho_{np} / \rho_{ref+L}} \quad (6)$$

The concentration of lubricant oil in refrigerants circulating in refrigeration system applications are less than $OMF=5$ wt.%. Nanoparticle mass concentration, NP_{conc} , in nanolubricants are high, but when mixed with refrigerants the nanoparticle concentration in the refrigerant-lubricant liquid mixtures are significantly low. These concentrations of nanoparticles in refrigerant-lubricant mixtures are limited by the stability characteristics of the nanoparticles and the ability of liquid phase to carry the nanoparticles in two-phase flows. Hence the nanoparticle mass, or volume, concentrations used for the refrigerant-lubricant mixture flow studies in this work were much lower than the nanoparticle concentration in the water based nanofluids studied by Buongiorno (2006) and other authors in literature. In this work, single-phase flow of R410A-AL2O3 NL mixture and R410A-ZnO NL mixture were tested at very low nanoparticle volume concentrations, ϕ , of 0.08 vol.% to 0.1 vol.% in refrigerant and lubricant mixtures.

The R410A two-phase flow baseline tests at selected mass fluxes and refrigerant vapor qualities were repeated multiple times and in different days during the experimental campaign. After the R410A-POE tests and the system cleaning operation, the selected R410A baseline tests were repeated to confirm the repeatability of the experimental HTC and $\Delta P/L$ results. The system cleaning operation is explained in details in earlier paragraph of this subsection. After the R410A-ZnO NL mixture tests and cleaning operation, the R410A baseline tests were not repeatable

because of ZnO nanoparticle deposition inside the test section tube. Hence, the test section refrigerant copper tube was replaced with a new tube and the R410A was tested to confirm repeatability of HTC and $\Delta P/L$ results. The test section with new tube was able to have repeatability of the R410A two-phase flow baseline tests. The R410A-AL₂O₃ NL mixture was then tested in the test section with the new installed copper tube. Once the tests and cleaning operation were done, the R410A baseline tests were again not repeatable because of AL₂O₃ nanoparticle deposition inside the test section tube.

3.3. Data Reduction

The refrigerant inlet quality was determined from a heat balance across the preheater. The heat transfer capacity of the preheater was measured from the water/ethylene-glycol (ETW) mixture side of the heat exchanger according to equation (7). High accuracy thermocouples measure the ETW mixture temperature entering, $T_{ETW,in}$, and leaving, $T_{ETW,out}$, the heat exchanger. A high accuracy Coriolis flow meter measures the mass flow rate, \dot{m}_{ETW} , of the ETW mixture. Pressure and temperature of the subcooled liquid refrigerant were measured at the inlet of the preheater to determine the enthalpy of the refrigerant at the inlet, $h_{ref,preheater,in}$. A high accuracy Coriolis flow meter measures the refrigerant flow rate, \dot{m}_{ref} , and the enthalpy of the refrigerant at the outlet of the pre-heater, $h_{ref,preheater,out}$, was calculated by equation (8). It should be noticed that the percent difference between the measured heat transfer rate from the ETW side (equation (7)) and from the refrigerant side (equation (8)), i.e., the heat balance of the pre-heater, was within 3% from calibration tests.

The length of the insulated, 12.7 mm (0.5 inch) O.D., copper tubing between the preheater outlet and test section inlet was about 5.5 meter and had had a maximum heat gain of

$\dot{q}_{Gain,Pipeline}=26\text{W}$ from ambient, this heat gain was evaluated using equation (9) during the heat balance single-phase flow tests. This heat gain as a function of temperature difference between the ambient and refrigerant was estimated, as shown in Figure 25 and equation (10), and was included in the calculations, shown in equation (11), to estimate the correct refrigerant enthalpy, $h_{ref,in}$, at the inlet of the test section during the two-phase flow tests. The enthalpy, $h_{ref,out}$, at the outlet of the test section was evaluated based of the heat input to the refrigerant while flowing in the test section of length L_{HT} , as shown in equation (12).

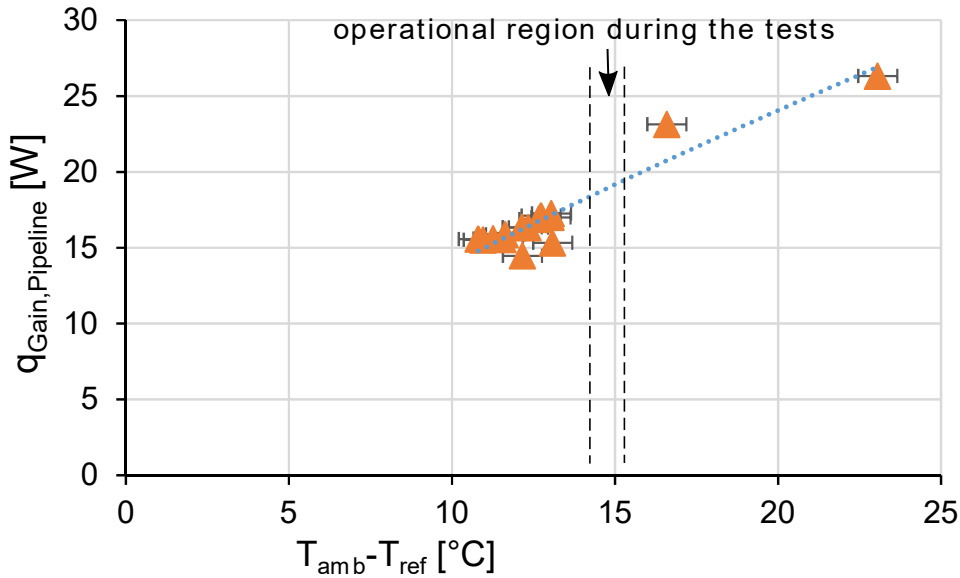


Figure 25: Calibration of the test section by measuring the heat gain to the refrigerant in the copper pipeline installed from the preheater outlet to the test section inlet.

$$\dot{q}_{ETW} = \dot{m}_{ETW} \cdot c_{p,ETW} \cdot (T_{ETW,in} - T_{ETW,out}) \quad (7)$$

$$h_{ref,preheater,out} = h_{ref,preheater,in} + \frac{\dot{q}_{ETW}}{\dot{m}_{ref}} \quad (8)$$

$$\dot{q}_{Gain,PineLine} = \dot{m} \left(\frac{\pi}{4} D_h^2 \right) [c_{p,ref} (T_{ref,in} - T_{ref,Preheater_out})] \quad (9)$$

$$\dot{q}_{Gain,PineLine} = f \left(T_{amb} - \frac{T_{ref,in} + T_{ref,preheater,out}}{2} \right) \quad (10)$$

$$h_{ref,in} = h_{ref,preheater,out} + \frac{\dot{q}_{Gain,PineLine}}{\dot{m}_{ref}} \quad (11)$$

$$h_{ref,out} = h_{ref,in} + \frac{\ddot{q}_{avg} \frac{\pi}{4} D_h^2 \cdot L_{HT}}{\dot{m}_{ref}} \quad (12)$$

The oil presence in the refrigerant affected the refrigerant liquid enthalpy and vapor qualities; this was accounted in vapor quality calculation using the methods described by Hu et al. (2008). The vapor quality at the inlet, x_{in} , and outlet, x_{out} , of the test section was then evaluated using Hu et al. (2008) equation (13). The vapor qualities at the inlet and outlet were averaged to get the average vapor quality of the test section, $x_{avg} = (x_{in} + x_{out})/2$. Lottin et al. (2003) provided the enthalpy, h_{oil} , for lubricant and Engineering Equation Solver (EES) provided the refrigerant enthalpy, h_{ref} .

$$\begin{aligned} x_{in} &= (h_{ref,in} - OMF \cdot h_{oil} - (1 - OMF) \cdot h_{ref,x=0}) / h_{fg,ref} \\ x_{out} &= (h_{ref,out} - OMF \cdot h_{oil} - (1 - OMF) \cdot h_{ref,x=0}) / h_{fg,ref} \end{aligned} \quad (13)$$

The heat transfer coefficient, HTC , in equation (14) was the average of the local heat transfer coefficient and the heat flux, \ddot{q}_{avg} , in equation (15) was the average of the local heat fluxes calculated at 15 location along the length of the test section tube (5 on top of the tube, 5 on bottom of the tube, and 5 on side of the tube). \bar{m} was the locations on the top, side, and bottom of the inner wall of the test section tube. \bar{l} was the locations along the length of the test section tube. The change of refrigerant vapor quality from the inlet and outlet of the test section was small; hence the presented averaged HTC could be viewed as quasi-local for the averaged refrigerant vapor quality

in the test section.

$$HTC = HTC_{exp} = \frac{1}{15} \sum_{\bar{m}=1}^{\bar{m}=3} \sum_{\bar{l}=1}^{\bar{l}=5} \dot{q}_{\bar{l}\bar{m}} / (T_{s,\bar{l}\bar{m}} - T_{bub}) \quad (14)$$

$$\dot{q}_{avg} = \frac{1}{15} \sum_{\bar{m}=1}^{\bar{m}=3} \sum_{\bar{l}=1}^{\bar{l}=5} \dot{q}_{\bar{l}\bar{m}} \quad (15)$$

The experimental data was presented in this work with averaged HTC_{exp} , \dot{q}_{avg} , and x_{avg} . No local values were used to present the data. The experimental averaged HTC and experimental pressure drop ΔP was used to calculate the heat transfer factor, HTF , and the pressure drop factor, PDF , according to equations (16) and (17), respectively. The HTC_0 and the ΔP_0 were the representative R410A baseline heat transfer coefficient and pressure drop for the oil free cases. For each test with refrigerant R410A-POE oil (or with R410A-nanolubricant NL), the measured HTC and ΔP were compared with the corresponding HTC_0 and ΔP_0 at the same mass flux, heat flux, and refrigerant vapor quality. The HTF and PDF were then calculated and they represented the figure of merits that isolated and quantified the effects on the heat transfer coefficient and on the pressure drop due to the presence of POE oil, or nanolubricant, in the base R-410A refrigerant.

$$HTF = [(HTC - HTC_0) / HTC_0] \times 100 [\%] \quad (16)$$

$$PDF = [(\Delta P - \Delta P_0) / \Delta P_0] \times 100 [\%] \quad (17)$$

The refrigerant saturated temperature or the bubble point temperature, T_{bub} , was calculated according to equation (18) (Sawant et al. 2007; Thome 1995), to include the effect of oil presence in R410A bubble point temperature. The T_{bub} was the average bubble point temperature of the test section, as it was evaluated using x_{avg} . The presence of oil in refrigerant results in higher bubble point temperature than the saturation temperature of the pure refrigerant and this effect was significant at vapor qualities above 0.9. The refrigerant-oil bubble temperatures of this work were

close to the saturation temperatures of refrigerant R410A for measured absolute pressures as the vapor qualities were never above 0.8. The experimentally measured saturation pressures, P_{ref} , two-phase flow temperature measured with inline thermocouples at the inlet of the test section, $T_{ref,in}$, and the outlet of the test section, $T_{ref,out}$, and refrigerant vapor qualities at the location of inline thermocouples, x_{in} and x_{out} , were used to evaluate the constants $A_0=6.3801E-03$, $A_1=-4.0375E-04$, $A_2=-3.4902E-05$, $a_0=-2394.50$, $b_0=15.51$, and the polynomials a and b , as per the methods provided by Sawant et al. (2007) and Thome (1995). The T_{bub} in equation (18) accounted for deviations of the refrigerant R410A composition used in the present work from the standard blend properties due to the presence of stray impurities as a result of manufacturing processes, and the presence of oil in the liquid refrigerant. The difference between the measured saturated temperatures, $T_{ref,in}$, with the inline thermocouple of the test section and the evaluated bubble point temperature, T_{bub} , with equation (18) was in general very small. For example, this difference was less than 0.2°C in the examples provided in Table 2 to Table 5.

$$T_{bub} = a / \left[\ln(P_{ref}) - b + \left(\frac{A_2}{A_1} \right) x_{avg} \right] \text{ [K]} \quad (18)$$

$$\text{where, } a = a_0 + 182.52(\omega) - 724.21(\omega^3) + 3868(\omega^5) - 5268.9(\omega^7)$$

$$b = b_0 - 0.72212(\omega) + 2.3914(\omega^3) - 13.779(\omega^5) + 17.066(\omega^7)$$

$$\omega = 0.01 \cdot OMF / [1 - x_{avg} / (1 - 0.01 \cdot OMF)]$$

The local wall surface temperatures on the inner wall of the refrigerant copper tube at top, side, and bottom surfaces were evaluated using the equations (19), (20), and (21), respectively. These equations were derived from the cylindrical coordinate heat conduction equation to project the thermocouple measurements on the copper block to the inner wall of the smooth tube. The $0.5D_h \times 1.44547$ radians value in the second heat transfer resistance term in equations (19) and (21) was the circumference of the groove cut in the top and bottom copper blocks, which was in contact

with the refrigerant copper tube. The thermal resistance $R_{ThermalPaste}$ accounted for the inverse thermal conductivity of the thermal paste, which was in between the copper block groove and refrigerant copper tube and thermal paste around the thermocouples, and it also accounted for the thermal resistance due to micro-air gaps in between the copper block groove and refrigerant copper tube. The local thermal resistances', $R_{ThermalPaste,\bar{l}}$, values were corrected such that the local wall surface temperatures, $T_{s,\bar{l}}$, of the experimental single-phase flow R410A tests matched the local wall surface temperatures' predictions from Gnielinski correlation. The length of the tube was divided into $\bar{l}=5$ sections, corresponding to the 5 thermocouples that were present in each levels on copper block. The description of thermocouple locations at different levels on copper blocks and nomenclature information for local wall surface temperatures, local heat fluxes, and local heat transfer coefficient is provided in Figure 9 and Figure 8.

$$T_{s,\bar{l},Top} = T_{\bar{l},lev} + \dot{q}_{\bar{l},Top} \left[\frac{2 \ln \left(\frac{D_h + t}{D_h} \right)}{2\pi L \alpha_{\bar{l},Top} k_{Cu}} + \frac{L_{TC,Top,\bar{l}}}{k_{Cu} (0.5 D_h 1.44547) L \alpha_{\bar{l},Top}} + R_{ThermalPaste,\bar{l}} \right] \quad (19)$$

$$T_{s,\bar{l},Side} = T_{\bar{l},levelMid} + (\dot{q}_{\bar{l},Top} + \dot{q}_{\bar{l},Bottom}) \left[\frac{\ln \left(\frac{D_h + t}{D_h} \right)}{2\pi L \alpha_{\bar{l},Top} k_{Cu}} + R_{ThermalPaste,\bar{l}} \right] \quad (20)$$

$$T_{s,\bar{l},Bottom} = T_{\bar{l},lev} + \dot{q}_{\bar{l},Bottom} \left[\frac{2 \ln \left(\frac{D_h + t}{D_h} \right)}{2\pi L \alpha_{\bar{l},Bottom} k_{Cu}} + \frac{L_{TC,Bottom,\bar{l}}}{k_{Cu} (0.5 D_h 1.44547) L \alpha_{\bar{l},Bottom}} + R_{ThermalPaste,\bar{l}} \right] \quad (21)$$

The local heat fluxes at the inner wall of the refrigerant copper tube at top, side, and bottom surfaces were evaluated using equations (22), (23), and (24), respectively. The $Lr=0.1016$ m (4 in.) was the distance between the thermocouples in level1 and level2 on top slab/block of copper, and between the thermocouples in level5 and level6 on bottom slab/block of copper.

$$\ddot{q}_{\bar{i},Top} = \frac{(T_{\bar{i},level1} - T_{\bar{i},level2})}{\frac{Lr}{k_{Cu}} \frac{\pi}{4} D_h^2 \cdot La_{\bar{i},Top}} \quad (22)$$

$$\ddot{q}_{\bar{i},Side} = \frac{(\ddot{q}_{\bar{i},Top} + \ddot{q}_{\bar{i},Bottom})}{2} \quad (23)$$

$$\ddot{q}_{\bar{i},Bottom} = \frac{(T_{\bar{i},level6} - T_{\bar{i},level5})}{\frac{Lr}{k_{Cu}} \frac{\pi}{4} D_h^2 \cdot La_{\bar{i},Bottom}} \quad (24)$$

The heat transfer coefficients for the single-phase flow tests were calculated according to equation (25). The heat flux, \ddot{q}_{avg} , and wall surface temperature, T_s , were average of the local heat fluxes and local wall surface temperatures calculated at 15 location along the length of the test section tube. Liquid refrigerant or refrigerant-oil mixture temperatures at the inlet and outlet of test section were measured using inline thermocouples, and were averaged to get the single-phase fluid temperature, T_{ref} .

$$HTC = HTC_{exp} = \ddot{q}_{avg} / (T_s - T_{ref}) \quad (25)$$

The experimental data set reported in Appendix-C and Appendix-D presents the series of two-phase and single-phase flow tests, respectively, conducted during the experimental campaign. The data reduction calculations were carried out in Engineering Equation Solver (EES), while the EES code is provided in Appendix-E along with a sample data reduction calculations for a two-phase flow test.

Table 2 to Table 5.presents sample data reduction calculations for two-phase flow tests of R410A, R410A-POE, R410A-ZnO NL, and R410A-Al2O3 NL mixtures, respectively, at same average vapor quality, heat flux, mass flux. Each table shows temperature measurements at the copper blocks. The calculated local wall surface temperatures, local heat fluxes, local heat transfer coefficients, mass flux, average vapor quality, refrigerant bubble temperature, average heat flux, average heat transfer coefficient, heat transfer factor, and pressure drop factor are also shown in

the table. The table also provides information of the figures where the calculated HTC , $\Delta P/L$, HTF , and PDF were plotted.

The R410A test, in

Table 2, had local heat fluxes and surface wall temperatures within $\pm 12\%$. Such uniformities were not observed for the tube calorimeters with tube-in-tube counter flow design and tube with wrapped tape heater design by Wong (2015). The $\pm 12\%$ variations in local heat fluxes and surface wall temperatures were considered reasonably uniform for the current test section design in this work. The change in the vapor quality along the length of the tube varied from 0.1 for high mass fluxes to 0.22 for low mass fluxes, hence the presented averaged HTC could be viewed as quasi-local for the corresponding averaged refrigerant vapor quality in the test section. Hence, the data for the two-phase flow tests were reported as average heat fluxes, \bar{q}_{avg} , average heat transfer coefficients, $HTC_{exp} = HTC_{avg}$, and average refrigerant vapor qualities, x_{avg} , in the plots of this work.

Table 2: Sample data reduction calculations for two-phase flow boiling of R410A at $x_{avg}=0.5$, $\ddot{q}=15 \text{ kW/m}^2$, $\dot{m}=165 \text{ kg/m}^2\text{-s}$, $OMF=N.A.$, $NP_{conc}=N.A.$, and flow pattern type=Annular.

Equations	Description						
	Thermocouple readings [°C] placed on copper blocks and refrigerant copper tube.						
	T1	T2	T3	T4	T5	Location of thermocouple	
	17.0	17.4	17.5	17.2	16.9	level1	on top slab/block of copper
	15.0	15.1	15.2	14.9	14.9	level2	on top slab/block of copper
	13.5	12.8	13.0	12.5	13.5	level3	on top copper block
	10.6	9.2	9.8	10.3	10.1	levelMid	on Refrigerant copper tube
	9.6	9.7	9.6	9.5	9.9	level4	on bottom copper block
	12.0	12.4	12.6	12.4	12.1	level5	on bottom slab/block of copper
	14.2	14.4	14.7	14.6	14.2	level6	on bottom slab/block of copper
	Local wall surface temperatures [°C] on inner wall of the refrigerant tube						
Used in equation (14)	$T_{s,1}$	$T_{s,2}$	$T_{s,3}$	$T_{s,4}$	$T_{s,5}$	Location of local wall surface temperature	
Equation (19)	10.3	10.9	10.6	10.7	10.3	Top	on top of refrigerant copper tube
Equation (20)	10.0	10.0	9.8	9.4	10.4	Side	on side of refrigerant copper tube
Equation (21).	9.5	9.3	9.3	9.0	9.5	Bottom	on bottom of refrigerant copper tube

Local heat fluxes [kW/m²] on inner wall of the refrigerant tube							
Used in equation (14)	\ddot{q}_1	\ddot{q}_2	\ddot{q}_3	\ddot{q}_4	\ddot{q}_5	Location of local heat flux	
Equation (22)	14.1	16.4	15.6	16.1	14.0	Top	on top of refrigerant copper tube
Equation (23)	14.7	15.3	14.6	14.0	15.7	Side	on side of refrigerant copper tube
Equation (24)	15.4	14.3	14.6	13.9	14.6	Bottom	on bottom of refrigerant copper tube
Local heat transfer coefficients [kW/m²-K] at the refrigerant tube							
$\frac{\ddot{q}_{\bar{l}\bar{m}}}{(T_{s,\bar{l}\bar{m}} - T_{bub})}$	HTC_1	HTC_2	HTC_3	HTC_4	HTC_5	Location of local HTC	
$\frac{\ddot{q}_{\bar{l},Top}}{(T_{s,\bar{l},Top} - T_{bub})}$	3.4	3.4	3.4	3.4	3.2	Top	on top of refrigerant copper tube
$\frac{\ddot{q}_{\bar{l},Side}}{(T_{s,\bar{l},Side} - T_{bub})}$	3.8	3.9	3.8	4.0	3.5	Side	on side of refrigerant copper tube
$\frac{\ddot{q}_{\bar{l},Bottom}}{(T_{s,\bar{l},Bottom} - T_{bub})}$	4.6	4.4	4.5	4.7	4.0	Bottom	on bottom of refrigerant copper tube
Variables							
$\dot{m}/\left(\frac{\pi}{4}D_h^2\right)$	\dot{m}	166	[kg/m ² -s]	Mass flux			
$\frac{(x_{in} + x_{out})}{2}$	x_{avg}	0.51	[-]	Average vapor quality			
	x_{in}	0.45	[-]	Inlet vapor quality			
$(x_{out} - x_{in})$	Δx	0.12	[-]	Vapor quality change in test section			
Equation (31)	ω	0	[kg/kg]	Local oil mass fraction			
Used in equation (18)	$P_{ref,in}$	975	[kPa]	Test section inlet pressure			
	$T_{ref,in}$	5.8	[°C]	Test section inlet inline thermocouple			
Equation (18)	T_{bub}	6.0	[°C]	Calculated refrigerant saturated temperature			

$\frac{1}{15} \sum_{\bar{m}=1}^{\bar{m}=3} \sum_{\bar{l}=1}^{\bar{l}=5} T_{s,\bar{l}\bar{m}}$	$T_{s,avg}$	9.9	[°C]	Average inner wall surface temperature
Equation (15)	\ddot{q}_{avg}	14.9	[kW/m ²]	Heat flux
Equation (14) and (16)	HTC	3.9	[kW/m ² -K]	shown by green void square in Figure 52 (a) at $x_{avg}=0.51$ and $\dot{m}=165$ kg/m ² -s.
Used in equation (17)	$\Delta P/L$	829	[Pa/m]	
Used in equations (16)	HTC_o	3.9	[kW/m ² -K]	
Equations (16)	HTF	0.2	[%]	shown by a solid black line in Figure 33 (a) and Figure 34 (a)
Used in equation (17)	$\Delta P/L_o$	823	[Pa/m]	
Equation (17)	PDF	0.7	[%]	shown by a solid black line in Figure 33 (b) and Figure 34 (b)

Table 3: Sample data reduction calculations for two-phase flow boiling of R410A-POE at $x_{avg}=0.5$, $\ddot{q}=15$ kW/m², $\dot{m}=165$ kg/m²-s, $OMF=2.4$ wt.%, $NP_{conc}=N.A.$, and flow pattern type=Annular.

Equations	Description						
	Thermocouple readings [°C] placed on copper blocks and refrigerant copper tube.						
	T1	T2	T3	T4	T5	Location of thermocouple	
	16.4	16.9	16.8	16.5	16.2	level1	on top slab/block of copper
	14.4	14.5	14.5	14.2	14.1	level2	on top slab/block of copper
	12.8	12.1	11.7	11.3	12.4	level3	on top copper block
	51.0	8.7	9.0	9.7	9.4	levelMid	on Refrigerant copper tube
	9.2	9.2	9.1	9.2	9.6	level4	on bottom copper block
	11.9	12.2	12.4	12.5	12.3	level5	on bottom slab/block of copper
	14.1	14.3	14.5	14.6	14.5	level6	on bottom slab/block of copper

Local wall surface temperatures [°C] on inner wall of the refrigerant tube							
Used in equation (14)	$T_{s,1}$	$T_{s,2}$	$T_{s,3}$	$T_{s,4}$	$T_{s,5}$	Location of local wall surface temperature	
Equation (19)	9.5	10.1	9.3	9.4	9.1	Top	on top of refrigerant copper tube
Equation (20)	9.6	9.6	9.1	8.9	9.7	Side	on side of refrigerant copper tube
Equation (21).	9.2	8.8	8.8	8.7	9.2	Bottom	on bottom of refrigerant copper tube
Local heat fluxes [kW/m²] on inner wall of the refrigerant tube							
Used in equation (14)	\dot{q}_1	\dot{q}_2	\dot{q}_3	\dot{q}_4	\dot{q}_5	Location of local heat flux	
Equation (22)	14.3	16.6	16.1	16.5	14.4	Top	on top of refrigerant copper tube
Equation (23)	14.8	15.7	14.6	14.2	16.1	Side	on side of refrigerant copper tube
Equation (24)	15.5	14.7	14.3	13.7	15.0	Bottom	on bottom of refrigerant copper tube
Local heat transfer coefficients [kW/m²-K] at the refrigerant tube							
$\frac{\dot{q}_{\bar{l}m}}{(T_{s,\bar{l}m} - T_{bub})}$	HTC_1	HTC_2	HTC_3	HTC_4	HTC_5	Location of local HTC	
$\frac{\dot{q}_{\bar{l},Top}}{(T_{s,\bar{l},Top} - T_{bub})}$	5.0	4.7	5.8	5.6	5.3	Top	on top of refrigerant copper tube
$\frac{\dot{q}_{\bar{l},Side}}{(T_{s,\bar{l},Side} - T_{bub})}$	5.1	5.3	5.6	5.8	4.8	Side	on side of refrigerant copper tube
$\frac{\dot{q}_{\bar{l},Bottom}}{(T_{s,\bar{l},Bottom} - T_{bub})}$	6.2	6.6	6.2	6.2	5.3	Bottom	on bottom of refrigerant copper tube
Variables							
$\dot{m}/\left(\frac{\pi}{4}D_h^2\right)$	\dot{m}	163	[kg/m ² -s]	Mass flux			

$\frac{(x_{in} + x_{out})}{2}$	x_{avg}	0.47	[-]	Average vapor quality
	x_{in}	0.41	[-]	Inlet vapor quality
$(x_{out} - x_{in})$	Δx	0.13	[-]	Vapor quality change in test section
Equation (31)	ω	4.3	[wt.%]	Local oil mass fraction, 0.0043 [kg/kg]
Used in equation (18)	$P_{ref,in}$	975	[kPa]	Test section inlet pressure
	$T_{ref,in}$	6.4	[°C]	Test section inlet inline thermocouple
Equation (18)	T_{bub}	6.5	[°C]	Calculated refrigerant saturated temperature
$\frac{1}{15} \sum_{\bar{m}=1}^{\bar{m}=3} \sum_{\bar{l}=1}^{\bar{l}=5} T_{s,\bar{l}\bar{m}}$	$T_{s,avg}$	9.3	[°C]	Average inner wall surface temperature
Equation (15)	\dot{q}_{avg}	15.1	[kW/m ²]	Heat flux
Equation (14) and (16)	HTC	5.6	[kW/m ² -K]	shown by green solid square in Figure 53 (a) at $x_{avg}=0.47$ and $\dot{m}=165$ kg/m ² -s.
Used in equation (17)	$\Delta P/L$	1203	[Pa/m]	
Used in equations (16)	HTC_o	3.8	[kW/m ² -K]	
Equations (16)	HTF	48	[%]	shown by green solid square in Figure 33 (a) at $x_{avg}=0.47$ and $\dot{m}=165$ kg/m ² -s
Used in equation (17)	$\Delta P/L_o$	774	[Pa/m]	
Equation (17)	PDF	55	[%]	shown by green solid square in Figure 33 (b) at $x_{avg}=0.47$ and $\dot{m}=165$ kg/m ² -s

Table 4: Sample data reduction calculations for two-phase flow boiling of R410A-ZnO NL at $x_{avg}=0.5$, $\ddot{q}=15 \text{ kW/m}^2$, $\dot{m}=165 \text{ kg/m}^2\text{-s}$, $OMF=2.4 \text{ wt.}\%$, $NP_{conc}=20 \text{ wt.}\%$, and flow pattern type=Annular.

Equations	Description						
	Thermocouple readings [°C] placed on copper blocks and refrigerant copper tube.						
	T1	T2	T3	T4	T5	Location of thermocouple	
	18.1	18.7	18.7	18.4	18.1	level1	on top slab/block of copper
	16.1	16.3	16.4	16.1	16.1	level2	on top slab/block of copper
	14.4	13.8	13.5	13.2	14.3	level3	on top copper block
	11.8	10.2	10.6	11.3	11.3	levelMid	on Refrigerant copper tube
	10.8	10.8	10.7	10.9	11.3	level4	on bottom copper block
	13.4	13.7	14.0	14.2	14.0	level5	on bottom slab/block of copper
	15.6	15.8	16.1	16.3	16.1	level6	on bottom slab/block of copper
	Local wall surface temperatures [°C] on inner wall of the refrigerant tube						
Used in equation (14)	$T_{s,1}$	$T_{s,2}$	$T_{s,3}$	$T_{s,4}$	$T_{s,5}$	Location of local wall surface temperature	
Equation (19)	11.2	11.8	11.0	11.3	11.0	Top	on top of refrigerant copper tube
Equation (20)	11.1	11.1	10.7	10.4	11.7	Side	on side of refrigerant copper tube
Equation (21).	10.7	10.4	10.4	10.4	11.0	Bottom	on bottom of refrigerant copper tube

Local heat fluxes [kW/m²] on inner wall of the refrigerant tube							
Used in equation (14)	\ddot{q}_1	\ddot{q}_2	\ddot{q}_3	\ddot{q}_4	\ddot{q}_5	Location of local heat flux	
Equation (22)	14.3	16.8	16.3	16.5	14.5	Top	on top of refrigerant copper tube
Equation (23)	14.7	15.7	14.8	14.2	16.2	Side	on side of refrigerant copper tube
Equation (24)	15.3	14.7	14.3	13.7	15.1	Bottom	on bottom of refrigerant copper tube
Local heat transfer coefficients [kW/m²-K] at the refrigerant tube							
$\frac{\ddot{q}_{\bar{l}\bar{m}}}{(T_{s,\bar{l}\bar{m}} - T_{bub})}$	HTC_1	HTC_2	HTC_3	HTC_4	HTC_5	Location of local HTC	
$\frac{\ddot{q}_{\bar{l},Top}}{(T_{s,\bar{l},Top} - T_{bub})}$	3.0	3.1	3.4	3.3	3.0	Top	on top of refrigerant copper tube
$\frac{\ddot{q}_{\bar{l},Side}}{(T_{s,\bar{l},Side} - T_{bub})}$	3.2	3.3	3.4	3.4	3.0	Side	on side of refrigerant copper tube
$\frac{\ddot{q}_{\bar{l},Bottom}}{(T_{s,\bar{l},Bottom} - T_{bub})}$	3.6	3.6	3.5	3.3	3.2	Bottom	on bottom of refrigerant copper tube
Variables							
$\dot{m}/\left(\frac{\pi}{4}D_h^2\right)$	\dot{m}	165	[kg/m ² -s]	Mass flux			
$\frac{(x_{in} + x_{out})}{2}$	x_{avg}	0.49	[-]	Average vapor quality			
	x_{in}	0.43	[-]	Inlet vapor quality			
$(x_{out} - x_{in})$	Δx	0.12	[-]	Vapor quality change in test section			
Equation (31)	ω	4.4	[wt.%]	Local oil mass fraction, 0.0044 [kg/kg]			
Used in equation (18)	$P_{ref,in}$	974	[kPa]	Test section inlet pressure			
	$T_{ref,in}$	6.3	[°C]	Test section inlet inline thermocouple			
Equation (18)	T_{bub}	6.3	[°C]	Calculated refrigerant saturated temperature			

$\frac{1}{15} \sum_{\bar{m}=1}^{\bar{m}=3} \sum_{\bar{l}=1}^{\bar{l}=5} T_{s,\bar{l}\bar{m}}$	$T_{s,avg}$	10.9	[°C]	Average inner wall surface temperature
Equation (15)	\ddot{q}_{avg}	15.1	[kW/m ²]	Heat flux
Equation (14) and (16)	HTC	3.3	[kW/m ² -K]	shown by purple plus symbol in Figure 37 (a) at day 1, $x_{avg}=0.49$ and $\dot{m}=165$ kg/m ² -s, also shown by green void square in Figure 54 (a) at $x_{avg}=0.47$ and $\dot{m}=165$ kg/m ² -s.
Used in equation (17)	$\Delta P/L$	1076	[Pa/m]	shown by purple plus symbol in Figure 37 (b) at day 1, $x_{avg}=0.49$ and $\dot{m}=165$ kg/m ² -s.
Used in equations (16)	HTC_o	3.8	[kW/m ² -K]	
Equations (16)	HTF	-14	[%]	shown by green void square in Figure 33 (a) at $x_{avg}=0.49$ and $\dot{m}=165$ kg/m ² -s
Used in equation (17)	$\Delta P/L_o$	795	[Pa/m]	
Equation (17)	PDF	35	[%]	shown by green void square in Figure 33 (a) at $x_{avg}=0.49$ and $\dot{m}=165$ kg/m ² -s

Table 5: Sample data reduction calculations for two-phase flow boiling of R410A-Al2O3 NL at $x_{avg}=0.5$, $\ddot{q}=15$ kW/m², $\dot{m}=165$ kg/m²-s, $OMF=2.4$ wt.%, $NP_{conc}=20$ wt.%, and flow pattern type=Annular.

Equations	Description						
	Thermocouple readings [°C] placed on copper blocks and refrigerant copper tube.						
	T1	T2	T3	T4	T5	Location of thermocouple	
	15.8	16.3	16.4	16.3	16.3	level1	on top slab/block of copper
	13.9	13.9	13.9	13.9	14.3	level2	on top slab/block of copper
	12.5	12.0	11.7	11.8	13.1	level3	on top copper block
	51.0	10.2	10.1	10.5	10.8	levelMid	on Refrigerant copper tube

	10.6	10.9	11.2	11.2	11.2	level4	on bottom copper block
	13.2	13.7	14.1	14.1	13.5	level5	on bottom slab/block of copper
	15.4	15.7	16.1	16.1	15.7	level6	on bottom slab/block of copper
Local wall surface temperatures [°C] on inner wall of the refrigerant tube							
Used in equation (14)	$T_{s,1}$	$T_{s,2}$	$T_{s,3}$	$T_{s,4}$	$T_{s,5}$	Location of local wall surface temperature	
Equation (19)	10.3	10.8	10.6	10.7	10.0	Top	on top of refrigerant copper tube
Equation (20)	10.4	10.4	9.8	9.7	10.7	Side	on side of refrigerant copper tube
Equation (21).	10.0	9.7	9.5	9.2	9.9	Bottom	on bottom of refrigerant copper tube
Local heat fluxes [kW/m²] on inner wall of the refrigerant tube							
Used in equation (14)	\dot{q}_1	\dot{q}_2	\dot{q}_3	\dot{q}_4	\dot{q}_5	Location of local heat flux	
Equation (22)	14.0	17.0	17.2	16.9	13.8	Top	on top of refrigerant copper tube
Equation (23)	14.8	15.6	15.1	14.2	15.9	Side	on side of refrigerant copper tube
Equation (24)	15.7	14.3	14.0	13.3	15.1	Bottom	on bottom of refrigerant copper tube
Local heat transfer coefficients [kW/m²-K] at the refrigerant tube							
$\frac{\dot{q}_{i\bar{m}}}{(T_{s,i\bar{m}} - T_{bub})}$	HTC_1	HTC_2	HTC_3	HTC_4	HTC_5	Location of local HTC	
$\frac{\dot{q}_{i,Top}}{(T_{s,i,Top} - T_{bub})}$	3.5	3.7	3.9	3.7	3.5	Top	on top of refrigerant copper tube
$\frac{\dot{q}_{i,Side}}{(T_{s,i,Side} - T_{bub})}$	3.6	3.8	4.2	4.0	3.5	Side	on side of refrigerant copper tube

$\frac{\ddot{q}_{\bar{l},\text{Bottom}}}{(T_{s,\bar{l},\text{Bottom}} - T_{bub})}$	4.3	4.2	4.3	4.3	3.9	Bottom	on bottom of refrigerant copper tube
	Variables						
$\dot{m}/\left(\frac{\pi}{4}D_h^2\right)$	\dot{m}	167	[kg/m ² -s]				Mass flux
$\frac{(x_{in} + x_{out})}{2}$	x_{avg}	0.47	[-]				Average vapor quality
	x_{in}	0.41	[-]				Inlet vapor quality
$(x_{out} - x_{in})$	Δx	0.12	[-]				Vapor quality change in test section
Equation (31)	ω	4.3	[wt.%]				Local oil mass fraction, 0.0043 [kg/kg]
Used in equation (18)	$P_{ref,in}$	975	[kPa]				Test section inlet pressure
	$T_{ref,in}$	6.0	[°C]				Test section inlet inline thermocouple
Equation (18)	T_{bub}	6.2	[°C]				Calculated refrigerant saturated temperature
$\frac{1}{15} \sum_{\bar{m}=1}^{\bar{m}=3} \sum_{\bar{l}=1}^{\bar{l}=5} T_{s,\bar{l}\bar{m}}$	$T_{s,avg}$	10.1	[°C]				Average inner wall surface temperature
Equation (15)	\ddot{q}_{avg}	15.1	[kW/m ²]				Heat flux
Equation (14) and (16)	HTC	3.9	[kW/m ² -K]				shown by red void diamond in Figure 37 (a) at day 1, $x_{avg}=0.47$ and $\dot{m}=165$ kg/m ² -s, also shown by green void square in Figure 55 (a) at $x_{avg}=0.47$ and $\dot{m}=165$ kg/m ² -s.
Used in equation (17)	$\Delta P/L$	1047	[Pa/m]				shown by red void diamond in Figure 37 (b) at day 1, $x_{avg}=0.47$ and $\dot{m}=165$ kg/m ² -s.
Used in equations (16)	HTC_o	3.8	[kW/m ² -K]				
Equations (16)	HTF	3.7	[%]				shown by green void square in Figure 34 (a) at $x_{avg}=0.47$ and $\dot{m}=165$ kg/m ² -s
Used in equation (17)	$\Delta P/L_o$	775	[Pa/m]				
Equation (17)	PDF	35	[%]				shown by green void square in Figure 34 (a) at $x_{avg}=0.47$ and $\dot{m}=165$ kg/m ² -s

3.4. Heat Balance at Test Section

Installation of thermocouples and plate heaters on copper block was followed by insulation of the test section, as shown in Figure 26. The copper tubing at the inlet and outlet of the test section and copper blocks of the test section were heavily insulated to prevent heat gain from the higher temperature ambient atmosphere surrounding the test section. The copper tubing of the system were insulated with commercially available flexible closed-cell elastomeric insulation having thermal resistance of $0.99 \text{ m}^2\text{-K/W}$ per 25 mm insulation thickness (R value of $5.5 \text{ ft}^2\text{-hr-}^\circ\text{F/Btu}$ per inch), while the test section copper blocks were insulated with about 15 cm (6 inch) thick expanded polystyrene foam insulation having thermal resistance of $0.67 \text{ m}^2\text{-K/W}$ per 25 mm insulation thickness (R value $3.8 \text{ ft}^2\text{-hr-}^\circ\text{F/Btu}$ per inch).



Figure 26: Tube calorimeter (test section) after insulation.

The single-phase flow R410A, R410A-POE, and R410A-nanolubricant tests were used to determine the heat balances at the test section, and the heat balances were evaluated using equation (26), equation (27), and equation (28). The single-phase flow test data used to calculate the heat balances are provided in Table 6. The heat balance at the test section was within $\pm 3\%$ as shown

in Figure 27 and the last column of Table 6. The detailed EES equations for calculation of the heat balance at the test section are also provided in Appendix-E.

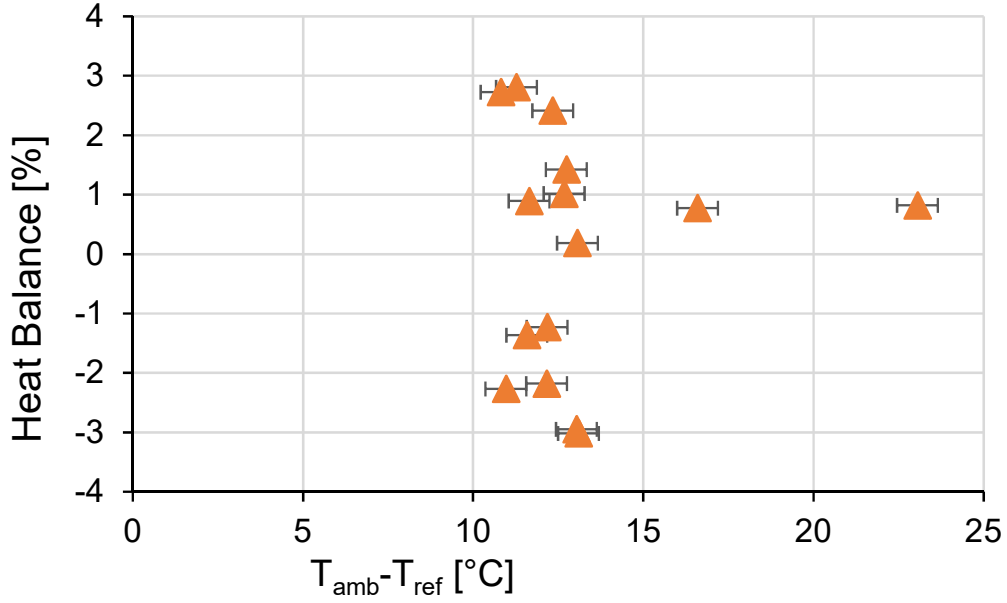


Figure 27: Heat balance between the refrigerant side and electric heaters side in the test section estimated by using equation (28).

$$\dot{q}_{PlateHeaters} = \sum_{l=1}^5 \dot{q}_{l,Top} \frac{\pi}{4} D_h^2 \cdot La_{l,Top} + \sum_{l=1}^5 \dot{q}_{l,Bottom} \frac{\pi}{4} D_h^2 \cdot La_{l,Bottom} \quad (26)$$

$$\dot{q}_{ref,TestSection} = \dot{m} \left(\frac{\pi}{4} D_h^2 \right) c_{p,ref} (T_{ref,out} - T_{ref,in}) \quad (27)$$

$$Heat\ Balance = \frac{(\dot{q}_{ref,TestSection} - \dot{q}_{PlateHeaters})100}{(\dot{q}_{ref,TestSection} + \dot{q}_{PlateHeaters})0.5} \quad (28)$$

Table 6: Single-phase test data for heat balance at test section.

Fluid	OMF [wt.%]	NP_{conc} [wt.%]	\dot{m} [kg/m ² -s]	\dot{q}_{avg} [kW/m ²]	P_{in} [kPa]	$T_{ref,in}$ [°C]	$T_{ref,out}$ [°C]	T_{amb} [°C]	$\dot{q}_{plateHeaters}$ [kW]	$\dot{q}_{ref,TestSection}$ [kW]	Heat Balance [%]
R410A	0	0	198	8.5	1460	6.0	14.3	20.9	0.179	0.184	2.7
R410A	0	0	199	8.7	1744	6.1	14.0	21.0	0.181	0.177	-2.3
R410A	0	0	207	9.0	1406	5.9	14.1	22.7	0.187	0.190	1.4
R410A	0	0	208	8.7	1401	5.9	13.8	22.9	0.182	0.182	0.2
R410A	0	0	208	8.8	1437	5.7	13.8	21.0	0.184	0.189	2.8
R410A	0	0	209	8.2	1422	5.7	13.3	21.8	0.172	0.176	2.4
R410A	0	0	209	8.5	1706	5.8	13.3	21.1	0.176	0.174	-1.4
R410A	0	0	209	8.8	1471	5.8	13.4	22.6	0.182	0.177	-3.0
R410A-POE	3	0	209	8.8	1499	5.8	13.8	22.5	0.183	0.185	1.0
R410A-ZNO NL	3	14	208	8.7	1486	5.7	13.4	21.7	0.182	0.178	-2.2
R410A-ZNO NL	3	14	241	8.5	1455	5.6	12.0	21.9	0.179	0.173	-3.0
R410A-Al2O3 NL	3	20	207	8.6	1741	5.7	13.6	21.3	0.179	0.181	0.9
R410A-Al2O3 NL	3	20	240	8.4	1665	5.8	12.3	21.2	0.174	0.172	-1.2

3.5. Uncertainty Analysis

The error analysis and uncertainty propagation outlined by Taylor and Kuyatt (1994) were used for calculating the theoretical experimental uncertainties in EES, which are summarized in Table 7. A sample uncertainties calculation in EES for a two-phase flow test is provided in Appendix-F. In Table 7 the second column of Table 7, ‘Accuracy and Uncertainty’ shows the error when the calibrated sensors accuracy were used in uncertainty propagation calculations. The third column of Table 7, ‘Fluctuation in recordings’ shows calculated propagated uncertainties when the sensor’s fluctuation, with a confidence level of 2σ , were used as the accuracy of the sensors. The experimental uncertainty of the differential pressure, ΔP , transducer was within $\pm 0.07\%$ (FS=full scale) but the fluctuations of $\pm 36\%$ in the measured two-phase flow pressure drops during the experiments caused the *PDF* to have a propagated uncertainty error of about $\pm 51\%$. The measurements of pressure drop during the single-phase flow showed the readings to fluctuate within $\pm 1.3\%$. Thus, the high fluctuations recorded in the pressure drops during the two-phase flow were possibly due to perturbations in the pressure coming from the wavy nature of the two-phase flow of refrigerant and nanolubricant liquid and refrigerant vapor interface. Several tests were repeated multiple times during the experimental campaign to assess the repeatability of the experimental results due to the variability of parameters that control the thermal and flow boundary conditions of the system components. The parameters included the precision and tolerance in meeting the set points of a test, composition change of the R410A fluids during the charging and recovery processes, and the contamination of the system with residual lubricant left after cleaning and purging operations. The fourth column of Table 7 express the repeatability error, with a confidence level of 2σ , in the heat transfer and pressure drop calculations. The repeatability values were expressed as error bars in the two-phase flow heat transfer and pressure drop plots. The

fluctuation error values were expressed as error bars for the single-phase flow heat transfer plots.

The repeatability in HTF and PDF measurements were $\pm 8\%$ and $\pm 8.6\%$, respectively. For a sample R410A test calculation, in

Table 2, the evaluated HTF was 0.2% and the PDF was 0.7%, confirming the repeatability of R410A tests.

Table 7: Experimental uncertainties and repeatability

Variables	Accuracy and Uncertainty	Fluctuation in recordings (2σ)	Repeatability at same nominal test conditions
Measured			
P_{ref}	$\pm 0.1\%$ FS	$\pm 0.4\%$	
ΔP	$\pm 0.07\%$ FS	$\pm 36\%$	
\dot{m}	$\pm 0.04\%$	$\pm 4.3\%$	
T^w	$\pm 0.1^\circ\text{C}$	$\pm 0.1^\circ\text{C}$	
T_{inline}	$\pm 0.1^\circ\text{C}$	$\pm 0.6^\circ\text{C}$	
$T_{ref-oil}$	$\pm 0.1^\circ\text{C}$	$\pm 0.6^\circ\text{C}$	
Derived			
T_{bub}	$\pm 0.1^\circ\text{C}$	$\pm 0.6^\circ\text{C}$	
$T_{s,\bar{l}}$	$\pm 0.2^\circ\text{C}$	$\pm 0.2^\circ\text{C}$	
x_{avg}	± 0.02	± 0.04	
\dot{m}	$\pm 0.04\%$	$\pm 4.3\%$	
\dot{q}_{avg}	$\pm 3.8\%$	$\pm 3.8\%$	$\pm 3.8\%$
HTC	$\pm 3.5\%$	$\pm 4.6\%$	$\pm 5.4\%$
$\Delta P/L$	± 0.5 Pa/m ($\pm 0.07\%$)	$\pm 36\%$	$\pm 6\%$
HTF	± 5.2	± 6.8	± 8
PDF	± 0.1	± 51	± 8.6
HTC^S	$\pm 3.9\%$	$\pm 3.8\%$	
HTF^S	$\pm 5.6\%$	$\pm 8\%$	

^S single-phase flow tests, ^w welded thermocouples attached on copper blocks, $T_{\bar{l},level}$

3.6. Estimation of oil mass fraction at the test section

Zürcher et al. (1998) correlation accounted for the presence of oil in the calculation of two-phase frictional pressure drop in smooth tubes. The frictional two-phase pressure drop gradient is evaluated using equation (29), where f_F is Fanning friction factor for turbulent flow, \dot{m} is the mass flux, ρ_f is the density of the liquid-phase, D_h is the tube internal diameter, μ_{oil} is the dynamic viscosity of oil, and μ_{ref} is the dynamic viscosity of refrigerant. The two-phase frictional multiplier $(\phi_l^2)_{ref}$ for pure refrigerant is obtained from Friedel (1979) correlation. The exponent n for R407C/(ester type ISO Grade 68) mixture is evaluated using equation (30), where ω was the local oil mass fraction as shown by equation (31). The increase in the concentration of the oil in liquid refrigerant due to its evaporation was accounted by ω . It is important to note that the word ‘local’ for ω was not a localized point in the test section tube, however it was used to distinct ω from the *OMF*.

$$(dP/dz)_{frict} = [2f_F \dot{m}^2 / (\rho_l D_h)] (\phi_l^2)_{ref} [\mu_{oil} / \mu_{ref}]^{n \cdot \omega} \quad (29)$$

$$n = \omega \left(3.583 \cdot \frac{OMF}{100} + 0.0616 \right) \quad (30)$$

$$\omega = 0.01 \cdot OMF / [1 - x / (1 - 0.01 \cdot OMF)] \quad (31)$$

A comparison of the experimental pressure drop of R410A, R410A-POE, R410A-ZnO NL, and R410A-Al2O3 NL with the predicted results using Zürcher et al. (1998) correlations is shown in Figure 28 (a). The correlation showed the best agreement for R410A data, shown by blue filled circles, but did not capture the effect of a presence of POE oil or POE based nanolubricants.

The *OMF* of the R410A-POE oil injection-extraction tests were 3 wt.% and were precisely measured during experimentation by recording the displacement of the piston of the lubricant

syringe pump. The measured test section pressure drops for the R410A-POE oil injection-extraction tests are shown by yellow filled triangles in Figure 28. The pressure drops and *OMF* data of the of the R410A-POE oil injection-extraction tests were used to scale the exponent *n* in equation (30) to a new exponent *n* as shown in equation (32), so that the pressure drops for R410A-POE oil injection-extraction tests were well predicted.

$$n = \omega \left(3.583 \cdot \frac{OMF}{100} + 0.0616 \right) \cdot 180 \quad (32)$$

Figure 28 (b) shows that with a new exponent (*n*) the R410A-POE oil injection-extraction tests were well predicted. However, the oil circulation tests of R410A-POE, R410A-ZnO NL, and R410A-Al₂O₃ NL were within +150% and -25%, where the oil circulation tests with vapor quality *x*>0.35 had predictions beyond +25%.

Throughout experimentation, the *OMF* was determined by measuring the masses of the refrigerant and oil charged into the system, for the oil circulation tests the charged mass of oil was aimed to have the *OMF* of 3 wt.%. However, the predictions in Figure 28 (b) suggested that the value of 3 wt.% of *OMF* was much higher than the actual *OMF* circulating in the test section.

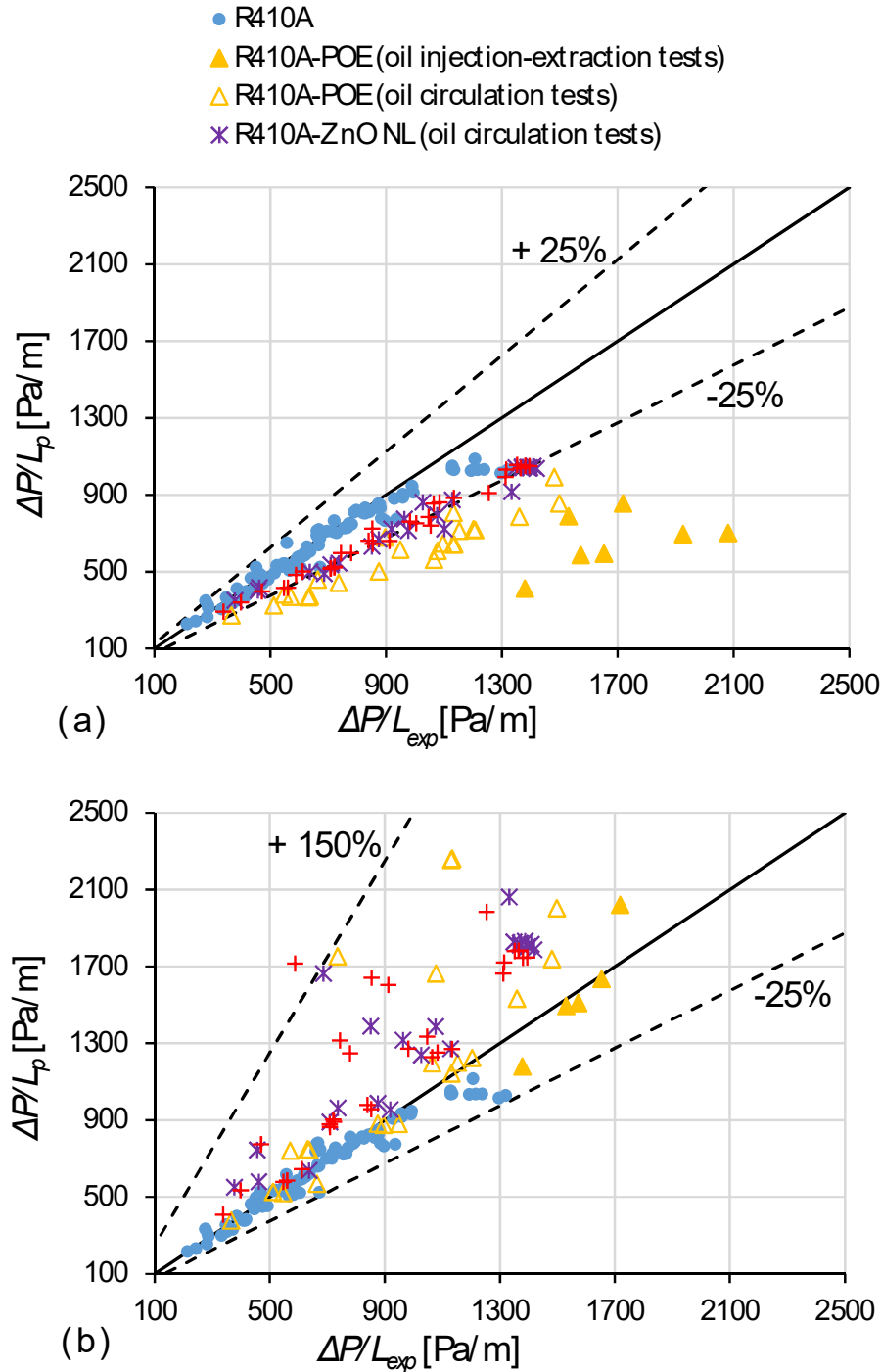
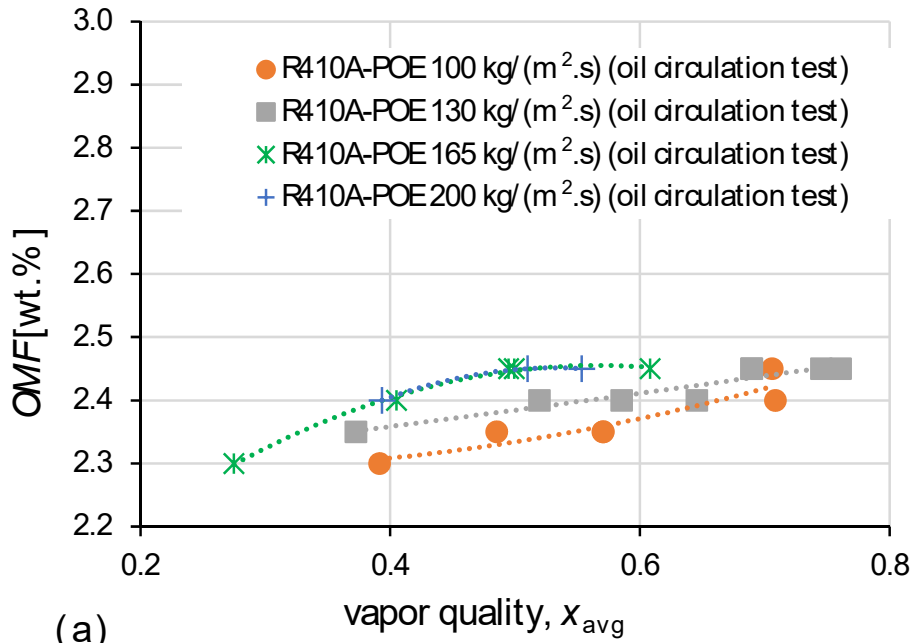


Figure 28: Prediction of smooth tube two-phase flow total pressure drop using (a) (Zürcher et al. 1998) correlation and (b) (Zürcher et al. 1998) correlation prediction with modified exponent n .

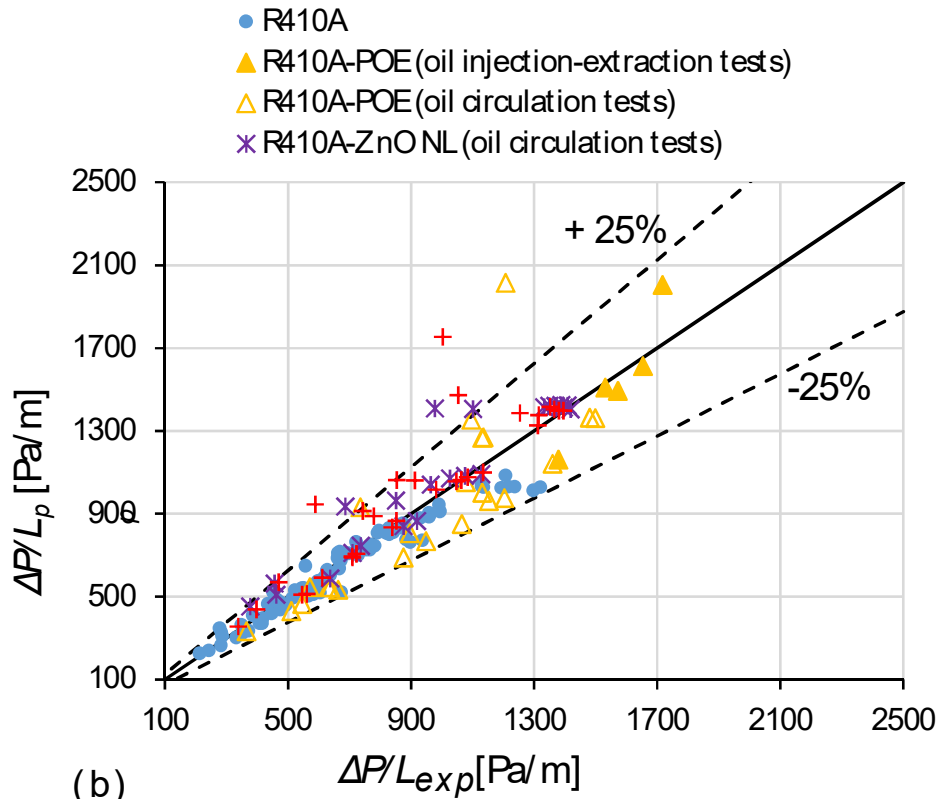
The whole test apparatus loop was divided into several smaller tube-sections, and the mass of oil retained in each tube-section was estimated in a simulation. For the tube-sections of the loop

with a two-phase flow of refrigerant flow, the Rouhani and Axelsson (1970) void fraction model and Hewitt and Hall-Taylor (1970) annular flow modeling methods were used to calculate the liquid film thickness of refrigerant-oil mixture. The details to calculate the liquid film thickness is provided in layer section of this document, in equation (62) through equation (65). The liquid film thickness and the length of the tube-section provided volume of liquid refrigerant-oil mixture in that tube-section, further the local oil mass fraction, ω , was used to evaluate the mass of oil present in the tube-section. The total mass of oil injected into the test apparatus loop was balanced with the summation of oil retained in each smaller tube-sections of the test loop to estimate the *OMF* circulating through the test section. The simulation results, as shown in Figure 29 (a), showed the *OMF* in test section was 2.4 ± 0.1 wt.% for all oil circulation tests that increased with the mass flux at the test section. When *OMF* of 2.4 wt.% was used for all oil circulation tests in the Zürcher et al. (1998) correlation, with modified exponent n , the prediction for all experimental pressure drop data (shown in Figure 29 (b)) were within +25% and -25% for tests with vapor quality $x < 0.66$ and within +80% and -25% for $x \geq 0.66$. The pressure drop prediction supported the simulation *OMF* results, and gave the true *OMF* of the oil circulation tests. The calculations for total pressure drop per unit length, $\Delta P/L$, for a sample R410A test at $x_{avg} = 0.37$ and $\dot{m} = 165$ kg/m²-s is provided in Appendix-E.

Figure 30 shows the experimental total pressure drop measured for R410A-POE oil injection-extraction tests and oil circulation tests at various mass fluxes at a vapor quality of 0.60. For same testing conditions the pressure drop measured for R410A-POE oil circulation tests were 50%, 35%, and 13% lower than R410A-POE oil injection-extraction tests at 100 kg/m²-s, 130 kg/m²-s, and 165 kg/m²-s, respectively.



(a)



(b)

Figure 29: (a) System volume simulation to determine OMF in the test section, and (b) (Zürcher et al. 1998) correlation prediction of two-phase flow total pressure drop with modified exponent n and OMF determined from the simulation.

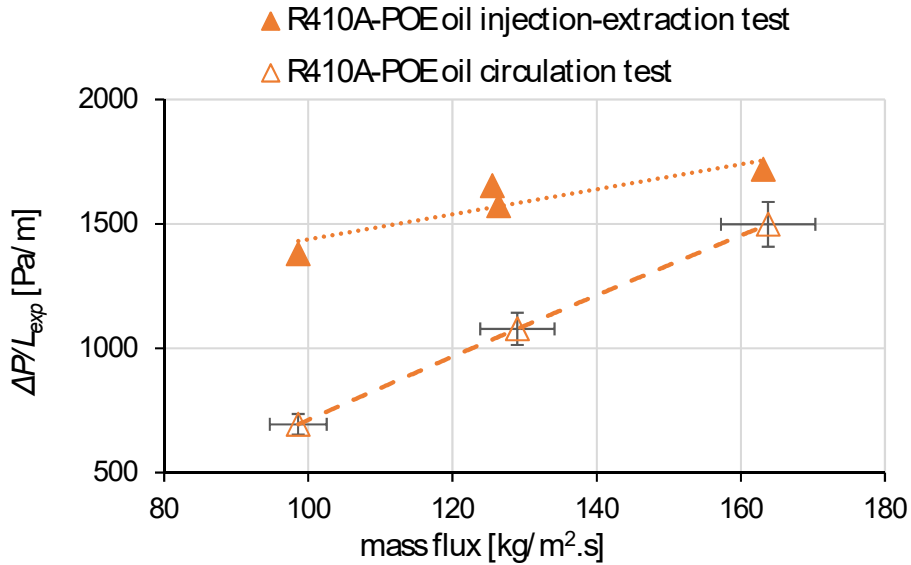


Figure 30: Total pressure drop for R410A-POE oil injection-extraction tests and oil circulation tests at $x=0.60$

During experimentation the oil was injected 4.3 m (14 ft.) before the test section to ensure the liquid refrigerant and lubricant were well mixed before entering the test section for both ‘oil injection-extraction tests’ and ‘oil circulation tests’. In case of R410A-POE oil circulation tests, the POE oil was circulating through the system for a much extended period of time, for more than an hour, allowing the R410A vapor to get absorbed in the POE oil, and the R410A and POE oil to attain equilibrium mixture. In case of R410A-POE oil injection-extraction tests, the POE oil was not circulating in the test apparatus’ loop, it was injected before the test section and then extracted after the test section. There was a chance the R410A and POE oil did not attain equilibrium mixture for oil injection-extraction tests, and could have been the reason for oil injection-extraction tests to have higher pressure drops than oil circulation tests. Following paragraph studies the possibility of pressure drop rise due to non-equilibrium mixing of R410A and POE oil.

At 5°C and refrigerant-oil mixture equilibrium, about 40 wt.% of R410A vapor gets absorbed in the POE oil to reach the maximum vapor solubility, the mixture’s dynamic and

kinematic viscosity decrease by 98%, and the density is increased by 3.8% (Cavestri and Schafer 2000). Incomplete mixing or non-equilibrium of the liquid refrigerant and the injected oil, before the mixture reaching the test section, as in case of oil injection-extraction tests, will have less vapor R410A absorbed in the POE oil. This will result in the liquid refrigerant-oil mixture to have higher viscosities and higher pressure drops. The presence of refrigerant-oil mixture, at 3 wt.% *OMF* and in non-equilibrium condition, that is with 98% higher viscosity and 3.8% lower density, at the test section had increase in the higher pressure drop by only 2.1% and 2.4% as per Friedel (1979) correlation and Zürcher et al. (1998) correlation, respectively, in comparison to well mixed and equilibrium refrigerant-oil mixture at the test section. However the measured increase in pressure drops for oil injection-extraction tests were higher than 13%, as discussed earlier. Thus, the equilibrium mixing or non-equilibrium mixing conditions for the oil circulation tests and the oil injection-extraction tests, respectively, was not the reason for different pressure drops as observed in Figure 30.

The high pressure drops for R410A-POE oil injection-extraction tests were due to higher *OMF* of 3 wt.% at the test section, while the low pressure drops for R410A-POE oil circulation tests were due to lower *OMF* of 2.4 wt.% at the test section as shown by the simulation result in Figure 29 (a). Figure 29 (a) also showed the increase in *OMF* with an increase in mass flux for the R410A-POE oil circulation tests. As the mass flux increased, the pressure drop of the R410A-POE oil circulation tests increased, as shown by open-triangles in Figure 30, this increase in the pressure drop was due to increase in the *OMF* at the test section.

4. Results and Discussion

The following chapter presents the experimental tests results and discusses the findings. Flow pattern images captured at the sight glass helped to identify the flow regime inside the smooth tube test section. The influence of flow patterns and nanoparticle deposition on heat transfer and pressure drop are studied.

In addition, I contributed measuring that data on internally-enhanced fin copper tubes, which were presented in Bigi (2018) PhD dissertation for Bigi model validation. These data on finned copper tubes served as preliminary findings that motivated the present work. Because the goal of this PhD research was to advance the fundamental understanding of the effects of the nanoparticles in the two-phase flow of refrigerant and nanolubricant mixtures, the results presented in this section are only the data that were measured on smooth copper tubes. By eliminating the internal fins, it was able to decouple their influence on the nanoparticles migration and lubricant flow near the inner walls of the tube. This approach allowed to isolate and quantify the macroscopic effect on the two-phase flow heat transfer coefficient due to the nanoparticles Brownian motion and thermophoresis.

4.1. Flow patterns of R410A, R410A-POE, and R410A-nanolubricant mixtures

Table 8 shows the high-resolution camera image of two-phase flow of R410A at a mass flux of $165 \text{ kg/m}^2\text{-s}$ at different refrigerant vapor qualities. The images were captured with a CCD camera with microscopic lens at sight glass tube mounted after the test section, with an aim to observe the nature of the liquid-vapor interface and flow pattern. The sight glass surrounding was

close to ambient temperature and it was not subjected to external heat flux, the flow conditions were fairly adiabatic in the sight glass tube. The liquid-vapor interface was clearly visible for R410A through the sight glass tube. As the vapor quality was increased, the images showed the transition of flow pattern from stratified wavy to annular flow. The description on the field of view of camera images at the sight glass is provided in Figure 31.

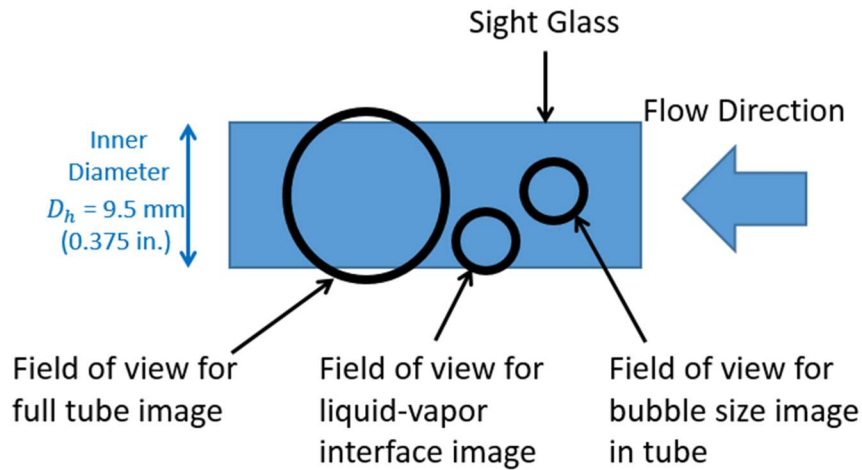
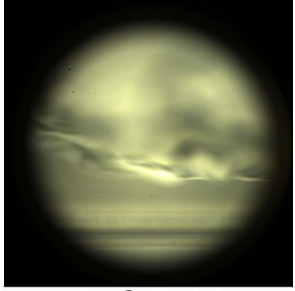
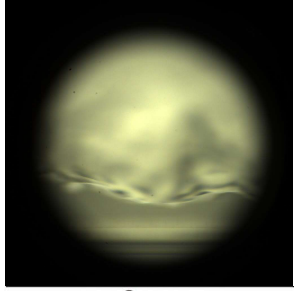
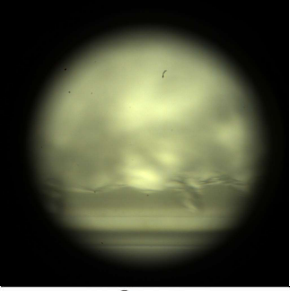

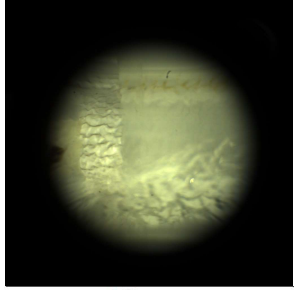
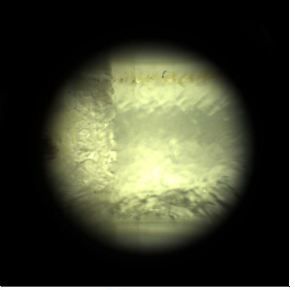


Figure 31: Field of view of camera images of two-phase flows at the sight glass tube.

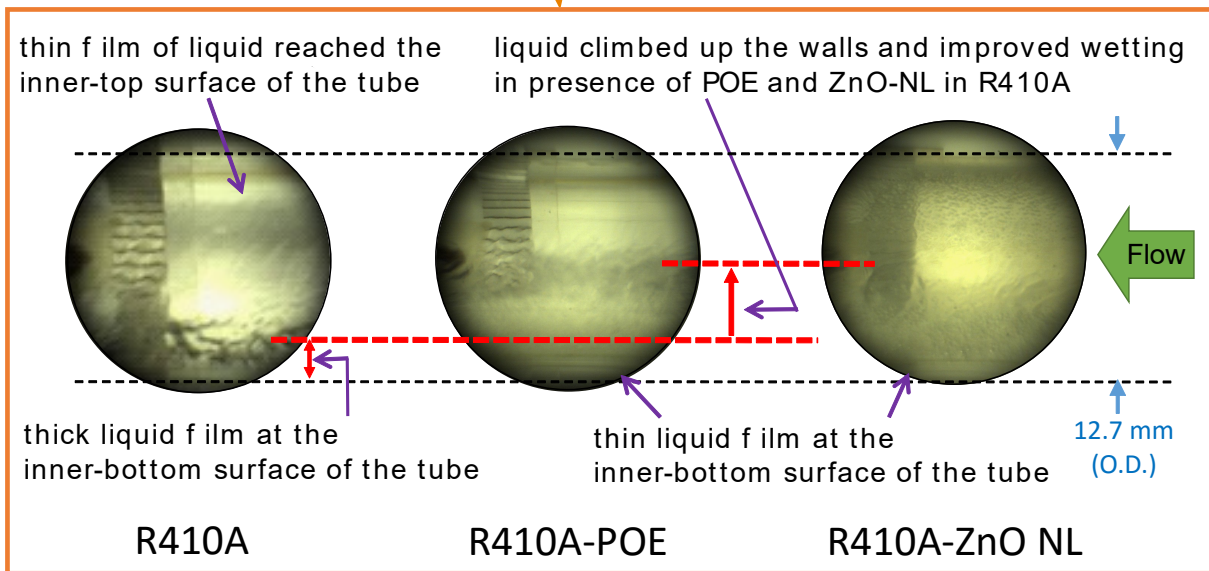
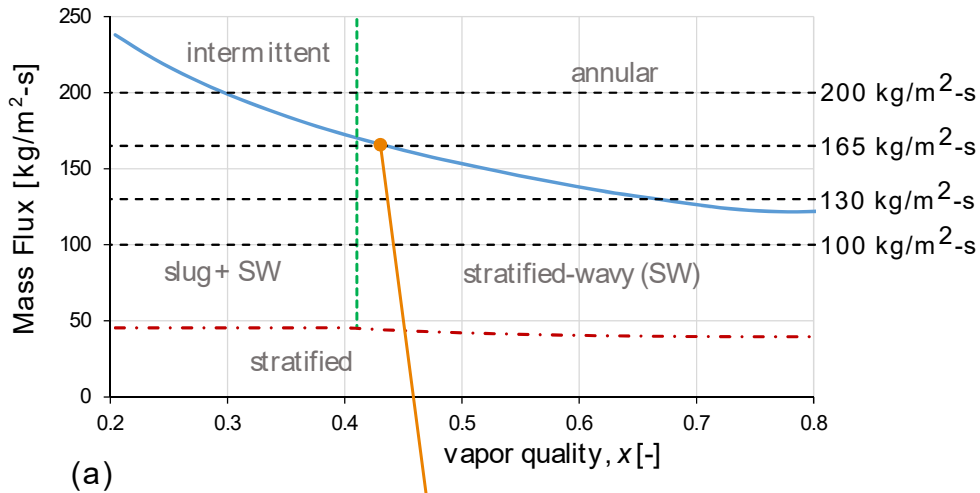
Figure 32 (a) shows a flow pattern map for R410A refrigerant two-phase flow, in 9.5 mm I.D. smooth horizontal tube, generated using the Thome and Hajal (2003) and Wojtan et al. (2005) model. The map predicted the transition of slug-stratified-wavy flow to annular flow to occur at vapor quality of $x=0.43$ for R410A at the mass flux of $165 \text{ kg/m}^2\text{-s}$. Figure 32 (b) shows the flow pattern images recorded at the sight glass tube at the exit of the test section using a camera for R410A, R410A-POE, and R410A-ZnO NL mixtures' flow at $\dot{m}=165 \text{ kg/m}^2\text{-s}$ and $x=0.43$. No clear images were available for R410A-Al₂O₃ NL mixtures flow, hence were not shown. Image of R410A flow pattern at $x=0.43$ in Figure 32 (b) and Table 8 showed a thick stratified liquid at the inner-bottom side of the sight glass tube, as well as very thin film, with ripples, of liquid R410A

Table 8: Images of two-phase flow of R410A at $T_{sat}=6.1^{\circ}\text{C}$, $\dot{m}=165\text{ kg/m}^2\text{-s}$, and $\dot{q}=0\text{ kW/m}^2$ at different refrigerant vapor qualities through a sight glass tube.

Liquid-vapor interface image	 ~ 3 mm	 ~ 3 mm	 ~ 3 mm
Full tube image	 ~13 mm	 ~13 mm	 ~13 mm
Vapor quality at sight glass	0.43	0.57	0.65
Comment	Stratified wavy, large waves at an interval of 0.17 seconds, transition started	Annular and wavy, large waves at an interval of 0.07 seconds and less	Annular

near the inner-top side of the glass tube wall, this confirmed the start of the transition from slug-stratified-wavy flow to annular flow and applicability of Thome and Hajal (2003) and Wojtan et al. (2005) flow pattern map for R410A.

In Figure 32 (b), flow pattern images of R410A-POE and R410A-ZnO NL mixtures showed presence of annular film at $\dot{m}=165\text{ kg/m}^2\text{-s}$ and $x=0.43$. However, in comparison to R410A, the annular film of R410A-POE and R410A-ZnO NL had thinner liquid film thickness at the bottom of the tube as the liquid had climbed up the walls of the tube because of higher surface tension than R410A. R410A-Al₂O₃ NL flow patterns were visually observed and the recorded



(b)

Figure 32: (a) Flow pattern map for R410A two-phase flow in 9.5 mm I.D. smooth horizontal tube (generated with Wojtan et al. (2005) model for $T_{sat}=6.1^{\circ}\text{C}$ and $\dot{q}=15\text{ kW/m}^2$, assuming a fixed value of $\dot{m}=165\text{ kg/m}^2\text{-s}$), and (b) Flow pattern images of two-phase flow of R410A, R410A-POE, and R410A-ZnO NL mixtures at $\dot{m}=165\text{ kg/m}^2\text{-s}$, and $\dot{q}=0\text{ kW/m}^2$, and $x=0.43$.

images were too limited, hence the images were not provided for comparison. Observations showed that there was not much difference between the flow patterns of refrigerant-lubricant mixture and refrigerant-nanolubricant mixtures with ZnO or Al₂O₃ nanoparticles. This was due

to the low local concentration of nanoparticles within the liquid refrigerant and lubricant phases of the two-phase flow for thermodynamic qualities of the mixture less than 0.7.

Table 9 shows the high-speed camera image of two-phase flow of R410A-POE mixture at *OMF* of 2.4 wt.% and mass flux of 165 kg/m²-s at different refrigerant vapor qualities. The images were recorded to observe the nature of the liquid-vapor interface, the flow pattern in the tube, and the bubble sizes. The liquid-vapor interface was unclear in the presence of the POE oil in R410A, while the curvature of the sight glass tube made the observation more difficult. In comparison to R410A in absence of POE oil, the images showed that the R410A-POE mixture had an earlier transition from stratified wavy to annular flow. R410A-POE mixtures have higher mixture viscosity and surface tension than R410A, this caused the liquid to climb up the wall of the horizontal smooth tube in stratified flow and improve wetting, and thus promoted an early annular flow formation (Shen and Groll 2005).

Table 10 shows the high-speed camera image of two-phase flow of R410A-ZnO NL mixture at *OMF* of 2.4 wt.% and mass flux of 165 kg/m²-s at different refrigerant vapor qualities. R410A-ZnO NL mixture's liquid-vapor interface was unclear in the images, also the flow pattern images were similar to R410A-POE mixture's flow. It was impossible to make a comparison of the bubble sizes for R410A-POE and R410A-ZnO NL mixture. It is important to note that the observed bubbles in the sight glass tube were formed during the boiling process that occurred in the test section tube. These bubbles further travelled downstream of the test section, possibly coalescing together while in the flow, before they were viewed and recorded at the sight glass tube. The images also show the ZnO nanoparticle adhering to the wall of the sight glass tube.

Table 9: Images of two-phase flow of R410A-POE mixture at 2.4 wt.% OMF, $T_{sat}=6.1^{\circ}\text{C}$ and $\dot{m}=165\text{ kg/m}^2\text{-s}$ at different refrigerant vapor qualities through a sight glass tube.

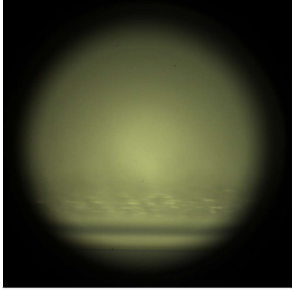
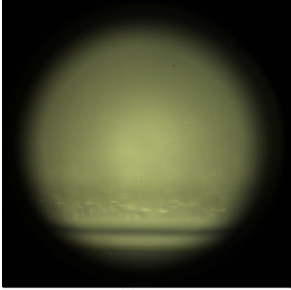
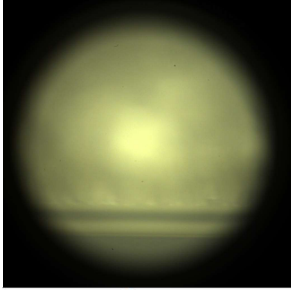
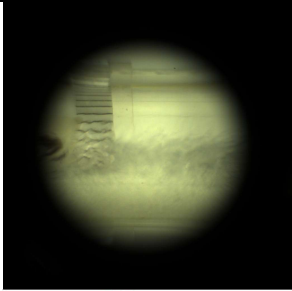

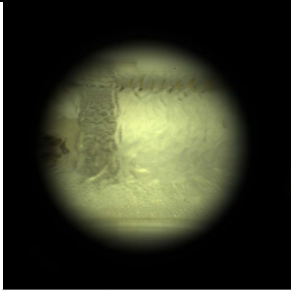
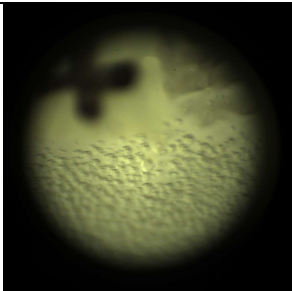
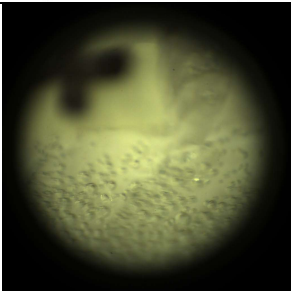
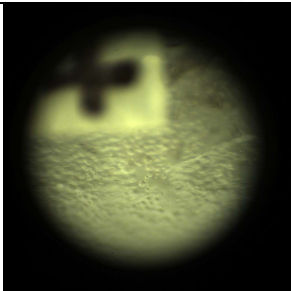
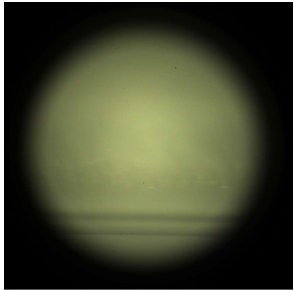
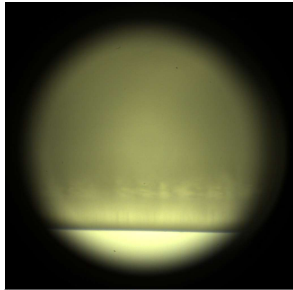
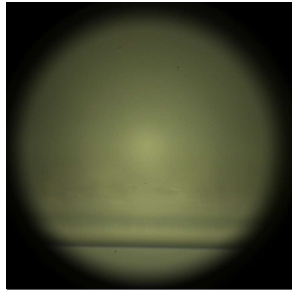
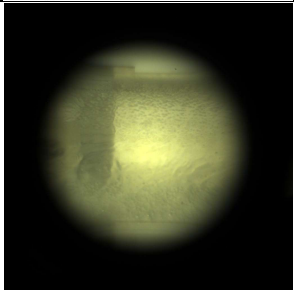

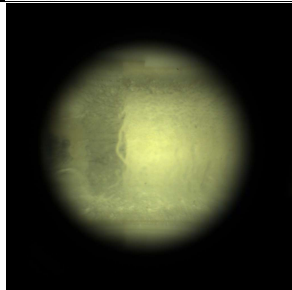
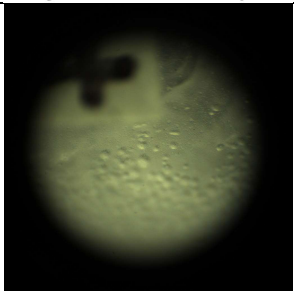
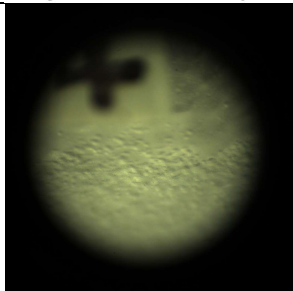
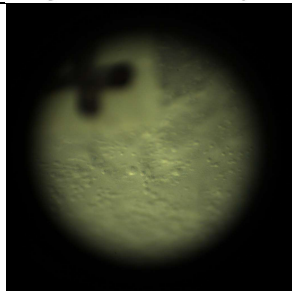
Liquid-vapor interface image	 ~ 3 mm	 ~ 3 mm	 ~ 3 mm
Full tube image	 ~13 mm	 ~13 mm	 ~13 mm
Bubble size	 ~ 3 mm	 ~ 3 mm	 ~ 3 mm
Vapor quality at sight glass	0.44	0.53	0.64
Comment	Stratified-wavy flow, thin ripples of R410A-POE started to reach the inner-top of the tube.	Annular flow, thin ripples of liquid R410A-POE at the inner-top surface of the tube.	Annular flow, ripples of liquid R410A-POE thickened at top of the tube.

Table 10: Images of two-phase flow of R410A-ZnO NL mixture at 20 wt.% NP_{conc} , 2.4 wt.% OMF , $T_{sat}=6.1^{\circ}C$, $\dot{m}=165 \text{ kg/m}^2\text{-s}$, and $\dot{q}=0 \text{ kW/m}^2$ at different refrigerant vapor qualities through a sight glass tube.

Liquid-vapor interface image	 ~ 3 mm	 ~ 3 mm	 ~ 3 mm
Full tube image Note: Nanoparticle disposition was seen on the inner side walls of the tube.	 ~13 mm	 ~13 mm	 ~13 mm
Bubble size	 ~ 3 mm	 ~ 3 mm	 ~ 3 mm
Vapor quality at sight glass	0.46	0.55	0.64
Comment	Stratified-wavy flow, nanoparticles seen on the inner-side of the glass tube.	Annular flow, thin ripples of R410A-ZnO NL at inner-top side of the tube.	Annular flow, ripples of R410A-ZnO NL thickened at inner-top side of the tube.

4.2. Heat Transfer Factor and Pressure Drop Factor

Figure 33 shows *HTF* and *PDF* for R410A-POE lubricant mixture (continuous lines) and R410A-ZnO NL mixture (dotted lines). The 0% in the plots represents the R410A baseline tests in absence of lubricants. (The calculations of *HTF* for a sample R410A test at $x_{avg}=0.37$ and $\dot{m}=165$ kg/m²-s is provided in Appendix-E.) Figure 33 (a) shows the *HTF* of R410A-POE increased with an increase in the refrigerant quality, and was about 45% higher than R410A at vapor quality of 0.5. R410A-POE mixture had enhanced heat transfer for all mass fluxes, but the enhancement did not drop significantly at higher mass fluxes as was observed by Thome (2010) and Zürcher et al. (1998) for R134a and R407C refrigerants with ester type oil. R410A-POE mixtures had higher surface tension than R410A and it helped the liquid to climb up the wall of the horizontal smooth tube and improve wetting of the heat transfer surface (Kedzierski and Kaul 1998; Shen and Groll 2005), thus improving heat transfer of R410A in the presence of POE oil. Kedzierski and Kaul (1998) observed a flow-boiling enhancement of R134a-POE oil mixtures, and attributed it to the increase in the bubble nucleation site density in the presence of lubricant excess layer. However, the possibility of increased nucleate site density in the presence of R410A-POE mixture needs future investigation.

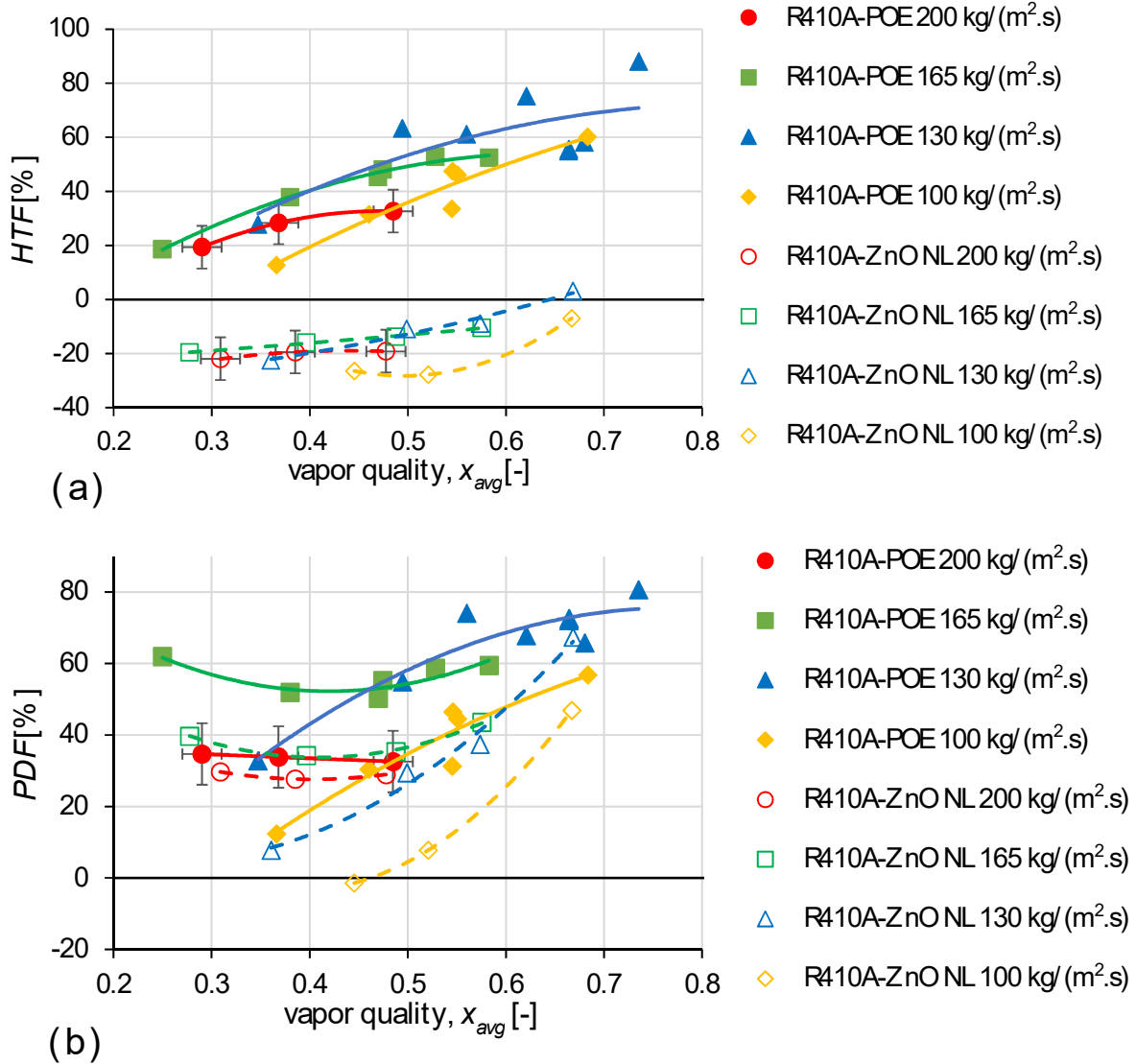


Figure 33: (a) Heat Transfer Factor (HTF) and (b) Pressure Drop Factor (PDF) of R410A-POE and R410A-ZnO NL mixtures. $T_{sat}=6.1^{\circ}\text{C}$, $\dot{q}=15\text{ kW/m}^2$, $OMF=2.4\text{ wt.}\%$.

Figure 33 (a) shows that at refrigerant vapor quality of 0.5, the presence of ZnO nanoparticles in the mixture decreased the HTF by 18% in average, with respect to R410A's HTF . R410A-POE and R410A-ZnO NL mixture tests at the mass flux of $165\text{ kg/m}^2\text{-s}$ and $200\text{ kg/m}^2\text{-s}$, shown by solid and void squares and circles data points, had the transition from stratified-wavy and intermittent to annular two-phase flow at vapor quality of about 0.43. This transition slowed the rate of increase (reduced the slope) of HTF curve for R410A-POE tests with the vapor quality

increase. The R410A-POE tests at a mass flux of $100 \text{ kg/m}^2\text{-s}$, shown by solid diamonds, were always in the stratified-wavy two-phase flow regime and the HTF increased at the same rate with the increase in the quality because of the increasing liquid circumferential wetting angle inside the copper tube. The R410A-POE tests at a mass flux of $130 \text{ kg/m}^2\text{-s}$, shown by solid triangles data points, had scattering at high vapor qualities. The definite reason for the observed scattering was not understood during experimentation. To analyze the test series, it was decided to use a polynomial fit for the data points as shown by blue solid line. The R410A-POE tests at a mass flux of $130 \text{ kg/m}^2\text{-s}$ changed from stratified-wavy to annular flow regime at vapor quality above 0.65 and thus the rate of increase of HTF may reduced at a much higher quality, but was not experimentally observed. At $130 \text{ kg/m}^2\text{-s}$ the HTF of R410A-ZnO NL tests, shown by void triangles, showed a continuous increase, while, at $100 \text{ kg/m}^2\text{-s}$ the HTF of R410A-ZnO NL tests, shown by void diamonds, showed sudden enhancement in heat transfer at vapor qualities above 0.52.

Figure 33 (b) shows that at mass flux of $100 \text{ kg/m}^2\text{-s}$ and $130 \text{ kg/m}^2\text{-s}$, in the stratified-wavy flow regime at vapor qualities less than 0.6, the presence of ZnO nanoparticles in the mixture lowered the PDF by about 30% with respect to R410A-POE mixture's PDF . With the increase in the vapor quality, at $100 \text{ kg/m}^2\text{-s}$ and $130 \text{ kg/m}^2\text{-s}$, the rate of increase of PDF of R410A-POE tests reduced, but the rate of increase of PDF of R410A-ZnO NL tests was enhanced. At mass flux of $165 \text{ kg/m}^2\text{-s}$, the R410A-ZnO NL still had about 20% lower pressure drops than R410A-POE. At mass flux of $200 \text{ kg/m}^2\text{-s}$, both R410A-POE and R410A-ZnO NL tests, shown by solid and void circles data points respectively, showed no change in the PDF as the flow regime transitioned from intermittent to annular flow at vapor quality above 0.43. Also, the PDF for R410A-ZnO NL tests were the same as R410A-POE tests.

Figure 34 shows *HTF* and *PDF* for R410A-POE lubricant mixture (continuous lines) and R410A-Al₂O₃ NL mixture (dotted lines). Figure 34 (a) shows that at vapor quality of 0.5 the R410A-Al₂O₃ NL *HTF* was 34% and 67% below the *HTF* of flow boiling of R410A and R410-POE, respectively, at a low mass flux of 100 kg/m²-s. The *HTF* of R410A-Al₂O₃ NL tests increased with mass flux, and at $x=0.5$ it increased to 7% above *HTF* of R410A, but was still lower than R410A-POE by 42% at 165 kg/m²-s. At 100 kg/m²-s and 130 kg/m²-s the *HTF* of R410A-Al₂O₃ NL tests, shown by void diamonds and triangles data points, suggested a sudden enhancement of heat transfer at vapor qualities above 0.5. At 130 kg/m²-s and vapor quality above 0.6, the heat transfer performance of R410A-Al₂O₃ NL was higher than R410A, and *HTF* of R410A-Al₂O₃ NL increased to 20% at $x=0.7$. Like R410A-POE tests discussed in Figure 33 (a), the R410A-Al₂O₃ NL mixture tests at mass flux of 165 kg/m²-s and 200 kg/m²-s transitioned from stratified-wavy and intermittent to annular flow regime at vapor quality of about 0.43, and this resulted in the rate of increase of *HTF* to slow down. The R410A-Al₂O₃ NL tests *HTF* at 165 kg/m²-s were higher than 200 kg/m²-s, but because of their experimental uncertainty, their heat transfer performance was similar to those of pure refrigerant R410A. The heat transfer performance of R410A-Al₂O₃ NL tests at high vapor quality for mass fluxes at and above 165 kg/m²-s were not recorded because of the test apparatus limitations to achieve such conditions.

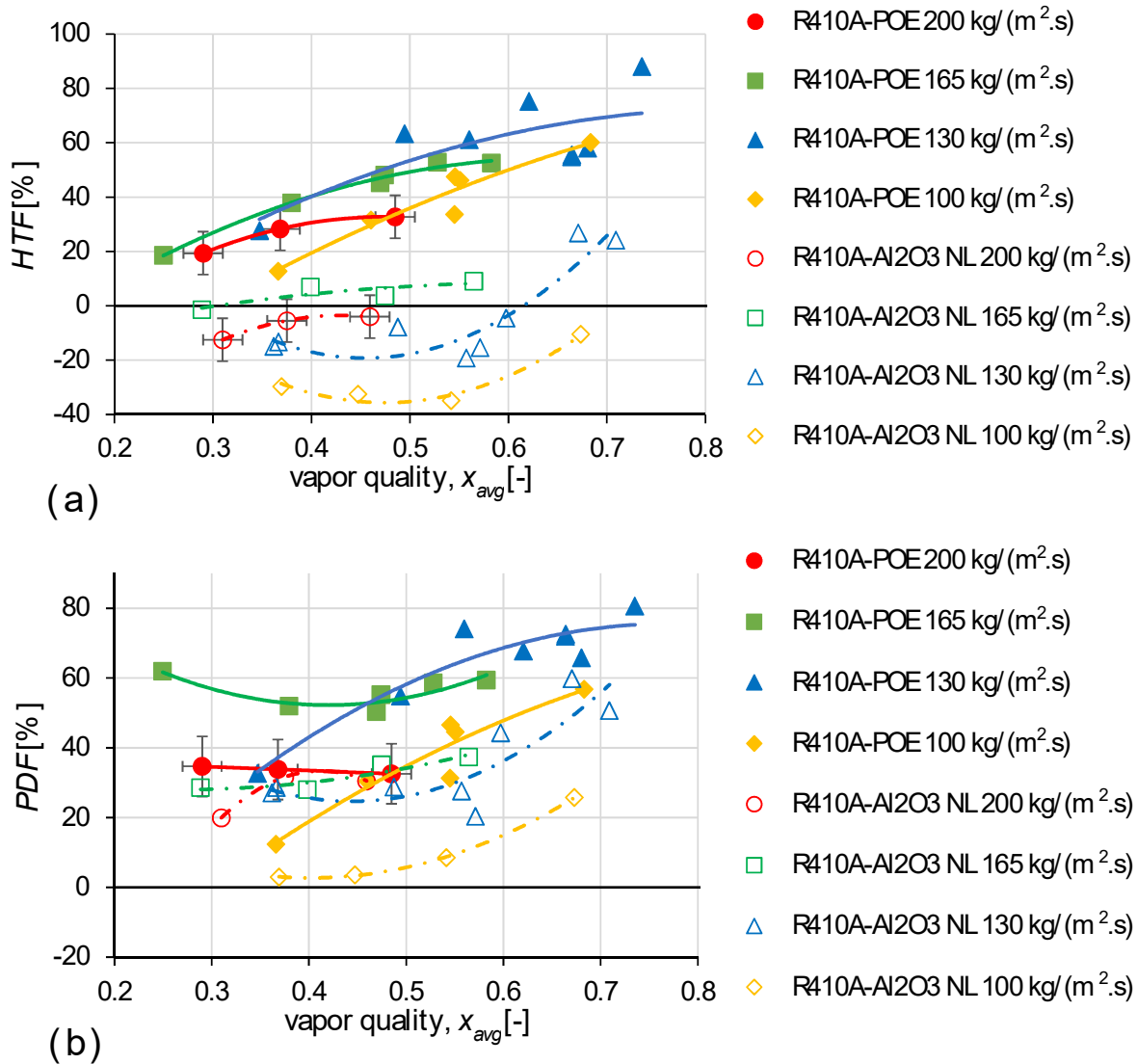


Figure 34: (a) Heat Transfer Factor (*HTF*) and (b) Pressure Drop Factor (*PDF*) of R410A-POE and R410A-Al₂O₃ NL mixtures. $T_{sat}=6.1^{\circ}\text{C}$, $\ddot{q}=15\text{ kW/m}^2$, $OMF=2.4\text{ wt.}\%$.

Figure 34 (b) shows that at mass flux of 100 kg/m²-s and 130 kg/m²-s, in the stratified-wavy flow regime at vapor quality of 0.5, the presence of Al₂O₃ nanoparticles in the mixture caused the *PDF* to decrease by an average of 26% below R410A-POE mixture's *PDF*. Similar to the R410A-ZnO tests in Figure 33 (b), the rate of change of *PDF* of R410A-Al₂O₃ NL tests at 100 kg/m²-s and 130 kg/m²-s, shown by void diamonds and triangles in Figure 34 (b), increased when augmenting the vapor quality. At mass flux of 165 kg/m²-s, the R410A-Al₂O₃ NL still had

about 15% lower pressure drops than R410A-POE, and the *PDF* of R410A-Al₂O₃ NL, shown by void square data points, increased once the flow regime transitioned from stratified-wavy to annular flow at vapor quality above 0.43. At mass flux of 200 kg/m²-s, the R410A-Al₂O₃ NL tests suggested a sudden rise in *PDF* from 20% at $x=0.3$ to 31.6% at $x=0.38$.

The slope of *PDF* curves of R410A-ZnO NL tests in Figure 33 (b) and R410A-Al₂O₃ NL tests in Figure 34 (b) at a mass flux of 100 kg/m²-s and 130 kg/m²-s, increased when the vapor quality increased. On the other hand, for the same mass fluxes, the slope of *PDF* curves of R410A-POE tests decreased with increasing vapor quality. This suggested that as the vapor quality increased and more the liquid circumferential wetting angle increased in the stratified-wavy flow regime, more and more of ZnO and Al₂O₃ nanoparticles approached the inner wall of the copper tube and contributed to increase the pressure drop. At low nanoparticle concentration, the acceleration pressure drops, equation (35), for R410A-POE and R410A-nanolubricant mixtures were similar. The calculated acceleration pressure drops for R410A-POE and R410A-nanolubricant mixtures had a difference of less than 20 Pa/m. Hence, the difference in the measured total pressure drops of R410A-POE and R410A-nanolubricant mixtures were due to change in the frictional pressure drops. The ZnO and Al₂O₃ nanoparticles affected the frictional pressure drops as they approached the inner wall of the copper tube. The observed rate of rising of *PDF* for R410A-ZnO tests was higher than the rate of rising of *PDF* for R410A-Al₂O₃ tests, suggesting that non-spherical ZnO nanoparticles had more wall shear stress than the spherical Al₂O₃ nanoparticles. At mass fluxes of 165 kg/m²-s and above, the *PDF*s of both R410A-ZnO NL and R410A-Al₂O₃ NL were same in magnitude, suggesting the effect of particle shape had a non-measurable effect on wall shear stress and on the frictional pressure drop.

In wavy-stratified flow and at mass flux of $165 \text{ kg/m}^2\text{-s}$, even though R410A-nanolubricant mixtures had 19% higher dynamic viscosity than R410A-POE, the R410A-ZnO NL had more than 20% lower pressure drops than R410A-POE, while the R410A-Al₂O₃ NL had more than 15% lower pressure drops than R410A-POE. These results were in contrast to the pressure drop findings in the literature for nanofluids and nanorefrigerants. The *PDF* had repeatability within $\pm 8.6\%$ as described under the section of ‘Uncertainty Analysis’. Thus, for mass flux tests of $165 \text{ kg/m}^2\text{-s}$ and lower, the error (repeatability) bars for *PDF* results of R410A-POE and R410A-ZnO NL in Figure 33 (b) and for *PDF* results of R410A-POE and R410A-Al₂O₃ NL in Figure 34 (b) would appear to partially overlap.

The test section refrigerant copper tube was replaced with a new tube after the completion of the R410A-ZnO NL mixture tests. The repeated baseline R410A tests in the new test section tube confirmed repeatability of *HTC* and $\Delta P/L$ results. The R410A-Al₂O₃ NL mixture was then tested in the new test section copper tube. R410A-ZnO NL and R410A-Al₂O₃ NL mixtures were tested in the test section with two different refrigerant copper tube, and both the mixture showed similar and lower pressure drops with respect to R410A-POE mixture. This confirms that the nanoparticles did negatively affected the total pressure drop, even though the error bars were partially overlapping for the pressure drop results.

R410A-Al₂O₃ NL tests had an average of 15% higher *HTF* than R410A-ZnO NL tests at vapor quality of 0.5 and mass fluxes above $165 \text{ kg/m}^2\text{-s}$. However, the heat transfer performance of R410A-POE mixture was more than 42% than R410A-ZnO NL and R410A-Al₂O₃ NL mixtures. At lower mass fluxes of $100 \text{ kg/m}^2\text{-s}$ and $130 \text{ kg/m}^2\text{-s}$, the *HTFs* of R410A-ZnO NL tests in Figure 33 (a) and R410A-Al₂O₃ NL tests in Figure 34 (a) showed sudden enhancement only at vapor quality above 0.5. At lower vapor quality, in the stratified-wavy two-phase flow

regime, the nanoparticles suspended in POE were detrimental for heat transfer with measured *HTFs* well below -10%. The nanoparticles came closer to the wall of the tube as the flow transitioned towards annular with an increase in the void fraction and decrease of the annular film thickness, which was evident from sudden rise observed in the *PDFs*. The higher nanoparticle concentration in the annular liquid film at the wall aided in improving the *HTFs*. On the contrary, for non-annular flow in a smooth copper tube of 7.9 mm I.D., for *OMF* of 2 wt.%, NP_{conc} of 0.08 wt.%, and vapor quality less than 0.073, Henderson et al. (2010), observed *HTC* enhancements between 50% and 101% for R134a-POE-CuO mixture compared to R134a-POE with an insignificant effect on the pressure drop. Henderson et al. (2010) showed that for flow boiling of R134a-SiO₂, NP_{conc} of 0.05-0.5 wt.% and vapor quality less than 0.276, the *HTC* decreased by 55% below the R134a baseline due to unstable nanoparticle suspension. Henderson observed the SiO₂ aggregates particles deposited on the tube wall during the test and suggested that the deposition acted as a thermal resistance to the heat transfer. The other reason suggested for the degradation of the R134a-SiO₂ *HTC* was the decrease in the effective thermal conductivity of the nanofluid with the aggregation and loss of SiO₂ nanoparticles. In the current paper, nanolubricant samples were extracted from the test setup after flow boiling tests and they revealed some aggregation and settling of ZnO nanoparticles in the POE lubricant. Al₂O nanoparticles had higher stability in POE than ZnO nanoparticles. Low stability of ZnO nanoparticles, resulting in aggregation and settling-sedimentation, could be one reason for the R410A-ZnO NL tests to have lower *HTF* than the R410A-Al₂O₃ NL tests, but needs further investigation in future work. Visual observations showed ZnO and Al₂O₃ nanoparticles' sparingly deposited on the inner walls of their respective flow boiling tubes. This observation supports that the degradation of R410A-

nanolubricant heat transfer, when compared to R410A-POE case, was not due to an increased thermal resistance of deposited nanoparticles on the wall.

4.3. Effect of nanoparticle deposition on heat transfer

The ZnO and Al₂O₃ nanoparticles deposited on the inner wall of the smooth tubes when the single-phase flow and two-phase flow boiling tests were conducted with R410A-ZnO NL and R410A-Al₂O₃ NL mixtures. Figure 35 shows images taken with a micro-borescope high definition CCD camera inside the two smooth tubes. The viewing angle of the camera was along the axis of the tube and it captured the nanoparticle deposition/settling around the circumference of the tube. The images showed both ZnO and Al₂O₃ nanoparticles as white color layer on the inner wall of their respective tubes after the tests were completed. It is worth to note in here that the Kim et al. (2007), Cieśliński and Kaczmarczyk (2015), and Bigi (2018) suggested that the nanoparticles were pulled towards the boiling surface due to increase in concentration of nanoparticles in the evaporating microlayer beneath a growing bubble or due to induced micro-suction effect from the depression caused by the bubble departure from the nucleation sites. The Van der Waals force between the nanoparticles and heated surface caused the nanoparticle disposition and surface modification (Wen et al. 2011).

The system was thoroughly cleaned after the tests to remove all the lubricant and most of the suspended nanoparticles. However, the system cleaning operations, as explained in section 3.1 Components of the Experimental Test and under subsection of Oil Separator, could not entirely remove the nanoparticle which firmly adhered on the inner tube walls. R410A single-phase flow and two-phase flow test, in the absence of lubricant, were conducted on nanoparticle deposited tube. These tests allowed studying the effect of fouled heat transfer surfaces due to potential

nanoparticle deposition, and establish baselines for R410A tests to study the effects of the other variables on heat transfer.

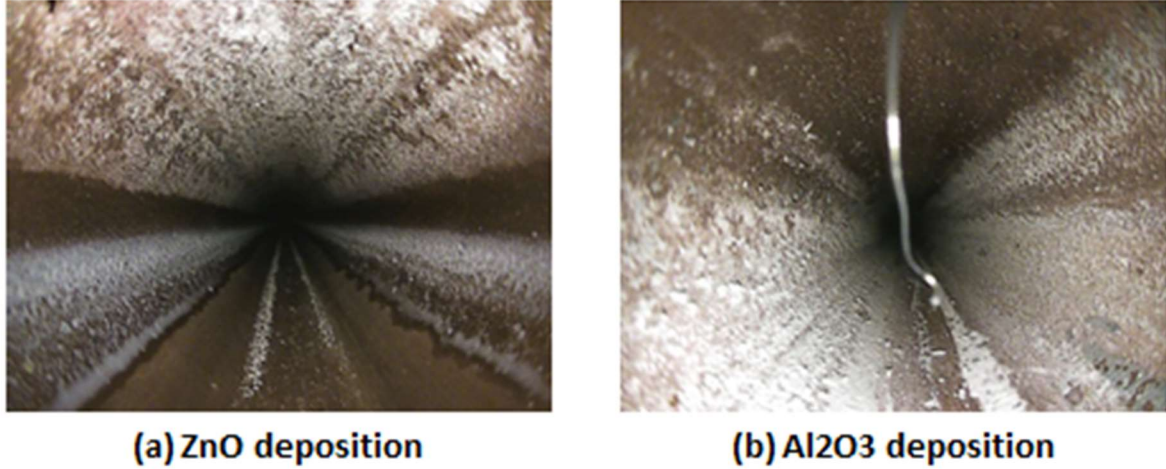


Figure 35: (a) ZnO deposition and (b) Al₂O₃ deposition, on the inner wall of the tube calorimeter.

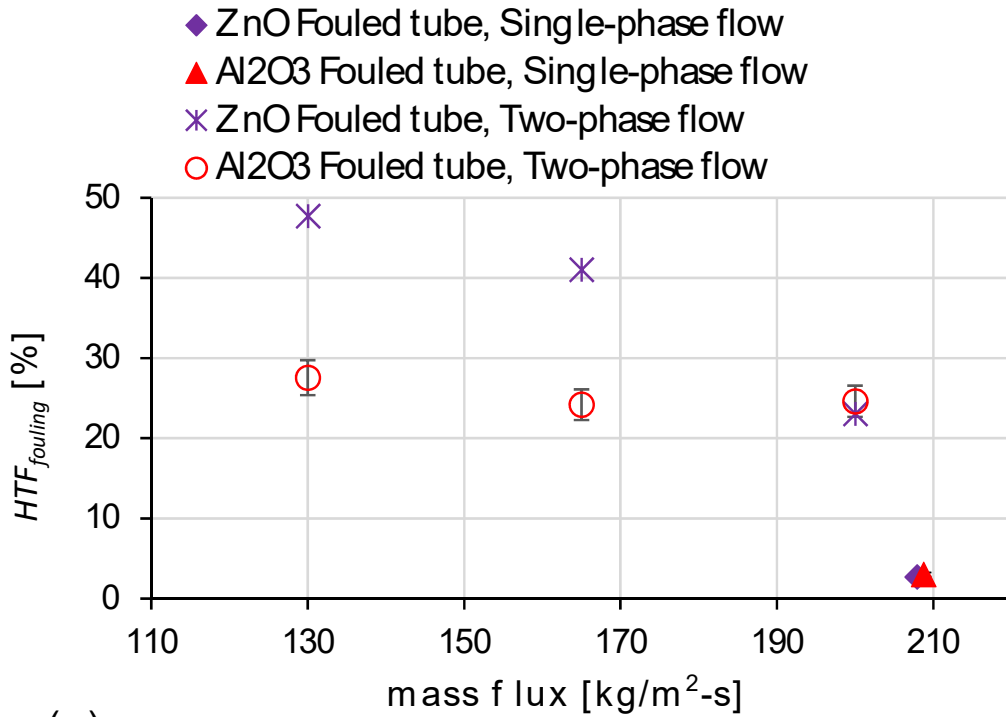
Figure 36 (a) shows percent increase in HTC for single-phase heat transfer and two-phase flow boiling of R410A, in absence of lubricant, in nanoparticle deposited tube with respect to a clean tube. The y-axis of the figure, $HTF_{fouling}$, fouling heat transfer factor, was calculated using equation (33). Figure 36 (b) shows percent increase in the pressure drop (ΔP) for two-phase flow boiling of R410A in nanoparticle deposited tube with respect to a clean tube. The y-axis of the figure, $PDF_{fouling}$, fouling pressure drop factor, was calculated using equation (34). The pressure drops for single-phase flow tests were not presented in the figure because they were too small to be measured with our sensors. The HTC and ΔP of R410A on nanoparticle deposited tube were termed as $HTC_{fouled\ tube}$ and $\Delta P_{fouled\ tube}$.

$$HTF_{fouling} = \frac{HTC_{fouled\ tube} - HTC_{clean\ tube}}{HTC_{clean\ tube}} \times 100 \quad (33)$$

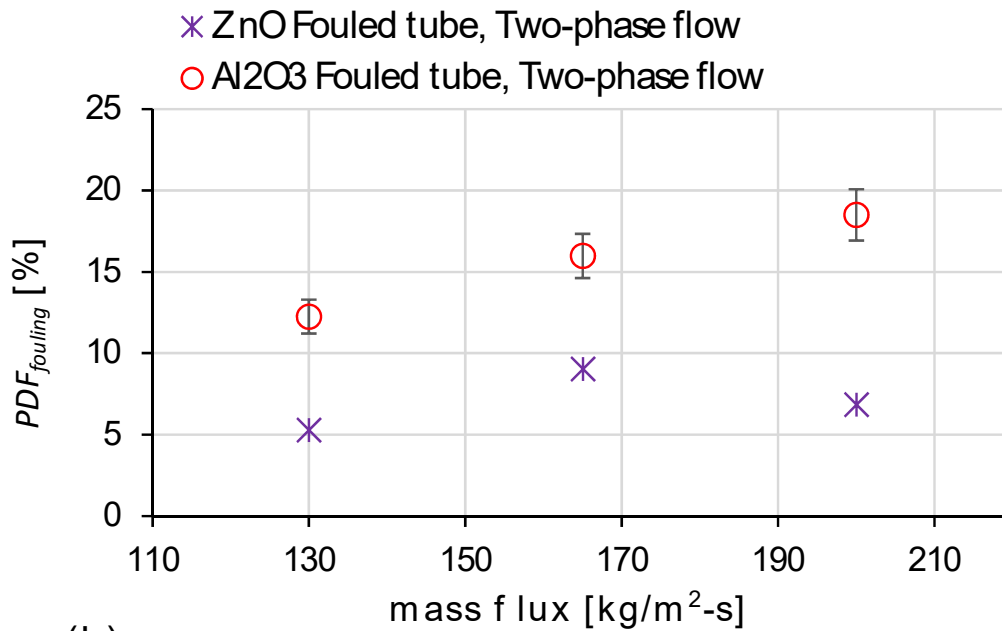
$$PDF_{fouling} = \frac{\Delta P_{fouled\ tube} - \Delta P_{clean\ tube}}{\Delta P_{clean\ tube}} \times 100 \quad (34)$$

Figure 36 (a) shows that at the mass flux of 207 kg/m²-s the single-phase flow $HTF_{fouling}$ of R410A on ZnO deposited tube, shown by a diamond, was increased to 2.7% and $HTF_{fouling}$ of R410A on Al₂O₃ deposited tube, shown by a triangle, was increased to 3%. Figure 36 (a) also shows that the two-phase flow boiling $HTF_{fouling}$ of R410A on ZnO and Al₂O₃ deposited tubes were improved for mass flux from 130 kg/m²-s to 200 kg/m²-s. The deposition of ZnO and Al₂O₃ nanoparticles on tube wall resulted in an increase of the tube roughness, and thus friction factor. The evaluated single-phase friction factor increased by 3.8% and 1.7% for ZnO and Al₂O₃ deposited tubes, respectively, that resulted in improvement of the convective heat transfer for single-phase flow of R410A in fouled tubes. The corresponding increase in the tube relative roughness when evaluated using Colebrook equation were 400% and 170% for ZnO and Al₂O₃ deposited tubes, respectively.

Figure 36 (a) also shows that the two-phase flow boiling $HTF_{fouling}$ of R410A on ZnO deposited tube, shown by crosses, was 23% at a mass flux of 200 kg/m²-s, and with a decrease in a mass flux to 130 kg/m²-s the HTC was further improved by 25% and the corresponding $HTF_{fouling}$ was 48%. While, the two-phase flow boiling $HTF_{fouling}$ of R410A on Al₂O₃ deposited tube, shown by circles, was 25% at a mass flux of 200 kg/m²-s, and with a decrease in mass flux to 130 kg/m²-s the HTC was increased by only 3% such that the $HTF_{fouling}$ was 28%. Literature study revealed that Henderson et al. (2010) observed 50% HTC enhancement for R134a and POE mixture two-phase flow boiling in CuO nanoparticles deposited tube, while the researchers concluded that the enhancement was due to the boiling surface modification due to CuO nanoparticles deposition and strong adhesion to the heat transfer surface.



(a)



(b)

Figure 36: (a) $HTF_{fouling}$ and (b) PDF_{fouled} , of R410A in absence of lubricant. (Two-phase flow tests were conducted at $T_{sat}=6.1^{\circ}\text{C}$, $x=0.49$, and $\dot{q}=15\text{ kW/m}^2$, while the single-phase flow tests were conducted at $T_{ref}=9.6^{\circ}\text{C}$ and $\dot{q}=8.7\text{ kW/m}^2$)

Figure 36 (b) shows that at all mass fluxes the two-phase flow pressure drops were higher for nanoparticle deposited tube compared to a clean tube, which suggests a possible increase in the tube roughness and the friction factor. The ΔP_{fouled} for ZnO deposited tube, shown by crosses, were within 5% and 10%, and were also lower than Al₂O₃ deposited tube and did not change with the mass flux. The ΔP_{fouled} for Al₂O₃ deposited tube, shown by circles, increased with mass flux from 12% at 130 kg/m²-s to 19% at 200 kg/m²-s. The two-phase friction factor were evaluated from the experimental pressure drop results in Figure 36 (b), the deposition of nanoparticles caused the two-phase friction factor for ZnO deposited tube and Al₂O₃ deposited tube to increase by an average of 11% and 19%, respectively.

The friction factor was increased by 19% as an input to Kandlikar (1990) correlation to simulate the effect of fouling on two-phase flow heat transfer. This resulted in the predicted HTC for the fouled tube to increase by 15% compared to the predicted HTC for the clean tube. However, Figure 36 (a) shows that the improvement, $HTF_{fouling}$, in the heat transfer coefficients for the two-phase flows were greater than 25%. From these results, it was concluded that the improved heat transfer coefficient was due to modified surface characteristics and increased nucleation site density that was due to nanoparticle deposition on the inner surface of the tube.

Kim et al. (2010), during the subcooled flow boiling experimentation, observed improvements in the heat transfer performance of water-Al₂O₃ and water-ZnO nanofluids, and Kim attributed this improvement to nanoparticle deposition on the boiling surface that modified the surface characteristics, like the nucleation site density. However, Sarafraz and Hormozi (2014) and Sarafraz et al. (2014) observed decrease in the heat transfer performance for water-Al₂O₃ nanofluid with time due to increase in nanoparticle sedimentation and scaling on the heat transfer surface. In current work, R410A-ZnO NL and R410A-Al₂O₃ NL mixtures' two-phase saturated

flow boiling tests were recorded over several days, as shown in Figure 37, to study the influence of a change in boiling surface characteristic due to ZnO and Al₂O₃ nanoparticle deposition on the tube's inner heat transfer surface.

Figure 37 (a) shows that at the mass flux of 200 kg/m²-s, shown by cross and circle symbols, the *HTC* for both the R410A-ZnO NL and R410A-Al₂O₃ NL mixtures increased gradually by 34% over 9 days. The *HTC* of R410A-Al₂O₃ NL was 18% higher the *HTC* of R410A-ZnO NL and stayed consistent over the 9 days. At mass flux of 165 kg/m²-s, shown by plus and diamond symbols, the *HTC* of R410A-ZnO NL increased at a much lower rate compared to the *HTC* increase of R410A-Al₂O₃ NL, over the period of 8 days the rise in *HTC* for R410A-ZnO NL and R410A-Al₂O₃ NL tests were 14% and 28%, respectively. At mass flux of 130 kg/m²-s, shown by solid-triangle and square symbols, when the flow was stratified-wavy, the *HTC* of R410A-ZnO NL did no change beyond its error bars, but over the period of next 6 days the rise in *HTC* for R410A-Al₂O₃ NL tests was 42%.

Figure 37 (b) shows the total pressure drop per unit length, $\Delta P/L$, over several days for both R410A-ZnO NL and R410A-Al₂O₃ NL mixtures reduced with time, but the reduction was negligible because the variations of pressure drops due to nanoparticle sedimentation were within the error bars of the measurements.

The acceleration (momentum) pressure drop, $\Delta P/L_{mom}$ in equation (35), was subtracted from the experimental total pressure drop, $\Delta P/L_{exp,2-pha}$ in Figure 37 (b), to obtain a two-phase frictional pressure drop, $\Delta P/L_{frict,2-pha}$ as shown in equation (36). The two-phase friction multiplier, $(\phi_l^2)_{ref+}$, for the flow of refrigerant-lubricant mixture was evaluated using correlation provided by Zürcher et al. (1998), as shown in equation (29).

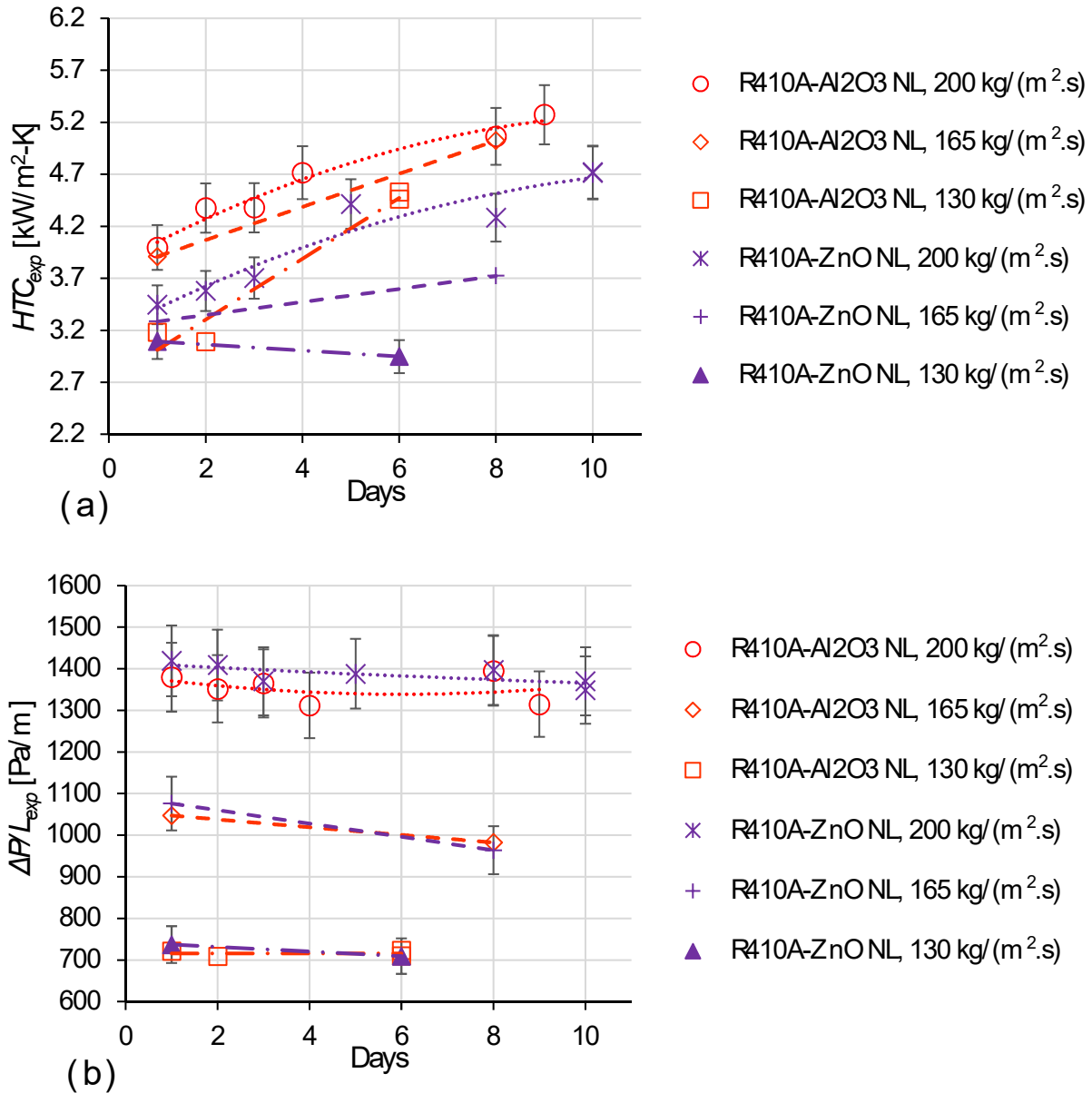


Figure 37: (a) HTC and (b) Pressure drop data for repeated tests of R410A-ZnO NL mixture and R410A-Al₂O₃ NL mixture over several days in a smooth copper tube at $x=0.48$ and 15 kW/m^2 .

The two-phase frictional pressure drop and the two-phase multiplier were used to evaluate single-phase frictional pressure drop, $\Delta P/L_{frict,1-phase}$ as shown in equation (37). The single-phase frictional pressure drop was then used to evaluate single-phase friction factor, f , using Colebrook

equation, shown in equation (38), and wall shear stress, $\tau_w = (f/8)\rho_{f,v}(\dot{m}/\rho_{f,b})^2$. The dimensionless laminar sublayer thickness was then evaluated using the theoretical equation $\delta_v^+ = V_i/V_* = (\dot{m}/\rho_{f,b})/\sqrt{\tau_w/\rho_{f,v}}$. The equation for dimensionless laminar sublayer thickness is discussed later in section ‘5.4.3 Definition for the dimensionless laminar sublayer thickness’. The evaluated dimensionless laminar sublayer thickness for R410A-ZnO NL and R410A-Al₂O₃ NL tests in Figure 37 was within 15 and 16.5. This small change in the δ_v^+ was too small to be able to cause considerable change in *HTC* as observed in Figure 37 (a). The literature work have shown the dispersed nanoparticles in basefluid that did not vary the friction factor (Nikulin, Moita, et al. 2019), while this analysis showed that the modified friction factor and wall shear stress due to nanoparticle deposition insignificantly altered the *HTC*. This could further support the possibility of an increase in *HTC* due to improvement in nucleate boiling.

$$\Delta P/L_{mom} = \frac{\dot{m}^2}{L_{TestSection}} \left\{ \left[\frac{x_{out}^2}{\alpha_{out}\rho_{ref,g}} - \frac{(1-x_{out})^2}{(1-\alpha_{out})\rho_{ref+L,l}} \right] - \left[\frac{x_{in}^2}{\alpha_{in}\rho_{ref,g}} - \frac{(1-x_{in})^2}{(1-\alpha_{in})\rho_{ref+L,l}} \right] \right\} \quad (35)$$

$$\Delta P/L_{frict,2-phase} = \Delta P/L_{exp,2-phase} - \Delta P/L_{mom} \quad (36)$$

$$\Delta P/L_{frict,1-phase} = \frac{\Delta P/L_{frict,2-phase}}{(\phi_l^2)_{ref+L}} \quad (37)$$

$$\frac{1}{\sqrt{f}} = -2\log \left(\frac{\varepsilon/D_h}{3.7} + \frac{2.51}{Re\sqrt{f}} \right) \quad (38)$$

The nanoparticle deposition or sedimentation may increase or decrease the nucleation density at the heated surface depending on the deposited nanoparticle agglomerate size and change in the wettability at the surface. Agglomerated nanoparticles when inside the cavities, split them into multiple nucleation sites to increase the nucleation site density (Vafaei 2015), and thus they

can enhance *HTC*. Or, the nanoparticles at the heated surface may detach and transfer momentum to the growing bubbles by collision (Kedzierski 2011), thus improving two-phase *HTC* for pure R410A in fouled heated tube.

It is often implied that flows are universally similar over a smooth surface and dimensionless laminar sublayer δ_v^+ is constant, which was also evident from the evaluated δ_v^+ for R410A-ZnO NL and R410A-Al₂O₃ NL tests. However, through flow experiments, Chriss and Caldwell (1984) suggested that δ_v^+ was not a constant and it varied from 8 to 20. The variability in δ_v^+ was not due to the local small scaled irregularities, but was a result of flow variability that extended upstream of the flow over a large distance. A rough patch of nanoparticle deposition upstream of the flow could be responsible for the large variability in δ_v^+ , thinning of laminar sublayer thickness or reduction in δ_v^+ help enhance the *HTC*. It is worth noting that the laminar sublayer thickness was in the order of 0.1 mm, and its measurement was not possible with the test setup. Additional future research should focus on experimentally determining the actual dependence of *HTC* on δ_v^+ in the presence of nanoparticles.

The R410A-ZnO NL and R410A-Al₂O₃ NL mixtures tests, shown in Figure 37 (a), showed *HTC* improvement with time as more surface area got covered with nanoparticle deposition with time, this improvement was possibly due to an increase in the nucleation site density on the copper tube surface or due to more nanoparticles at the heated surface detaching from the deposition and transferring momentum to the growing bubbles by collision. This behavior agreed with the observation from the literature; when cleaning the test section after the CuO-POE-R134a flow boiling tests, (Henderson et al. 2010) observed that the repeated 1% OMF POE-R134a test showed more than 50% *HTC* enhancement above the original baseline test. Henderson et al. concluded that the boiling surface was modified due to CuO nanoparticles deposition and strong

adhesion to the heat transfer surface. (Henderson et al. 2010) suggested the degradation of the R134a-SiO₂ nanofluid's *HTC* was the decrease in the effective thermal conductivity of the nanofluid with the aggregation and loss of SiO₂ nanoparticles. Previous experimental work (Cremaschi et al. 2017) and current work's Buongiorno model prediction showed that decrease of the effective thermal conductivity of the fluid due to decrease in the nanoparticle concentration did not significantly alter the *HTC*.

4.4. Effect of nanoparticle agglomeration and concentration on heat transfer

The non-spherical ZnO nanoparticles, of elongated structures with an aspect ratio of up to 3, had surface weighted diameters of 20 nm to 40 nm after their manufacturing. While, the peak of number-weighted diameter for ZnO nanoparticles dispersed in POE along with proprietary polymeric surfactant was 125 nm when measured using DLS instrument, as shown in Figure 38. The DLS measurement of the extracted ZnO NL sample from the test apparatus showed an increase in the number-weighted diameter of the nanoparticles to 825 nm, as shown by the dotted line in the plot of Figure 38, suggesting deactivation of surfactant and thus agglomeration of the nanoparticles. The figure also shows the ZnO nanoparticles, in the nanolubricant sample extracted from the system after flow boiling tests, settled under gravity over a week leaving a greenish tinge to the colorless POE oil. The surfactant when not attached to the nanoparticles may affect *HTC*, studies (Nikulin, Khliyeva, et al. 2019; Peng et al. 2011) have shown that different types of surfactants may assist or degrade the *HTC*, but the degree to which the proprietary surfactant could influence the *HTC* was not measurable in the current work.

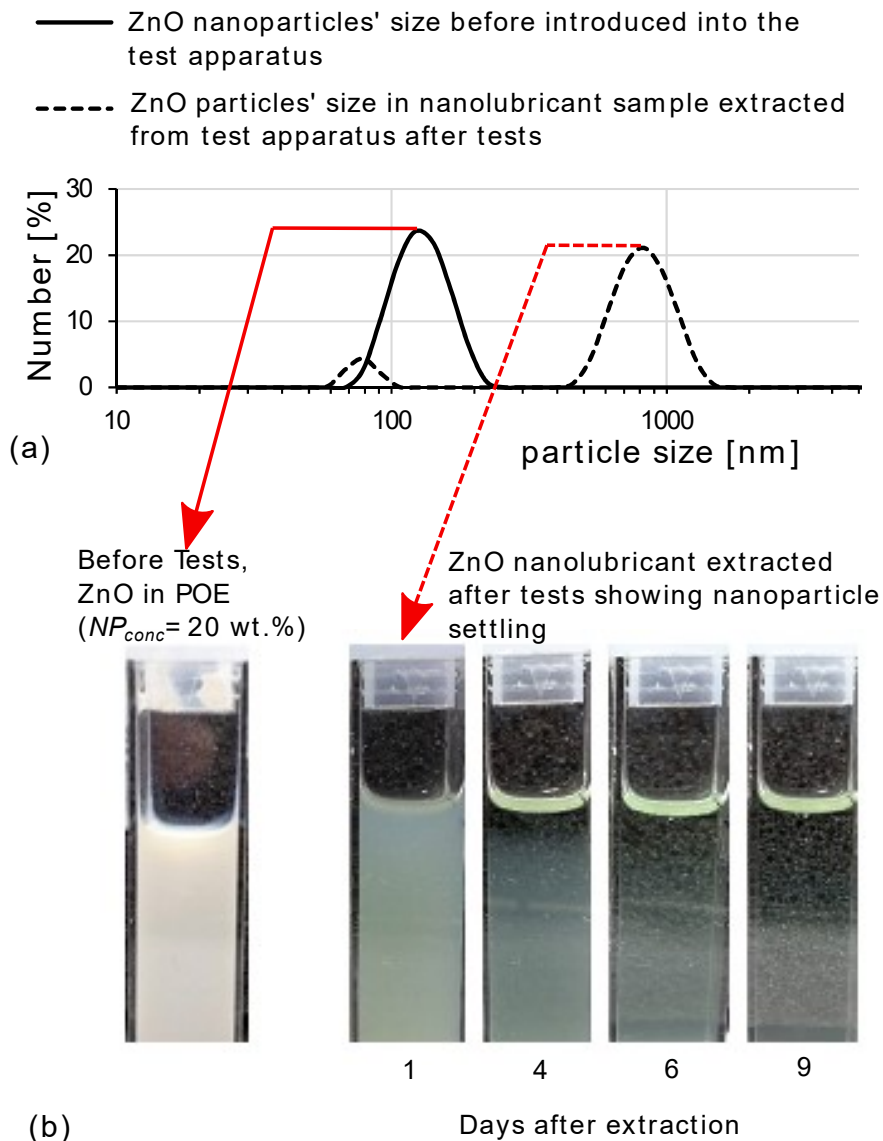


Figure 38: (a) Number-weighted diameter of ZnO nanoparticles with DLS instrument and (b) corresponding settling characteristics of ZnO nanoparticles in the extracted nanolubricant sample after tests.

The spherical Al₂O₃ nanoparticles had surface weighted diameters of 40 nm after their manufacturing. While, the peak of number-weighted diameter for Al₂O₃ nanoparticles dispersed in POE along with proprietary polymeric surfactant was 68 nm when measured using DLS instrument, as shown in Figure 39. The DLS measurement of the extracted Al₂O₃ NL sample from the test system showed an increase in the number-weighted diameter of the nanoparticles to 100

nm, as shown by the dotted line in the plot of Figure 39, suggesting some agglomeration of the nanoparticles. The figure shows the Al₂O₃ nanoparticles in the extracted Al₂O₃ NL sample partially settled under gravity over a week while the rest Al₂O₃ nanoparticles remained dispersed over an extended period.

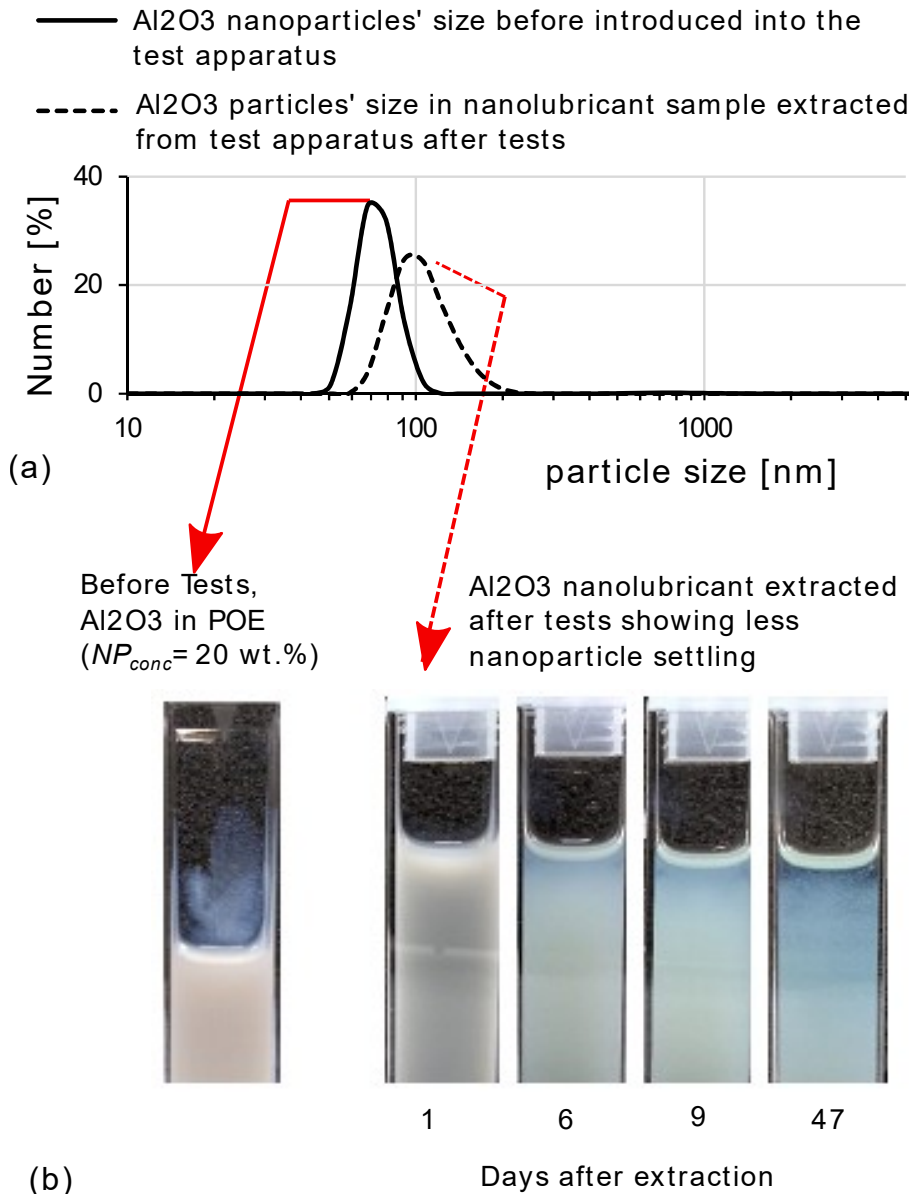


Figure 39: (a) Number-weighted diameter of Al₂O₃ nanoparticles with DLS instrument and (b) corresponding settling characteristics of Al₂O₃ nanoparticles in the extracted nanolubricant sample after tests.

For single-phase flow heat transfer condition at same Reynolds number and NP_{conc} of 20 wt.% in the POE lubricant, the experimental HTC R410A-ZnO NL mixture was 0.8% higher than of R410A-POE mixture HTC , and the experimental HTC R410A-AL₂O₃ NL mixture was 0.6% higher than of R410A-ZnO NL mixture HTC . Buongiorno (2006) model for the same condition predicted R410A-ZnO NL HTC to be 1.3% higher than HTC of R410A-POE, and the R410A-AL₂O₃ NL HTC to be just 0.1% higher than HTC of R410A-ZnO NL. Nanoparticle deposition on the tube wall had increased the single-phase friction factor, as explained under Figure 35 and Figure 36, by 3.8% and 1.7% for ZnO and Al₂O₃ deposited tubes, respectively. In addition, the nanoparticle size increased above 40 nm due to agglomeration, explained under Figure 38 and Figure 39, to 825 nm and 100 nm for ZnO and Al₂O₃ nanoparticles, respectively. Parameters like; increased single-phase friction factor due to nanoparticle deposition and increased nanoparticle size or changed aspect ratio due to agglomeration did not alter the Buongiorno (2006) model output significantly to justify the difference between the R410A-POE, R410A-ZNO NL, and R410A-AL₂O₃ NL mixtures' single-phase HTC .

When the input of ZnO nanoparticle mass concentration in POE oil was lowered to 14 wt.%, Buongiorno (2006) model predicted R410A-ZnO NL HTC to be 0.8% higher than HTC of R410A-POE, and R410A-AL₂O₃ NL HTC to be 0.6% higher than HTC of R410A-ZnO NL, thus the results were consistent with the experimental findings. Buongiorno model showed the change in the suspended nanoparticle concentration had a significant effect on the single-phase convective heat transfer than other studied parameters. This finding was similar to the numerical simulation finding by Yuan et al. (2018), where the authors showed that increasing particle volume concentration was more effective to increase the heat transfer than increasing the aspect ratio.

In a system, with continuous alternating evaporation and condensation, the ZnO nanoparticle deposition could have decreased its concentration in the circulating refrigerant-oil mixture, as was observed by (Lin et al. 2017). Similar lowering of Al₂O₃ concentration and thus lowered *HTC* was not observed. The decrease of ZnO nanoparticle concentration from the R410A-ZnO NL mixture flowing through the test section was possible due to the visually observed agglomeration of ZnO nanoparticles that settled in different components of the system and were then lost from the flow. ZnO NL stayed as a stable suspension for months. However, the ZnO nanoparticles appeared to agglomerate and settle once the ZnO NL was injected into the system during tests, as could be seen in flow sight glass in Figure 40 (a). Al₂O₃ NL also stayed as a stable suspension for months, and the Al₂O₃ nanoparticles did not appear to agglomerate and settle with same intensity as that of ZnO nanoparticles when the Al₂O₃ NL was injected into the system during tests, as could be seen in flow sight glass placed before the test section in Figure 40 (a).

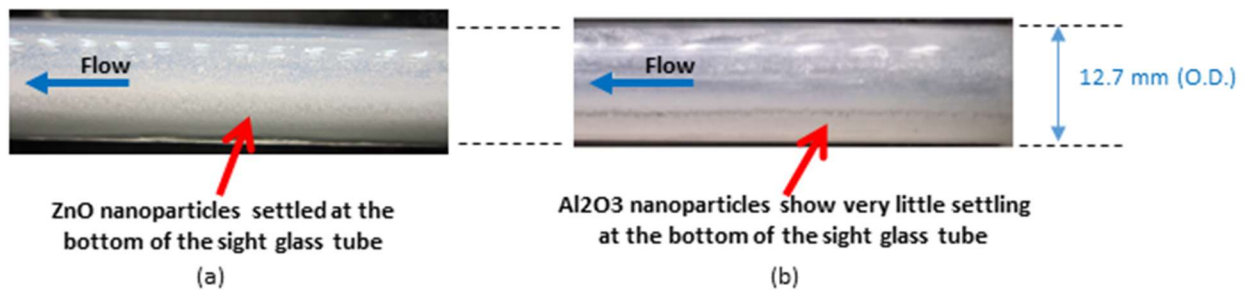


Figure 40: (a) ZnO nanoparticles settling in sight glass, and (b) Al₂O₃ nanoparticles settling in sight glass.

In one of our simulation case study at same Reynolds number, the ZnO nanoparticle concentration in the turbulent layer was kept constant at 27 wt.%, and the nanoparticle concentration in the laminar sublayer was increased from zero to much higher concentration than in the turbulent layer. This study was performed to understand the effect of nanoparticle

aggregation near the wall and in the laminar sublayer. The increase in the nanoparticle concentration in the laminar sublayer from zero to twice the nanoparticle concentration in the turbulent layer increased the effective thermal conductivity, k_v , by 1.5%, increased the viscosity, μ_v , by 4.4%, and increased the laminar sublayer thickness, δ_v , by 4.4%. Here, the increase in the laminar sublayer thickness ($\delta_v = u_i \cdot \mu_v / \tau_{wall}$) was due to increase the laminar sublayer viscosity, μ_v , and not due to insignificantly changed interface velocity, u_i , and wall shear stress, τ_{wall} . The HTC in the laminar sublayer, which simply can be represented as the ratio (k_v / δ_v), decreased by 2.1%, while the net convective HTC , equation (Equation (76)), decreased by 1.4%. The analysis suggested that the nanoparticle aggregation at the wall was harmful for the convective heat transfer due to thickening of the laminar sublayer. This could not have been the reason for lowered R410A-ZnO NL experimental HTC in contrast to the previous paragraph discussion, as the agglomerated ZnO nanoparticles settled under gravity only on the bottom surface of the horizontal tube and this should have also decreased the nanoparticle concentration in the turbulent layer.

5. Heat transfer and pressure drop models

We recall in here that, Bigi's original model combined the Buongiorno (2006) model for nanofluid convective heat transfer with the Kedzierski (2012) model for pool boiling of refrigerant-nanolubricant mixtures on finned heated surface. First, a brief summary of Buongiorno (2006) and Kedzierski (2011) models are given in this chapter. Bigi (2018) conducted an initial experimental validation of his model for internally finned copper tubes, and the simulation predictions had about $\pm 50\%$ deviation with respect to the experimental data. One of the reason given in Bigi PhD dissertation for the deviation was the assumption of constant nanoparticles concentration in the turbulent layer. The concentration of nanoparticles in the turbulent layer did not increase when they diffused from laminar sublayer towards the turbulent layer. Another limitation of the model originally developed by Bigi was the assumption of the two-phase convective multiplier, F , in the superposition model to be independent of the nanoparticle concentration. These two limitations were addressed and the model upgrades are given in the later sections of this chapter.

This chapter shows the Brownian diffusivity equations was updated in order to extend Bigi's original model to non-spherical nanoparticles, such as ZnO nanoparticles. Finally, following a similar approach presented in Bigi and Cremaschi (2019) paper, the slip mechanisms effects for non-spherical nanoparticles were theoretically investigated. And it will pointed out later in this chapter, in comparison with the spherical nanoparticle case, the non-spherical nanoparticles diffuse slowly under Brownian motion to uniformly disperse in the base refrigerant-lubricant mixture.

The chapter also presents sample calculations to evaluate the predicted heat transfer coefficient using the newly developed superposition model for two-phase flow tests of R410A, R410A-POE, R410A-ZnO NL, and R410A-Al₂O₃ NL mixtures. At the end of the chapter the deviation between the experimental data and predicted heat transfer coefficient are presented.

5.1. Thermophysical properties of nanolubricants

Kedzierski et al. (2017) provided the measurements of liquid kinematic viscosity, density, and thermal conductivity for Al₂O₃ and ZnO nanoparticles based nanolubricants, at atmospheric pressure and within temperature range of 14.85°C and 44.85°C. A Stabinger-type viscometer measured the dynamic viscosity and the density of the liquid, and a transient hot wire instrument measured the thermal conductivity of the nanolubricants. Most of the measurements for nanofluids' thermal conductivity in the literature were done using transient hot-wire method, the details of working of the transient hot-wire apparatus can be found in the paper by Xuan & Li (2000). The thermal conductivity of nanofluid was termed as 'effective' thermal conductivity as it was a mixture of two or more components. The kinematic viscosity, density, and thermal conductivity increased with increasing nanoparticle mass fraction. The kinematic viscosity and density decreased with increasing temperature for polyolester (POE) lubricant and POE based nanolubricants.

Kedzierski's research work regarding improving the performance of R134a chillers, commonly using RL32-3MAF polyolester (POE) lubricant, made the author choose this particular POE lubricant for measurements. A polymeric surfactant maintained dispersion of the nanoparticles in the POE lubricant; however, the author could not provide property information of the surfactant due to its proprietary nature. Kedzierski et al. (2017) reported the use of density of Al₂O₃ nanoparticle as $\rho_{np} = 3600 \text{ kg/m}^3$ and ZnO nanoparticles as $\rho_{np} = 5610 \text{ kg/m}^3$, also using

the measured data of density of the nanolubricants, the author reverse engineered the surfactant specific volume as; $1/\rho_s [m^3/kg] = 0.0005840 + (0.0003240 \times (T[in\ kelvin]/273.15))$. The measured nanolubricant effective thermal conductivities were compared with the Maxwell equation. The Maxwell equation predicted the Al₂O₃ nanolubricant measurements within $\pm 1\%$, but it under predicted the ZnO nanolubricant measurements by 70%. The Maxwell equation was a heterogeneous media model for well-dispersed spherical particles, hence could not have predicted the ZnO nanolubricant data. The Hamilton–Crosser model, which modified the Maxwell’s equation had a sphericity (Ψ) parameter, to make it valid for non-spherical particles. The sphericity was defined as the ratio of the surface area of a sphere (a sphere whose volume was equal to the volume of the particle) to the actual surface area of the particle. After setting the sphericity to $\Psi = 0.55$ for ZnO nanoparticle, the Hamilton–Crosser model predicted the ZnO nanolubricant thermal conductivity measurements within $\pm 1\%$. (For readers reference; a sphere has a sphericity of 1.0 and a cube has a sphericity of 0.806.)

The Al₂O₃ nanoparticle was spherical in shape, and the ZnO nanoparticle had both spherical and elongated structures that form tetrapod shapes. The spherical Al₂O₃ and non-spherical-tetrapod ZnO nanoparticles had surface weighted diameters of 40 nm and 20 nm, respectively, after their manufacturing. The number weighted based average equivalent diameters, measured using DLS, for the Al₂O₃ and the ZnO nanoparticles were 127 nm \pm 3 nm and 135 nm \pm 3 nm, respectively. A number weighted size closely represented the actual projected dimension of a nanoparticle, hence was much larger than the surface weighted diameters. Kedzierski et al. (2017) noted that the number weighted projected size was more suitable for viscosity measurements, as the profile drag of nanoparticles was generally larger than the skin friction. The area based on surface weighted diameter was useful for determining the amount of surfactant

necessary to produce a stable dispersion of nanoparticles in the nanofluid. The measured nanolubricant viscosities by a Stabinger-type viscometer were compared with the viscosity model by Kedzierski et al. (2017). As per the viscosity model, the liquid kinematic viscosity of the nanolubricant was a sum the viscosity of a pure lubricant and pseudo-viscosities for surfactant and nanoparticles, where each pseudo-viscosity accounts for the interaction between the nanoparticle and the surfactant. The number weighted based diameters, $D_p = 127$ nm for the Al₂O₃ nanoparticle and $D_p = 135$ nm for the ZnO nanoparticle, and temperature were used as inputs for the viscosity model. The viscosity model predicted the measured data within $\pm 20\%$.

Bigi et al., (2015), Cremaschi et al., (2015) and Kedzierski et al., (2017) provided the measurements and thermophysical models for the liquid kinematic viscosity, density, and thermal conductivity for Al₂O₃ and ZnO nanoparticles and RL32-3MAF POE lubricant based nanolubricants. Kedzierski et al. (2017) suggested sphericity of $\Psi = 0.55$ for ZnO nanoparticles and was used in the thermal conductivity model. A polymeric surfactant maintained dispersion of the nanoparticles in the POE lubricant; however, the nanolubricant supplier ‘Nanophase Technologies Corporation’ and Kedzierski et al. (2017) using the same nanolubricant, could provide limited property information of the surfactant due to its proprietary nature. The effect of the surfactant on the heat transfer characteristic was captured (Kedzierski 2003a, 2011; Kedzierski et al. 2017) in an empirical model for pool boiling studies of R134a-(POE_RL68H)-Al₂O₃ nanorefrigerant. This pool boiling model is discussed later in the report and was extrapolated to the current study using similar nanorefrigerants.

5.2. Application of existing two-phase flow boiling pressure drop correlations

A comparison of experimental total pressure drop per unit length, $\Delta P/L$, of R410A, R410A-POE, R410A-ZnO NL, and R410A-Al₂O₃ NL with the predicted results using literature correlations is shown in Figure 41. The y-axis of the figure, $\Delta P/L_{corr_div}$, is percent deviation of correlation prediction of total pressure drop, $\Delta P/L_p$, from experimental total pressure drop, $\Delta P/L_{exp}$, and was calculated using equation (39). The literature correlations summarized in Table 11 were for frictional pressure drop. The total pressure drops were obtained by adding the momentum pressure drop from equation (35) to the literature frictional pressure drop prediction. The mean absolute deviation for these correlations' prediction for the experimental data was calculated using equation (40), and are summarized in Table 12.

$$\Delta P/L_{corr_div} = \left[\frac{\Delta P/L_p - \Delta P/L_{exp}}{\Delta P/L_{exp}} \right] \times 100 [\%] \quad (39)$$

$$\text{Mean Absolute Deviation} = \frac{1}{\text{Data points}} \sum \left(\left| \frac{\Delta P/L_p - \Delta P/L_{exp}}{\Delta P/L_{exp}} \right| 100 \right) [\%] \quad (40)$$

For R410A data, the correlation by Hu et al. (2009) showed the most deviation than other correlations. The refrigerate, oil type, oil mass fraction, and heat flux of the current work was similar to work of Hu et al. (2009), and the Hu et al. correlation was applicable for smooth tubes with internal diameters less than 6.34 mm and mass fluxes above 200 kg/m²-s. The experimental tests of this work were done in a larger diameter tube of 9.5 mm and at lower mass fluxes, leading the Hu et al. (2009) correlation to predict -63% lower pressure drops. The same correlation had a mean absolute deviation above 70% for all R410-lubricant mixtures. Choi et al. (2001) presented a total pressure drop correlation for R410A-lubricant mixture's evaporation and condensation in smooth and micro-fin tubes. The correlation well-predicted pressure drop for R410A in the

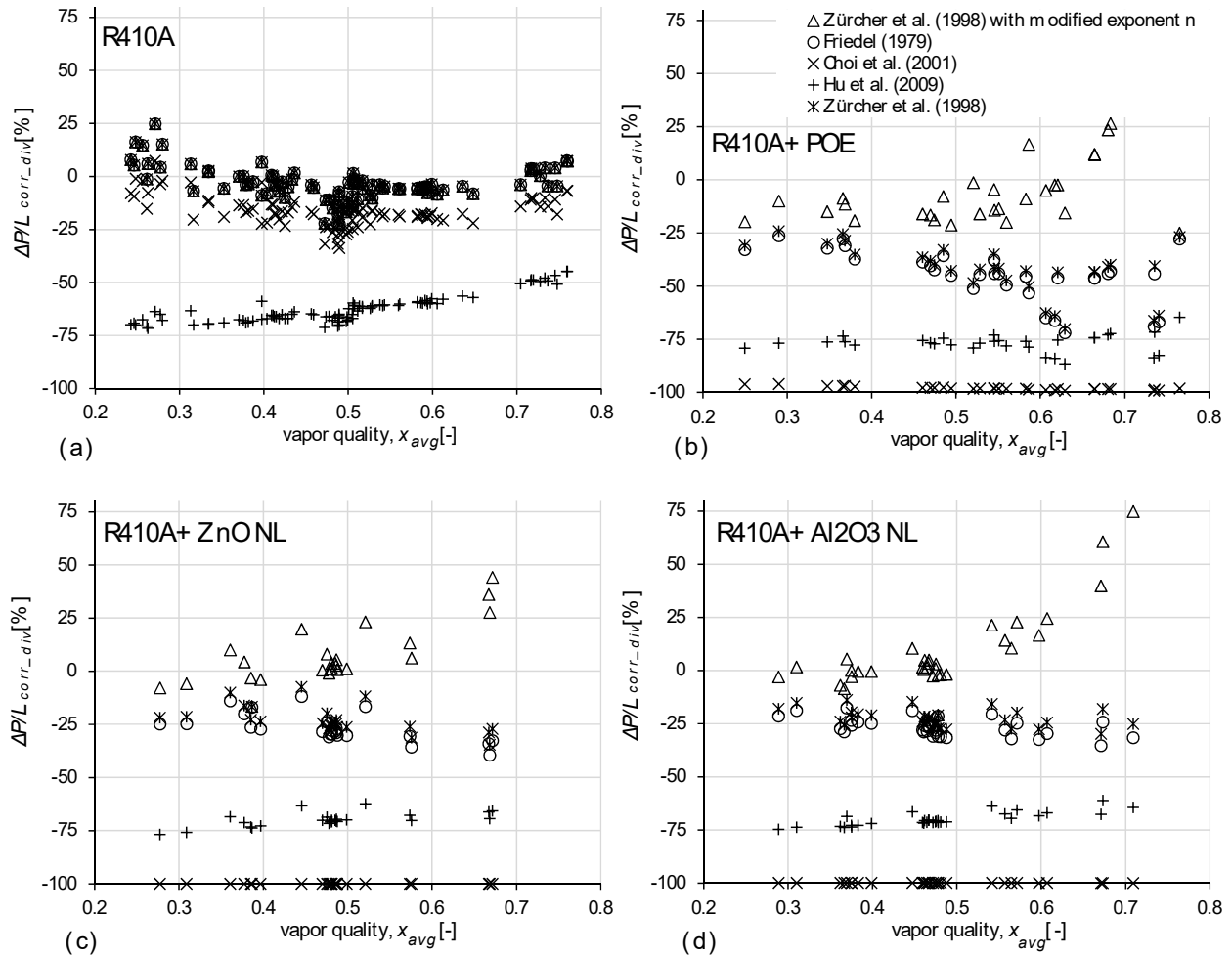


Figure 41: Prediction of smooth tube total pressure drop using literature correlations for (a) R410A, (b) R410A-POE, (c) R410A-ZnO NL, and (d) R410A-Al₂O₃ NL mixtures.

absence of oil with a mean absolute deviation of 17%. The correlation, however, did not well predict the pressure drop for R410A-lubricant mixtures, showing highest mean absolute deviation of 98%. Zürcher et al. (1998) correlation, equation (29), well predicted the experimental pressure drops for R410A, R410A-ZnO NL, and R410A-AL₂O₃ NL within $\pm 30\%$, however the predictions

Table 11: Literature pressure drop correlations.

Reference	Correlation	Tube orientation [fluid] {range}
Friedel (1979)	$(dP/dz)_{frict} = [2 \cdot f_F \cdot \dot{m}^2 / (\rho_{f,bv} \cdot D_h)] \phi_l^2$ $\phi_l^2 = C_{F1} + \frac{3.24 \cdot C_{F2}}{Fr_{bv}^{0.045} \cdot We^{0.035}}$ $f_F = f_{lo}/4, f_{lo} = \frac{0.184}{[\dot{m} \cdot D_h / \mu_{f,bv}]^{0.2}}, f_g = \frac{0.184}{[\dot{m} \cdot D_h / \mu_g]^{0.2}}$ $C_{F1} = (1-x)^2 + x^2 \left(\frac{\rho_{f,bv}}{\rho_g} \right) \left(\frac{f_{go}}{f_{lo}} \right)$ $C_{F2} = x^{0.78} (1-x)^{24} \left(\frac{\rho_{f,bv}}{\rho_g} \right)^{0.91} \left(\frac{\mu_g}{\mu_{f,bv}} \right)^{0.19} \left(1 - \frac{\mu_g}{\mu_{f,bv}} \right)^{0.7}$ $Fr_{bv} = \dot{m}^2 / (\rho_{f,bv}^2 \cdot g \cdot D_h), We = \frac{\dot{m}^2 \cdot D_h}{\sigma} \left(\frac{x}{\rho_g} + \frac{1-x}{\rho_{f,bv}} \right)$	Horizontal and vertical [all fluids] {4 mm ≤ D _h , μ _f /μ _g < 1000}
Choi et al. (2001)	$(dP/dz)_{frict} + (dP/dz)_{mom}$ $= \frac{\dot{m}^2}{L_{\Delta P}} \left[\frac{f_{lo} \cdot L_{\Delta P}}{D_h} \cdot \left(\frac{1}{\rho_{ref,xout}} + \frac{1}{\rho_{ref,xin}} \right) + \left(\frac{1}{\rho_{ref,xout}} - \frac{1}{\rho_{ref,xin}} \right) \right]$ $f_{lo} = \frac{0.00506}{[\dot{m} \cdot D_h / \mu_{f,bv}]^{0.0951}} \left[\frac{(x_{out} - x_{in}) h_{fg,bv}}{g \cdot L_{\Delta P}} \right]^{0.1554}$ <p style="text-align: right;">was from NIST database</p>	Horizontal smooth and micro-fin tube [R410A, R134a, R32, R22, R125, R32, R407C, R32/R134a, R134a-SUS369 ester-m, R134a-SUS150 ester-b, R12-SUS150, R12-SUS300, R22-SUS150, R22-SUS300] {5.5 mm ≤ D _h ≤ 11.1 mm 0 wt.% ≤ OMF ≤ 5 wt.%}
Hu et al. (2009)	$(dP/dz)_{frict} = [2 \cdot f_g \cdot x^2 / (\rho_g \cdot D_h)] \phi_g^2$ $f_g = \frac{0.046}{[x \cdot \dot{m} \cdot D_h / \mu_g]^{0.2}}$ $\phi_g^2 = 1 + (0.095 + 1.38D_h - 0.132D_h^2) X_{tt}^{(0.795 - 0.05D_h)}$ $X_{tt} = \left(\frac{1-x}{x} \right)^{0.9} \left(\frac{\rho_g}{\rho_{f,bv}} \right)^{0.5} \left(\frac{\mu_{f,bv}}{\mu_g} \right)^{0.1}$	Horizontal [R410A-RB68EP oil] {2 mm ≤ D _h ≤ 6.34 mm 0.2 ≤ x _{in} ≤ 0.7, Δx=0.2 0 wt.% ≤ OMF ≤ 5 wt.% 200 kg/m ² -s ≤ ḡ ≤ 400 kg/m ² -s}
Zürcher et al. (1998)	$(dP/dz)_{frict} = [2 \cdot f_F \cdot \dot{m}^2 / (\rho_{f,bv} \cdot D_h)] \phi_l^2 (\mu_{oil} / \mu_{ref})^{n\omega}$ <p style="text-align: center;">ϕ_l² from Friedel (1979)</p> $n = \omega(3.583 \cdot 0.01 \cdot OMF + 0.0616)$ $\omega = 0.01 \cdot OMF / [1 - x / (1 - 0.01 \cdot OMF)]$	[R407C, R407C-ester type oil] {0 wt.% ≤ OMF ≤ 5 wt.% 100 kg/m ² -s ≤ ḡ ≤ 300 kg/m ² -s}

for R410-POE mixture were lower than -30%. Zürcher et al. (1998) correlation, equation (29), along with the modified exponent n , equation (32), well predicted all the experimental pressure drops data within $\pm 25\%$ (for tests with vapor quality $x < 0.66$), with the mean absolute deviation 7%, 24%, 10%, and 12% for R410A, R410A-POE, R410A-ZnO NL, and R410A-AL₂O₃ NL mixtures, respectively.

Table 12: Mean absolute deviation between correlations prediction and experimental $\Delta P/L$.

Fluids:	R410A	R410A-POE	R410A-ZnO NL	R410A-AL ₂ O ₃ NL
Data points:	91	31	25	32
Correlations	Mean Absolute Deviation [%]			
Friedel (1979)	7	45	27	27
Choi et al. (2001)	17	98	100	100
Hu et al. (2009)	63	77	70	70
Zürcher et al. (1998)	7	43	23	23
Zürcher et al. (1998) with modified exponent n	7	24	10	12

5.3. Application of existing two-phase flow boiling heat transfer correlations

A comparison of experimental HTC of R410A, R410A-POE, R410A-ZnO NL, and R410A-Al₂O₃ NL with the predicted results using literature correlations is shown in Figure 42. The y-axis of the figure, HTC_{corr_div} , is the percent deviation of predicted heat transfer coefficient, HTC_p , from experimental heat transfer coefficient, HTC_{exp} , and was calculated using equation (41). The literature correlations are summarized in Table 13. The mean absolute deviations, in percentage, were calculated using equation (42), and are summarized in Table 14.

$$HTC_{corr_div} = \frac{HTC_p - HTC_{exp}}{HTC_{exp}} \times 100 [\%] \quad (41)$$

$$\text{Mean Absolute Deviation} = \frac{1}{\text{Data points}} \sum \left(\frac{|HTC_p - HTC_{exp}|}{HTC_{exp}} \times 100 \right) [\%] \quad (42)$$

The correlation showing the best agreement for R410A data were from Wattelet et al. (1994), Kandlikar (1990), Zou et al. (2010), and Kattan et al. (1998), with mean absolute deviations of 19%, 17%, 6%, and 18% respectively. The correlations by Kandlikar (1990) and Zou et al. (2010) did not predict well for R410-POE mixture but were in good agreement with R410-nanolubricant mixtures. It should be highlighted in here that not all correlations were explicitly formulated to predict HTC for R410A or R410A-POE mixture in a smooth copper tube. Wattelet et al. (1994) and Kattan et al. (1998) correlations were suited for R410A and for thermal and flow boundary conditions closest to those of the present paper. Wattelet et al. (1994) correlation was for 60%/40% azeotrope mixture of R32/R125 which had close composition to R410A, and Hu et al. (2008) provided coefficients for R410A-RB68EP to be used along with Kattan et al. (1998) correlation. Kattan et al. (1998) correlation predicted local $HTCs$ in stratified flow, stratified-wavy flow, intermittent flow, annular flow, and annular flow with partial dryout occurring at high vapor qualities. The correlations in Figure 42 (c) and Figure 42 (d) used thermophysical properties of the

R410A-nanolubricant mixtures, and few were able to predict the HTC within mean absolute deviations 25% for nanolubricants, but the same correlation did not capture well the HTC of R410A-POE mixture. This suggested that the physics of the presence of oil and physics of nanoparticle interaction with the heater's wall and liquid refrigerant-oil mixture was not captured in these correlations.

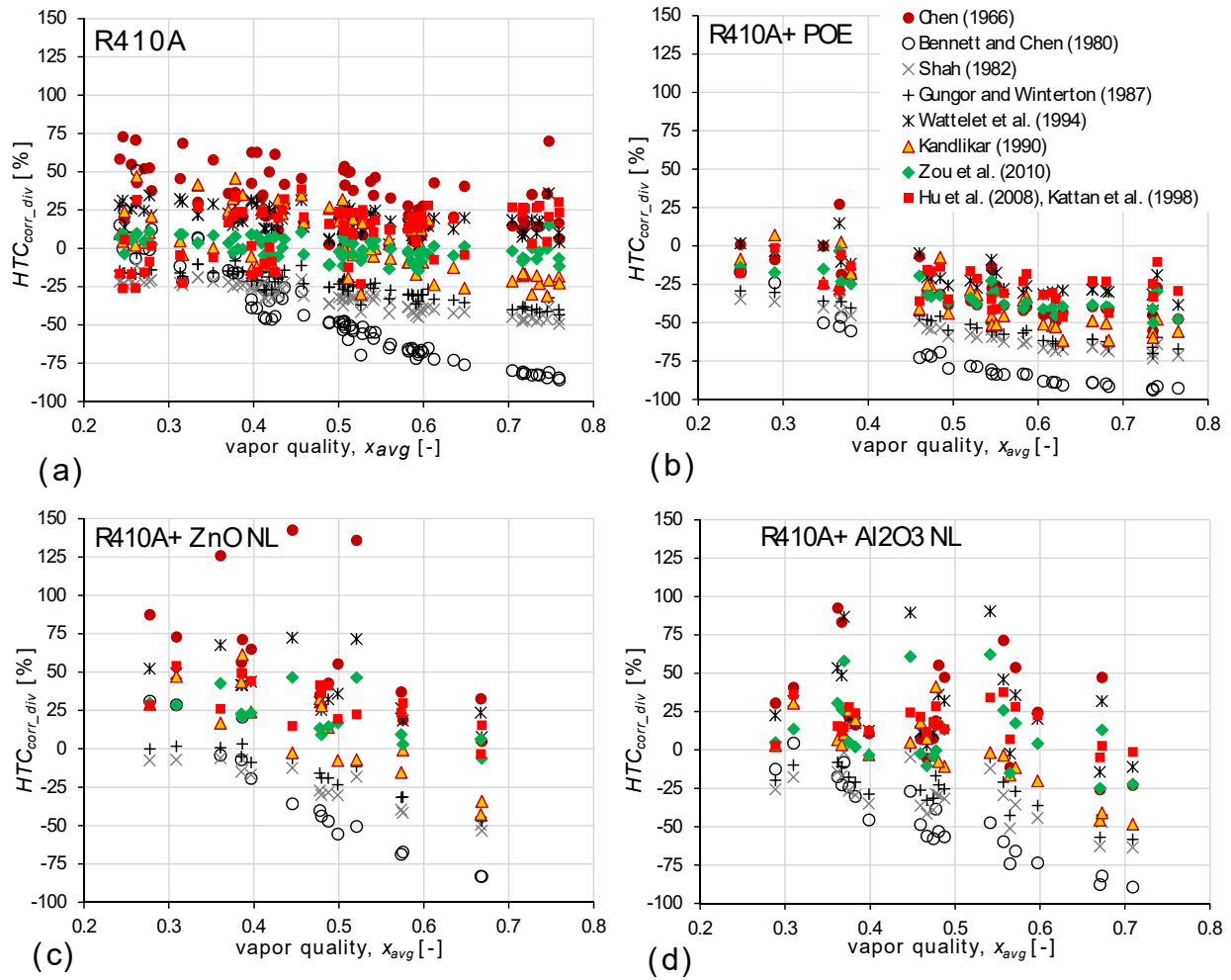


Figure 42: Prediction of smooth tube HTC using literature correlations for (a) R410A, (b) R410A-POE, (c) R410A-ZnO NL, and (d) R410A-Al₂O₃ NL mixtures.

Table 13: Literature two-phase flow boiling heat transfer correlations.

Reference	Correlation	Tube orientation [fluid]{range}
Chen (1966)	$HTC = F \cdot HTC_{Dittus-Boelter} + S \cdot HTC_{Forster-Zuber}$ $HTC_{Dittus-Boelt} = 0.023 Re_{fo,bv}^{0.8} Pr_{f,bv}^{0.4} k_{f,bv} / D_h$ $HTC_{Forster-Zube} = \frac{0.00122 k_{f,bv}^{0.79} c_{p,f,bv}^{0.45} \rho_{f,bv}^{0.75}}{\sigma^{0.5} \mu_{f,bv}^{0.29} h_{fg,bv}^{0.24} \rho_g^{0.24}} (T_{s,avg} - T_{bub})^{0.24} (P_{T_s,avg} - P_{T_{bub}})^{0.75}$ $F = 2.35 \left(0.213 + \frac{1}{X_{tt}} \right)^{0.736}$ $S = 1 / \left[1 + 2.53 \times 10^{-6} (Re_{fo} F^{1.25})^{1.17} \right]$ $X_{tt} = \left(\frac{1-x}{x} \right)^{0.9} \left(\frac{\rho_g}{\rho_{f,bv}} \right)^{0.5} \left(\frac{\mu_{f,bv}}{\mu_g} \right)^{0.1}, Re_{fo} = (1-x) \dot{m} D_h / \mu_{f,bv}$	Vertical [water and hydrocarbons] $\{1770 \leq Re_{fo} \leq 1.3E5 \text{ for } D_h=9.5 \text{ mm}\}$ $0.01 \leq x \leq 0.71$ $0.63 \text{ W/m}^2 \leq \dot{q} \leq 63 \text{ W/m}^2$
Bennett and Chen (1980)	$HTC = F \cdot HTC_{Dittus-Boelter} + S \cdot HTC_{Forster-Zube}$ $F = (0.213 + X_{tt}^{0.5})^{1.78} [(Pr_{f,bv} + 1)/2]^{0.444}$ $S = 0.9622 \tan^{-1} \left[\frac{Re_{fo,bv} F^{1.25}}{61800} \right]$	Vertical [ethylene glycol, water and hydrocarbons] $\{9.5 \leq Re_f \leq 60E5 \text{ for } D_h=9.5 \text{ mm}\}$ $0.001 \leq x \leq 0.3$ $7 \text{ W/m}^2 \leq \dot{q} \leq 30 \text{ W/m}^2$ $0.16 \text{ kg/m}^2\text{-s} \leq \dot{m} \leq 1600 \text{ kg/m}^2\text{-s}$ $0.16 \leq X_{tt} \leq 300$
Shah (1982)	$HTC = \max(z1, z2, z3, z4) \cdot HTC_{Dittus-Boelter}$ $z1 = 230 Bo^{0.5}$ $z2 = 1.8 [Co(0.38 Fr_{bv}^{-0.3})^n]^{-0.8}$ $z2 = 1.8 [Co(0.38 Fr_{bv}^{-0.3})^n]^{-0.8}$ $z3 = Fs \cdot Bo^{0.5} \exp \left\{ 2.47 [Co(0.38 Fr_{bv}^{-0.3})^n]^{-0.15} \right\}$ $z4 = Fs \cdot Bo^{0.5} \exp \left\{ 2.47 [Co(0.38 Fr_{bv}^{-0.3})^n]^{-0.1} \right\}$ $Fs = 14.7 \text{ if } Bo > 0.0011, Fs = 15.43 \text{ if } Bo < 0.0011$ $n = 0 \text{ if } Fr_{bv} > 0.04 \text{ or vertical tube, } n = 1 \text{ if } Fr_{bv} \leq 0.04$ $Fr_{bv} = \dot{m}^2 / (\rho_{f,bv}^2 \cdot g \cdot D_h), Co = \left(\frac{1-x}{x} \right)^{0.8} \left(\frac{\rho_g}{\rho_{f,bv}} \right)^{0.5}, Bo = \dot{q} / (\dot{m} \cdot h_{fg,bv})$	Horizontal and vertical [all fluids] $\{0.008 \leq Co \leq 4\}$ $0.00001 \leq Bo \leq 0.005$ $0.0003 \leq Fr_{bv} \leq 0.04$

Gungor and Winterton (1987)	$HTC = (E1 \cdot E2 + S1 \cdot S2)HTC_{Dittus-Boelter}$ $E1=1 + 3000Bo^{0.86}, S1 = 1.12 \left(\frac{1-x}{x}\right)^{-0.75} \left(\frac{\rho_g}{\rho_{f,bv}}\right)^{-0.41}$ <p>If tube is horizontal and $Fr_{bv} < 0.05$ then $E2 = Fr_{bv}^{(0.1-2Fr_{bv})}$ and $S2 = Fr_{bv}^{0.5}$, else $E2 = S2 = 1$.</p>	<p>Horizontal and vertical [R11, R12, R22, R113, R114, ethylene glycol and water] {$2.95 \text{ mm} \leq D_h \leq 32 \text{ mm}$ $0 \leq x \leq 0.99$ $0.35 \text{ kW/m}^2 \leq \dot{q} \leq 91534 \text{ kW/m}^2$ $12.4 \text{ kg/m}^2\text{-s} \leq \dot{m} \leq 61518 \text{ kg/m}^2\text{-s}$}</p>
Wattelet et al. (1994)	$HTC = (HTC_{cb}^{2.5} + HTC_{nb}^{2.5})^{1/2.5}$ <p>For $Fr_{bv} < 0.25$ $HTC_{cb} = 1.32Fr_{bv}^{0.2}(1 + 1.925X_{tt}^{-0.83})HTC_{Dittus-Boelter}$, else $HTC_{cb} = (1 + 1.925X_{tt}^{-0.83})HTC_{Dittus-Boelter}$ $HTC_{nb} = HTC_{Cooper}$ $HTC_{Cooper} = 55 \left(\frac{P_{sat}}{P_{crit}}\right)^{0.12} \left[-\log_{10} \left(\frac{P_{sat}}{P_{crit}}\right)\right]^{0.12} M^{-0.5} \dot{q}^{0.67}$</p>	<p>Horizontal [R12, R22, R134a, and a 60%/40% azeotropic mixture of R32/R125] {$7 \text{ mm} \leq D_h \leq 10.9 \text{ mm}$ $1.2 \text{ m} \leq L_{HT} \leq 2.4 \text{ m}$ $4^\circ\text{C} \leq T_{sat} \leq 15^\circ\text{C}$ for R32/R125 $0.01 \leq x \leq 0.91$ $1.8 \text{ kW/m}^2 \leq \dot{q} \times 10^3 \leq 40 \text{ kW/m}^2$ $175 \text{ kg/m}^2\text{-s} \leq \dot{m} \leq 6706 \text{ kg/m}^2\text{-s}$}</p>
Kandlikar (1990)	$HTC = \max(HTC_{NBD}, HTC_{CBD})$ $\frac{HTC_{NBD}}{HTC_{cht,Gnielinski}} = \left[0.6683 \left(\frac{\rho_{f,bv}}{\rho_g}\right)^{0.1} x^{0.16} (1-x)^{0.64} f_2(Fr_{bv}) \right. \\ \left. + 1058Bo^{0.7} F_K (1-x)^{0.8} \right]$ $\frac{HTC_{CBD}}{HTC_{cht,Gnielinski}} = \left[1.1360 \left(\frac{\rho_{f,bv}}{\rho_g}\right)^{0.45} x^{0.72} (1-x)^{0.08} f_2(Fr_{bv}) \right. \\ \left. + 667.2Bo^{0.7} F_K (1-x)^{0.8} \right]$ <p>$F_K=1.63$ for R134a used in current work, as F_K for R410A was not known. $f_2(Fr_{bv}) = (25Fr_{bv})^{0.3}$ for $Fr_{bv} < 0.04$ in horizontal tubes, else $f_2(Fr_{bv})=1$. $HTC_{cht,Gnielinski}$ = equation (69)</p>	<p>Horizontal and vertical [Refrigerants, nitrogen, neon, and water] {$0.5 \leq Pr_{bv} \leq 2000$ $2300 \leq Re_{fo,bv} \leq 1E4$ $5 \text{ mm} \leq D_h \leq 25 \text{ mm}$ $0.001 \leq x \leq 0.98$ $0.3 \text{ kW/m}^2 \leq \dot{q} \leq 2280 \text{ kW/m}^2$ $13 \text{ kg/m}^2\text{-s} \leq \dot{m} \leq 8179 \text{ kg/m}^2\text{-s}$}</p>
Zou et al. (2010)	$HTC = \left[(F \cdot HTC_{Dittus-Boelter})^2 + (S \cdot HTC_{Cooper})^2 \right]^{0.5}$ $F = \left[1 + xPr_{f,bv} \left(\frac{\rho_{f,bv}}{\rho_g} - 1\right) \right]^{0.35}$ $S = 1 / \left[1 + 0.055F^{0.1} Re_{fo}^{0.16} \right]$	<p>Horizontal [R170/R290] {$D_h = 8 \text{ mm}$ $0.35 \text{ MPa} \leq P_{sat} \leq 0.57 \text{ MPa}$ $0.1 \leq x \leq 0.75$ $13.1 \text{ kW/m}^2 \leq \dot{q} \leq 65.5 \text{ kW/m}^2$ $63.6 \text{ kg/m}^2\text{-s} \leq \dot{m} \leq 102.5 \text{ kg/m}^2\text{-s}$}</p>

<p>Hu et al. (2008), Kattan et al. (1998)</p>	$HTC = [\theta_{dry} HTC_{Dittus-Boelter} + (2\pi - \theta_{dry}) HTC_{wet}] / 2\pi$ $HTC_{wet} = (HTC_{cb}^3 + HTC_{nb}^3)^{1/3}$ $HTC_{nb} = HTC_{Cooper}$ $HTC_{cb} = C Re_f^{m_1} Pr_{f,bv}^{0.4} k_{f,bv} / D_h$ <p>As per Hu et al. (2008), for R410A-RB68EP mixture; $C=0.027$, $m_1=0.635$</p> $Re_f = \frac{4(1-x)\dot{m} \left[\frac{\pi D_h (1-\alpha)}{2(2\pi - \theta_{dry})} \right]}{(1-\alpha)\mu_{f,bv}}$ <p>θ_{dry} equations provided by Kattan et al. (1998) α=Rouhani and Axelsson (1970) void fraction</p>	<p>Horizontal [R407, R407-oil, R410A-RB68EP oil] {$D_h=6.34$ mm $T_{sat}=5^\circ\text{C}$ $0.2 \leq x_{in} \leq 0.7$, $\Delta x=0.2$ $0 \text{ wt.\%} \leq OMF \leq 5 \text{ wt.\%}$ $7.56 \text{ kW/m}^2 \leq \dot{q} \leq 15.12 \text{ kW/m}^2$ $200 \text{ kg/m}^2\text{-s} \leq \dot{m} \leq 400 \text{ kg/m}^2\text{-s}$}</p>
---	---	---

Table 14: Mean absolute deviation between correlations prediction and experimental HTC .

Correlations	Fluids:			
	R410A	R410A-POE	R410A-ZnO NL	R410A-Al2O3 NL
Data points:	79	31	16	23
	Mean Absolute Deviation [%]			
Chen (1966)	31	32	63	54
Bennett and Chen (1980)	47	76	43	47
Shah (1982)	32	58	24	32
Gungor and Winterton (1987)	25	53	17	25
Wattelet et al. (1994)	19	22	40	32
Kandlikar (1990)	17	39	25	17
Zou et al. (2010)	6	33	21	19
Hu et al. (2008), Kattan et al. (1998)	18	25	31	18

5.4. Heat transfer modeling for nanolubricants

5.4.1 Forced flow convection of nanofluids

Buongiorno (2006) described the presence of seven relative (slip) velocities between the nanoparticle and base fluid while considering the convective flow heat transfer of nanofluids, the mechanisms were: Brownian diffusion, thermophoresis, inertia, Magnus effect, diffusiophoresis, fluid drainage, and gravity. Due to a higher order of magnitude, the Brownian diffusion and thermophoresis were the only important slip mechanisms considered while developing a two-component nonhomogeneous equilibrium model for the convective heat transfer that accounted for mass, momentum, and energy transfer. Buongiorno used his model to build a new Nusselt number correlation for turbulent flow, as shown in equation (43). Bigi and Cremaschi (2019) studied the slip of spherical Al₂O₃ nanoparticles in R410A-POE liquid mixture and also found that Brownian diffusion and thermophoresis were dominant than the other mechanisms. Bigi and Cremaschi (2019) also showed that beyond the laminar sublayer, that is in the turbulent sublayer and the turbulent core of the flow, the nanoparticles were entrained in the fluid turbulent eddies and moved homogeneously with the liquid; thus the concentration of nanoparticles stayed uniform in the turbulent layer.

Buongiorno (2006) model predicted enhancement in the convective heat transfer with an increase in the nanoparticle volumetric concentrations. The enhancement in the heat transfer was due to thinning of laminar (or viscous) sublayer near the wall due to the reduction in the viscosity of the fluid inside the laminar sublayer, due to the diffusion of nanoparticles from laminar sublayer towards turbulent layer under the influence of thermophoresis. Buongiorno defined a parameter $N_{BT} = D_B/D_T$, which was a ratio between Brownian and thermophoretic diffusivities

that helped in determining the concentration and distribution of nanoparticles in the laminar sublayer and bulk or turbulent layer (turbulent sublayer and turbulent core), and thus helped to evaluate the thermophysical properties of the nanofluid mixture in the respective layers. The convective heat transfer coefficient, HTC_{cht} , was evaluated as shown in equation (44). The friction factor, f , was obtained using the Colebrook equation, shown in equation (38), and the tube roughness for the smooth tube was chosen as $1.5 \mu\text{m}$ as per manufacturers data. The bulk Reynolds number was evaluated as $Re_b = \dot{m}D_h/\mu_{f,b}$, while the Prandtl number in the turbulent layer and laminar sublayer were evaluated as $Pr_b = \mu_{f,b} \cdot c_{p f,b}/k_{f,b}$ and $Pr_v = \mu_{f,v} \cdot c_{p f,v}/k_{f,v}$, respectively.

$$Nu_b = \frac{\frac{f}{8}(Re_b - 1000)Pr_b}{1 + \delta_v^+ \sqrt{\frac{f}{8}(Pr_v^{2/3} - 1)}} \quad (43)$$

$$HTC_{cht} = Nu_b k_{f,b}/D_h \quad (44)$$

5.4.2 Diffusion of non-spherical nanoparticles

This work highlights the influence of slip of non-spherical ZnO nanoparticles in R410A-POE liquid mixture due to Brownian diffusion and thermophoresis in contrast to spherical Al₂O₃ nanoparticles. This work contributes by analyzing ZnO nanoparticles' slip mechanism in R410A-POE liquid mixture, which was never done before. ZnO nanoparticles in R410A-POE liquid mixture because of non-spherical shape would tend to collide more than spherical Al₂O₃ nanoparticles; therefore the ZnO and Al₂O₃ nanoparticle motion under the influence of shear was studied. R410A-ZnO NL liquid mixture had higher dynamic viscosity than R410A-Al₂O₃ NL liquid mixture; therefore the ZnO and Al₂O₃ nanoparticle motion under the influence of spatial variation in viscosity was also studied.

The diffusivity of spherical Al₂O₃ nanoparticles and non-spherical ZnO nanoparticles in laminar sublayer due to Brownian motion, D_B , was calculated using equation (45) (Bigi and Cremaschi 2019) and equation (46) (Savithiri et al. 2011), respectively.

$$D_B = k_B T / (3\pi\mu_v d_p) \quad (45)$$

$$D_B = [k_B T / (3\pi\mu_v d_{np} a)] \cdot [\ln(a) - 0.662 + 0.917a - 0.05a^2] \quad (46)$$

where, k_B is the Boltzmann's constant, T is the fluid temperature, μ_v is the viscosity in laminar sublayer, a is the aspect ratio, and d_{np} with a unit of meter is the spherical nanoparticle diameter, or its dimension measured perpendicular to along its major axis for non-spherical nanoparticles. For ZnO nanoparticles, the aspect ratio, a , was 3.

The diffusivity of Al₂O₃ nanoparticles and ZnO nanoparticles in laminar sublayer due to thermophoresis, D_T , was calculated with equation (47) (Buongiorno 2006).

$$D_T = \beta \frac{\mu_v}{\rho_v} \left(\frac{\ddot{q} \delta_v}{k_v} \right) \frac{1}{T} \quad (47)$$

where, β is the proportionality factor, \ddot{q} is the heat flux at the wall, δ_v is the thickness of the laminar sublayer, ρ_v is the mixture density in laminar sublayer, k_v is the effective thermal conductivity of the mixture in laminar sublayer. The proportionality factor, β , for spherical Al₂O₃ nanoparticles in R410A-POE mixture was estimated by (Bigi and Cremaschi 2019), as shown in equation (48), and was used for non-spherical ZnO nanoparticles as well in this work.

$$\beta = \omega \cdot 7.1026 \left(\frac{d_{np} \times 10^{-9}}{2} \right)^{-1.579} + (1 - \omega) 6270 \left(\frac{d_{np} \times 10^{-9}}{2} \right)^{-1.819} \quad (48)$$

where, ω is the local oil mass fraction. For single-phase flow $\omega = \frac{OMF}{100}$, and for two-phase flow

$$\omega = \frac{OMF}{100} / \left[1 - x / \left(1 - \frac{OMF}{100} \right) \right].$$

The non-spherical ZnO nanoparticles diffused slowly under Brownian motion than spherical Al₂O₃ nanoparticles because of their large aspect ratio. Hence, under same flow boundary conditions of single-phase flow, the concentration of ZnO nanoparticles would be lower in the laminar sublayer of R410A-ZnO NL mixture than the Al₂O₃ nanoparticles in the laminar sublayer of R410A-Al₂O₃ NL mixture. Numerical simulations by Yuan et al. (2018) have shown elongated ZnO nanoparticles have random motion in the turbulent bulk flow and orient their long axis along the flow direction near the wall and have increased friction factor. This aligning effect of elongated nanoparticles was not captured in the model described in this work.

Phillips et al. (1992) provided equation (49) for nanoparticle flux due to the collision of particles moving at different velocities in adjoin shear layers. The nanoparticle flux, J_c , occurred normal to the shear induced flow and in the direction of lower collision frequencies, that is towards the wall of the tube.

$$J_c = -K_c d_p^2 \left(\phi^2 \frac{d\dot{\gamma}}{dy} + \phi \dot{\gamma} \frac{d\phi}{dy} \right) \quad (49)$$

where, K_c is the proportionality constant, d_p is the nanoparticle diameter, ϕ is the nanoparticle volume fraction, $\dot{\gamma}$ is the local shear rate, and y is the distance measured from the wall towards the center of the tube. For laminar sublayer $\dot{\gamma}$ is constant and can be approximated as $\dot{\gamma} = G/(\rho_b \delta_v)$, where G is the mass flux of the fluid in the tube, and ρ_b is the density of the bulk liquid refrigerant-nanolubricant mixture. Thus, the nanoparticle flux due to shear influence, J_c , in laminar sublayer reduces to equation (50).

$$J_c = -K_c d_p^2 \phi \frac{G}{\rho_b \delta_v} \frac{d\phi}{dy} \quad (50)$$

The simplified equation (51) of diffusivity due to shear motion, D_C , for laminar sublayer was obtained from equation (50), where ϕ_v is the average nanoparticle volume fraction in the laminar sublayer.

$$D_C = K_c d_p^2 \phi_v \frac{G}{\rho_b \delta_v} \quad (51)$$

Nanoparticle concentration gradient, ϕ , give rise to viscosity gradient that resist motion of the particles transverse to the direction of the flow. Phillips et al. (1992) provided equation (52) to calculate nanoparticle flux due to viscosity gradient.

$$J_\mu = -K_\mu d_p^2 \dot{\gamma} \phi^2 \frac{1}{\mu} \left(\frac{d\mu}{d\phi} \frac{d\phi}{dy} \right) \quad (52)$$

where, K_μ is the proportionality constant, μ is the fluid dynamic viscosity. The simplified equation (53) of diffusivity due to viscosity gradient, D_μ , for laminar sublayer was obtained from equation (52), where μ_v is the average dynamic viscosity in the laminar sublayer.

$$D_\mu = K_\mu d_p^2 \frac{G}{\rho_{Lb} \delta_v} \frac{\phi_v^2 (\mu_b - \mu_v)}{\mu_v (\phi_b - \phi_v)} \quad (53)$$

where, μ_v is the viscosity in laminar sublayer, μ_b and ϕ_b are the viscosity and nanoparticle concentration of the bulk liquid refrigerant-nanolubricant mixture in the turbulent layer.

Phillips et al. (1992) predicted the proportionality constant K_c as 0.41 for spherical nanoparticles, and the same was used for Al₂O₃ nanoparticles. The proportionality constant K_c was assumed to be doubled for non-spherical ZnO nanoparticles because they would tend to collide more than spherical Al₂O₃ nanoparticles. Phillips et al. (1992) predicted the proportionality K_μ as 0.62, and the same was used for ZnO and Al₂O₃ nanoparticles.

To study the relevance of slip mechanisms, the diffusion time, $t_D = d_p^2 / \text{Diffusivity}$, was calculated. t_D was the time taken by the nanoparticle to diffuse a length equivalent to its diameter,

d_p . Table shows the diffusion time for ZnO and Al₂O₃ nanoparticles in R410A-nanolubricant mixtures under the influence of different slip mechanisms. Studies by Bigi and Cremaschi 2019 showed Brownian diffusion and thermophoresis were dominant mechanisms for Al₂O₃ nanoparticles in R410A-Al₂O₃ NL.

Table 15. Diffusion time of nanoparticles under the influence of different slip mechanisms.

Nanoparticles in R410A-NL mixture	Brownian diffusion $t_D = d_p^2/D_B$ [s]	Thermophoretic diffusion $t_D = d_p^2/D_T$ [s]	Shear induced diffusion $t_D = d_p^2/D_C$ [s]	Viscosity gradient induced diffusion $t_D = d_p^2/D_\mu$ [s]	Test Type
ZnO	6E-05	7E-09	1E+04	1E+09	single-phase flow
ZnO	8E-05	3E-09	8E+04	1E+10	two-phase flow
Al ₂ O ₃	2E-05	8E-09	5E+03	7E+07	single-phase flow
Al ₂ O ₃	3E-05	3E-09	3E+04	6E+08	two-phase flow

The calculations in column 2 and 3 in Table 15 show the diffusion times, t_D , for ZnO nanoparticles were similar to Al₂O₃ nanoparticles, hence the Brownian diffusion and thermophoresis were also dominant mechanisms for ZnO nanoparticles in R410A-ZnO NL mixture. The calculations in column 4 and 5 in Table 15 show the order of magnitude of shear induced and viscosity gradient induced diffusions were very high for non-spherical ZnO nanoparticles than the Brownian and Thermophoretic diffusion. Hence, the ZnO nanoparticle slip under the influence of shear induced and viscosity gradient induced diffusions were neglected in the analysis. Thus, in this work, the non-sphericity of ZnO nanoparticles were only captured through the Brownian diffusivity, D_B in equation (46), and through thermophysical property models provided by Bigi et al., (2015), Cremaschi et al., (2015) and Kedzierski et al., (2017). The ZnO nanoparticles diffused slowly under Brownian motion than Al₂O₃ nanoparticles because of their large aspect ratio for same nanoparticle mass concentration, $NP_{conc}=20$ wt.%, and flow boundary conditions of single phase flow, hence the concentration of ZnO nanoparticles were 70%

lower in the laminar sublayer of R410A-ZnO NL mixture than the Al₂O₃ nanoparticles in the laminar sublayer of R410A-Al₂O₃ NL mixture.

Nanoparticles tend to migrate from region of higher shear rate to region of lower shear rate, but the migration under non-uniform shear rate was negligible in the turbulent region, that is beyond laminar sublayer, as the nanoparticles were entrained in the fluid turbulent eddies and moved homogeneously with the liquid (Bigi and Cremaschi 2019). Homogeneous nanoparticles distribution resulted in no viscosity gradient in the turbulent flow, thus the nanoparticle motion was not influenced by the absence viscosity gradient in the turbulent region.

5.4.3 Definition for the dimensionless laminar sublayer thickness

Buongiorno (2006) suggested a constant value for the dimensionless laminar sublayer thickness, δ_v^+ , that had to be determined empirically. Instead, the definition for the dimensionless laminar sublayer thickness was introduced in the present work, $\delta_v^+ = V_i/V_*$, where $V_* = \sqrt{\tau_w/\rho_{f,v}}$ was the friction velocity, and V_i was the laminar sublayer and turbulent layer interface velocity. V_i was approximated to the average velocity of the fluid $u_{avg} = \dot{m}/\rho_{f,b}$, where \dot{m} was the mass flux and $\rho_{f,b}$ was the liquid density of the turbulent layer. Using the dimensionless laminar sublayer thickness definition helped introduced δ_v^+ dependence on the wall shear stress, $\tau_w = (f/8)\rho_{f,v}u_{avg}^2$.

5.4.4 Mass balance of nanoparticles in laminar sublayer and turbulent core

Buongiorno (2006) model considered a constant nanoparticle mass concentration at the turbulent layer (turbulent sublayer and turbulent core), and it was NP_{conc} as inputted by the user during computation. However, in reality, the nanoparticles diffused from laminar sublayer towards turbulent layer under the influence of thermophoresis, because the thermophoresis was more

dominant than Brownian diffusion. This diffusion increased the concentration of the nanoparticles in the turbulent layer above NP_{conc} , which was not accounted for in Buongiorno (2006) model. The total mass of nanoparticle, m_{np} , in the flow was calculated from the known concentration of nanoparticles in oil, NP_{conc} , oil mass fraction of oil, OMF , and mass flux, \dot{m} , of the refrigerant-lubricant mixture flowing through the test section. The mass of nanoparticles in the turbulent sublayer and turbulent core, $m_{np,b}$, was calculated with equation (54). While the mass of nanoparticles in the laminar sublayer was calculated with equation (55). Newton-Raphson method was further used to solve for nanoparticle volume concentration in the turbulent layer, ϕ_b , from the total mass of nanoparticle, $m_{np} = f(\phi_b)$, in equation (56).

$$m_{np,b} = \pi(D_h - \delta_f)\rho_{np}(\delta_f - \delta_v)[\phi_b/(1 - \phi_b)] \quad (54)$$

$$m_{np,v} = -\pi(D_h - \delta_f)\rho_{np}\frac{D_B}{D_T}\delta_v \cdot \ln\left[\frac{1 - \phi_b}{1 - \phi_b e^{(-D_T/D_B)}}\right] \quad (55)$$

$$m_{np} = f(\phi_b) = m_{np,b} + m_{np,v} \quad (56)$$

Buongiorno defined a parameter $N_{BT} = D_B/D_T$, which was a ratio between Brownian and thermophoretic diffusivities that helped in determining the concentration and distribution of nanoparticles in the laminar sublayer. The nanoparticle concentration distribution in the laminar sublayer was provided by Buongiorno (2006), as shown in equation (57), where $y = [(D_h/2) - r]$ was the radial distance away from the wall and towards the center of the tube. The average nanoparticle volume concentration in the laminar sublayer, ϕ_v , was estimated by Buongiorno (2006) as in equation (58).

$$\phi = \phi_b e^{-\left(\frac{1}{N_{BT}}\right)\left(1 - \frac{y}{\delta_v}\right)} \quad (57)$$

where, $N_{BT} = D_B/D_T$

$$\phi_v = \phi_b (D_B/D_T) [1 - e^{(-D_T/D_B)}] \quad (58)$$

$$\phi_b = \frac{NP_{conc,b}}{NP_{conc,b} + (1 - NP_{conc,b}) \rho_{np} / \rho_{ref+L,b}} \quad (59)$$

$$\phi_v = \frac{NP_{conc,v}}{NP_{conc,v} + (1 - NP_{conc,v}) \rho_{np} / \rho_{ref+L,v}} \quad (60)$$

The nanoparticle volume concentration in the turbulent layer, ϕ_b , and laminar sublayer, ϕ_v , were then used to evaluate liquid properties in those respective layers using thermophysical property models provided by Bigi et al., (2015), Cremaschi et al., (2015) and Kedzierski et al., (2017). The nanoparticle mass concentration in the turbulent layer, $NP_{conc,b}$, and laminar sublayer, $NP_{conc,v}$, were calculated using equation (59) and equation (60), respectively.

The refrigerant saturated temperature, T_{bub} , was used to evaluate thermophysical properties in the turbulent layer. The laminar sublayer fluid temperature, T_v , was used to evaluate liquid properties in the sublayer, and it was the average of the wall temperature and refrigerant saturated temperature, $T_v = (T_w + T_{sat})/2$. In the current work, for case of constant/average wall heat flux, \dot{q}_{avg} , the experimentally measured wall temperature of the tube was not used as an input to the modified Buongiorno model. The wall temperature was estimated from Newton's law of cooling, equation (61), as per Buongiorno (2006) method for solving this model. It is important to note that the estimated wall temperature, T_w , was high than the experimentally measured wall temperature, $T_{s,avg}$ (shown in Figure 47). Buongiorno (2006) and Bigi (2018) had verified the single-phase heat transfer model for nanofluids. To be consistent with work of Buongiorno (2006)

and Bigi (2018), the present model in this work estimates the wall temperature, T_w , using equation (61) used it to calculate laminar sublayer temperature, T_v .

$$\begin{aligned} T_w &= T_{bub} + \dot{q}_{avg}/HTC_{cht}, \text{ for two-phase flow tests} \\ T_w &= T_{ref,1-phase} + \dot{q}_{avg}/HTC_{cht}, \text{ for single-phase flow tests} \end{aligned} \quad (61)$$

The above mass balance modification to the Buongiorno model showed that for R410A-Al2O3 NL single-phase flow heat transfer test ($T_{ref-oil}=9.6^\circ\text{C}$, $\dot{q}=8.7 \text{ kW/m}^2$, $\dot{m}=207 \text{ kg/m}^2\text{-s}$, $OMF=3 \text{ wt.}\%$, and $NP_{conc}=20 \text{ wt.}\%$), the nanoparticle mass concentration in the turbulent layer, $NP_{conc,b}$, was about 36% higher than the nanoparticle mass concentration originally estimated by the Buongiorno (2006) model. The higher nanoparticle mass concentration in the turbulent layer reduced the bulk Reynolds number Re_b by -0.6% and increased the bulk Prandtl number by Pr_b by 0.3%. This modification caused the modified Buongiorno model to predict the single-phase HTC_{cht} lower by about 18% compared to the original Buongiorno model.

Figure 43 shows the nanoparticle concentration gradient in the laminar sublayer for different values of $N_{BT} = D_B/D_T$, evaluated using equation (57). Curve (c) and (d) in Figure 43 shows that larger N_{BT} values will cause the nanoparticles to distribute more uniformly in the laminar sublayer because of the stronger effect of Brownian motion, and the average nanoparticle concentration in laminar sublayer, ϕ_v , would be closer to the turbulent layer bulk concentration, ϕ_b . Curve (a) and (b) in Figure 43 shows that for smaller N_{BT} values more nanoparticles will move away from the heated wall because of the stronger effect of thermophoresis, and thus the concentration of nanoparticles in laminar sublayer would decrease.

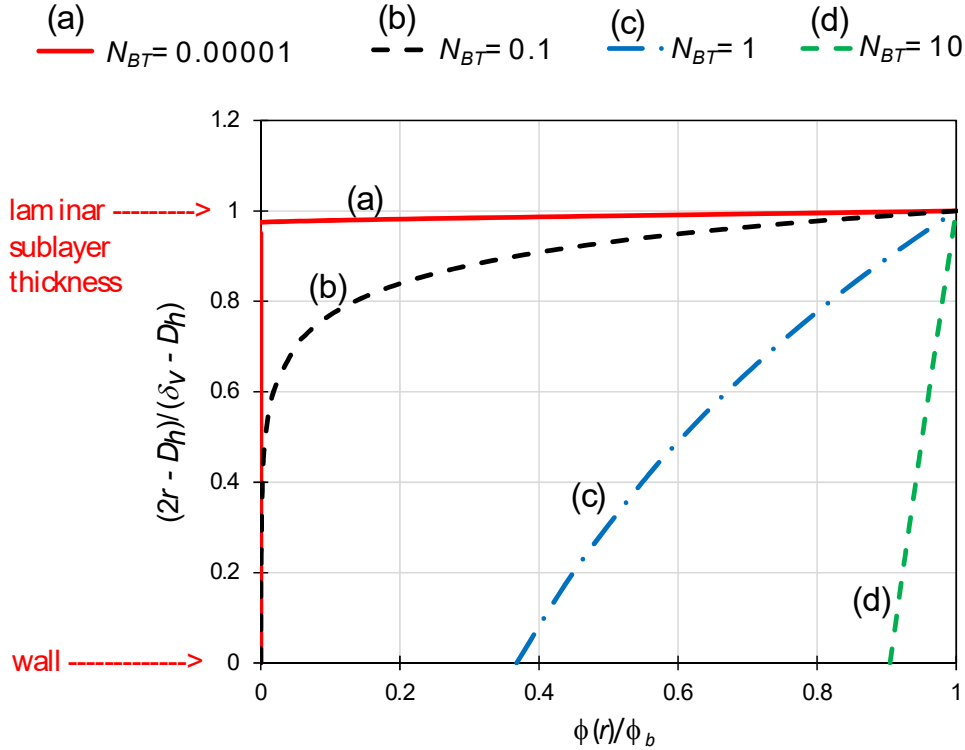


Figure 43: Influence of N_{BT} on nanoparticle distribution in the laminar sublayer.

The N_{BT} was in the order of 0.00001 for R410A-ZnO NL and R410A-AL2O3 NL tests in this work, as the effect of thermophoresis on ZnO and Al2O3 nanoparticles was stronger to move them away from the heated wall. Table 16 shows a sample calculations of N_{BT} with D_B and D_T for R410A-ZnO NL and R410A-Al2O3 NL mixtures. Curve (a) in Figure 43 was the nanoparticle concentration gradient for R410A-ZnO NL and R410A-Al2O3 NL mixtures in the laminar sublayer. The red solid line in Figure 44 shows the nanoparticle distribution in the laminar sublayer and turbulent layer for R410A-ZnO NL and R410A-Al2O3 NL mixtures. This ‘not to the scale’ red solid line curve in Figure 44 represents the curve (a) in Figure 43 at N_{BT} of 0.00001. For smaller N_{BT} values, more nanoparticles moved away from the heated wall because of the stronger effect of thermophoresis, and thus the average volume concentration value of nanoparticles in laminar sublayer decreased to about $\phi_v \approx 1E-07 \text{ m}^3/\text{m}^3$ ($NP_{conc,v} \approx 0.0005 \text{ wt.}\%$).

In the turbulent layer, the nanoparticles were entrained in the fluid turbulent eddies and moved homogeneously with the liquid (Bigi and Cremaschi 2019), therefore the nanoparticle volume concentration in the turbulent layer, ϕ_b , was uniform, with an average value of about $\phi_b \approx 0.005 \text{ m}^3/\text{m}^3$ ($NP_{conc,v} \approx 15 \text{ wt.}\%$).

In the turbulent layer, the nanoparticles were entrained in the fluid turbulent eddies and moved homogeneously with the liquid (Bigi and Cremaschi 2019), therefore the nanoparticle volume concentration in the turbulent layer, ϕ_b , was uniform. The buffer layer, or turbulent sublayer, was a region in between the laminar sublayer and turbulent layer, as shown in Figure 44. The buffer layer was extremely thin compared to the thickness of the laminar sublayer and the effect of turbulent eddies on nanoparticles were high in this layer as per the analysis by Buongiorno (2006) for water based nanofluids and Bigi (2018) for R410A-Al₂O₃ NL. Thus, the buffer layer, or turbulent sublayer, was considered integral part of the turbulent layer in the model developed by Buongiorno (2006).

Buongiorno (2006) provided equation (57) for an approximated profile of the nanoparticle distribution curve, and considered the uniform nanoparticle concentration, ϕ_b , in the entire turbulent layer. The approximated curve is shown by red solid curve in Figure 44. The buffer layer, or turbulent sublayer, was thin and was considered integral part of the turbulent layer. Therefore, Buongiorno model neglected the continuity of the nanoparticle distribution curve at the intersection of the turbulent layer and laminar sublayer. A reasonable nanoparticle distribution profile with physical base would be the dashed red curve in Figure 44, joining the low nanoparticle concentrations in laminar sublayer and high concentration in turbulent layer with a smooth transition through the buffer layer. Buongiorno model calculated the average nanoparticle volume concentration in the turbulent layer, ϕ_b , and average nanoparticle volume concentration in laminar

sublayer, ϕ_v in equation (58). These average nanoparticle concentration values were then used to evaluate liquid properties in those respective layers using thermophysical property models. Same approach was used in the present model of this work, where the buffer layer was considered integral part of the turbulent layer, and nanoparticle concentrations were averaged for laminar sublayer and turbulent layer.

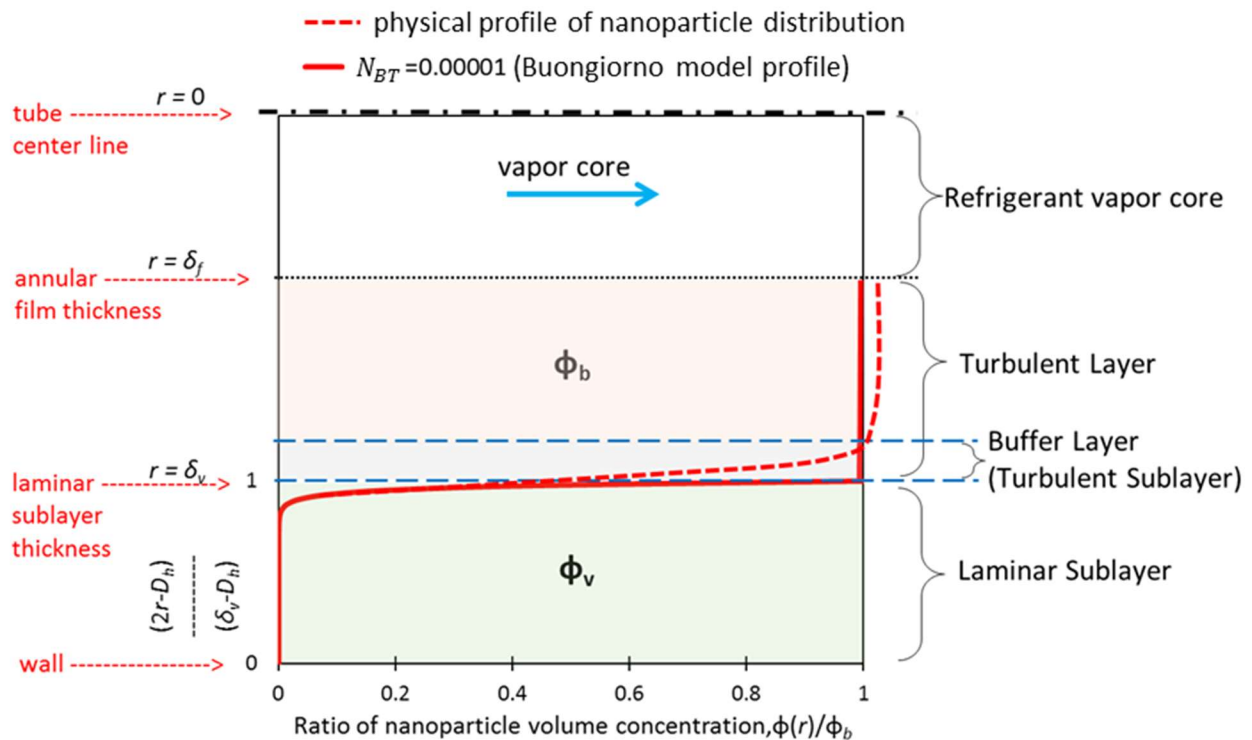


Figure 44: Nanoparticle distribution in the laminar sublayer and turbulent layer in two-phase flow.

Bigi (2018) concluded that when N_{BT} were higher, because of stronger Brownian diffusion, the nanoparticles distributed more uniformly and the average nanoparticle concentration in laminar sublayer was closer to the turbulent layer bulk concentration. This caused the nanofluid at the wall to behave like pure fluid with higher viscosity and higher thermal conductivity, while its heat transfer performance was closer to a particle free fluid. While at low nanoparticle concentrations

as for refrigerant-nanolubricant mixtures studied, the change in N_{BT} did not significantly changed the heat transfer performance.

At low nanoparticle concentrations, changing the value of N_{BT} from 0.00001 to 10 increased the dynamic viscosity $\mu_{f,v}$ and liquid mixture density $\rho_{f,v}$ in the laminar sublayer by only 0.02% and 0.009%, respectively. The small change in viscosity and density negligibly altered the laminar sublayer thickness. The thinning or thickening of the laminar sublayer thickness and its effect on heat transfer was more dependent on nanoparticle diffusion towards the turbulent layer and changing the density of the liquid, $\rho_{f,b}$, in the turbulent layer.

5.4.5 Annular film thickness and laminar sublayer thickness

The annular film thickness, δ_f , was assumed uniform for the two-phase horizontal flow and was estimated as per methods described by Bigi (2018) and Hewitt and Hall-Taylor (1970). The liquid mass flow rate in the tube was given by equation (62). Hewitt and Hall-Taylor (1970) provided equation (63) to estimate the mass flow rate of liquid flowing in the annular film.

$$\dot{m}_f = \dot{m} \frac{\pi}{4} D_h^2 (1 - x_{avg}) \quad (62)$$

$$\dot{m}_f = \frac{2\pi\rho_{f,bv}}{\mu_{f,bv}} \left\{ \left[\tau_{ifg} (D_h/2 - \delta_f) + \frac{1}{2} \frac{dp}{dz} (D_h/2 - \delta_f)^2 \right] \left[\frac{1}{4} (D_h/2)^2 - (D_h/2 - \delta_f)^2 \right] - \frac{1}{2} (D_h/2 - \delta_f)^2 \ln \left(\frac{D_h/2}{D_h/2 - \delta_f} \right) - \frac{1}{16} \frac{dp}{dz} (D_h/2)^2 - (D_h/2 - \delta_f)^2 \right\} \quad (63)$$

If the experimental pressure drop was unknown in equation (63), it could be estimated by literature correlations. Bigi (2018) and Hewitt and Hall-Taylor (1970) provided the total pressure drop as in equation (64) for horizontal tube, where the first term in the equation was frictional pressure drop and the second term in the equation was momentum pressure drop.

$$\frac{dp}{dz} = \frac{-4\tau_{ifg}}{D_h} - \frac{-2x_{avg}\dot{m}^2}{\alpha^2\rho_g} \left(\frac{4\dot{q}_{avg}}{\dot{m}D_h h_{fg}} \right) \quad (64)$$

The momentum pressure drop provided in equation (35) could be used to replace the momentum pressure drop component in equation (64). However, the length of the test section and information of change of refrigerant vapor quality over the length of the test section will have to be provided as an input to the model.

The shear stress at the interface of annular liquid film and gas core, τ_{ifg} , needed in equation (63) and equation (64) was evaluated using equation (65). In equation (65), f_{ifg} was the interfacial friction factor between the annular liquid film and gas core, generally estimated from empirical correlations, while Bigi (2018) evaluated it with $f_{ifg} = 0.079(\dot{m}x_{avg}D_h/\mu_g)^{-0.5}(1 + 300\delta_f/D_h)$. The void fraction, α , was calculated according to the theoretical definition, $\alpha = ((D_h - \delta_f)/D_h)$, while it could also be calculated using Rouhani and Axelsson (1970) void fraction model.

$$\tau_{ifg} = \frac{1}{2}f_{ifg}\rho_g \left(\frac{\dot{m}x_{avg}}{\rho_g\alpha} \right)^2 \quad (65)$$

For current model, the average vapor quality and average wall heat flux were used as inputs in above equation (62) through equation (65), and the equations were solved iteratively to find the annular film thickness, δ_f .

For single phase flow δ_f in equation (54) and equation (55) is to be replaced with half of the hydraulic diameter of the smooth tube, $\delta_f = 0.5D_h$. The laminar sublayer thickness, δ_v , was evaluated as in equation (66). At high vapor qualities in two-phase flows, when the annular film thickness was same as the laminar sublayer thickness, as shown in Figure 49, the δ_v thickness was limited to 98% of δ_f to allow for solution convergence.

$$\delta_v = \left(\frac{8}{f}\right) \frac{\mu_{f,v} \rho_{f,b}}{\rho_{f,v} \dot{m}} \quad (66)$$

Equation (43) through equation (66) were solved iteratively to evaluate the convective heat transfer coefficient, HTC_{cht} . The C++ script reported in Appendix-G presents the modified Buongiorno model to evaluate the convective heat transfer coefficient for nanofluids. The code also has the equations for calculating the diffusion time of nanoparticles under the influence of different slip mechanisms.

5.4.6 Modified Buongiorno model predictions of experimental results

The single-phase flow heat transfer data was used to check the validity of the modified Buongiorno model. Figure 45 shows single-phase flow heat transfer factors, HTF , for R410A-POE, R410A-ZnO NL, and R410A-Al₂O₃ NL mixtures calculated using experimental data and modified Buongiorno model prediction. Figure 45 (a) were the tests at same mass flux of 207 kg/m²-s, and Figure 45 (b) were the tests at same Reynolds number of 13900. The experimental heat transfer factors, HTF_{exp} , was evaluated using equation (67). The HTC_{exp} was the experimental heat transfer coefficient of R410A-POE, R410A-ZnO NL, and R410A-Al₂O₃ NL mixtures, while the $HTC_{exp,R410A}$ was the baseline experimental heat transfer coefficient of R410A in absence of lubricant and at same flow conditions as the R410A-lubricant test. The predicted heat transfer factors, $HTF_{cht,p}$, was evaluated using equation (68). The HTC_{cht} was the modified Buongiorno model predicted convective heat transfer coefficient of R410A-POE, R410A-ZnO NL, and R410A-Al₂O₃ NL mixtures calculated using equation (44), while the $HTC_{cht,R410A}$ was the predicted convective heat transfer coefficient of R410A in absence of

lubricant and at same flow conditions as the R410A-lubricant test, also calculated using equation (44). $HTC_{cht,R410A}$ was the baseline for predicted HTC_{cht} of R410A-POE and R410A-nanolubricant tests. The experimental HTC_{exp} and predicted HTC_{cht} for the single-phase flow tests are provided in Appendix-D.

$$HTF_{exp} = \frac{HTC_{exp} - HTC_{exp,R410A}}{HTC_{exp,R410A}} \times 100 \quad (67)$$

$$HTF_{cht,p} = \frac{HTC_{cht} - HTC_{cht,R410A}}{HTC_{cht,R410A}} \times 100 \quad (68)$$

The calculated single-phase experimental HTF s of R410A-lubricant mixtures were always lower than HTF s of R410A. Figure 45 (a) shows that at same mass flux of 207 kg/m²-s the experimental HTF s for R410A-POE, R410A-ZnO NL, and R410A-Al₂O₃ NL mixture were -18% (Re=12836), -21% (Re=12702), and -20% (Re=12620), respectively. The modified Buongiorno model predicted the HTF s as -7%, -8.9%, and -8.6% for R410A-POE, R410A-ZnO NL, and R410A-Al₂O₃ NL mixture, respectively. For same mass flux tests, the fluid viscosity increased and the bulk Reynolds number decreased with the addition of ZnO and Al₂O₃ nanoparticles to the R410A-POE mixture, resulting in thickening of laminar sublayer and thus lowering the HTC for R410A-nanolubricant mixtures. R410A-ZnO NL had lower HTF than R410A-Al₂O₃ NL due to loss of ZnO nanoparticles due to agglomeration. The modified Buongiorno model was successful in predicting the trend of HTC for fluids at different nanoparticle concentration.

Figure 45 (b) shows that at same Reynolds number of 13900 (turbulent flow) the experimental HTF s for R410A-POE, R410A-ZnO NL, and R410A-Al₂O₃ NL mixture were -15%, -14%, and -13.5%, respectively. The modified Buongiorno model predicted HTF s as 7.7%, 8.6%, and 9.1% for R410A-POE, R410A-ZnO NL, and R410A-Al₂O₃ NL mixture, respectively. The experimental results at same Reynolds number showed the HTC of R410A-ZnO NL was

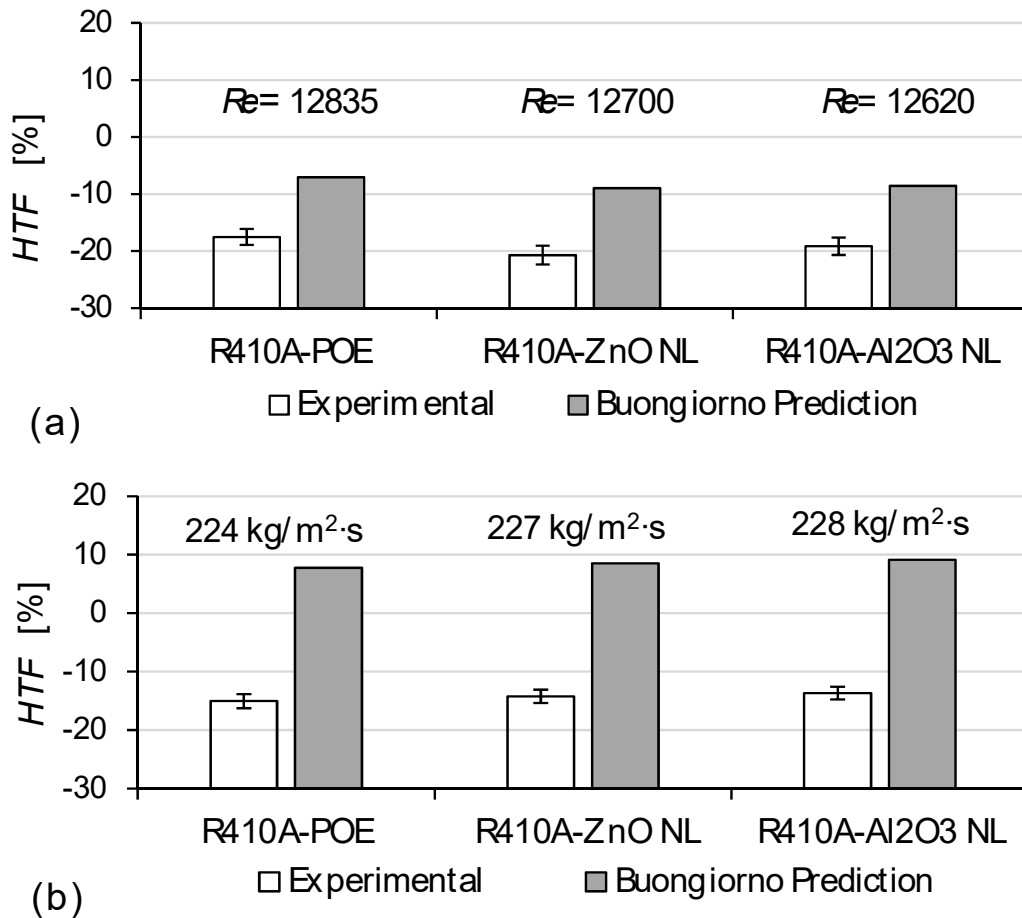


Figure 45: Experimental and modified Buongiorno model predicted HTF for (a) Single-phase flow HTF at same mass flux of $\dot{m}=207 \text{ kg/m}^2\text{-s}$ and (b) single-phase HTF at same Reynolds number of $Re=13900$, for R410A-POE, R410A-Al₂O₃ NL ($NP_{conc}=20 \text{ wt.}\%$), and R410A-ZnO NL ($NP_{conc}=14 \text{ wt.}\%$) mixtures. ($\dot{q}=8.7 \text{ kW/m}^2$, $OMF=3 \text{ wt.}\%$)

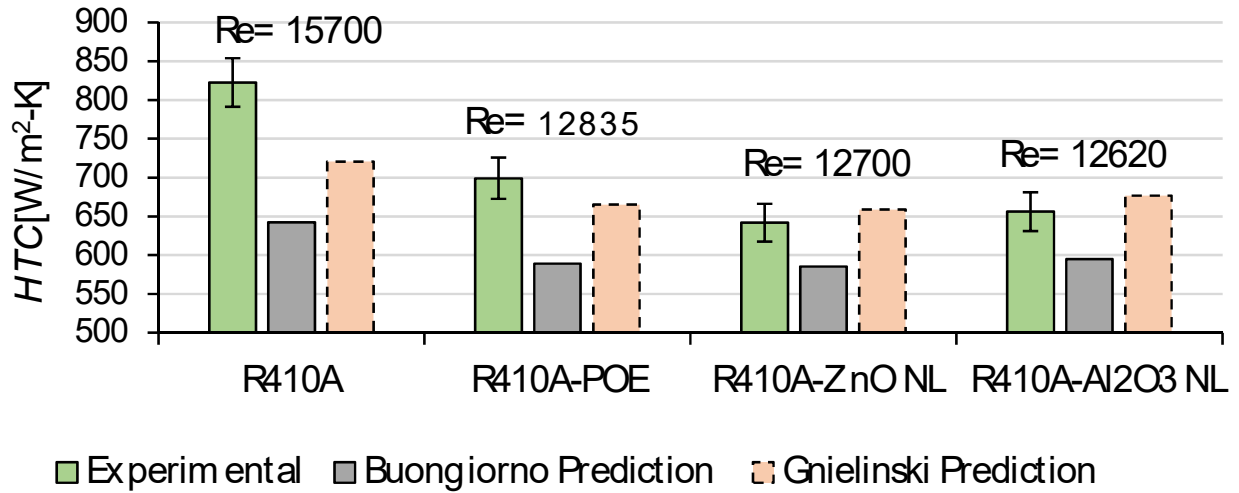
0.43% higher than HTC of R410A-POE, and the HTC of R410A-Al₂O₃ NL was 0.88% higher than HTC of R410A-POE. For same Reynolds number, the modified Buongiorno model successfully predicted increase in the HTC with addition of nanoparticles to the base fluid, the prediction showed the HTC of R410A-ZnO NL was 0.46% higher than HTC of R410A-POE and the HTC of R410A-Al₂O₃ NL was 1% higher than HTC of R410A-POE. The increase in HTC were very small as the tests were conducted at very low nanoparticle volume concentrations. At

same Reynolds number, the base fluid in the presence of nanoparticles flowed at higher fluid velocities because of its increased viscosity due to the dispersion of nanoparticles. The higher velocity nanofluid have higher laminar sublayer and turbulent layer interface velocity, this decreases the laminar sublayer thickness and thus aid in increasing the HTC .

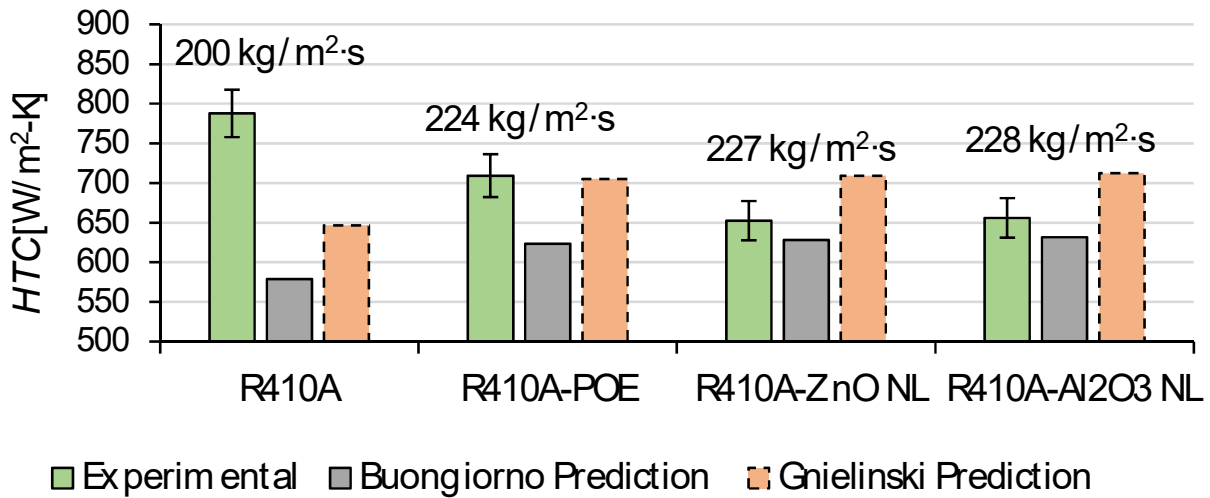
Figure 46 shows single-phase flow convective heat transfer coefficients, HTC , for R410A, R410A-POE, R410A-ZnO NL, and R410A-Al₂O₃ NL mixtures for experimental data (HTC_{exp} in Appendix-D), modified Buongiorno model prediction (HTF_{cht} in equation (44)), and Gnielinski correlation prediction ($HTF_{cht,Gnielinski}$ in equation (69)). Gnielinski correlation (Gnielinski 1976) is a classical turbulent flow convective heat transfer coefficients equation presented in all engineering textbooks. This correlation is for pure fluids, and do not account for the presence of nanoparticles in the flow. The bulk fluid thermophysical properties of R410A-ZnO NL and R410A-Al₂O₃ NL mixture were calculated in presence of nanoparticles, and the properties were then used in equation (69).

$$HTC_{cht,Gnielinski} = \frac{k_{f,bv}}{D_h} \left[\frac{\frac{f}{8} (Re_{fo,bv} - 1000) Pr_{bv}}{1 + 12.7 \sqrt{\frac{f}{8}} (Pr_{bv}^{2/3} - 1)} \right] \quad (69)$$

Figure 46 (a) were the tests at same mass flux of 207 kg/m²-s, and Figure 46 (b) were the tests at same Reynolds number of 13900. For the single flow tests, Figure 46 (a) shows that at mass flux of 207 kg/m²-s the experimental HTC_{exp} for R410A, R410A-POE, R410A-ZnO NL, and R410A-Al₂O₃ NL mixtures were 22%, 16%, 9%, and 9%, respectively, higher than the HTC_{cht} prediction by the modified Buongiorno model. While, experimental HTC_{exp} for R410A and R410A-POE were 12% and 5%, respectively, higher than the $HTF_{cht,Gnielinski}$ prediction by the



(a)



(b)

Figure 46: Experimental HTC_{exp} , modified Buongiorno model predicted HTC_{cht} , and Gnielinski correlation predicted $HTC_{cht,gnielinski}$ for (a) Single-phase flow HTC at same mass flux of $\dot{m}=207 \text{ kg/m}^2\text{-s}$ and (b) single-phase HTC at same Reynolds number of $Re=13900$ for R410A ($OMF=0 \text{ wt.}\%$), R410A-POE, R410A-Al₂O₃ NL ($NP_{conc}=20 \text{ wt.}\%$, $OMF=3 \text{ wt.}\%$), and R410A-ZnO NL ($NP_{conc}=14 \text{ wt.}\%$, $OMF=3 \text{ wt.}\%$) mixtures. ($\dot{q}=8.7 \text{ kW/m}^2$)

Gnielinski correlation. And, experimental HTC_{exp} for R410A-ZnO NL and R410A-Al₂O₃ NL mixtures were 2.6% and 3.2%, respectively, lower than the $HTF_{cht,gnielinski}$. Figure 46 (b)

shows that at Reynolds number of 13900 the experimental HTC_{exp} for R410A, R410A-POE, R410A-ZnO NL, and R410A-Al₂O₃ NL mixtures were 27%, 12%, 3.7%, and 3.7%, respectively, higher than the HTC_{cht} prediction by the modified Buongiorno model for the single flow tests. While, experimental HTC_{exp} for R410A and R410A-POE were 18% and 0.6%, respectively, higher than the $HTF_{cht,Gnielinski}$ prediction by the Gnielinski correlation. And, experimental HTC_{exp} for R410A-ZnO NL and R410A-Al₂O₃ NL mixtures were 8.7% and 8.6%, respectively, lower than the $HTF_{cht,Gnielinski}$.

The Buongiorno (2006) model for HTC_{cht} , shown in equation (44), was validated for water based nanofluids' single-phase turbulent flow convective heat transfer, and the modified Buongiorno model predicted the experimental HTC_{exp} data of R410A-nanolubricant mixtures' single phase flow tests with mean absolute deviation of 7.5%. The mean absolute deviation was calculated using equation (41). The model successfully predicted the experimental HTC_{exp} data of R410A-nanolubricant mixtures, and the model was also able to predict the change in the HTC of R410A-POE with addition of nanoparticles to the mixture for same mass flux and same Reynolds number cases.

Figure 47 shown temperature measurement along the length of the tube for R410A single-phase flow test at $\dot{m}=207$ kg/m²-s and in absence of lubricant. The green dash line was the experimental liquid refrigerant temperature, $T_{ref,exp}$, inside the tube, which was measured at the inlet, $T_{ref,in}$, and outlet inline thermocouples, $T_{ref,out}$, at the test section. The black solid circles were the locally measured inner wall surface temperatures, $T_{s,\bar{l}}$. These local inner wall surface temperatures were average of the three local temperatures on top, side, and bottom of the inner wall surface (equations (19), (20), and (21)), $T_{s,\bar{l}} = (T_{s,\bar{l},Top} + T_{s,\bar{l},Side} + T_{s,\bar{l},Bottom})/3$. The subscript \bar{l} represents the local location on the tube. The red crosses were the local surface

temperatures, $T_{s,\bar{l},Gnielinski}$, evaluated for Gnielinski correlation using equation (70). The purple dashed line was the wall temperature, $T_{s,Buongiorno}$, estimated by Buongiorno model's iterative method explained in previous section. The modified Buongiorno model needed measured average heat flux and average refrigerant bulk liquid temperature as input, and using iterative method, as explained in previous section for equation (61), calculated the $T_{s,Buongiorno}$.

The wall temperature, $T_{s,Buongiorno}$, from Buongiorno model was about 13°C higher than the experimental wall temperature. The wall temperature, $T_{s,Gnielinski}$, from Gnielinski correlation was on average 2°C higher than experimental wall temperature. The mean absolute deviation of the modified Buongiorno model HTC_{cht} for R410A single phase flow tests were 24%, and was high because of large wall temperature predictions. The Buongiorno modified model predicted the HTC_{cht} for R410A fluid with large deviation. The experimental data of R410A were in agreement with the Gnielinski correlation with 15% mean absolute deviation of $HTC_{cht,Gnielinski}$ from HTC_{exp} .

$$T_{s,\bar{l},Gnielinski} = T_{ref,\bar{l}} + \left(\sum_{\bar{m}=1}^{\bar{m}=3} \dot{q}_{\bar{l}\bar{m}} \right) / HTC_{cht,Gnielinski} \quad (70)$$

As the experimental data of R410A were in agreement with the Gnielinski correlation, better than Buongiorno modified model. Therefore, the HTF plots in Figure 45 were repeated and Gnielinski correlation was used to predict baseline R410A heat transfer coefficient as in equation (71). Figure 48 shows single-phase flow heat transfer factors, HTF , for R410A-POE, R410A-ZnO NL, and R410A-Al2O3 NL mixtures calculated using experimental data and this works' model prediction. The experimental heat transfer factors, HTF_{exp} , was evaluated using equation (67). The predicted heat transfer factors, $HTF_{cht,p}$, was evaluated using equation (71). The Gnielinski correlation prediction data for the single-phase flow tests are provided in Appendix-D.

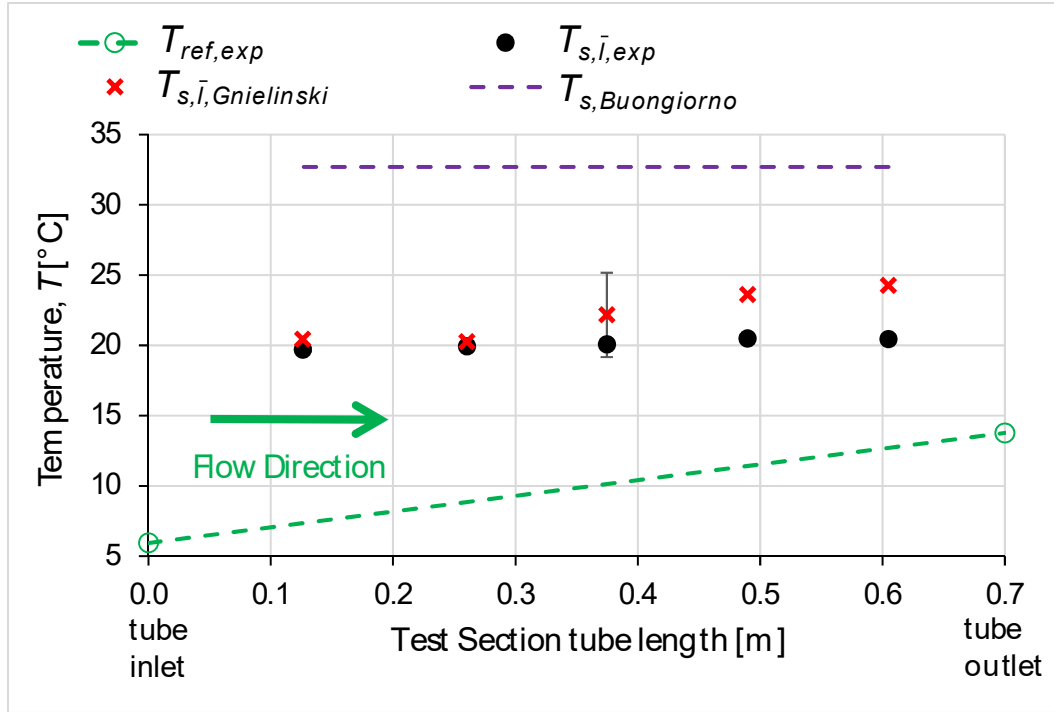


Figure 47: Local inner wall surface temperatures along the length of tube for R410A test at $\dot{m}=207 \text{ kg/m}^2\text{-s}$, $\ddot{q}=8.7 \text{ kW/m}^2$, and $OMF=0 \text{ wt.}\%$.

$$HTF_{cht,p} = \frac{HTC_{cht} - HTC_{cht,Gnielinski,R410A}}{HTC_{cht,Gnielinski,R410A}} \times 100 \quad (71)$$

Figure 48 (a) shows that at same mass flux of $207 \text{ kg/m}^2\text{-s}$ the experimental HTF_{exp} for R410A-POE, R410A-ZnO NL, and R410A-Al₂O₃ NL mixture were -18% (Re=12836), -21% (Re=12702), and -20% (Re=12620), respectively. The presented model (modified Buongiorno model with Gnielinski correlation for baseline) predicted the $HTF_{cht,p}$ as -17%, -19%, and -19% for R410A-POE, R410A-ZnO NL, and R410A-Al₂O₃ NL mixture, respectively. Figure 48 (b) shows that at same Reynolds number of 13900 (turbulent flow) the experimental HTF_{exp} for R410A-POE, R410A-ZnO NL, and R410A-Al₂O₃ NL mixture were -15%, -14%, and -13.5%, respectively. The presented model predicted the $HTF_{cht,p}$ as -3.6%, -2.9%, and -2.3% for R410A-POE, R410A-ZnO NL, and R410A-Al₂O₃ NL mixture, respectively.

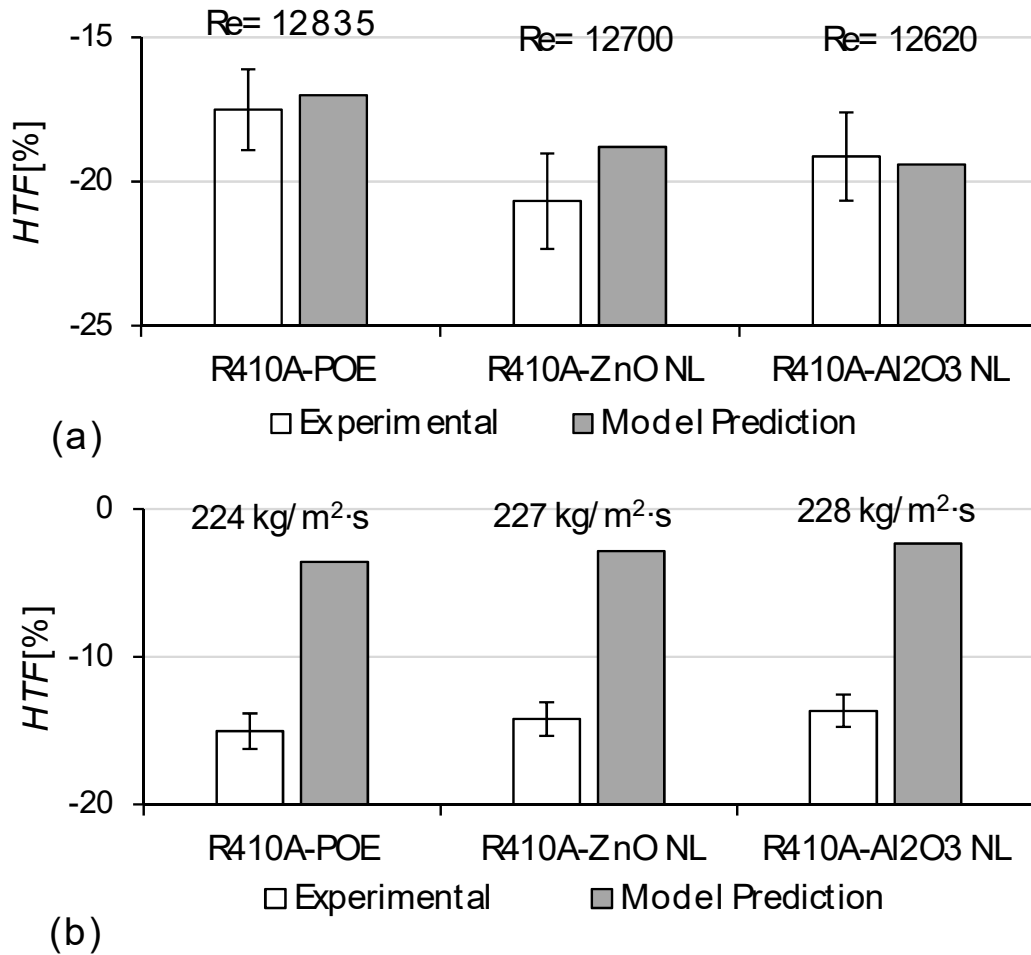


Figure 48: Experimental and present model predicted HTF for (a) Single-phase flow HTF at same mass flux of $\dot{m}=207 \text{ kg/m}^2\text{-s}$ and (b) single-phase HTF at same Reynolds number of $Re=13900$, for R410A-POE, R410A-Al₂O₃ NL ($NP_{conc}=20 \text{ wt.}\%$), and R410A-ZnO NL ($NP_{conc}=14 \text{ wt.}\%$) mixtures. ($\dot{q}=8.7 \text{ kW/m}^2$, $OMF=3 \text{ wt.}\%$, R410A-lubricant predicted by modified Buongiorno model, and the baseline R410A was predicted using Gnielinski correlation)

The Gnielinski correlation, $HTC_{cht,Gnielinski,R410A}$, well predicted baseline R410A HTC_{exp} . And, it was intentionally used in Figure 48 to calculate R410A baseline, so the modified Buongiorno model predictions could be studied for R410A-nanolubricants. Figure 48 also showed the modified Buongiorno model was successful in predicting the change in the HTC of R410A-POE with addition of nanoparticles to the mixture for same mass flux and same Reynolds number cases.

5.4.7 Pool boiling of the refrigerant and nanolubricant mixture

A semi-theoretical model was developed by Kedzierski (2003a, 2003b) to predict the pool boiling heat transfer, \ddot{q}_{pL} , for refrigerant (R123) and lubricant (naphthenic mineral oil, York-C) mixtures on a rough horizontal flat surface, as shown in equation (73). The bubble departure radius, r_b , and thermal boundary layer parameter, λ , that were fitted to the lubricant excess concentration at the surface and the heat transfer measurements for different oil concentrations. Kedzierski (2003b) provided an improved wall superheat dependent thermal boundary layer parameter and generalized the model to be used with other refrigerant-lubricant mixtures. The model had three main assumptions; the lubricant lifted from the lubricant excess layer at the heated surface as lubricant caps on bubbles and it caused a dominant lubricant mass transfer, the lubricant excess layer had linear temperature profile in its thermal boundary layer and was exponential on outside, and the lubricant excess layer consisted nearly pure lubricant. The model predicted that the lubricant viscosity and miscibility were influential in determining the magnitude of the *HTC*. The lubricant excess layer thickness, l_e , was evaluated by Kedzierski (2003a) as shown in equation (72).

With the pool boiling experiments of R134a, ISO VG 68 POE oil, and Al₂O₃ nanoparticles on a horizontal rectangular flat surface, Kedzierski (2011) developed a semi-empirical pool-boiling model to predict the heat transfer enhancement caused by the transfer of momentum from the nanoparticles to the bubbles, as shown in equation (74). This model had the bubble departure frequency and nucleation site density enveloped in an empirical constant and did not account for the possible change in the bubble characteristic and reduction of heat transfer due to the filling of cavities by nanoparticles for different refrigerant-nanolubricant pairs. The model estimated the heat flux of a nanolubricant refrigerant mixture, \ddot{q}_{np} , by applying a correction factor to the previous

heat flux model, equation (73), of Kedzierski (2003a). The model assumed that the nanoparticles were well dispersed in the lubricant excess layer of thickness l_e , and the nanoparticles did not affect the nucleation site density nor the departure frequency. The Kedzierski (2011) model successfully calculated the increase in boiling performance if the input nanoparticle diameter was reduced below 10 nm.

The nanoparticle volume fraction in the laminar sublayer, ϕ_v evaluated with equation (58), represented the concentration of nanoparticles at the heater's surface, and was used as the nanoparticle volume fraction, ϕ , input in equation (74). As shown in Figure 49, the lubricant excess layer thickness, l_e evaluated with equation (72), were in the same order of magnitude or larger than the laminar sublayer thickness, δ_v evaluated with equation (66). During fluid flow, in contrast to pool boiling conditions, the lubricant inside the laminar sublayer was undisturbed by the turbulent diffusion effects, while the lubricant in the turbulent layer was diffused in the flow. Thus, the magnitude of the lubricant excess layer thickness was limited by the laminar sublayer thickness. Therefore, for flow boiling, the l_e in equation (73) was evaluated with equation (66). The fluid thermophysical properties in equation (73) and equation (74), with subscript bv , were evaluated at refrigerant saturation temperatures using models provided by Bigi et al., (2015), Cremaschi et al., (2015) and Kedzierski et al., (2017). The nucleate boiling heat transfer coefficient, HTC_{nb} , from Kedzierski model was evaluated as in equation (75). The average wall temperature, $T_{s,avg}$, in equation (75) was measured experimentally.

$$l_e = \frac{\omega \cdot (T_{bub} + 273.15) \cdot \sigma_{f,bv}}{5.9 \times 10^{-7} (1 - \omega) \rho_L h_{fg,bv} (T_{s,avg} - T_{bub})} \quad (72)$$

$$\ddot{q}_{pL} = 5.9 \times 10^{-7} (1 - \omega) \rho_L h_{fg,bv} (T_{s,avg} - T_{bub})^2 k_L (1 - e^{-\lambda l_e / r_b}) / [\omega \cdot (T_{bub} + 273.15) \cdot \sigma_{f,bv}] \quad (73)$$

where, $l_e \leq \delta_v$

$$\frac{\ddot{q}_{np}}{\ddot{q}_{pL}} = 1 + \frac{3.45 \times 10^{-9} \phi \sigma_{f,bv} \nu_L \rho_g (\omega)^2}{D_{np}^4 (\ddot{q}_{pL})^{3/2} \rho_{f,bv} (\rho_{np} - \rho_{f,bv}) g (1 - \omega)^2} \quad (74)$$

where, $\phi = \phi_v$

$$HTC_{nb} = \ddot{q}_{pL} / (T_{s,avg} - T_{bub}), NP_{conc} = 0 \quad (75)$$

$$HTC_{nb} = \ddot{q}_{np} / (T_{s,avg} - T_{bub}), NP_{conc} > 0$$

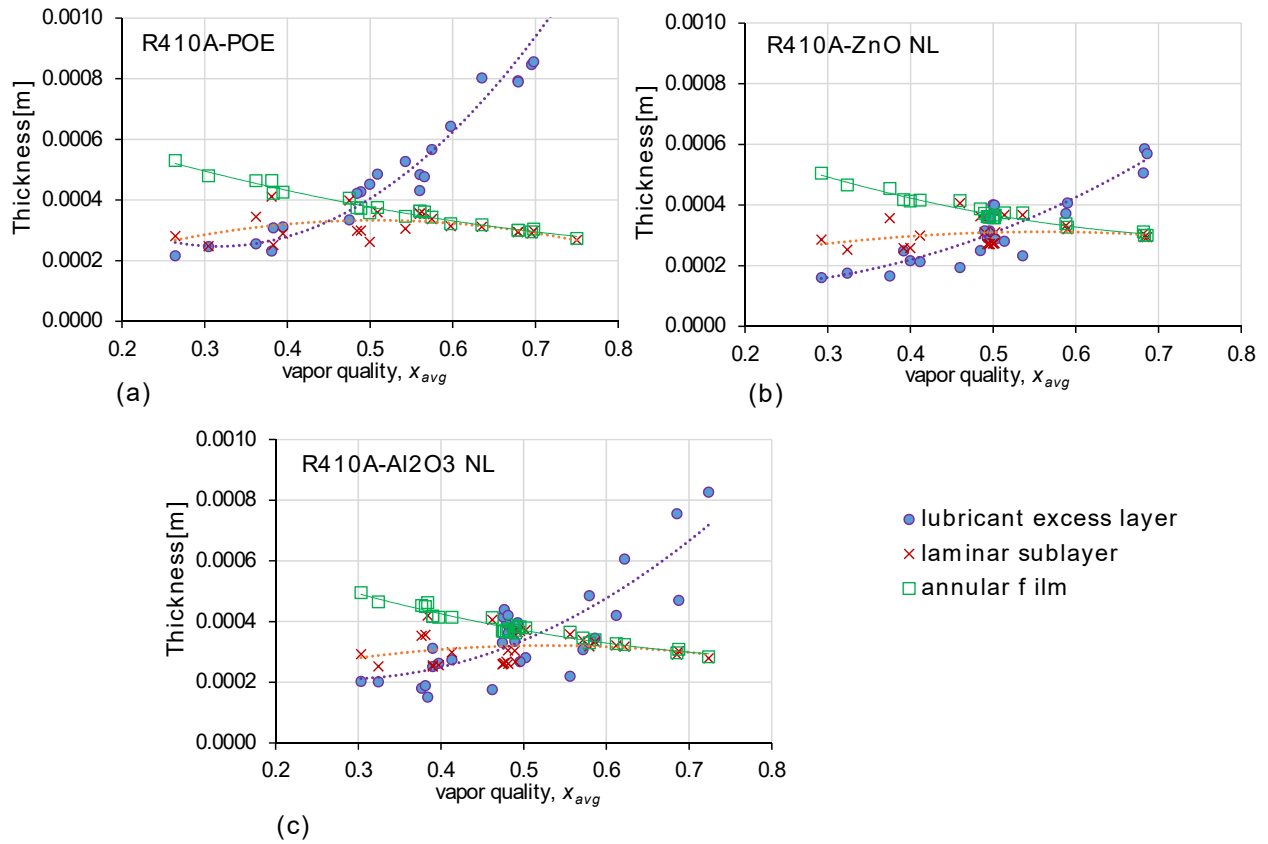


Figure 49: Lubricant excess layer, laminar sublayer, and annular film thickness for the two-phase flow experimental tests of (a) R410A-POE, (b) R410A-ZnO NL, and (c) R410A-Al2O3 NL

5.4.8 Superposition model for saturated flow boiling

A new superposition model, shown in equation (76), following J. C. Chen (1966) approach, was developed that estimated the flow boiling heat transfer coefficient, HTC_p , for the refrigerant-nanolubricant mixtures,

$$HTC_p = S \cdot HTC_{nb} + F \cdot HTC_{cht} \quad (76)$$

Where, S and F were the suppression factor and two-phase convective multiplier, respectively. $S \cdot HTC_{nb}$ was the microconvective and $F \cdot HTC_{cht}$ was the macroconvective mechanism of heat transfer during two-phase flow boiling. HTC_{nb} was the nucleate pool boiling heat transfer coefficient from Kedzierski model, equation (75). HTC_{cht} was the single phase convective heat transfer coefficient from Buongiorno model, equation (44). The suppression factor S was chosen the same as the one used by other authors (John C. Chen 1966; W. Chen and Fang 2014), as shown in equation (77). The two-phase convective multiplier, F , as shown in equation (78), was obtained using regression of the smooth tube experimental data for the saturated flow boiling of R410A refrigerant in absence and presence of POE oil and nanolubricants.

$$S = 1 / \left[1 + 2.53 \times 10^{-6} (Re_{fo} F^{1.25})^{1.17} \right], \quad Re_{fo} = (1 - x) \dot{m} D_h / \mu_{f,bv} \quad (77)$$

$$F = 1.5 \times 2.35 \left(0.213 + \frac{1}{X_{tt}} \right)^{(0.736 \times 0.2)} \left(\frac{\sigma_{f,bv}}{\sigma_{f,ref,OMF=0}} \right)^{(3.284 - 3.787 \cdot Fr_{bv})} \left[\frac{k_{f,v}/\delta_v}{(k_{f,v}/\delta_v)_{NP_{conc}=0}} \right]^{\left(\frac{7.8}{x^{1.4}} \right)^n} \quad (78)$$

$$n = 1 \text{ for } NP_{conc} > 0 \text{ and } n = 0 \text{ for } NP_{conc} = 0,$$

$$X_{tt} = \left(\frac{1-x}{x} \right)^{0.9} \left(\frac{\rho_g}{\rho_{f,bv}} \right)^{0.5} \left(\frac{\mu_{f,bv}}{\mu_g} \right)^{0.1}, \quad Fr_{bv} = \dot{m}^2 / (\rho_{f,bv}^2 \cdot g \cdot D_h)$$

5.4.9 Correlation for two-phase convective multiplier

A total of 149 experimental data points of HTC_{exp} were used in the development of the two-phase convective multiplier, F , shown in equation (78), for the new superposition model of saturated two-phase flow boiling of R410A with POE and nanolubricants in a smooth tube. Once the nucleate boiling heat transfer coefficients, HTC_{nb} , single phase convective heat transfer coefficients, HTC_{cht} , and suppression factors, S , were evaluated using equation (75), equation (44), and equation (77), the desired two-phase convective multipliers, \bar{F} , was evaluated using equation (79) for all 149 tests. The data of these 149 tests are provided in Appendix-H. The equation for the desired two-phase convective multiplier, \bar{F} , was obtained by replacing the model HTC_p prediction in equation (76) with experimental HTC_{exp} . The desired two-phase convective multiplier, \bar{F} , values were then correlated with the thermophysical properties and non-dimensional numbers to obtain equation (78).

$$\bar{F} = (HTC_{exp} - S \cdot HTC_{nb}) / HTC_{cht} \quad (79)$$

F in equation (78) was a function of Martinelli parameter X_{tt} , Froude number Fr_{bv} , surface tension σ_f , laminar sublayer liquid thermal conductivity $k_{f,v}$, and laminar sublayer thickness, δ_v . The laminar sublayer thickness, δ_v , was evaluated as in equation (66). The friction factor, f , was obtained using the Colebrook equation, and the tube roughness for the smooth tube was chosen as $1.5 \mu\text{m}$ as per manufacturers data. R410A-POE mixture have higher surface tension than R410A, this caused the liquid to climb up the wall of the smooth horizontal tube in stratified flow and improve wetting, and thus helped to increase the heat transfer area (Kedzierski and Kaul 1998; Shen and Groll 2005). The term in equation (78) with the ratio of surface tension of refrigerant-lubricant (or nanolubricant) and surface tension of refrigerant in the absence of lubricant accounted for the increase in the HTC of R410A in presence of POE oil.

The ratio $k_{f,v}/\delta_v$ is the definition of the HTC in the laminar sublayer. The laminar sublayer thickness, δ_v , increased in the presence of nanoparticles, thus laminar sublayer thicknesses for R410A-NL mixtures were much higher than that for R410A-POE mixture; this caused the R410A-NL mixtures to have lower HTC than R410A-POE mixture. The term in equation (78) consisting of $k_{f,v}/\delta_v$ ratio accounts for the decrease in the HTC of refrigerant-lubricant mixture due to the increase in the laminar sublayer thickness with the addition of nanoparticles to the mixture.

Figure 50 shows the desired two-phase convective multiplier, \bar{F} , on x-axis and the correlated two-phase convective multiplier, F , on y-axis. Out of 149 data points of \bar{F} , a total of 133 data points of F were correlated within $\pm 20\%$. The data of \bar{F} and F are provided in the last two column of the table in Appendix-H.

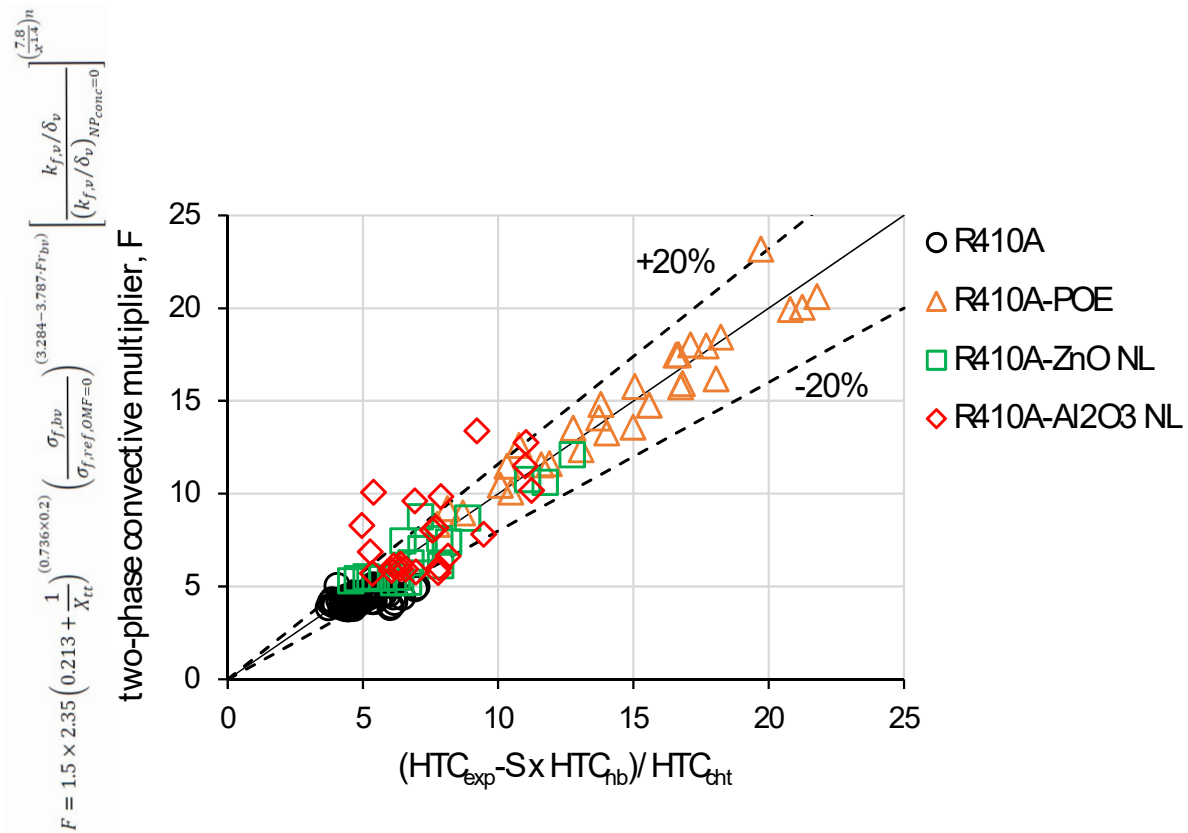


Figure 50: Correlation development for the two-phase convective multiplier, F

5.4.10 Superposition model sample calculation and effect of non-spherical nanoparticles on heat transfer

Table 16 in this sub-section presents sample calculations to evaluate the predicted HTC_p using the superposition model in equation (76), for two-phase flow tests of R410A, R410A-POE, R410A-ZnO NL, and R410A-Al₂O₃ NL mixtures. The selected sample test examples were at same average vapor quality of $x_{avg}=0.5$, average heat flux of $\ddot{q}=15$ kW/m², and mass flux of $\dot{m}=165$ kg/m²-s. Table 16 presents important variables needed in equations (43) through (78) to evaluate the predicted HTC_p of saturated two-phase flow boiling of R410A with POE and nanolubricants in a smooth tube.

The heat transfer model was independent of the length of the test section tube and no locally measured values along the test section length was used as an input to the model. The average vapor quality, x_{avg} , and average heat flux, \ddot{q}_{avg} , of the test section was used as an input to the model. Other input required for this model were mass flux, \dot{m} , oil mass fraction, OMF , nanoparticle mass concentration in POE, NP_{conc} , refrigerant saturation temperature, T_{bub} , experimental average wall surface temperature measurement, $T_{s,avg}$, and experimental pressure drop of the test section, $\Delta P/L_{exp}$. Modified Buongiorno model for HTC_{cht} require experimentally measured heat flux, \ddot{q}_{avg} , as input for iterative calculations to converge the tube wall temperature, T_w , in equation (61). Kedzierski model for HTC_{nb} does not require heat flux, \ddot{q}_{avg} , as input, but require experimentally measured tube wall temperature, $T_{s,avg}$, in equation (75). The experimental total pressure drop data of the test section, $\Delta P/L_{exp}$, was input to the presented superposition model, and $\Delta P/L_{exp}$ was used to calculate the annular film thickness, δ_f , in equation (63). The total

pressure drop in the model could be estimated using literature correlations, however the length of the evaporator tube and information of change of refrigerant vapor quality over the length of the tube will be required to calculate the momentum pressure drop, as in equation (35).

The non-sphericity of ZnO nanoparticles were only captured through the Brownian diffusivity, D_B in equation (46), and through thermophysical property models provided by Bigi et al., (2015), Cremaschi et al., (2015) and Kedzierski et al., (2017). The non-spherical ZnO nanoparticles diffused slowly under Brownian motion than spherical Al₂O₃ nanoparticles because of their large aspect ratio. The Brownian diffusivity for ZnO nanoparticles ($D_B=1.76E-11$ m²/s) was lower than the Brownian diffusivity for Al₂O₃ nanoparticles ($D_B=5.01E-11$ m²/s), as shown in row 29 of Table 16. The thermophoretic diffusivity for both ZnO and Al₂O₃ nanoparticles were similar ($D_T \cong 7.7E-7$ m²/s), as shown in row 30. As the Brownian motion was less strong for ZnO nanoparticles compared to Al₂O₃ nanoparticles, the thermophoresis effect push more ZnO nanoparticles away from laminar sublayer towards turbulent layer compared to that of Al₂O₃ nanoparticles. Hence, under same flow boundary conditions, the ZnO average nanoparticle mass concentration in laminar sublayer ($NP_{conc,v}=0.00036$ wt.%) was lower than the Al₂O₃ average nanoparticle mass concentration in laminar sublayer ($NP_{conc,v}=0.00089$ wt.%), as shown in row 14 of Table 16. And the ZnO average nanoparticle mass concentration in turbulent layer ($NP_{conc,b}=17$ wt.%) was higher than the Al₂O₃ average nanoparticle mass concentration in turbulent layer ($NP_{conc,b}=14$ wt.%), as shown in row 13 of Table 16.

As the ZnO average nanoparticle mass concentration in turbulent layer was higher than the Al₂O₃ average nanoparticle mass concentration in turbulent layer, the liquid density in turbulent layer of R410A-ZnO NL ($\rho_{f,b}=1185$ kg/m³) was also higher than the liquid density in turbulent layer of R410A-Al₂O₃ NL ($\rho_{f,b}=1178$ kg/m³), in row 19 of Table 16. The liquid density in

turbulent layer had proportional effect on the laminar sublayer thickness, as shown in equation (66). The calculated laminar sublayer thickness for R410A-ZnO NL ($\delta_v=0.000246$ m) was larger than the laminar sublayer thickness for R410A-Al₂O₃ NL ($\delta_v=0.000243$ m), in row 33 of Table 16. While, the thermal conductivity of the laminar sublayer fluid of R410A-ZnO NL ($k_{f,v}=0.0892$ W/m-K) was lower than the thermal conductivity of the laminar sublayer fluid of R410A-Al₂O₃ NL ($k_{f,v}=0.0894$ W/m-K), in row 16 of Table 16, because of low concentration of ZnO nanoparticles in laminar sublayer with respect to that of Al₂O₃ nanoparticles. The combined effect of thicker laminar sublayer and lower thermal conductivity in laminar sublayer caused the two-phase convective multiplier of R410A-ZnO NL ($F=6.29$) to be less than the two-phase convective multiplier of R410A-Al₂O₃ NL ($F=6.64$), as shown in row 47 of Table 16. The two-phase convective multiplier, F , had large influence on the predicted heat transfer coefficient HTC_p , leading the predicted heat transfer coefficient of R410A-ZnO NL ($HTC_p=3.08$ kW/m²-K) to be less than the predicted heat transfer coefficient of R410A-Al₂O₃ NL ($HTC_p=3.25$ kW/m²-K), as shown in row 50 of Table 16.

The last two rows of the Table 16 show the predicted and experimental HTC . The absolute deviations in the predictions were 4%, 2%, 6%, and 17% for R410A, R410A-POE, R410A-ZnO NL, and R410A-Al₂O₃ NL mixtures, respectively. The experimental and predicted HTC for sample R410A, R410A-POE, R410A-ZnO NL, and R410A-Al₂O₃ NL mixtures at $x_{avg}=0.5$, $\ddot{q}=15$ kW/m², and $\dot{m}=165$ kg/m²-s are plotted in Figure 52, Figure 53, Figure 54, and Figure 55, respectively, and are presented with green squares in the plots. The solution of these sample calculations are also presented in Appendix-H.

Table 16: Sample superposition model calculations for two-phase flow boiling of R410A, R410A-POE, R410A-ZnO NL, and R410A-Al2O3 NL at $x_{avg}=0.5$, $\dot{q}=15 \text{ kW/m}^2$, and $\dot{m}=165 \text{ kg/m}^2\text{-s}$.

#	Variables		R410A	R410A-POE	R410A-ZnO NL	R410A-Al2O3 NL	Reference Equation	Used to estimate
1	Vapor quality	x_{avg} [-]	0.51	0.49	0.50	0.49	equation (77) and (78)	S, F
2	Mass flux	\dot{m} [$\text{kg/m}^2\text{-s}$]	166	163	165	167	equation (62) to (66), (77) and (78)	S, F
3	Heat flux	\dot{q}_{avg} [kW/m^2]	14.9	15.1	15.2	15.1	equation (61)	HTC_{cht}
4	Pressure drop per unit length	$\Delta P/L_{exp}$ [Pa/m]	829	1203	1076	1047	equation (63)	HTC_{cht}
5	Oil mass fraction	OMF [wt.%]	N.A	2.4	2.4	2.4	equation (4)	
6	Nanoparticle mass concentration in POE only	NP_{conc} [wt.%]	N.A	N.A	20	20		
7	Calculated refrigerant saturation temperature	T_{bub} [$^{\circ}\text{C}$]	6.0	6.5	6.3	6.2	equation (73)	HTC_{nb}
8	Experimental wall temperature	$T_{s,avg}$ [$^{\circ}\text{C}$]	9.9	9.3	10.9	10.1	equation (73)	HTC_{nb}
9	Wall temperature as per Buongiorno model prediction	T_w [$^{\circ}\text{C}$]	35.4	39.6	41.4	40.6	equation (61)	HTC_{cht}
10	Local oil mass fraction	ω [kg/kg]	N.A	0.043	0.044	0.043	equation (73) and (74)	HTC_{nb}
11	Turbulent layer average nanoparticle volume concentration	ϕ_b [m^3/m^3]	N.A	N.A	0.006	0.007	equation (54), (55), and (56)	HTC_{cht}
12	Laminar sublayer average nanoparticle volume concentration	ϕ_v [m^3/m^3]	N.A	N.A	1.3E-07	4.91E-07	equation (74) and (58)	$HTC_{nb},$ HTC_{cht}
13	Turbulent layer average nanoparticle mass concentration	$NP_{conc,b}$ [wt.%]	N.A	N.A	17	14	equation (59)	

#	Variables		R410A	R410A- POE	R410A- ZnO NL	R410A- Al2O3 NL	Reference Equation	Used to estimate
14	Laminar sublayer average nanoparticle mass concentration	$NP_{conc,v}$ [wt.%]	N.A	N.A	0.00036	0.00089	equation (60)	
15	Turbulent layer thermal conductivity	$k_{f,b}$ [W/m-K]	0.0996	0.1002	0.2485	0.2221	equation (44)	HTC_{cht}
16	Laminar sublayer thermal conductivity	$k_{f,v}$ [W/m-K]	0.0905	0.0898	0.0892	0.0894	equation (78)	F
17	Laminar sublayer thermal conductivity in absence of nanoparticles	$k_{f,v, NP_{conc}=0}$ [W/m-K]	0.0905	0.0898	0.0898	0.0900	equation (78)	F
18	Turbulent layer density evaluated at NP_{conc}	$\rho_{f,bv}$ [kg/m ³]	1144	1137	1146	1145	equation (78) and (74)	F, HTC_{nb}
19	Turbulent layer density evaluated at $NP_{conc,b}$	$\rho_{f,b}$ [kg/m ³]	1144	1137	1185	1178	equation (66)	HTC_{cht}
20	Laminar sublayer density	$\rho_{f,v}$ [kg/m ³]	1079	1066	1061	1063	equation (66)	HTC_{cht}
21	Refrigerant vapor density	ρ_g [kg/m ³]	37.5	37.5	37.5	37.5	equation (78) and (74)	F, HTC_{nb}
22	Turbulent layer dynamic viscosity evaluated at NP_{conc}	$\mu_{f,bv}$ [Pa-s]	0.00015	0.00020	0.00021	0.00021	equation (78)	F
23	Turbulent layer dynamic viscosity evaluated at $NP_{conc,b}$	$\mu_{f,b}$ [Pa-s]	0.00015	0.00020	0.00025	0.00025	equation (77)	S
24	Laminar sublayer dynamic viscosity	$\mu_{f,v}$ [Pa-s]	0.00013	0.00015	0.00015	0.00015	equation (66)	HTC_{cht}
25	Refrigerant vapor dynamic viscosity	μ_g [Pa-s]	0.00001	0.00001	0.00001	0.00001	equation (78)	F
26	Surface tension evaluated at NP_{conc}	$\sigma_{f,bv}$ [N/m]	0.0078	0.0117	0.0117	0.0117	equation (73), (74), and (78)	F, HTC_{nb}
27	Surface tension of R410A in absence of oil	$\sigma_{f,ref, OMF=0}$ [N/m]	0.0078	0.0078	0.0078	0.0078	equation (78)	F
28	Enthalpy evaluated at NP_{conc}	$h_{fg,bv}$ [kJ/kg]	213	208	208	208	equation (73)	HTC_{nb}

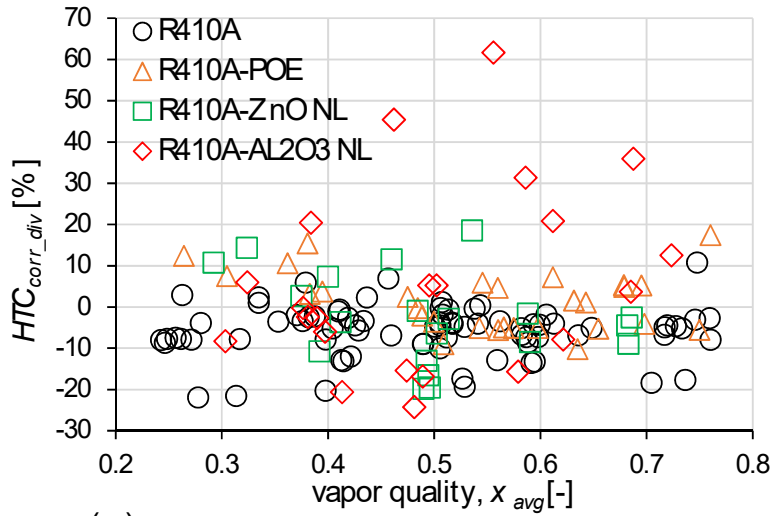
#	Variables		R410A	R410A- POE	R410A- ZnO NL	R410A- Al2O3 NL	Reference Equation	Used to estimate
29	Brownian diffusivity	D_B [m ² /s]	N.A	N.A	1.76E-11	5.01E-11	equation (45), (46), and (55)	HTC_{cht}
30	Thermophoretic diffusivity	D_T [m ² /s]	N.A	N.A	7.84E-07	7.59E-07	Equation (47) and (55)	HTC_{cht}
31	Ratio of Brownian and thermophoretic diffusivities	N_{BT} [-]	N.A	N.A	0.00002	0.00007	equation (57)	HTC_{cht}
32	Annular liquid film thickness	δ_f [m]	0.000330	0.000372	0.000366	0.000372	equation (54) and (55)	HTC_{cht}
33	Laminar sublayer thickness	δ_v [m]	0.000238	0.000241	0.000246	0.000243	Equation (54), (66) and (78)	$F, HTC_{nb},$ HTC_{cht}
34	Laminar sublayer thickness in absence of nanoparticles	$\delta_{v, NP_{conc}=0}$ [m]	0.000238	0.0002410	0.0002407	0.000238	equation (78)	F
35	Lubricant excess layer thickness	l_e [m]	N.A	0.000241	0.000246	0.000243	equation (72) and (73)	HTC_{nb}
36	Pool boiling heat fluxes for Kedzierski model	$\dot{q}_{pL}, \dot{q}_{np}$ [kW/m ²]	7.9	0.9	2.4	1.9	equation (73), (74) and (75)	HTC_{nb}
37	Martinelli parameter	X_{tt}	0.23	0.25	0.24	0.25	equation (78)	F
38	Froude number evaluated using NP_{conc}	Fr_{bv}	0.2	0.2	0.2	0.2	equation (78)	F
39	Liquid only Reynolds number	Re_{fo}	5149	3891	3718	3898	equation (77)	S
40	Turbulent layer Reynolds number	Re_b	10417	7611	6331	6432	equation (43)	HTC_{cht}
41	Turbulent layer Prandtl number	Pr_b	2.4	3.2	1.5	1.7	equation (43)	HTC_{cht}
42	Laminar sublayer Prandtl number	Pr_v	2.3	2.9	2.9	2.9	equation (43)	HTC_{cht}
43	friction factor	f	0.031	0.033	0.034	0.033	equation (38), (66)	HTC_{cht}
44	dimensionless laminar sublayer thickness	δ_v^+	16.1	15.5	15.4	15.5	equation (43)	HTC_{cht}
45	Nusselt number	Nu_b	49	43	17	19	equation (43) and (44)	HTC_{cht}

#	Variables		R410A	R410A- POE	R410A- ZnO NL	R410A- Al2O3 NL	Reference Equation	Used to estimate
46	Suppression factor	S	0.72	0.50	0.70	0.67	equation (77)	
47	Two-phase convective multiplier	F	4.41	11.63	6.29	6.64	equation (78)	
48	Nucleate boiling heat transfer coefficient	HTC_{nb} [kW/m ² -K]	2.01	0.35	0.52	0.49	equation (75)	
49	Convective heat transfer coefficient	HTC_{cht} [kW/m ² -K]	0.51	0.46	0.43	0.44	equation (44)	
50	Predicted heat transfer coefficient	HTC_p [kW/m ² -K]	3.70	5.46	3.08	3.25	equation (76)	
51	Experimental heat transfer coefficient	HTC_{exp} [kW/m ² -K]	3.87	5.58	3.28	3.91		

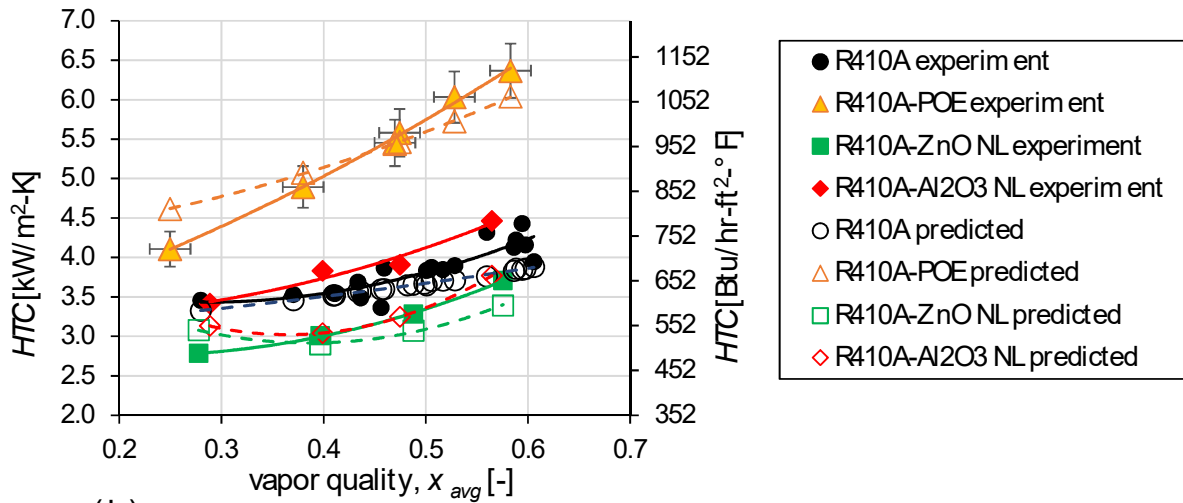
5.4.11 Prediction of Superposition model for saturated flow boiling

With the new superposition model the HTC of 145 data tests were predicted by equation (76) within $\pm 25\%$ as shown in Figure 51 (a). (The data of 149 experimental two-phase flow boiling tests are provided in Appendix-H.) Figure 51 (b) shows the experimental and predicted HTC for tests at $165 \text{ kg/m}^2\text{-s}$, the predicted model results followed the experimental data trends. Figure 52, Figure 53, Figure 54, and Figure 55 shows the experimental and predicted HTC for flow boiling tests of R410A, R410A-POE, R410A-ZnO NL, and R410A-Al₂O₃ NL, respectively. The experimental data of R410A-Al₂O₃ NL mixture was not captured well by the model and had a deviation in the prediction above $+25\%$. The mean absolute deviation of the predicted HTC from experimental data were 6.7% for R410A, 5.9% for R410A-POE mixture, 9.2% for R410A-ZnO NL mixture, and 16.8% for R410A-Al₂O₃ NL mixture.

The experimental results of HTC_{exp} in Figure 52, Figure 53, Figure 54, and Figure 55 are provided in Appendix-C. The sample calculation of experimental HTC_{exp} for R410A test at $x_{avg}=0.37$ and $\dot{m}=165 \text{ kg/m}^2\text{-s}$ is provided in Appendix-E, and sample calculations of experimental HTC_{exp} for R410A, R410A-POE, R410A-ZnO NL, and R410A-Al₂O₃ NL mixtures test at $x_{avg}=0.5$ and $\dot{m}=165 \text{ kg/m}^2\text{-s}$ are provided in Table 2 to Table 5.



(a)



(b)

Figure 51: (a) Superposition model HTC prediction deviation of all in-tube flow boiling experimental data of R410A, R410A-POE, R410A-ZnO NL, and R410A-AL2O3 NL mixtures, and (b) Experimental and predicted HTC of tests at $165 \text{ kg/m}^2\text{-s}$.

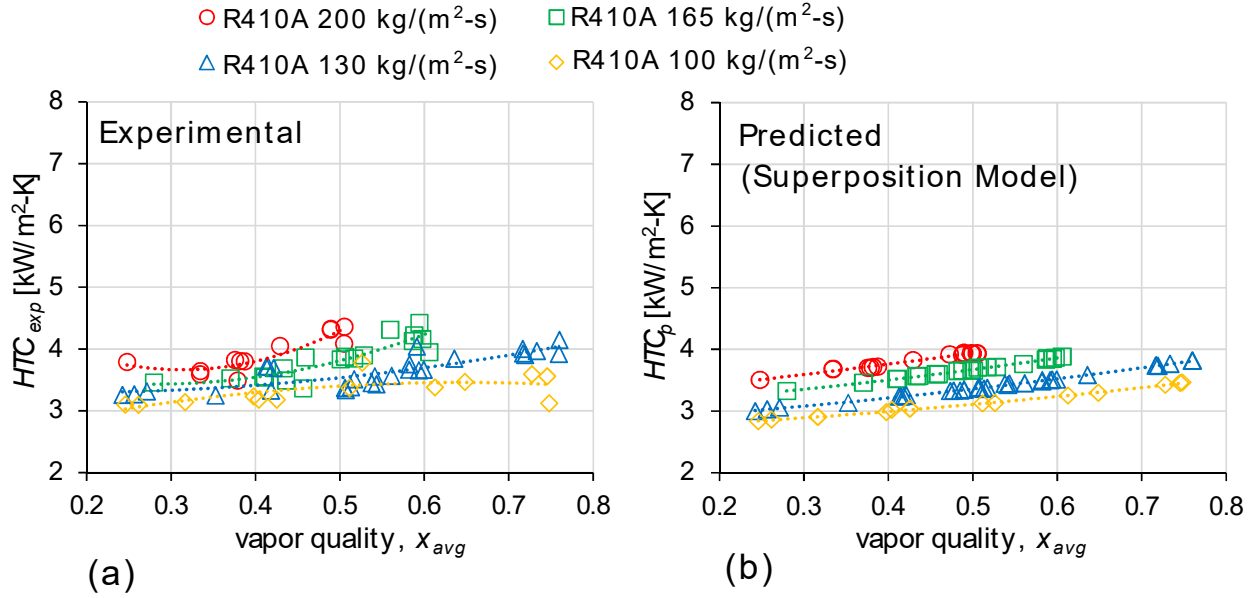


Figure 52: (a) Experimental and (b) predicted HTC of R410A flow boiling tests.

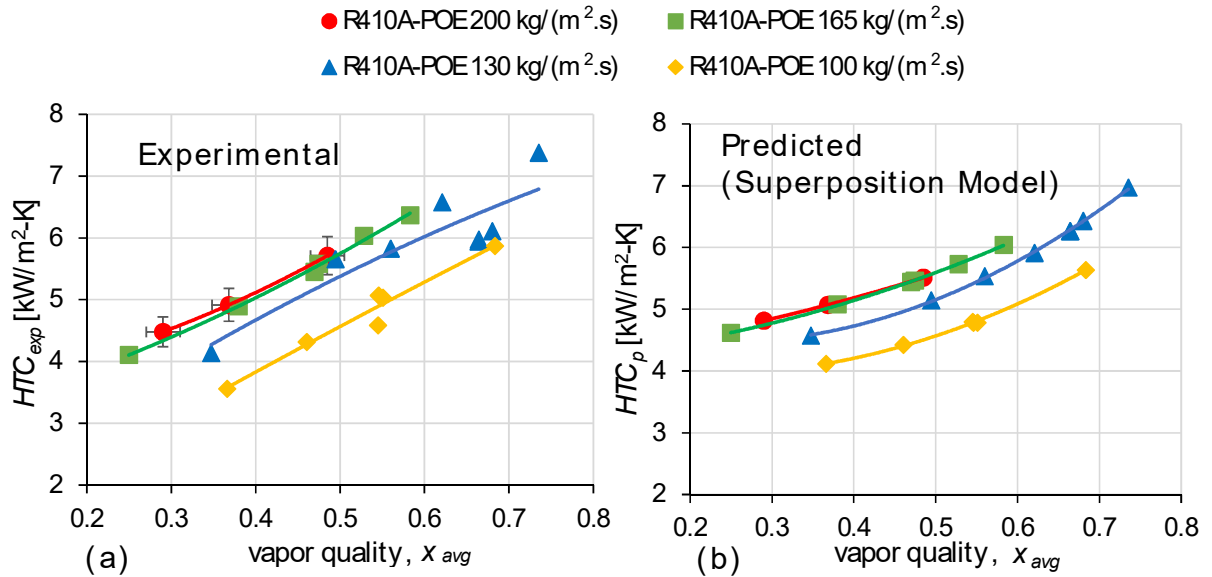


Figure 53: (a) Experimental and (b) predicted HTC of R410A-POE flow boiling tests.

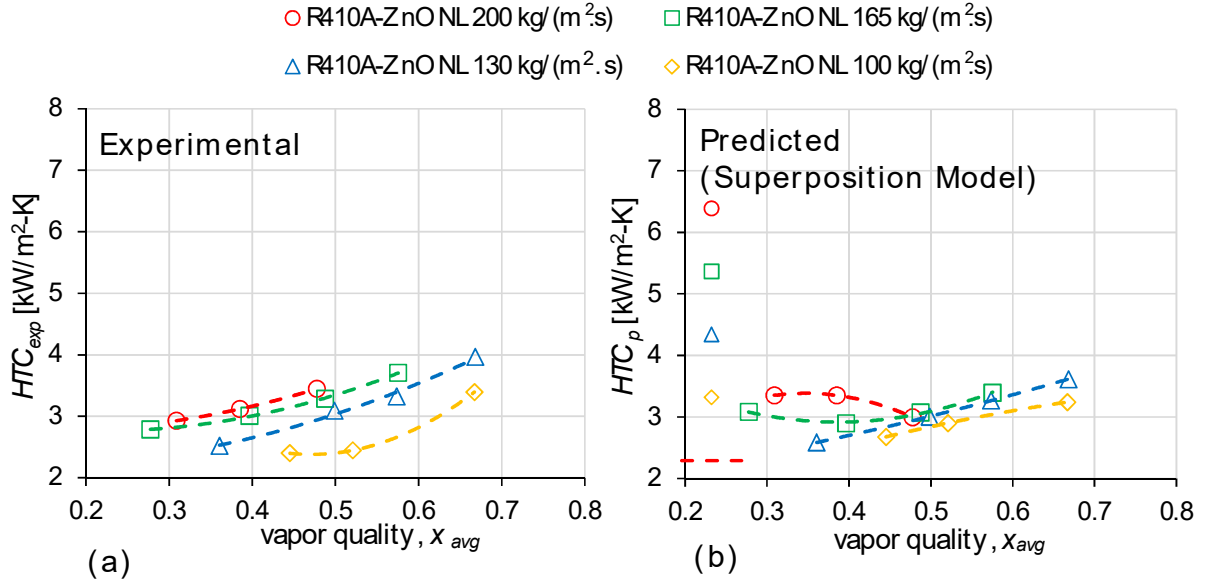


Figure 54: (a) Experimental and (b) predicted HTC of R410A-ZnO NL flow boiling tests.

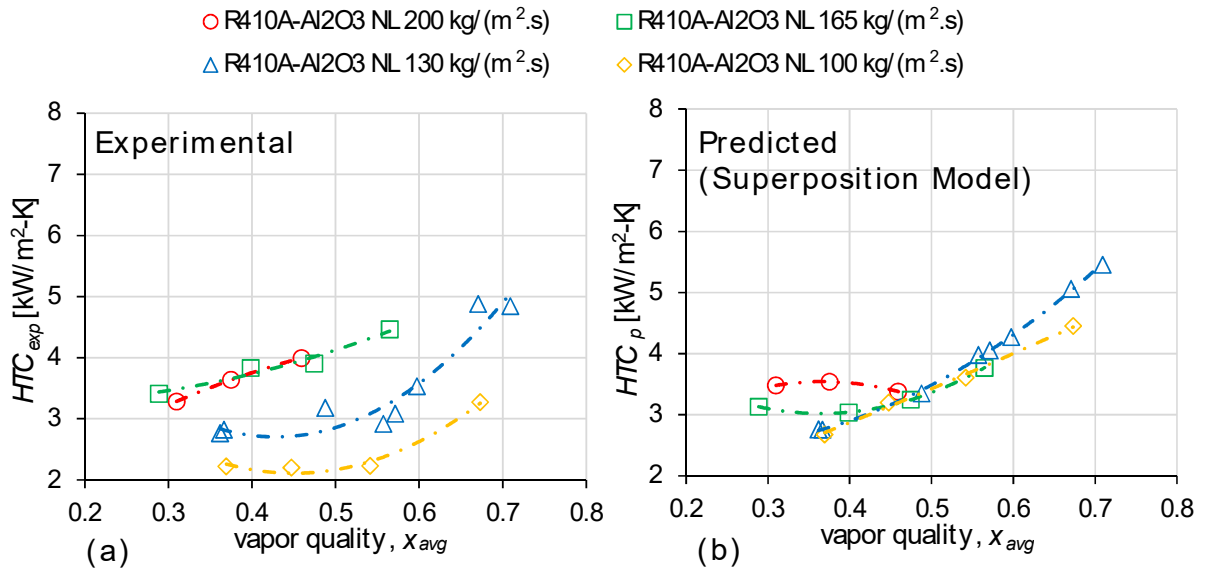


Figure 55: (a) Experimental and (b) predicted HTC of R410A-Al₂O₃ NL flow boiling tests.

Figure 56 shows HTC on y-axis and nanoparticle concentration ratio, $NP_{conc,v}/NP_{conc}$, on x-axis. The $NP_{conc,v} = \frac{m_{np}}{m_{np}+m_{oil}+m_{ref}}$ was the nanoparticle mass concentration in the refrigerant-lubricant mixture in the laminar sublayer, while $NP_{conc} = \frac{m_{np}}{m_{np}+m_{oil}}$ was the nanoparticle mass

concentration in POE oil and was constant at 20 wt.%. $NP_{conc}=20$ wt.% represented the nanoparticle mass concentration in POE, when the nanolubricant was introduced inside the test apparatus. Figure shows the predictions of HTC_p with a new superposition model, equation (76), for R410A-ZnO NL mixture at a mass flux of $165 \text{ kg/m}^2\text{-s}$ and at low, medium, and high refrigerant vapor qualities, when the nanoparticle mass concentration in the laminar sublayer, $NP_{conc,v}$, was increased. The red-solid circles were the experimental measured HTC for R410A-ZnO NL mixture, and the yellow-dashed line were the experimental measured HTC for R410A-POE mixture. The blue dotted lines, dashed-dot lines, and blue continuous lines represent the microconvective $S \cdot HTC_{nb}$, macroconvective $F \cdot HTC_{cht}$, and total HTC_p predictions, respectively.

The experimental tests shown by the red-solid circles in Figure 56, showed the HTC and $NP_{conc,v}$ increased with an increase in the vapor quality. The Figure 56 also shows the macroconvective heat transfer mechanism was dominant than the microconvective heat transfer mechanism. At refrigerant vapor qualities of $x=0.2$, $x=0.5$, and $x=0.72$, the corresponding $NP_{conc,v}/NP_{conc}$ ratios were 0.0001, 0.0002, and 0.0011, respectively. As the $NP_{conc,v}$ increased near the wall of the tube, the macroconvective heat transfer decreased as the laminar sublayer thickness increased, as predicted by the Buongiorno model, while the microconvective heat transfer or nucleate boiling heat transfer increased as more nanoparticles transferred momentum to the growing bubbles, as the predicted by the Kedzierski model.

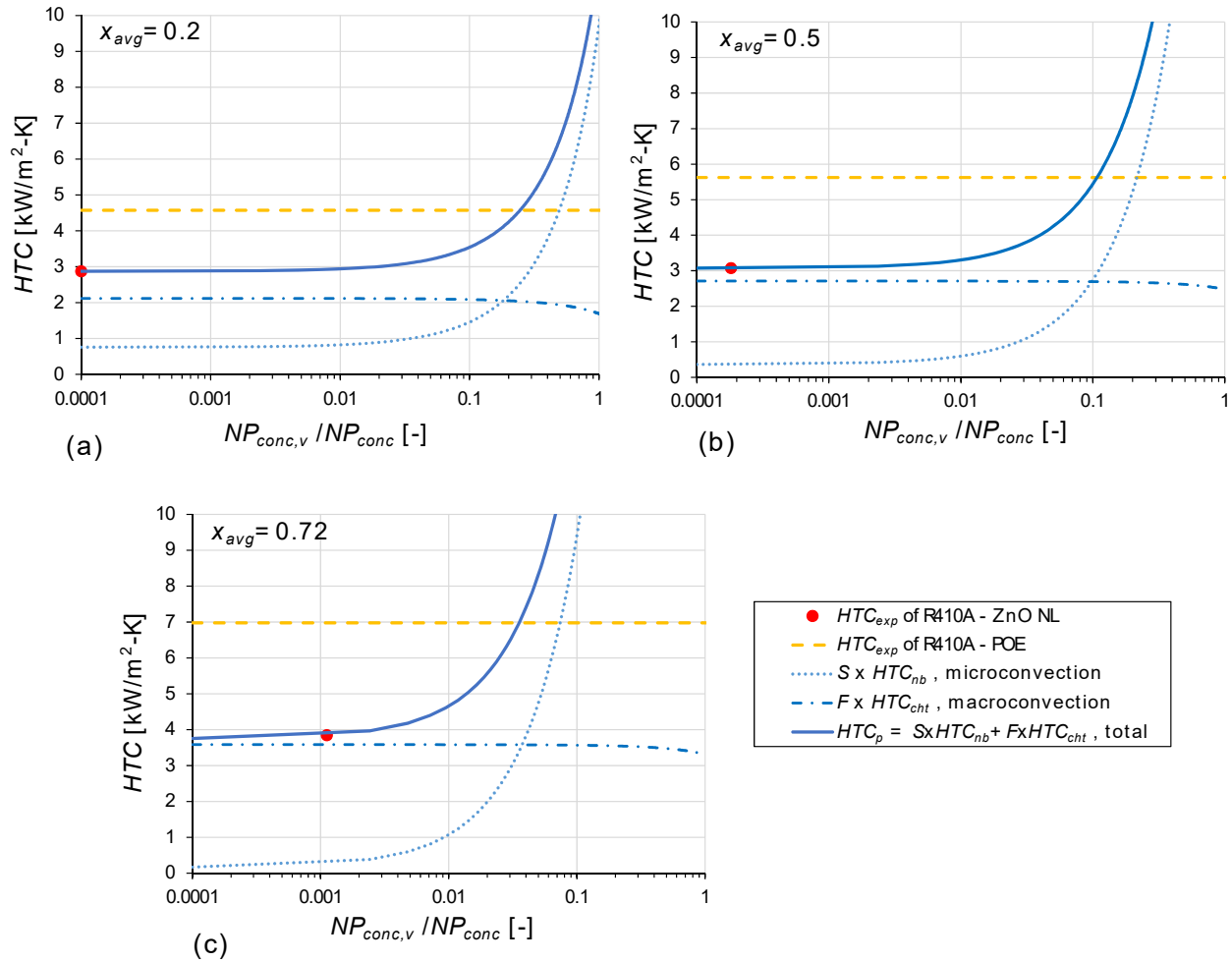


Figure 56: Superposition model HTC prediction of R410A-ZnO NL mixture at $\dot{m}=165 \text{ kg/m}^2\text{-s}$ and at refrigerant vapor qualities of (a) $x_{avg}=0.2$, (b) $x_{avg}=0.5$, and (c) $x_{avg}=0.72$, at different nanoparticle mass concentration in the laminar sublayer ($NP_{conc}=20 \text{ wt.}\%$).

Figure 56 showed that the nanoparticle mass concentration in the laminar sublayer, $NP_{conc,v}$, had to be increased, much higher than the concentration during the experimental tests, for the microconvective mechanism to be same or higher than the macroconvective mechanism due to improvement in nucleate boiling performance. As the $NP_{conc,v}$ increased, the observed rate of increase of microconvective mechanism was much higher than macroconvective mechanism. At refrigerant vapor qualities of $x=0.2$, $x=0.5$, and $x=0.72$, the predicted HTC_p of R410A-ZnO NL mixture, shown by the blue continuous line, was higher than the HTC of R410A-POE mixture,

shown by the yellow dashed line, when the $NP_{conc,v}/NP_{conc}$ ratio were increased to 0.25, 0.1, and 0.035, respectively.

Figure 57 shows superposition model's HTC_p predictions, evaluated using equation (76), for different relative roughness, ε/D_h , of the inner tube surface, at refrigerant vapor quality of $x=0.5$ and at the mass flux of $165 \text{ kg/m}^2 \cdot \text{s}$ for R410A-ZnO NL mixture. In Figure 57, the red-solid circle was the experimentally measured HTC for R410A-ZnO NL mixture, and the yellow-solid triangle was the experimentally measured HTC for R410A-POE mixture. The smooth tube relative roughness was 0.000157 as per manufacturer's data. In Figure 57, the blue dotted lines, dashed-dot lines, and continuous blue lines represent the microconvective $S \cdot HTC_{nb}$, macroconvective $F \cdot HTC_{cht}$, and total HTC_p predictions, respectively, for R410A-ZnO NL mixture when the relative roughness was increased. The figure showed that as the relative roughness was increased, the macroconvective and the total HTC_p was increased. The macroconvective heat transfer mechanism was dominant than the microconvective heat transfer mechanism, and the relative roughness had a negligible effect on the microconvective heat transfer. The increase in the macroconvective mechanism caused the total HTC_p to increase with the increase in the tube roughness. The relative roughness, ε/D_h , had to increase above 600% for the HTC_p of R410A-ZnO NL mixture to be higher than the HTC of R410A-POE mixture. The corresponding increase in the friction factor, Colebrook equation, was +3.4% and the corresponding decrease in the laminar sublayer thickness, evaluated using equation (66), was -2.7%. The combination of increase in the friction factor and decrease of the laminar sublayer thickness caused the increase of the macroconvective heat transfer and the total predicted HTC_p .

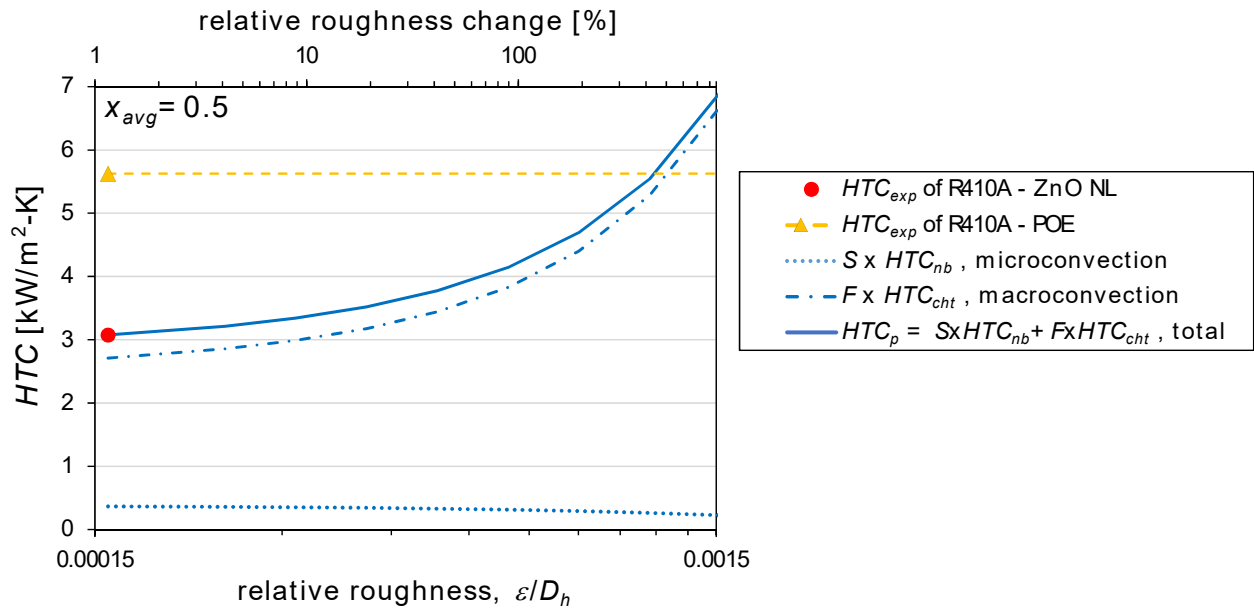


Figure 57: Superposition model HTC prediction of R410A-ZnO NL mixture at different relative roughness of the tube ($\dot{q}=15 \text{ kW/m}^2$, $\dot{m}=165 \text{ kg/m}^2\text{-s}$, and $x=0.5$)

6. Conclusions

In air conditioning systems, lubricating oil leaves the compressor and circulates through the other components. This lubricant acts as a contaminant affecting heat transfer and pressure losses in the heat exchangers. The literature indicated that mixtures of refrigerants and nanolubricants, that is, nanoparticles dispersed in the lubricant oils, have potentials to augment heat transfer exchange effectiveness in the evaporators and condensers.

This PhD work theoretically and experimentally investigated the effects of nanoparticles on the refrigerant R410A and POE mixture heat transfer. ZnO nanoparticles and Al₂O₃ nanoparticles in the R410A-lubricant mixture penalized the two-phase flow boiling heat transfer coefficient in the smooth tubes. To quantify enhancements or degradations in heat transfer coefficient and in pressure drop, ad-hoc figures of merit were defined as the heat transfer factor (*HTF*), and the pressure drop factor (*PDF*). The *HTF* of R410A-nanolubricant mixtures decreased by about 20% with respect to that of the R410A at vapor qualities below 0.6. The *HTF* was decreased by about 50% to 70% for ZnO NL and 30% to 70% for Al₂O₃ NL with respect to that of the R410A-POE mixture. R410A-Al₂O₃ NL tests had an average of 15% higher *HTF* than R410A-ZnO NL tests at vapor quality of 0.5 and mass fluxes above 165 kg/m²-s. Noticeable changes in the *HTFs* and *PDFs* were observed when the flow regime transitioned from stratified-wavy to annular flow. At mass fluxes above 130 kg/m²-s, the R410A-ZnO NL and R410A-Al₂O₃ mixtures followed the same trend as that of R410A-POE regarding the rate of change of *HTF*. At mass fluxes of 130 kg/m²-s and below, the rate of increase of *HTF* intensified as the flow

transitioned from stratified-wavy to annular flow pattern type.

Experiments also showed that long-term flow boiling testing of R410A-nanolubricant mixtures resulted in a continuous and gradual increase of the heat transfer coefficient. A possible explanation was that the nanoparticle deposition on the tube inner wall and its near wall interaction led to small but incremental enhancements in the nucleate boiling phenomena.

In wavy-stratified flow and at mass flux of $165 \text{ kg/m}^2\text{-s}$, even though R410A-nanolubricant mixtures had 19% higher dynamic viscosity than R410A-POE, the R410A-ZnO NL had more than 20% lower pressure drops than R410A-POE, while the R410A-Al₂O₃ NL had more than 15% lower pressure drops than R410A-POE. For annular-type flow and high mass flux tests, the pressure drops of R410A-lubricant with and without the nanoparticles were basically the same. Nanoparticle displacement closer to the inner wall occurred in annular flow at high vapor quality and it increased the frictional pressure drop, causing the *PDF* to increase with the increase in vapor quality. The pressure drop results also suggested that non-spherical ZnO nanoparticles had more wall shear stress than the spherical Al₂O₃ nanoparticles. However, at mass fluxes of $165 \text{ kg/m}^2\text{-s}$ and above, the nanoparticle shape had a non-measurable effect on wall shear stress and on the resulting pressure drop.

The ZnO nanoparticles slip mechanism in R410A-POE liquid mixture were theoretically investigated. Like spherical Al₂O₃ nanoparticles, the non-spherical ZnO nanoparticles also had Brownian motion and thermophoresis as dominant mechanisms. However, the non-spherical ZnO nanoparticles diffused slowly under Brownian motion; hence under same flow boundary conditions the ZnO average nanoparticle concentration in laminar sublayer was lower than the Al₂O₃ average nanoparticle concentration in laminar sublayer.

Buongiorno (2006) model was modified to consider nanoparticle mass balance within the

laminar sublayer and turbulent layer. The new modified model showed that the change in the suspended nanoparticle concentration in laminar sublayer and turbulent layer had a significant effect on the single-phase convective heat transfer. The change of the nanoparticle aspect ratio, the increase in nanoparticle size due to agglomeration, or the increase in tube roughness with nanoparticle deposition had less effect on the single-phase convective heat transfer. The model was successful in predicting the trend of the experimental single-phase convective HTC for R410A-Al₂O₃ NL and R410A-ZnO NL mixtures. The model was validated and thus can be used to evaluate the convective heat transfer component of the two-phase flow boiling of refrigerant-nanolubricant mixtures.

The modeling efforts of the present PhD research consisted in several upgrades of Bigi's (2018) superposition model. The mass conservation of nanoparticles during migration from the laminar sublayer near the wall to the adjacent turbulent layer near the gas core was implemented. The newly developed model also introduced the influence of nanoparticle concentration on the two-phase convective multiplier, F . The superposition model was developed by modifying and integrating a convective heat transfer model originally developed for nanofluids and a pool boiling model for nanolubricants. The new superposition model was more comprehensive because it accounted for the nanoparticle mass balance in the annular film, for the nanoparticle distribution due to slip velocities between the nanoparticles and the base fluid, for the transfer of momentum from the nanoparticles to the bubbles, and the laminar sublayer thickness dependency on the heat transfer.

The model accounted for the effect of increased laminar sublayer thickness and reduced thermal conductivity in laminar sublayer due to diffusion of nanoparticles towards the turbulent layer. These phenomena were responsible for the observed two-phase flow boiling heat transfer

coefficient degradation when using the present R410A-nanolubricant mixtures. However, if the nanoparticles were constrained in the laminar sublayer and near the wall of the tube, the predicted heat transfer coefficients from the simulations were higher than that of R410A- POE mixture. The analysis of this case revealed that the nucleate boiling contribution was significantly augmented for such scenario.

Experimental heat transfer data of saturated two-phase flow boiling of R410A with two nanolubricants in a smooth copper tube were used to validate the new superposition model. The model results followed the experimental data trends and had predicted mean absolute deviations less than 17%.

7. Recommendations for Future Work

The new superposition model developed in this work used limited experimental test data of two-phase flow heat transfer coefficient of R410A with two nanolubricants. The heat transfer performance of tests at high vapor qualities was not recorded because of test apparatus limitation to achieve such conditions. Also, the tests were conducted at one saturated pressure and one heat flux. It is suggested that flow boiling of R410A be recorded at high vapor qualities, and at different saturated pressures and heat fluxes. A comprehensive data covering a wide range of test conditions would be beneficial to revise the superposition model.

Kedzierski and Kaul (1998) observed a flow-boiling enhancement of R134a-POE oil mixtures and attributed it to the increase in the nucleate site density in the presence of lubricant excess layer. However, the possibility of increased nucleate site density in the presence of R410A-POE mixture needs future investigation because of the absence of observation in the current work and absence of the experimental data in the literature. In current work, the refrigerant vapor bubbles in the sight glass tube were formed during the boiling process that occurred in the test section tube. These bubbles further traveled downstream of the test section, possibly coalescing together while in the flow, before they were viewed and recorded at the sight glass tube. A special manufactured ITO (Indium Tin Oxide) coated transparent sight tube could help in the application of uniform heat flux at the sight tube and observe the formation of bubbles in the presence of lubricant excess layer during flow boiling of R410A-POE and R410A-nanolubricant mixtures.

The two-phase flow boiling of R410A refrigerant with Al₂O₃ based refrigerant-

nanolubricant mixtures in horizontal micro-fin tubes had shown enhancements in the *HTC* compared to the refrigerant-lubricant mixture in author's previous work (Cremaschi et al. 2017; Deokar et al. 2016). Based on the findings of the current work, the possibility of enhancement in micro-fin tubes could be due to the presence of thin laminar sublayer thickness at the tip of the fin, due to Gregorig effect, and higher nanoparticle concentration in the lubricant excess layer within the channels in-between the fins. Both effects could bring enhancement in heat transfer by improving the convection heat transfer at the tip of the fin and improving the pool boiling heat transfer at the bottom of the fins. Future investigation is needed to verify the above hypothesis. It is impossible to view and measure the thickness of the thin laminar sublayer thickness at the top of the fin due to curvature of the circular sight glass tube and the nearness in the refractive index of refrigerant and completely miscible refrigerant-lubricant mixture. However, modeling will help to estimate the thickness of the laminar sublayer thickness at the tip and in the channels of the fins. An ITO (Indium Tin Oxide) coated transparent sight tube with internal fins, and a high-resolution camera focused in-between and bottom of fins, could help to verify the improvement in the nucleation site density in the presence of high nanoparticle concentration.

The pressure drop results of the current work suggested that non-spherical nanoparticles had more wall shear stress than the spherical nanoparticles. However, at higher mass fluxes the nanoparticle shape had a non-measurable effect on wall shear stress and the resulting frictional pressure drop. Numerical simulations by Yuan et al. (2018) have shown elongated nanoparticles have random motion in the turbulent bulk flow and orient their long axis along the flow direction near the wall, but did not explain the reason for the increase in the friction factor for non-spherical nanoparticles. Detailed simulation work is needed to understand the difference a nanoparticle aspect ratio can have on two-phase friction factor at different mass fluxes and flow regimes.

References

- Abedini, E., A. Behzadmehr, S. M. H. Sarvari, and S. H. Mansouri. 2013. Numerical investigation of subcooled flow boiling of a nanofluid. *International Journal of Thermal Sciences*, 64:232–239.
- Abedini, E., T. Zarei, M. Afrand, and S. Wongwises. 2017. Experimental study of transition flow from single phase to two phase flow boiling in nanofluids. *Journal of Molecular Liquids*, 231:11–19.
- Ahuja, A. S. 1975. Augmentation of heat transport in laminar flow of polystyrene suspensions. I. Experiments and results. *Journal of Applied Physics*, 46(8):3408–3416.
- Alawi, O. A., N. A. C. Sidik, and A. S. Kherbeet. 2015. Measurements and correlations of frictional pressure drop of TiO₂/R123 flow boiling inside a horizontal smooth tube. *International Communications in Heat and Mass Transfer*, 61:42–48.
- Alvariño, P. F., J. M. S. Jabardo, A. Arce, and M. I. L. Galdo. 2013. A numerical investigation of laminar flow of a water/alumina nanofluid. *International Journal of Heat and Mass Transfer*, 59:423–432.
- Bang, I. C., and J. H. Kim. 2010. Thermal-Fluid Characterizations of ZnO and SiC Nanofluids for Advanced Nuclear Power Plants. *Nuclear Technology*, 170(1):16–27.
- Baqeri, S., M. A. Akhavan-Behabadi, and B. Ghadimi. 2014. Experimental investigation of the forced convective boiling heat transfer of R-600a/oil/nanoparticle. *International Communications in Heat and Mass Transfer*, 55:71–76.
- Bartelt, K., L. Liu, and A. Jacobi. 2008. Flow-Boiling of R-134a/POE/CuO Nanofluids in a Horizontal Tube (Vol. Paper 928). Presented at the International Refrigeration and Air Conditioning Conference, Purdue University.
- Bennett, D. L., and J. C. Chen. 1980. Forced convective boiling in vertical tubes for saturated pure components and binary mixtures. *AIChE Journal*, 26(3):454–461.
- Bi, S., K. Guo, Z. Liu, and J. Wu. 2011. Performance of a domestic refrigerator using TiO₂-R600a nano-refrigerant as working fluid. *Energy Conversion and Management*, 52(1):733–737.
- Bi, S., L. Shi, and L. Zhang. 2008. Application of nanoparticles in domestic refrigerators. *Applied Thermal Engineering*, 28(14):1834–1843.

- Bigi, A. A. M. 2018. *Investigation of Al₂O₃ nanoparticle laden lubricants and refrigerant mixtures during two-phase flow boiling*. (Dissertation). Auburn University, AL, USA.
- Bigi, A. A. M., and L. Cremaschi. 2019. Theoretical Investigation of Al₂O₃ Nanoparticle Slip Mechanisms in High-Viscosity Two-Component Mixture in Two-Phase Flow. *Journal of Heat Transfer*.
- Bigi, A. A. M., L. Cremaschi, and P. Deokar. 2017. Nanolubricants flow boiling heat transfer enhancement in a microfin tube evaporator—IRG0021. *Science and Technology for the Built Environment*, 23(6):960–969.
- Bigi, A. A. M., T. Wong, P. Deokar, and L. Cremaschi. 2015. Experimental Investigation on Heat Transfer and Thermophysical Properties of Mixtures of Al₂O₃ Nanolubricants and Refrigerant R410A. *ASHRAE Transactions*, 121:1G.
- Buongiorno, J. 2006. Convective Transport in Nanofluids. *Journal of Heat Transfer*, 128(3):240–250.
- Cavestri, R. C., and W. R. Schafer. 2000. Measurement of solubility, viscosity, and density of R-410A refrigerant/lubricant mixtures. Research Org.: Imagination Resources, Inc., Dublin, OH (US); American Society of Heating, Refrigerating and Air-Conditioning Engineers, Inc., Atlanta, GA (US).
- Chen, J. C. 1966. Correlation for Boiling Heat Transfer to Saturated Fluids in Convective Flow. *Industrial & Engineering Chemistry Process Design and Development*, 5(3):322–329.
- Chen, John C. 1966. Correlation for boiling heat transfer to saturated fluids in convective flow. *Industrial & Engineering Chemistry Process Design and Development*, 5(3):322–329.
- Chen, W., and X. Fang. 2014. A note on the Chen correlation of saturated flow boiling heat transfer. *International Journal of Refrigeration*, 48:100–104.
- Choi, J., M. Kedzierski, and P. Domanski. 2001. Generalized Pressure Drop Correlation for Evaporation and Condensation in Smooth and Micro-Fin Tubes. *International Institute of Refrigeration*.
- Choi, S. U., and J. A. Eastman. 1995. *Enhancing thermal conductivity of fluids with nanoparticles*. Argonne National Lab., IL (United States).
- Chriss, T. M., and D. R. Caldwell. 1984. Universal similarity and the thickness of the viscous sublayer at the ocean floor. *Journal of Geophysical Research: Oceans*, 89(C4):6403–6414.
- Cieśliński, J. T., and T. Z. Kaczmarczyk. 2015. Pool Boiling of Water–Al₂O₃ and Water–Cu Nanofluids Outside Porous Coated Tubes. *Heat Transfer Engineering*, 36(6):553–563.
- Ciloglu, D., and A. Bolukbasi. 2015. A comprehensive review on pool boiling of nanofluids. *Applied Thermal Engineering*, 84(Supplement C):45–63.

- CreMASchi, L. 2012. A Fundamental View of the Flow Boiling Heat Transfer Characteristics of Nano-Refrigerants (Vol. 7: Fluids and Heat Transfer, Parts A, B, C, and D, pp. 2779–2792). Presented at the ASME 2012 International Mechanical Engineering Congress and Exposition.
- CreMASchi, L., A. A. M. Bigi, T. Wong, and P. Deokar. 2015. Thermodynamic properties of Al₂O₃ nanolubricants: Part 1—Effects on the two-phase pressure drop. *Science and Technology for the Built Environment*, 21(5):607–620.
- CreMASchi, L., P. S. Deokar, and A. A. M. Bigi. 2017. Two phase flow boiling heat transfer coefficient and pressure drop of refrigerant and γ -Al₂O₃ based nanolubricant mixtures in a 9.5 mm smooth tube. In *Proceedings of the 2nd Thermal and Fluid Engineering Conference, TFEC2017, and 4th International Workshop on Heat Transfer, IWHT2017*. ASTFE.
- CreMASchi, L., Y. Hwang, and R. Radermacher. 2005. Experimental investigation of oil retention in air conditioning systems. *International Journal of Refrigeration*, 28(7):1018–1028.
- Deokar, P., L. CreMASchi, T. Wong, and Criscuolo, Gennaro. 2016. Effect of Nanoparticles Aspect Ratio on the Two Phase Flow Boiling Heat Transfer Coefficient and Pressure Drop of Refrigerant and Nanolubricants Mixtures in a 9.5 mm Micro-fin Tube (p. Paper No. 2098). Presented at the 16th International Refrigeration and Air Conditioning Conference at Purdue, West Lafayette, IN (USA): Purdue University.
- Ding, G., H. Peng, W. Jiang, and Y. Gao. 2009. The migration characteristics of nanoparticles in the pool boiling process of nanorefrigerant and nanorefrigerant–oil mixture. *International Journal of Refrigeration*, 32(1):114–123.
- Ding, Y., H. Chen, L. Wang, C.-Y. Yang, Y. He, W. Yang, W. P. Lee, L. Zhang, and R. Huo. 2007a. Heat Transfer Intensification Using Nanofluids. *KONA Powder and Particle Journal*, 25:23–38.
- Ding, Y., H. Chen, L. Wang, C.-Y. Yang, Y. He, W. Yang, W. P. Lee, L. Zhang, and R. Huo. 2007b. Heat Transfer Intensification Using Nanofluids. *KONA Powder and Particle Journal*, 25:23–38.
- Erdemir, A. 2013. *Large-scale Manufacturing of Nanoparticulate-Based Lubrication Additives for Improved Energy Efficiency and Reduced Emissions-Final Report* (No. No. ANL/ESD-13/6). Argonne National Lab.(ANL), Argonne, IL (United States).
- Fang, X., Y. Chen, H. Zhang, W. Chen, A. Dong, and R. Wang. 2016. Heat transfer and critical heat flux of nanofluid boiling: A comprehensive review. *Renewable and Sustainable Energy Reviews*, 62(Supplement C):924–940.
- Fang, X., R. Wang, W. Chen, H. Zhang, and C. Ma. 2015. A review of flow boiling heat transfer of nanofluids. *Applied Thermal Engineering*, 91(Supplement C):1003–1017.

- Faulkner, D., M. Khotan, and R. Shekarriz. 2003. Practical design of a 1000 W/cm² cooling system [high power electronics]. In *Nineteenth Annual IEEE Semiconductor Thermal Measurement and Management Symposium, 2003*. (pp. 223–230).
- Friedel, L. 1979. Improved friction pressure drop correlation for horizontal and vertical two-phase pipe flow. *Proc. of European Two-Phase Flow Group Meet., Ispra, Italy, 1979*.
- Gnielinski, V. 1976. New equations for heat and mass-transfer in turbulent pipe and channel flow. *International Chemical Engineering*, 16(2):359–368.
- Gungor, K. E., and R. H. S. Winterton. 1987. Simplified general correlation for saturated flow boiling and comparison of correlations with data. *Chemical Engineering Research and Design*, 65:148–156.
- Haramura, Y., and Y. Katto. 1983. *A new hydrodynamic model of critical heat flux, applicable widely to both pool and forced convection boiling on submerged bodies in saturated liquids* (Vol. 26).
- Henderson, K., Y.-G. Park, L. Liu, and A. M. Jacobi. 2010. Flow-boiling heat transfer of R-134a-based nanofluids in a horizontal tube. *International Journal of Heat and Mass Transfer*, 53(5):944–951.
- Hewitt, G. F., and N. S. Hall-Taylor. 1970. CHAPTER 4 - Simple Analytical Models of Annular Two-Phase Flow and their Applications. In *Annular Two-phase Flow* (pp. 50–75). Amsterdam: Pergamon.
- Hsu, Y. Y. 1962. On the Size Range of Active Nucleation Cavities on a Heating Surface. *Journal of Heat Transfer*, 84(3):207–213.
- Hu, Hai-tao, G. Ding, X. Huang, B. Deng, and Y. Gao. 2009. Pressure drop during horizontal flow boiling of R410A/oil mixture in 5mm and 3mm smooth tubes. *Applied Thermal Engineering*, 29(16):3353–3365.
- Hu, Haitao, G. Ding, and K. Wang. 2008. Heat transfer characteristics of R410A–oil mixture flow boiling inside a 7mm straight microfin tube. *International Journal of Refrigeration*, 31(6):1081–1093.
- Hu, Haitao, G. Ding, W. Wei, Z. Wang, and K. Wang. 2008. Heat transfer characteristics of R410A-oil mixture flow boiling inside a 7mm straight smooth tube. *Experimental Thermal and Fluid Science*, 32(3):857–869.
- Jung, S., and H. Kim. 2014. An experimental method to simultaneously measure the dynamics and heat transfer associated with a single bubble during nucleate boiling on a horizontal surface. *International Journal of Heat and Mass Transfer*, 73(Supplement C):365–375.
- Kamatchi, R., S. Venkatachalapathy, and N. Chandrasekaran. 2015. *Experimental investigation and mechanism of critical heat flux enhancement in pool boiling heat transfer with nanofluids* (Vol. 52).

- Kandlikar, S. G. 1990. A general correlation for saturated two-phase flow boiling heat transfer inside horizontal and vertical tubes. *Journal of Heat Transfer*, 112(1):219–228.
- Kathiravan, R., R. Kumar, A. Gupta, and R. Chandra. 2009. Characterization and Pool Boiling Heat Transfer Studies of Nanofluids. *Journal of Heat Transfer*, 131(8):081902–081902–8.
- Kattan, N., J. R. Thome, and D. Favrat. 1998. Flow Boiling in Horizontal Tubes: Part 3—Development of a New Heat Transfer Model Based on Flow Pattern. *Journal of Heat Transfer*, 120(1):156–165.
- Kattan, Nakhlé, J. R. Thome, and D. Favrat. 1998. Flow boiling in horizontal tubes: part 3—development of a new heat transfer model based on flow pattern. *Journal of Heat Transfer*, 120(1):156–165.
- Kedzierski, M. A. 2003a. A semi-theoretical model for predicting refrigerant/lubricant mixture pool boiling heat transfer. *International Journal of Refrigeration*, 26(3):337–348.
- Kedzierski, M. A. 2003b. Improved thermal boundary layer parameter for semi-theoretical refrigerant/lubricant pool boiling model (Vol. ICR0504, pp. 1–8). Presented at the International Congress of Refrigeration, Washington, D.C.
- Kedzierski, M. A. 2011. Effect of Al₂O₃ nanolubricant on R134a pool boiling heat transfer. *International Journal of Refrigeration*, 34(2):498–508.
- Kedzierski, M. A. 2012. R134a/Al₂O₃ Nanolubricant Mixture Pool Boiling on a Rectangular Finned Surface. *Journal of Heat Transfer*, 134(12):121501–121501–8.
- Kedzierski, M. A. 2013. Nanofluids, heat-transfer equipment and plain-vanilla. *Journal of Enhanced Heat Transfer*, 20 (1):93–94.
- Kedzierski, M. A., R. Brignoli, K. T. Quine, and J. S. Brown. 2017. Viscosity, density, and thermal conductivity of aluminum oxide and zinc oxide nanolubricants. *International Journal of Refrigeration*, 74(Supplement C):3–11.
- Kedzierski, M. A., and M. Gong. 2009. Effect of CuO nanolubricant on R134a pool boiling heat transfer. *International Journal of Refrigeration*, 32(5):791–799.
- Kedzierski, M. A., and M. P. Kaul. 1998. Horizontal Nucleate Flow Boiling Heat Transfer Coefficient Measurements and Visual Observations for R12, R134a and R134a/Ester Lubricant Mixtures. *International Journal of Fluid Mechanics Research*, 25(1–3):386–399.
- Kim, H. D., and M. H. Kim. 2007. Effect of nanoparticle deposition on capillary wicking that influences the critical heat flux in nanofluids. *Applied Physics Letters*, 91(1):014104.
- Kim, S., I. C. Bang, J. Buongiorno, and L. Hu. 2006. Effects of nanoparticle deposition on surface wettability influencing boiling heat transfer in nanofluids. *Applied Physics Letters*, 89(15):153107.

- Kim, S. J., I. C. Bang, J. Buongiorno, and L. W. Hu. 2007. Surface wettability change during pool boiling of nanofluids and its effect on critical heat flux. *International Journal of Heat and Mass Transfer*, 50(19):4105–4116.
- Kim, S. J., T. McKrell, J. Buongiorno, and L. Hu. 2010. Subcooled flow boiling heat transfer of dilute alumina, zinc oxide, and diamond nanofluids at atmospheric pressure. *Nuclear Engineering and Design*, 240(5):1186–1194.
- Kumar, D. S., and R. Elansezhian. 2012. Experimental study on Al₂O₃-R134a nano refrigerant in refrigeration system. *International Journal of Modern Engineering Research*, 2(5):3927–3929.
- Kurul, N., and M. Z. Podowski. 1990. Multidimensional effects in forced convection subcooled boiling. Presented at the Proceedings of the Ninth International Heat Transfer Conference, Jerusalem, Israel.
- Li, D., B. Hong, W. Fang, Y. Guo, and R. Lin. 2010. Preparation of Well-Dispersed Silver Nanoparticles for Oil-Based Nanofluids. *Industrial & Engineering Chemistry Research*, 49(4):1697–1702.
- Li, X., Y. Yuan, and J. Tu. 2015. A theoretical model for nucleate boiling of nanofluids considering the nanoparticle Brownian motion in liquid microlayer. *International Journal of Heat and Mass Transfer*, 91(Supplement C):467–476.
- Lin, L., Z. Chang, and G. Ding. 2019. Resuspension of deposited nanoparticles during pool boiling. *International Journal of Heat and Mass Transfer*, 130:230–239.
- Lin, L., H. Peng, Z. Chang, and G. Ding. 2017. Experimental research on degradation of nanolubricant–refrigerant mixture during continuous alternation processes of condensation and evaporation. *International Journal of Refrigeration*, 76:97–108.
- Liu, D.-W., and C.-Y. Yang. 2007. Effect of Nano-Particles on Pool Boiling Heat Transfer of Refrigerant 141b, (4272X):789–793.
- Liu, K. V., U. S. Choi, and K. E. Kasza. 1988. *Measurements of pressure drop and heat transfer in turbulent pipe flows of particulate slurries*. United States.
- Lottin, O., P. Guillemet, and J.-M. Lebreton. 2003. Effects of synthetic oil in a compression refrigeration system using R410A. Part I: modelling of the whole system and analysis of its response to an increase in the amount of circulating oil. *International Journal of Refrigeration*, 26(7):772–782.
- Mahbubul, I. M., R. Saidur, and M. A. Amalina. 2013. Heat Transfer and Pressure Drop Characteristics of Al₂O₃-R141b Nanorefrigerant in Horizontal Smooth Circular Tube. *5th BSME International Conference on Thermal Engineering*, 56:323–329.

- Malvandi, A., S. A. Moshizi, E. G. Soltani, and D. D. Ganji. 2014. Modified Buongiorno's model for fully developed mixed convection flow of nanofluids in a vertical annular pipe. *Computers & Fluids*, 89:124–132.
- Meng, X. 2017. *Coupling of nanofluid flow, heat transfer and nanoparticles sedimentation using OpenFOAM*. City, University of London.
- Nikulin, A., O. Khliyeva, V. Zhelezny, Yu. Semenyuk, N. Lukianov, and A. L. N. Moreira. 2019. How does change of the bulk concentration affect the pool boiling of the refrigerant oil solutions and their mixtures with surfactant and nanoparticles? *International Journal of Heat and Mass Transfer*, 137:868–875.
- Nikulin, A., A. S. Moita, A. L. N. Moreira, S. M. S. Murshed, A. Huminic, Y. Grosu, A. Faik, J. Nieto-Maestre, and O. Khliyeva. 2019. Effect of Al₂O₃ nanoparticles on laminar, transient and turbulent flow of isopropyl alcohol. *International Journal of Heat and Mass Transfer*, 130:1032–1044.
- Patra, N., P. Ghosh, R. S. Singh, and A. Nayak. 2019. Flow visualization in dilute oxide based nanofluid boiling. *International Journal of Heat and Mass Transfer*, 135:331–344.
- Peng, H., G. Ding, and H. Hu. 2011. Effect of surfactant additives on nucleate pool boiling heat transfer of refrigerant-based nanofluid. *Experimental Thermal and Fluid Science*, 35(6):960–970.
- Peng, H., G. Ding, H. Hu, W. Jiang, D. Zhuang, and K. Wang. 2010. Nucleate pool boiling heat transfer characteristics of refrigerant/oil mixture with diamond nanoparticles. *International Journal of Refrigeration*, 33(2):347–358.
- Peng, H., G. Ding, W. Jiang, H. Hu, and Y. Gao. 2009a. Heat transfer characteristics of refrigerant-based nanofluid flow boiling inside a horizontal smooth tube. *International Journal of Refrigeration*, 32(6):1259–1270.
- Peng, H., G. Ding, W. Jiang, H. Hu, and Y. Gao. 2009b. Measurement and correlation of frictional pressure drop of refrigerant-based nanofluid flow boiling inside a horizontal smooth tube. *International Journal of Refrigeration*, 32(7):1756–1764.
- Phillips, R. J., R. C. Armstrong, R. A. Brown, A. L. Graham, and J. R. Abbott. 1992. A constitutive equation for concentrated suspensions that accounts for shear-induced particle migration. *Physics of Fluids A: Fluid Dynamics*, 4(1):30–40.
- Podowski, M. Z. 2012. Toward mechanistic modeling of boiling heat transfer. *Nuclear Engineering and Technology*, 44(8):889–896.
- Rana, K. B., G. D. Agrawal, J. Mathur, and U. Puli. 2014. Measurement of void fraction in flow boiling of ZnO–water nanofluids using image processing technique. *Nuclear Engineering and Design*, 270:217–226.

- Rana, K. B., A. K. Rajvanshi, and G. D. Agrawal. 2013. A visualization study of flow boiling heat transfer with nanofluids. *Journal of Visualization*, 16(2):133–143.
- Rouhani, S. Z., and E. Axelsson. 1970. Calculation of void volume fraction in the subcooled and quality boiling regions. *International Journal of Heat and Mass Transfer*, 13(2):383–393.
- Sanukrishna, S. S., M. Murukan, and P. M. Jose. 2018. An overview of experimental studies on nanorefrigerants: Recent research, development and applications. *International Journal of Refrigeration*, 88:552–577.
- Sarafraz, M. M., and F. Hormozi. 2014. Forced convective and nucleate flow boiling heat transfer to alumina nanofluids. *Periodica Polytechnica Chemical Engineering*, 58(1):37–46.
- Sarafraz, M. M., F. Hormozi, and M. Kamalgharibi. 2014. Sedimentation and convective boiling heat transfer of CuO-water/ethylene glycol nanofluids. *Heat and Mass Transfer*, 50(9):1237–1249.
- Sarafraz, M. M., F. Hormozi, M. Silakhori, and S. M. Peyghambarzadeh. 2016. On the fouling formation of functionalized and non-functionalized carbon nanotube nano-fluids under pool boiling condition. *Applied Thermal Engineering*, 95(Supplement C):433–444.
- Sarafraz, M. M., T. Kiani, and F. Hormozi. 2016. Critical heat flux and pool boiling heat transfer analysis of synthesized zirconia aqueous nano-fluids. *International Communications in Heat and Mass Transfer*, 70(Supplement C):75–83.
- Savithiri, S., A. Pattamatta, and S. K. Das. 2011. Scaling analysis for the investigation of slip mechanisms in nanofluids. *Nanoscale Research Letters*, 6(1):471–471.
- Sawant, N. N. 2012. *Influence of Lubricant on Horizontal Convective Boiling in a Micro-fin Tube*. The Catholic University of America, Washington D. C.
- Sawant, N. N., M. A. Kedzierski, and J. S. Brown. 2007. *Effect of Lubricant on R410A Horizontal Flow Boiling*. National Institute of Standards and Technology Internal Report 7456.
- Shah, M. M. 1982. A new correlation for saturated boiling heat transfer: Equations and further study. *ASHRAE Transactions*, 185–196.
- Sharif, M. Z., W. H. Azmi, R. Mamat, and A. I. M. Shaiful. 2018. Mechanism for improvement in refrigeration system performance by using nanorefrigerants and nanolubricants – A review. *International Communications in Heat and Mass Transfer*, 92:56–63.
- Sheikholeslami, M., and D. D. Ganji. 2016. Nanofluid convective heat transfer using semi analytical and numerical approaches: A review. *Journal of the Taiwan Institute of Chemical Engineers*, 65(Supplement C):43–77.
- Shen, B., and E. A. Groll. 2005. Review Article: A Critical Review of the Influence of Lubricants on the Heat Transfer and Pressure Drop of Refrigerants, Part 1: Lubricant Influence on Pool and Flow Boiling. *HVAC&R Research*, 11(3):341–359.

- Shoghl, S. N., M. Bahrami, and M. Jamialahmadi. 2017. The boiling performance of ZnO, α -Al₂O₃ and MWCNTs/water nanofluids: An experimental study. *Experimental Thermal and Fluid Science*, 80:27–39.
- Taylor, B. N., and C. E. Kuyatt. 1994. Guidelines for evaluating and expressing the uncertainty of NIST measurement results.
- Thome, J. R. 1995. Comprehensive Thermodynamic Approach to Modeling Refrigerant-Lubricating Oil Mixtures. *HVAC&R Research*, 1(2):110–125.
- Thome, J. R. 2010a. Heat Transfer Engineering Data Book III. *Wolverine Tube, Inc., Chapter 15*.
- Thome, J. R. 2010b. Heat Transfer Engineering Data Book III. *Wolverine Tube, Inc., Chapter 16*.
- Thome, J. R., and J. E. Hajal. 2003. Two-Phase Flow Pattern Map for Evaporation in Horizontal Tubes: Latest Version. *Heat Transfer Engineering*, 24(6):3–10.
- Vafaei, S. 2015. Nanofluid pool boiling heat transfer phenomenon. *Powder Technology*, 277(Supplement C):181–192.
- Vafaei, S., and T. Borca-Tasciuc. 2014. Role of nanoparticles on nanofluid boiling phenomenon: Nanoparticle deposition. *Chemical Engineering Research and Design*, 92(5):842–856.
- Wang, C. H., and V. K. Dhir. 1993. Effect of Surface Wettability on Active Nucleation Site Density During Pool Boiling of Water on a Vertical Surface. *Journal of Heat Transfer*, 115(3):659–669.
- Wang, Y., K. H. Deng, B. Liu, J. M. Wu, and G. H. Su. 2017. A correlation of nanofluid flow boiling heat transfer based on the experimental results of AlN/H₂O and Al₂O₃/H₂O nanofluid. *Experimental Thermal and Fluid Science*, 80:376–383.
- Wasan, D. T., and A. D. Nikolov. 2003. Spreading of nanofluids on solids. *Nature*, 423:156.
- Wattelet, J., J. Chato, B. Christoffersen, J. Gaibel, M. Ponchner, P. Kenney, R. Shimon, T. Villaneuva, N. Rhines, and K. Sweeney. 1994. Heat Transfer Flow Regimes of Refrigerants in a Horizontal-Tube Evaporator. *Urbana*, 100:61801.
- Wei, W., G. Ding, H. Hu, and K. Wang. 2007. Influence of lubricant oil on heat transfer performance of refrigerant flow boiling inside small diameter tubes. Part I: Experimental study. *Experimental Thermal and Fluid Science*, 32(1):67–76.
- Wen, D. 2008. On the role of structural disjoining pressure to boiling heat transfer of thermal nanofluids. *Journal of Nanoparticle Research*, 10(7):1129–1140.
- Wen, D., M. Corr, X. Hu, and G. Lin. 2011. Boiling heat transfer of nanofluids: The effect of heating surface modification. *International Journal of Thermal Sciences*, 50(4):480–485.

- Wen, D., and Y. Ding. 2005. Effect of particle migration on heat transfer in suspensions of nanoparticles flowing through minichannels. *Microfluidics and Nanofluidics*, 1(2):183–189.
- Wen, D., L. Zhang, and Y. He. 2009. Flow and migration of nanoparticle in a single channel. *Heat and Mass Transfer*, 45(8):1061–1067.
- Wenzel, R. N. 1949. Surface Roughness and Contact Angle. *The Journal of Physical and Colloid Chemistry*, 53(9):1466–1467.
- White, S. B., A. J. Shih, and K. P. Pipe. 2010. Effects of nanoparticle layering on nanofluid and base fluid pool boiling heat transfer from a horizontal surface under atmospheric pressure. *Journal of Applied Physics*, 107(11):114302.
- Williams, W., J. Buongiorno, and L.-W. Hu. 2008. Experimental Investigation of Turbulent Convective Heat Transfer and Pressure Loss of Alumina/Water and Zirconia/Water Nanoparticle Colloids (Nanofluids) in Horizontal Tubes. *Journal of Heat Transfer*, 130(4):042412-042412–7.
- Wojtan, L., T. Ursenbacher, and J. R. Thome. 2005. Investigation of flow boiling in horizontal tubes: Part I—A new diabatic two-phase flow pattern map. *International Journal of Heat and Mass Transfer*, 48(14):2955–2969.
- Wong, T. 2015. *Development of a test facility and preliminary testing of flow boiling heat transfer of R410A refrigerant with Al₂O₃ nanolubricants*. Oklahoma State University.
- Xu, L., and J. Xu. 2012. Nanofluid stabilizes and enhances convective boiling heat transfer in a single microchannel. *International Journal of Heat and Mass Transfer*, 55(21):5673–5686.
- Xuan, Y., and Q. Li. 2000. Heat transfer enhancement of nanofluids. *International Journal of Heat and Fluid Flow*, 21(1):58–64.
- Yang, D., B. Sun, H. Li, C. Zhang, and Y. Liu. 2017. Comparative study on the heat transfer characteristics of nano-refrigerants inside a smooth tube and internal thread tube. *International Journal of Heat and Mass Transfer*, 113:538–543.
- Yuan, F., J. Lin, and J. Yu. 2018. Numerical Research on Convective Heat Transfer and Resistance Characteristics of Turbulent Duct Flow Containing Nanorod-Based Nanofluids. *Journal of Nanotechnology*, 2018.
- Zangeneh, A., A. Vatani, Z. Fakhroei, and S. M. Peyghambarzadeh. 2016. Experimental study of forced convection and subcooled flow boiling heat transfer in a vertical annulus using different novel functionalized ZnO nanoparticles. *Applied Thermal Engineering*, 109:789–802.
- Zhao, Y., M. Molki, M. M. Ohadi, F. H. Franca, and R. Radermacher. 2002. Flow boiling of CO₂ with miscible oil in microchannels/Discussion. *ASHRAE Transactions*, 108:135.

- Zhou, J., X. Luo, Z. Feng, J. Xiao, J. Zhang, F. Guo, and H. Li. 2017. Saturated flow boiling heat transfer investigation for nanofluid in minichannel. *Experimental Thermal and Fluid Science*, 85:189–200.
- Zou, X., M. Q. Gong, G. F. Chen, Z. H. Sun, Y. Zhang, and J. F. Wu. 2010. Experimental study on saturated flow boiling heat transfer of R170/R290 mixtures in a horizontal tube. *International Journal of Refrigeration*, 33(2):371–380.
- Zürcher, O., J. R. Thome, and D. Favrat. 1998. In-Tube Flow Boiling of R-407C and R-407C/Oil Mixtures Part II: Plain Tube Results and Predictions. *HVAC&R Research*, 4(4):373–399.

Appendix-A

Literature Review Summary

Reported below is a tabulated summary of the water and refrigerant based pool and flow boiling experimental studies available in the literature. For each studies, detailed information of the nanofluids, experimental test conditions, test section geometry, heat transfer results, pressure drop results, and correlations are provided.

Source	{nanoparticle image}{Size} (Concentration in nanofluid) Nanoparticle; basefluid {nanolubricant or oil mass fraction} <surfactant>	[Boiling type] T=temperature (°C); Tsat=saturation temperature (°C); P=Pressure (MPa); q''=Heat flux (kW/m ²); m''=Mass flux (kg/m ² -s); x=vapor quality;	Heating surface material {image}; Geometry; N=number of channels, D=Diameter (hydraulic), W=Width, H=Height, L=Length, [Flow image] (all dimensions in mm)	Heat transfer results in presence of nanofluid	Pressure drop result in presence of nanofluid	Developed or used correlations and equations
(Xu and Xu 2012)	{SEM, TEM} [40 nm] (0.2 wt.% or 0.052 vol.%) γ -Al ₂ O ₃ ; in water	[flow boiling] T = 25; P = 0.101; q'' = 0-1000; m'' = 171, 285 and 401	Platinum {-}; horizontal microchannel bottom heated; N=1; W = 0.1; H = 0.25; L = 7.5 [microscope]	17% enhancement and 10% lower heater surface temperature for single-phase forced convection; enhanced for boiling.	10% higher for single-phase liquid flow; smaller in the boiling flow region due to miniature bubbles with stable flow.	Force balance analysis on a growing bubble on a heated surface supplied with constant heat flux and in presence of nanoparticles structural disjoining pressure.
(Kim et al., 2007)	(0.001, 0.01, and 0.1 vol.%) [110 to 210 nm] Al ₂ O ₃ , [110 to 250 nm] ZrO ₂ , [20 to 40 nm] SiO ₂ ; in deionized water <no surfactant>	[pool boiling] P = 0.101; for flat plate q'' = 500	Stainless Steel-316 {SEM, EDS}; wire of D = 0.318; L = 120; flat plate of W = 5, L = 45	Deposition of nanoparticle porous layer during nucleate boiling, which improved wettability, had significant enhancement in CHF at nanoparticle concentrations of <0.1 vol.%. 52% for alumina nanofluids, 75% for zirconia nanofluids, and 80% for silica nanofluids.	No pressure drop data available.	Growth rate analysis of nanoparticle deposition from microlayer underneath growing bubbles.
(Kim et al., 2010)	[40 nm] (0.001, 0.01, and 0.1 vol.%) Al ₂ O ₃ , [77.4 nm] ZnO, [165.4 nm] diamond; in deionized water <no surfactant>	[vertical upward subcooled flow boiling]; P = 0.101; q'' = 100 to 7500; m'' = 1500, 2000, and 2500	Stainless Steel-316 tube {confocal microscopy}; D = 5.53; L = 100	CHF enhancement increased with the mass flux and nanoparticle concentration. The maximum CHF enhancements were 53%, 53%, and 38% for alumina, zinc oxide, and diamond nanofluids, respectively.	No pressure drop data available.	Chen correlation for flow boiling overpredicted the wall temperatures, and underpredicted the HTC's for water and nanofluids.

(Bartelt et al. 2008)	[30 nm] (4 vol.%) CuO in POE_RL68H; {0, 0.5, 1, and 2% OMF} in R134a. <surfactant used, 5% and 15% of the mass of the CuO>	[flow boiling] $T_{sat} = 3.6$ to 14.6 and 37.9 to 41 ; $q'' = 0.69$ to 3.06 ; $m'' = 125$ to 390 ; $x = 2.44\%$ to 6.33%	Smooth copper tube, $D = 7.9$; $L = 2000$	At 0.5% OMF, no HTC enhancement for CuO-POE-R134a above POE-R134a. At 1% and 2% OMF, HTC had enhancements between (42% and 82%) and (50% and 101%), respectively, for CuO-POE-R134a above POE-R134a. HTC enhancements increased with flow rate. The observed HTC enhancements were above their uncertainties. The saturation temperatures increased with nanolubricant OMF.	Nanolubricants had an insignificant effect on the pressure drop.	The baseline data of heat transfer was verified using Gnielinski correlation for fully developed single-phase turbulent flow in a smooth circular tube and Panek et al. (1992) correlation for convective two-phase boiling of pure R-134a.
-----------------------	--	--	--	---	--	---

(Henderso n et al. 2010)	CuO-POE-R134a [30 nm] (0.02, 0.04, and 0.08 nanoparticle vol.%) CuO in POE_RL68H; {0, 0.5, 1, and 2% OMF} in R134a. <surfactant used, 5% and 15% of the mass of the CuO>, and SiO2-R134a [200-300 nm] (0.05 and 0.5 vol.%) SiO2 in R134a <hexamethyldisilane>	[flow boiling] For CuO-POE-R134a: $T_{sat} = 3.6$ to 14.6 and 37.9 to 41 ; $q'' = 0.69$ to 3.06 ; $m'' = 125$ to 390 ; $x = 0.024$ to 0.073 ; and for SiO2-R134a: $T_{sat} = 35 \pm 2$; $q'' = 5.82$ to 16.17 ; $m'' = 137$ to 385 ; $x = 0.08$ to 0.27	Smooth copper tube, $D = 7.9$; $L = 2000$	The flow boiling of 0.05 vol% and 0.5 vol.% of SiO2-R134a showed the HTC for the nanofluids to decrease by about 55% below R134a HTC due to unstable nanoparticle suspension. The flow boiling of CuO-POE-R134a at low nanoparticle volume fraction of 0.02% showed no HTC enhancement. At 1% and 2% OMF (or nanoparticle volume fraction of 0.04% and 0.08%), the HTC had enhancements between (42% and 82%) and (50% and 101%), respectively, for CuO-POE-R134a above POE-R134a. After cleaning the test section, the 1% OMF POE-R134a tests showed more than 50% HTC enhancement above the base line, as the boiling surface was permanently modified due to CuO nanoparticles deposition. While R134a baseline was repeatable for the SiO2 deposited and then cleaned test section's boiling surface, as the deposition of coated SiO2 was not permanent on the boiling surface.	CuO-POE-R134a Nanolubricants had an insignificant effect on the pressure drop at all volume fractions, because the viscosity did not significantly changed at low nanoparticle concentrations.	N/A
(Faulkner et al. 2003)	(0.25 to 0.5 wt.%) Al2O3 and AlN; in water <surfactant used>	[Subcooled and saturated forced flow boiling] $P = 0.101$; $q'' = 100$ to 2750 ; $m'' = 500$, 725 , and 1000 ml/min	microchannel; $N=10$, $W = 0.5$ and 1 ; $H = 6$; $L = 10$	For different operating condition and nanofluid types, there was both improvement and degradation in heat transfer.	No pressure drop data available.	N/A

(Kedzierski and Gong 2009)	[30 nm] (1 vol.%) CuO in POE_RL68H; {0, 0.5, 1, and 2% OMF} in R134a. <surfactant used, 5% and 15% of the mass of the CuO>	[pool boiling] $T_{sat} = 4.45$; $q'' = 10$ to 120;	Copper; rough horizontal flat plate; $W = 32$, $L = 101.6$	At 0.5% OMF, heat transfer enhancements between 50% and 275% for CuO-POE-R134a with respect to POE-R134a. The amount of heat transfer enhancements decreases with increasing nanolubricant concentration. The increased effective thermal conductivity of the nanolubricant was responsible for only a small portion (about 20%) of the heat transfer enhancement.	No pressure drop data available.	N/A
(Kedzierski 2011)	{DLS}; [10 nm] (1.6 vol.%) Al ₂ O ₃ in POE_RL68H; {0, 0.5, 1, and 2% OMF} in R134a. <surfactant used, 15% and 20% of the mass of the Al ₂ O ₃ >	[pool boiling] $T_{sat} = 4.45$; $q'' = 7$ to 130;	Copper; rough horizontal flat plate; $W = 32$, $L = 101.6$. Average cavity radii for the surface was between 12 μm and 35 μm ($\pm 12\%$ uncertainty).	At 0.5% OMF and low heat fluxes, heat transfer enhancements of 400% for Al ₂ O ₃ -POE-R134a with respect to POE-R134a. The average heat flux improvement of Al ₂ O ₃ -POE-R134a over POE-R134a, for heat fluxes less than 40 kW/m ² and same superheat, were approximately 105%, 49%, and 155% for the 0.5%, the 1%, and the 2% OMF, respectively. The heat flux ratio for all of the mixtures decreased with respect to increasing heat flux. Aluminum oxide nanoparticles provided the most favorable benefit to the 2% mass fraction mixture.	No pressure drop data available.	A developed semi-empirical model predicted the heat transfer enhancement caused by the transfer of momentum from the nanoparticles to the bubbles. The model suggests that small particle size and large nanoparticle volume fraction improved boiling enhancement.

(Peng et al. 2009a)	{TEM}[40 nm] (0, 0.1, 0.2, and 0.5 wt%) CuO; in R113 <no surfactant>	[flow Boiling] P = 0.0783; $q'' = 3.08, 4.62, \text{ and } 6.16$; $m'' = 100, 150, \text{ and } 200$; $x = 0.25$ to 0.8.	Copper smooth tube; Geometry; D = 8.12, L=1400.	The HTC of CuO-R113 nanofluid was larger than that of pure R113, and the maximum HTC enhancement was 29.7%. The HTC enhancements, or impact factors, were 29.7%, 22.7%, and 25.6% at mass fluxes of 100, 150, and 200 $\text{kg/m}^2\text{-s}$, respectively, for 0.5 wt% CuO in R113.	No pressure drop data available.	Proposed a correlation to predict the HTC for refrigerant-based nanofluid flow boiling inside a smooth tube. The correlation predicted 93% of their experimental data within a deviation of $\pm 20\%$.
(Zhou et al. 2017)	{SEM}[28 nm] (0, 0.2, 0.5, and 1.0 wt%) Al_2O_3 ; deionized water < acetic acid, 0.05 wt.%>	[saturated flow boiling] T=95; P=0.101; $q''=18$ to 200; $m''=80$ to 350.	Minichannel; N=9 and 23; D=0.52, 0.92, and 2; W=0.3, 0.6, and 0.2, H=2, L=250.	The addition of nanoparticles resulted in enhancement of heat transfer. The averaged HTC enhancements were 11.2%, 15.4% and 18.7%, for 0.2 wt.%, 0.5 wt.% and 1.0 wt.% Al_2O_3 -water nanofluids, respectively. The HTC enhancements increased with reduced channel hydraulic diameter because of increased capillary effects.	No pressure drop data available.	Developed a theoretical HTC correlation that accounts for convective boiling and nucleate boiling heat transfer. The correlation predicted 94.2% of the experimental data within $\pm 20\%$. Used nanoparticle fractal distribution theory for convective heat transfer, and considered the probability distribution density of bubbles random growth

(G. Ding et al. 2009)	{TEM}[40 nm] CuO (0.5, 1, 1.5, and 2 grams); in R113 (30, 60, 90, and 120 grams), and lubricant oil RB68EP (0 and 10 grams) <no surfactant>	[pool boiling] T = 47.6; P = 0.101; q'' = 20.	Glass cylinder; Geometry; D = 30, H = 165.	No heat transfer data available.	No pressure drop data available.	Developed a nanoparticle immigration model. The model was sensitive to the calculation of mass fraction of the oil and more for average velocity of bubble, and predicted the experimental data within an average deviation of 7.7% to 38.4% for the CuO-R113-RB68EP mixtures.
(White et al. 2010)	[40 nm] (0% and 2.3 vol%) ZnO; deionized water <no surfactant> nanofluid by Nanophase Technologies, ZnO had elongated morphology	[pool boiling] P = 0.101; q'' = 24, 28, and 32; Four alternate boiling of deionized water and ZnO-nanofluid without cleaning surface.	Stainless Steel-316L {AFM and SEM}; horizontal 82.6 mm disc.	ZnO-water nanofluid showed 24% enhancement over water when boiling on clean-unroughened surface, but reduced in later test cycles when boiled on nanoparticle coated surface. While, the water boiling performance enhanced significantly by 62% after four cycles of boiling, when surface roughness increased from 0.06 μm to 0.44 μm .	No pressure drop data available.	Verified the experimental data with Gorenflo correlation for boiling coefficient that accounts for surface roughness.
(Zangeneh et al. 2016)	{SEM}[less than 50 nm] (ZnO(type I) at 0.005, 0.01 and 0.02 vol.%, ZnO(type II, III, IV) at 0.01 and 0.02 vol.%); deionized water <no surfactant> Two-step synthesis methods of nanoparticles.	[single phase forced convective, and partial subcooled flow boiling] T=30 to 50; P=0.101; q''=8 to 110; flow=2 to 4 L/min.; Re=1800 to 3600.	Stainless Steel; Vertical Cylindrical annulus; annulus ID=20; annulus OD=20; L=150.	The cylindrical shaped ZnO (type II, and III) nanoparticles showed better heat transfer performance than others did. The HTC ratio of ZnO (type I, II, III and IV) at 0.02 vol.% with respect to water was 5.14%, 8.14%, 5.75% and -6.75%, respectively.	No pressure drop data available.	Verified the experimental data with Chen model for the flow boiling, and Gnielinski equation for single phase forced convection.

(Shoghl et al. 2017)	{FESEM, SEM}[80 nm] (0.01 and 0.05 wt.%) α -Al ₂ O ₃ , [10-30 nm] (0.01 and 0.05 wt.%) ZnO, [10-20 nm OD, 10-30 μ m length] (0.01 and 0.02 wt.%) CNT, <no surfactant, only SDS for CNT nanofluid>	[pool boiling] P=0.101, q''=7-300.	Clean Stainless Steel (R_a =0.15 μ m), ZnO deposit on Stainless Steel (R_a =0.03-0.05 μ m), Al ₂ O ₃ deposit on Stainless Steel (R_a =0.05-0.06 μ m) CNT deposit on Stainless Steel (R_a =0.48-1.83 μ m) {AFM for surface roughness}; cylindrical rod; D=10.67, L=99.1	ZnO and α -Al ₂ O ₃ deteriorate the surface by making them smoother, while the CNTs improve the surface roughness. Resulting in degradation of HTC in case of pool boiling of pure water and ZnO-water boiling on ZnO nanoparticle coated surface and boiling of pure water and α -Al ₂ O ₃ -water boiling on α -Al ₂ O ₃ nanoparticle coated surface, while pool boiling of pure water and CNT-water-SDS boiling on CNT nanoparticle coated surface showed enhancements. Surface modification played a significant role in altering number of nucleation sites and bubble frequency.	No pressure drop data available.	The surface roughness of the nanoparticle coated heated surface was estimated using Gorenflo correlation by using the measured data obtained after boiling pure water on the coated surface. This estimated surface roughness value was used to calculate boiling heat transfer coefficient using the Gorenflo correlation.
----------------------	--	------------------------------------	--	--	----------------------------------	---

Appendix-B

LabVIEW Front Panel and Block Diagram

Reported below are the front panels and block diagram of LabVIEW program. The front panels were used to observe the process variables and to control the system conditions while conducting experiments, while the VIs (virtual instruments) in block diagram were used for evaluating and plotting the process variables.

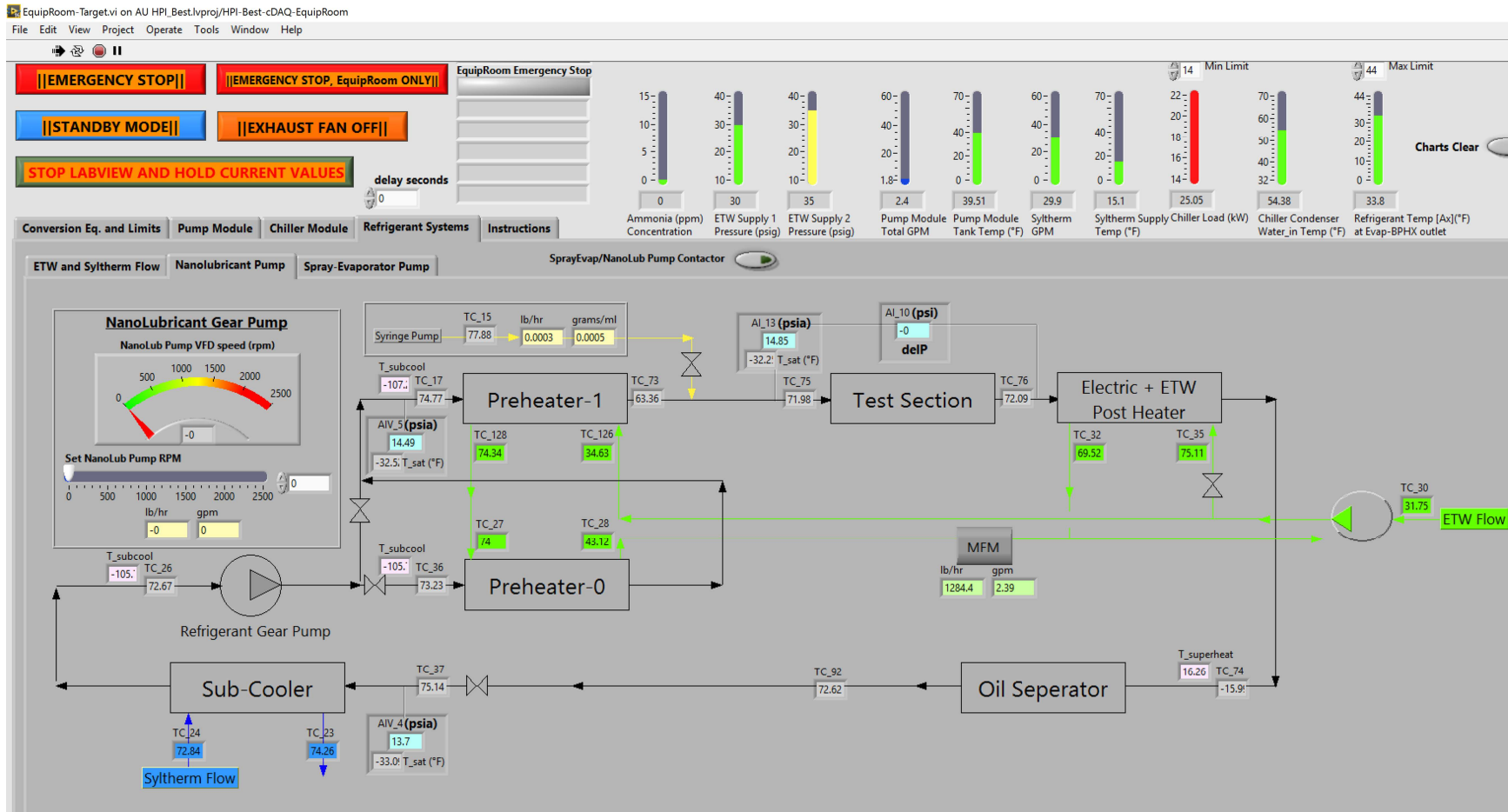
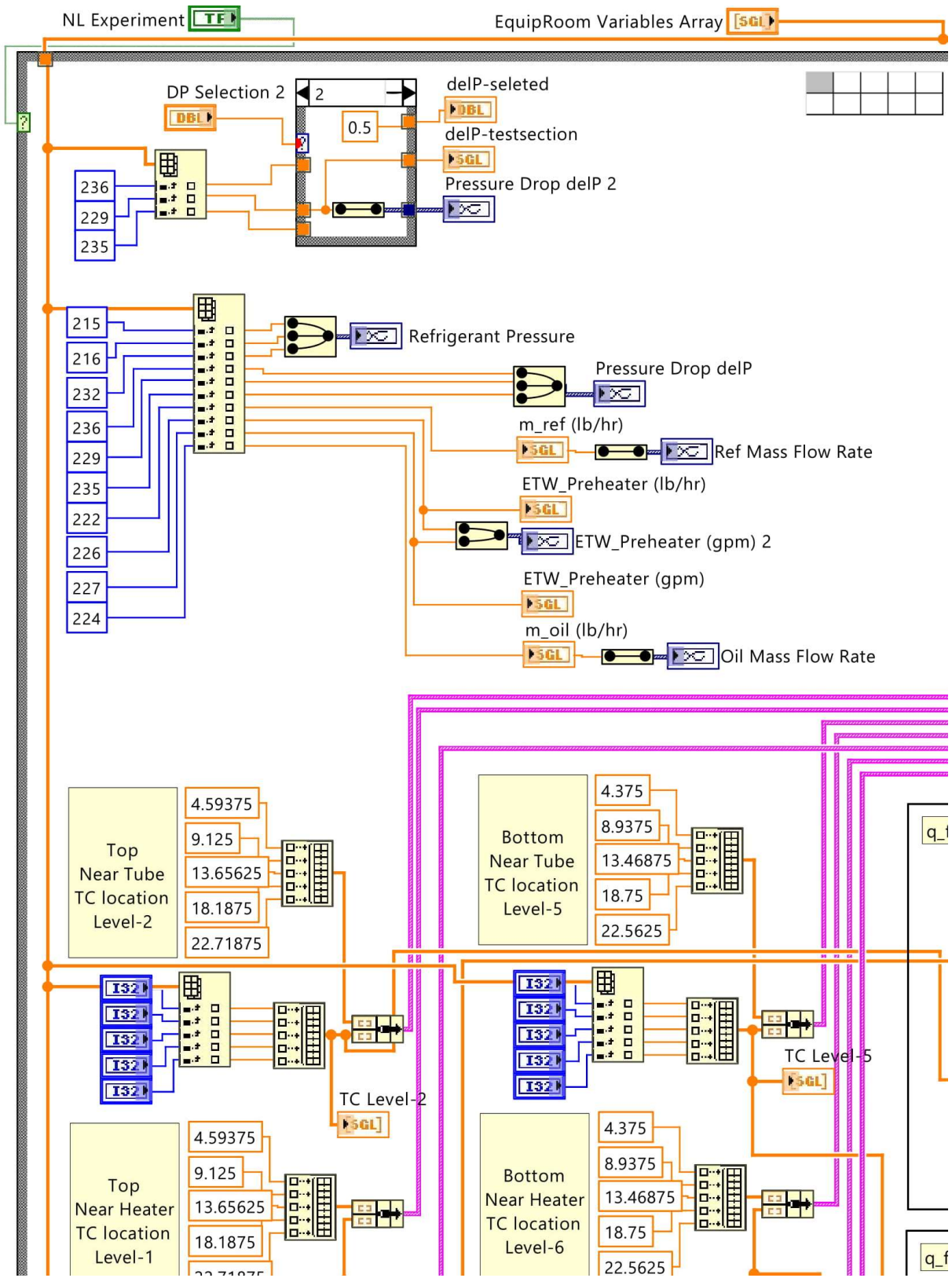
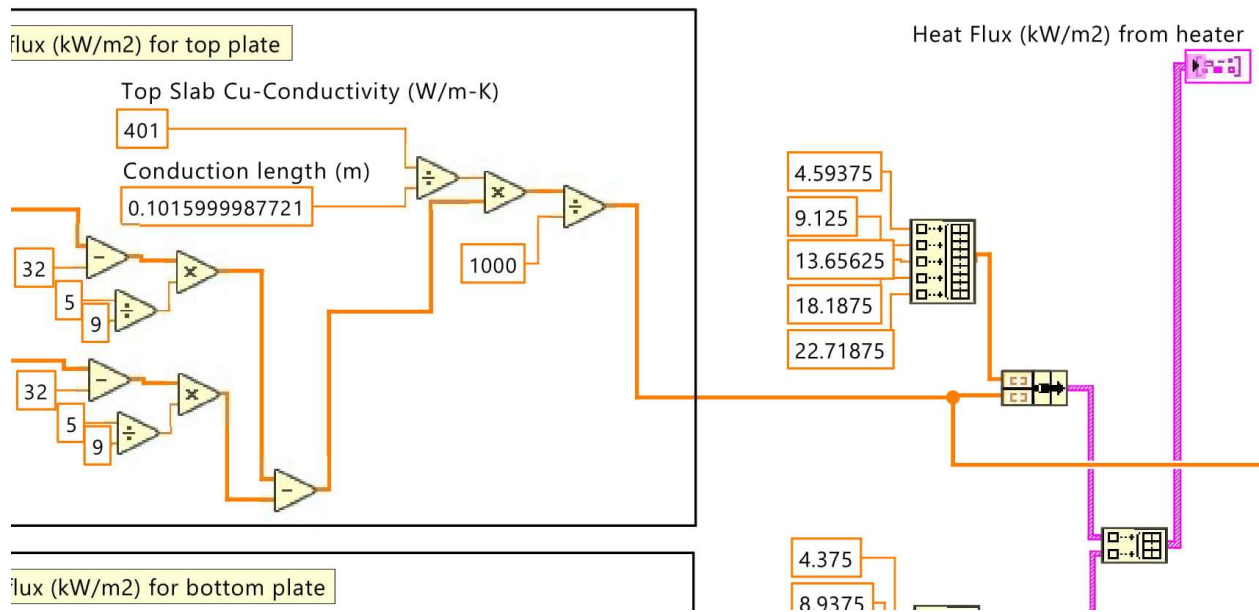
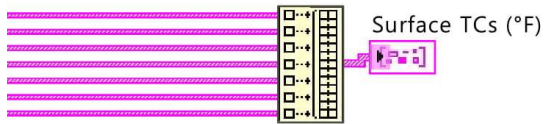
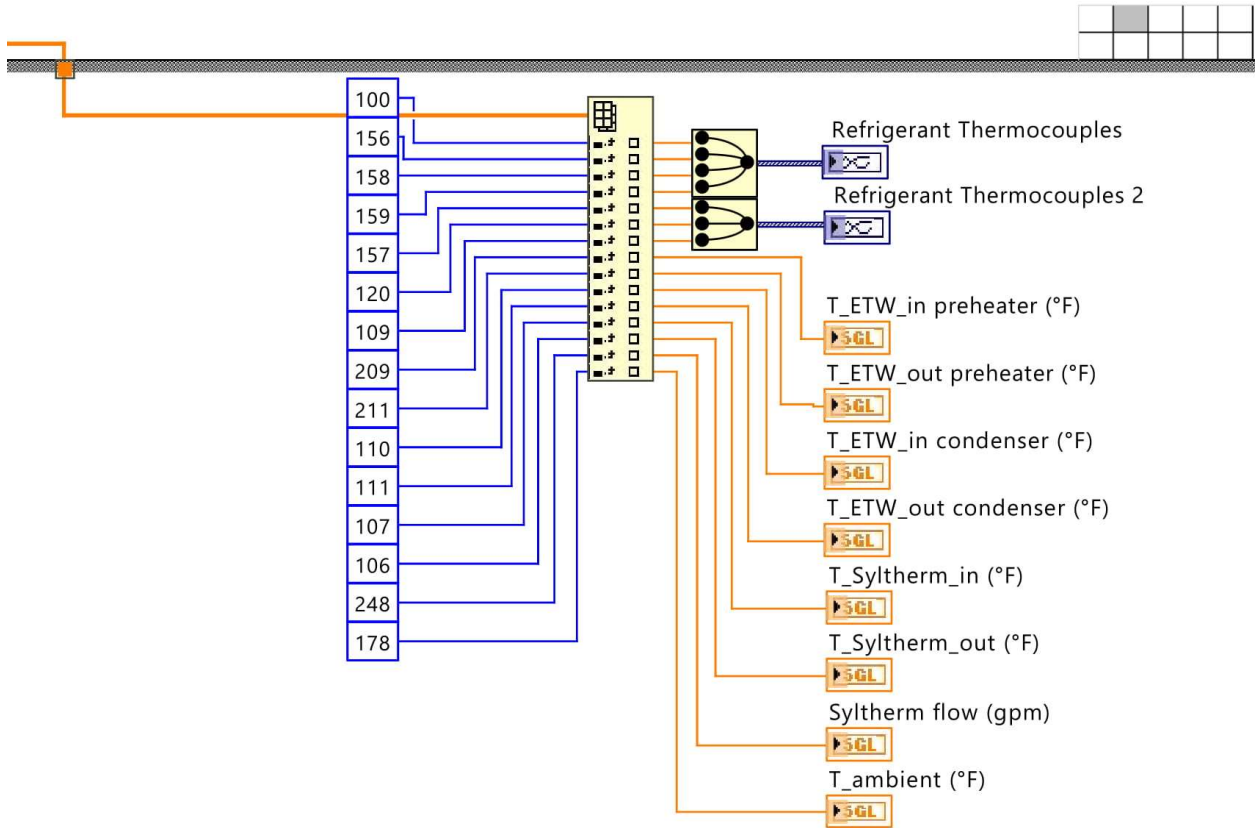


Figure 58: LabVIEW Front Panel with schematic of test apparatus showing process variables.



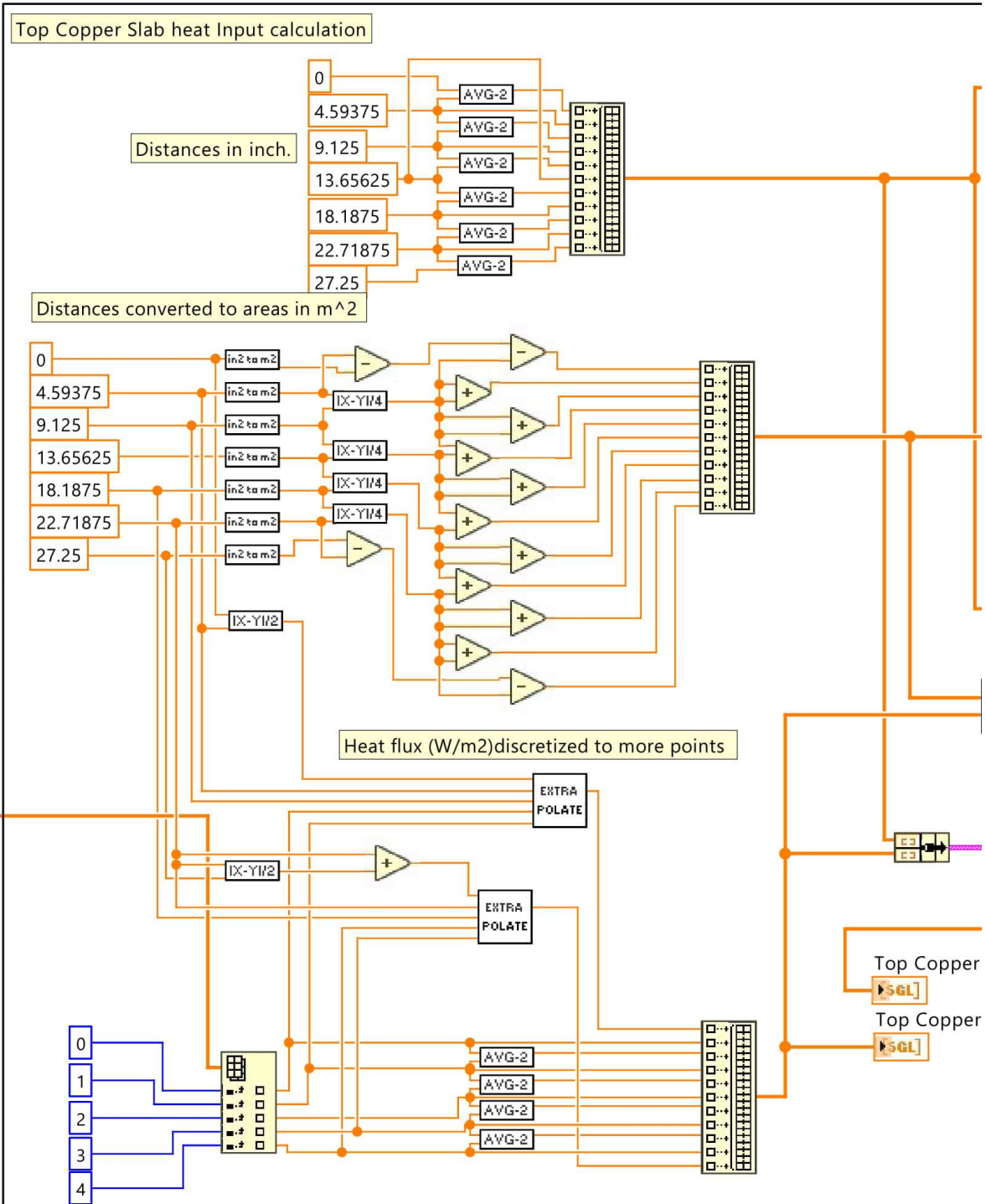
Figure 59: LabVIEW Front Panel with plots of process variables.

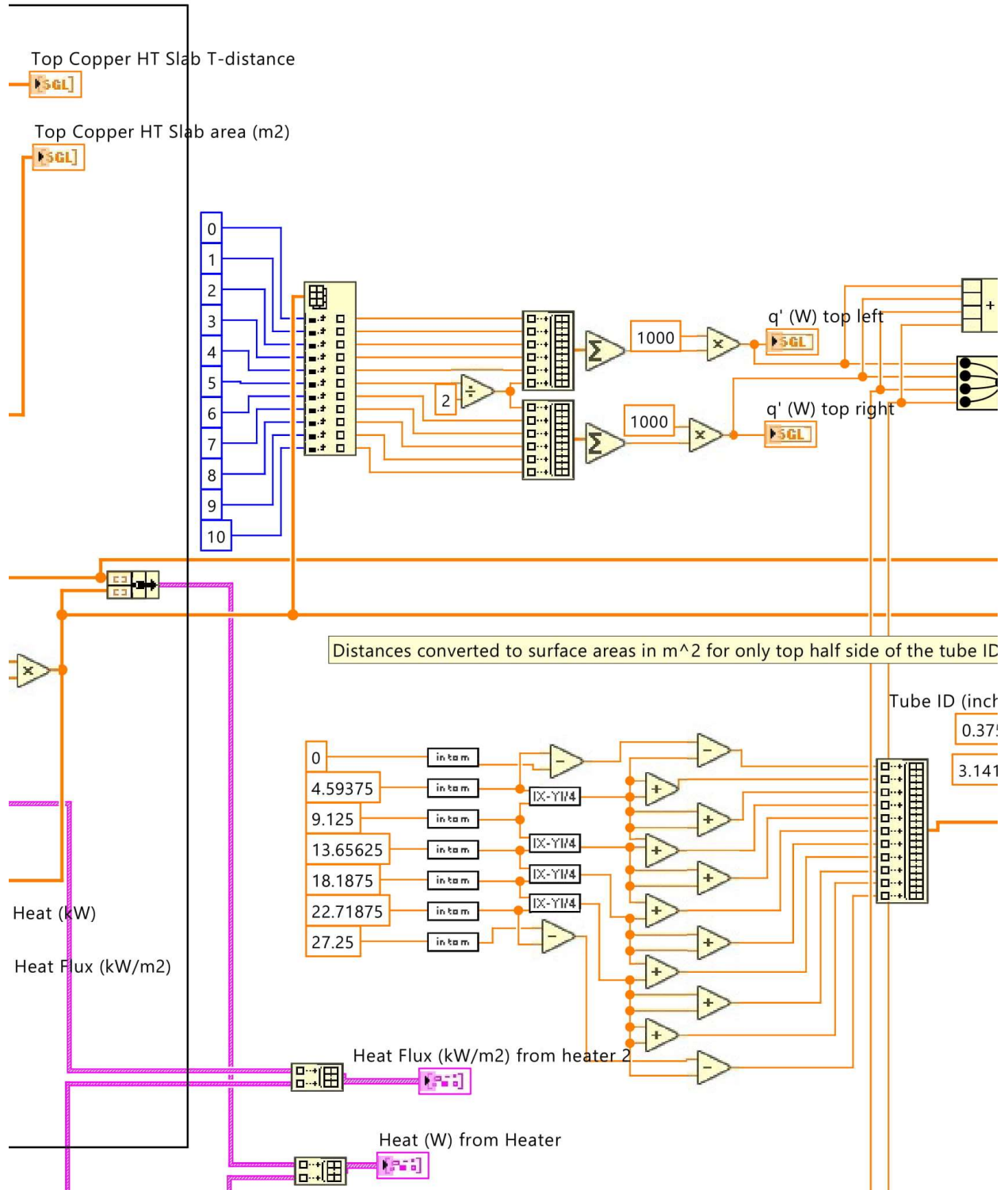
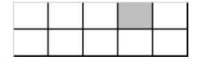


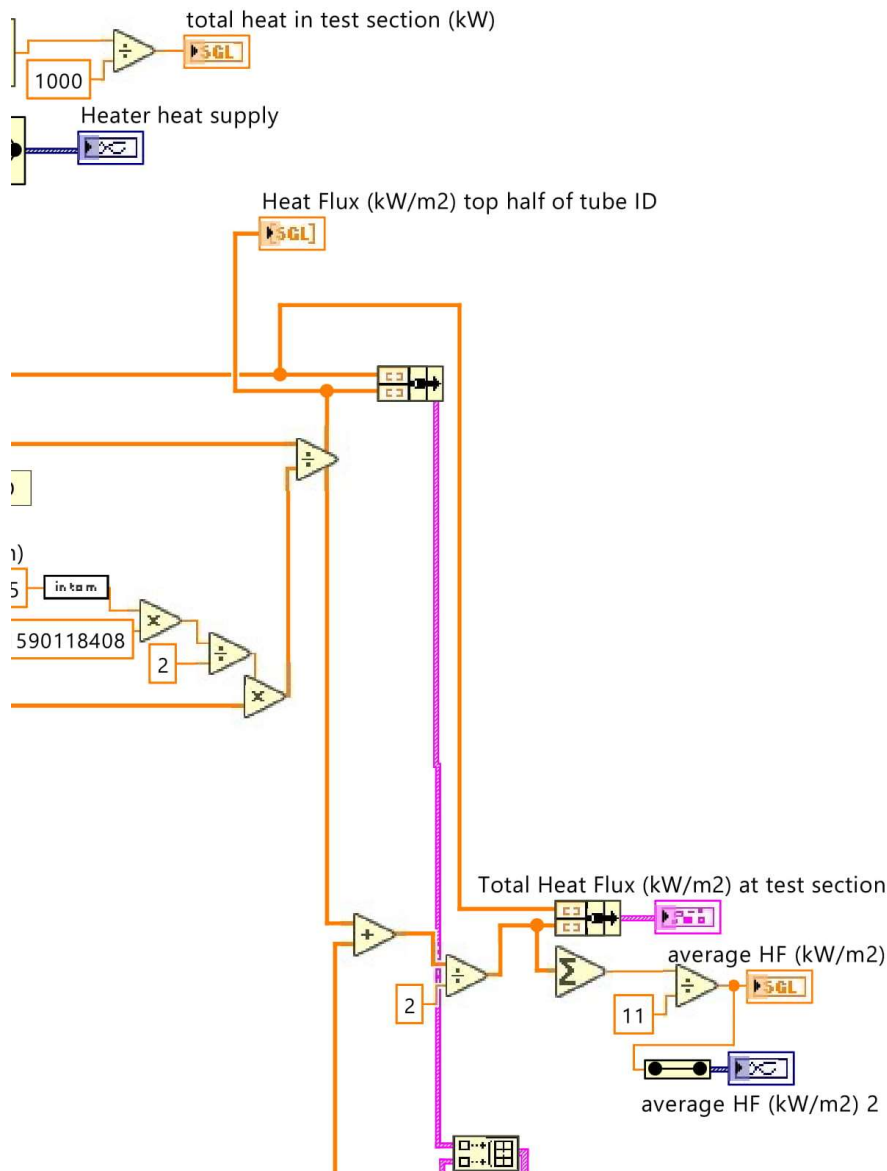


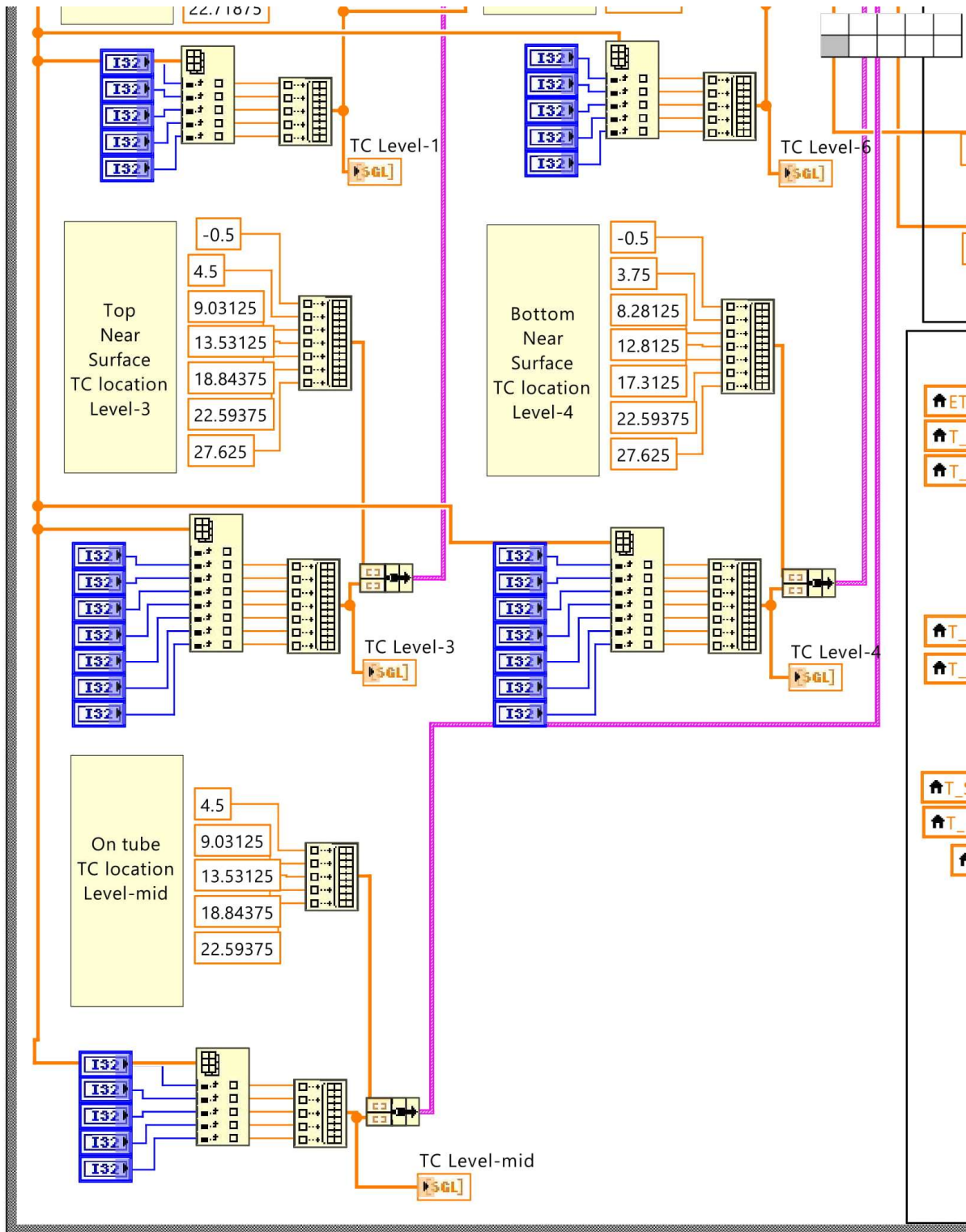
--	--	--	--

True

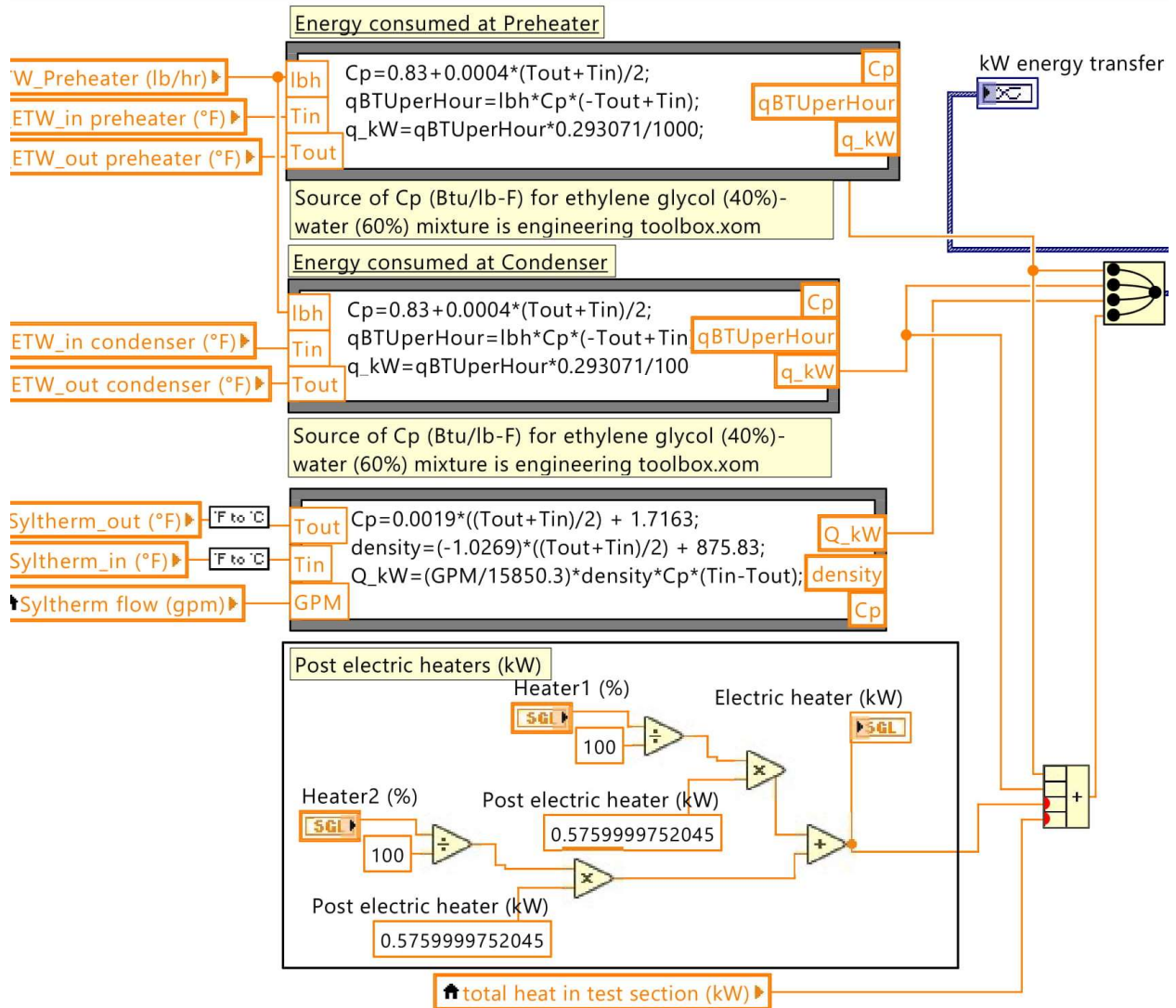
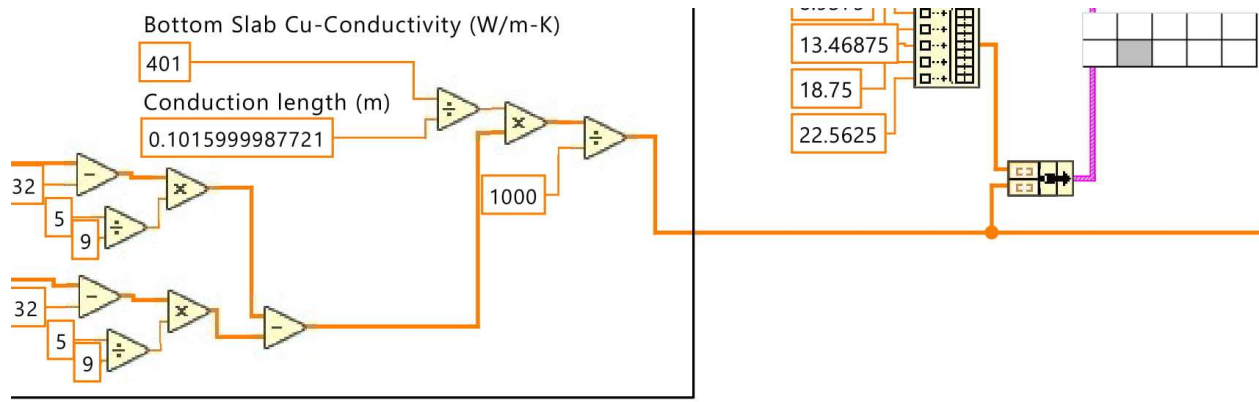


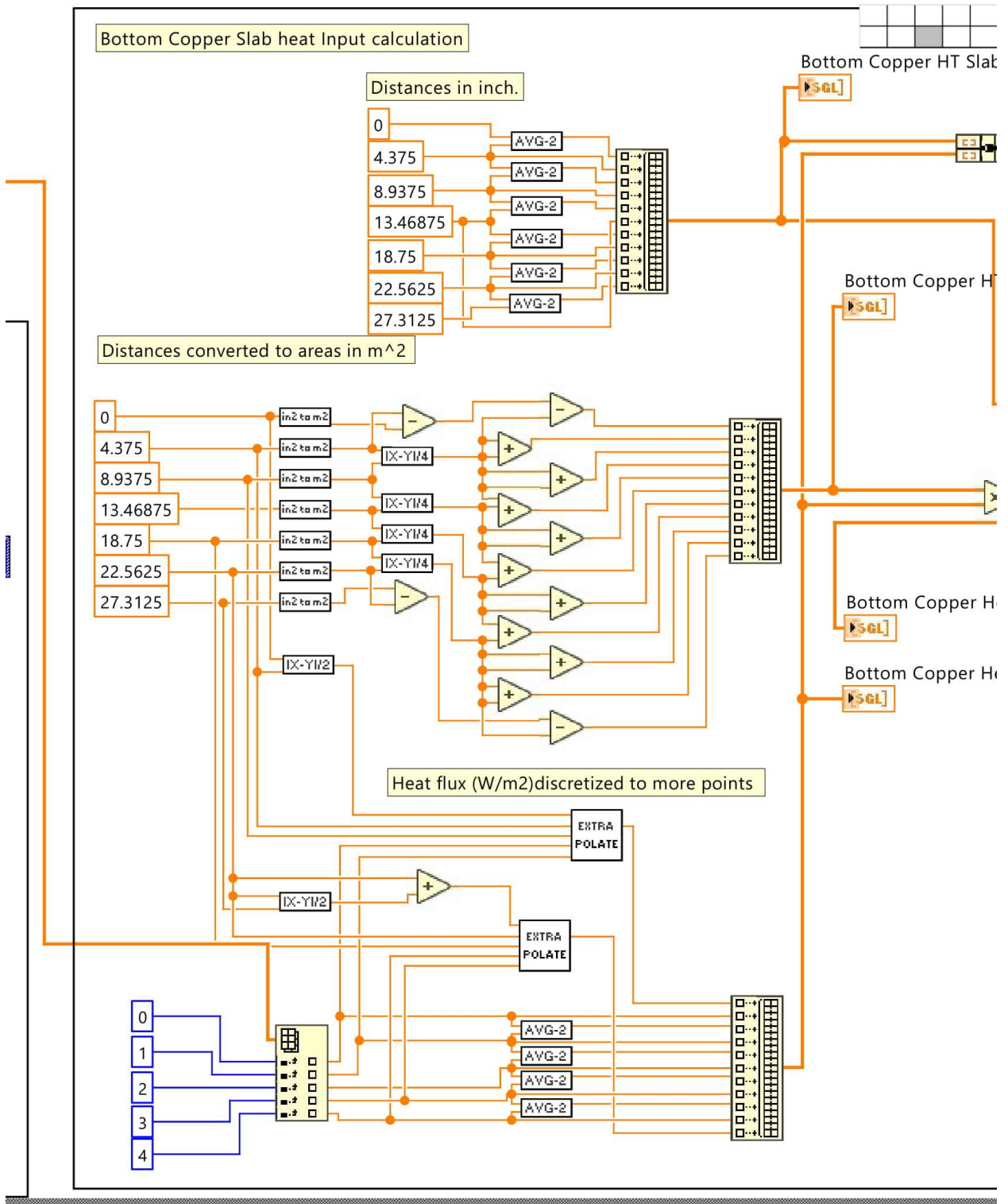


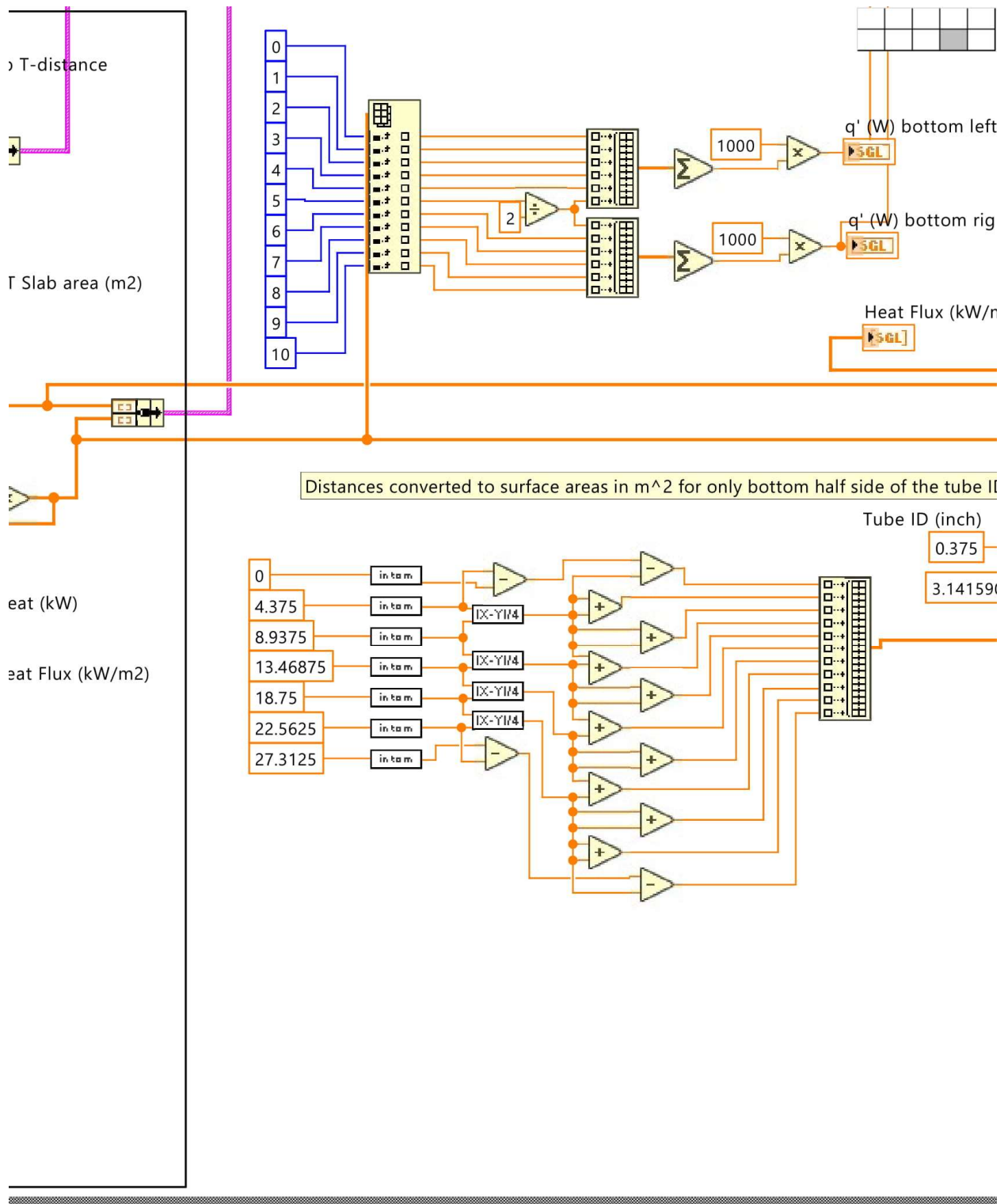




1. Default







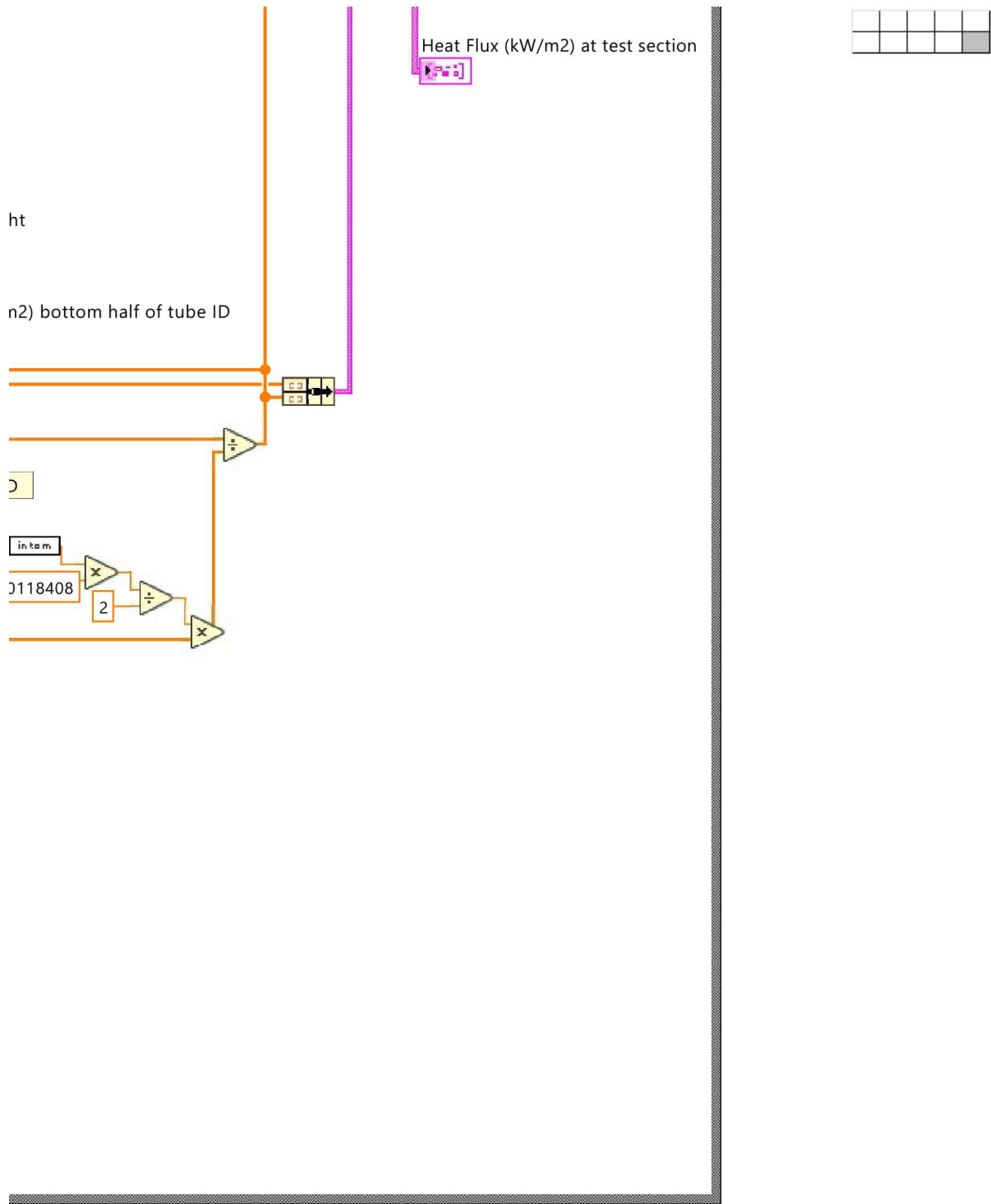


Figure 60: LabVIEW Block Diagram with coded VIs (virtual instruments).

Appendix-C

Two-Phase Flow Experimental Data Set

The data set reported below represents the series of saturated two-phase flow boiling tests conducted during the experimental campaign. At the beginning of each test series, the table lists the fluid tested. For each test, the conditions of the test section are provided, together with the heat transfer coefficient, pressure drop, heat transfer factor, and pressure drop factor. The average pressure drop of the test section, $P_{ref,avg}$, was the evaluated as $P_{ref,avg} = P_{ref,in} - \Delta P/2$.

Fluid	OMF [wt.%]	NP_{conc} [wt.%]	\dot{m} [kg/m ² -s]	\ddot{q}_{avg} [kW/m ²]	$P_{ref,avg}$ [kPa]	x_{in} [-]	$P_{ref,in}$ [kPa]	h_{in} [kJ/kg]	x_{avg} [-]	T_{bub} [°C]	$T_{s,avg}$ [°C]	HTC [kW/m ² -K]	$\Delta P/L$ [Pa/m]	HTF [%]	PDF [%]
R410A	0.0	0	100	14.9	969	0.43	969	300.3	0.53	5.8	9.8	3.78	408	11.3	-4.4
R410A	0.0	0	100	15.0	975	0.64	975	347.2	0.75	6.7	11.0	3.56	466	-4.6	-1.2
R410A	0.0	0	100	14.4	967	0.52	967	319.5	0.61	6.0	10.4	3.38	448	-5.0	-2.1
R410A	0.0	0	100	14.9	977	0.55	977	326.7	0.65	6.5	10.9	3.47	475	-4.0	2.3
R410A	0.0	0	100	15.5	970	0.64	971	347.1	0.75	6.4	11.5	3.12	515	-16.3	9.4
R410A	0.0	0	101	15.1	1001	0.63	1001	343.9	0.73	7.4	11.8	3.59	473	-3.4	0.3
R410A	0.0	0	101	14.9	973	0.22	974	255.9	0.32	5.4	10.3	3.14	283	0.3	0.0
R410A	0.0	0	101	15.2	1000	0.30	1000	273.7	0.40	6.5	11.3	3.24	332	1.4	-5.1
R410A	0.0	0	101	15.2	978	0.41	978	297.4	0.51	6.1	10.7	3.37	415	0.0	-1.1
R410A	0.0	0	102	14.8	976	0.15	977	241.3	0.25	5.3	10.2	3.10	214	-1.8	0.8
R410A	0.0	0	102	14.7	952	0.33	952	278.9	0.43	5.0	9.8	3.18	372	-1.5	0.6
R410A	0.0	0	102	14.7	951	0.16	951	243.7	0.26	4.6	9.4	3.10	244	-1.5	6.6
R410A	0.0	0	104	14.8	975	0.31	975	275.3	0.40	5.7	10.5	3.18	352	-0.5	-0.8
R410A	0.0	0	126	15.1	977	0.27	977	267.7	0.35	5.6	10.4	3.25	419	0.1	0.0
R410A	0.0	0	126	15.1	978	0.43	978	302.1	0.51	6.3	10.8	3.38	542	-3.5	-6.6
R410A	0.0	0	127	14.9	951	0.48	951	311.9	0.56	5.4	9.6	3.57	613	-1.4	0.0
R410A	0.0	0	127	14.9	977	0.68	977	354.8	0.76	6.8	10.7	3.92	663	-0.3	-0.9
R410A	0.0	0	127	14.7	974	0.64	974	346.5	0.72	6.6	10.4	3.91	662	-0.2	-0.8
R410A	0.0	0	127	14.9	974	0.68	974	355.0	0.76	6.7	10.4	4.15	669	5.5	0.0
R410A	0.0	0	127	14.9	975	0.50	976	317.0	0.58	6.2	10.4	3.67	620	-0.1	-0.7
R410A	0.0	0	127	14.9	974	0.18	974	247.5	0.26	5.3	9.9	3.27	285	-1.1	0.7
R410A	0.0	0	127	15.1	998	0.16	998	245.3	0.24	6.0	10.7	3.26	287	-2.2	10.1
R410A	0.0	0	127	14.9	976	0.52	977	320.8	0.60	6.3	10.5	3.67	621	-1.1	-1.9
R410A	0.0	0	128	15.0	970	0.64	970	345.6	0.72	6.4	10.3	4.01	677	2.5	1.4
R410A	0.0	0	128	15.0	975	0.51	975	318.9	0.59	6.1	9.9	4.04	626	9.6	-0.5
R410A	0.0	0	128	15.1	954	0.19	954	249.6	0.27	4.7	9.3	3.32	278	1.1	-9.1
R410A	0.0	0	128	15.0	974	0.34	975	282.1	0.42	5.8	10.3	3.33	494	0.4	-0.3
R410A	0.0	0	128	15.1	973	0.46	973	308.1	0.54	6.0	10.4	3.56	591	-0.4	-1.6
R410A	0.0	0	128	14.9	1000	0.65	1000	349.9	0.73	7.4	11.3	3.97	664	1.2	-0.7
R410A	0.0	0	128	14.9	977	0.34	977	281.4	0.41	5.7	9.8	3.73	475	12.6	-3.2
R410A	0.0	0	128	15.0	1002	0.44	1002	303.9	0.52	6.9	11.3	3.52	559	0.0	-4.2
R410A	0.0	0	128	15.1	976	0.64	977	345.7	0.72	6.8	10.7	3.93	672	0.5	0.7
R410A	0.0	0	128	15.1	979	0.43	979	300.7	0.51	6.3	10.9	3.37	523	-3.3	-9.0
R410A	0.0	0	128	14.3	976	0.52	976	320.3	0.59	6.3	10.3	3.66	628	-1.1	-0.3
R410A	0.0	0	128	15.0	966	0.34	966	282.5	0.42	5.4	9.5	3.70	480	11.4	-3.6
R410A	0.0	0	128	15.0	977	0.33	977	281.0	0.41	5.7	9.8	3.72	475	12.4	-2.7
R410A	0.0	0	129	15.2	978	0.56	978	328.4	0.64	6.5	10.5	3.85	668	1.6	3.0
R410A	0.0	0	129	15.1	973	0.43	973	300.9	0.51	6.2	10.7	3.34	545	-4.4	-5.3
R410A	0.0	0	129	15.1	973	0.50	973	317.1	0.58	6.1	10.1	3.75	638	2.3	2.2
R410A	0.0	0	130	15.0	972	0.46	972	308.8	0.54	6.2	10.7	3.43	605	-4.1	0.5
R410A	0.0	0	131	14.8	973	0.46	973	308.0	0.54	6.2	10.6	3.45	597	-3.2	-0.1

Fluid	OMF [wt.%]	NP_{conc} [wt.%]	\dot{m} [kg/m ² -s]	\ddot{q}_{avg} [kW/m ²]	$P_{ref,avg}$ [kPa]	x_{in} [-]	$P_{ref,in}$ [kPa]	h_{in} [kJ/kg]	x_{avg} [-]	T_{bub} [°C]	$T_{s,avg}$ [°C]	HTC [kW/m ² -K]	$\Delta P/L$ [Pa/m]	HTF [%]	PDF [%]
R410A	0.0	0	162	14.7	950	0.47	950	308.6	0.53	5.3	9.1	3.90	843	-1.3	-1.7
R410A	0.0	0	162	14.9	974	0.50	975	315.8	0.56	6.1	9.7	4.32	880	6.0	-2.7
R410A	0.0	0	162	15.0	1001	0.44	1002	304.0	0.50	6.8	10.8	3.83	772	-0.4	-5.4
R410A	0.0	0	163	15.0	977	0.53	977	323.3	0.59	6.3	9.8	4.43	959	4.7	0.3
R410A	0.0	0	164	14.9	974	0.52	975	321.7	0.59	6.2	9.9	4.13	930	-1.4	-1.6
R410A	0.0	0	164	15.1	976	0.40	977	294.5	0.46	5.8	9.8	3.87	767	3.8	2.1
R410A	0.0	0	164	15.1	975	0.54	976	324.0	0.60	6.3	10.0	4.16	961	-2.0	-0.1
R410A	0.0	0	164	14.7	965	0.46	965	306.7	0.52	5.7	9.6	3.85	822	-1.5	-2.1
R410A	0.0	0	164	15.2	978	0.39	978	293.9	0.46	5.9	10.4	3.36	756	-9.5	1.3
R410A	0.0	0	164	15.0	973	0.54	973	325.7	0.61	6.1	10.0	3.95	995	-7.8	2.2
R410A	0.0	0	165	15.1	974	0.31	974	275.5	0.37	5.6	9.9	3.53	628	-0.2	3.0
R410A	0.0	0	165	15.2	973	0.37	974	288.9	0.43	5.8	9.9	3.69	717	0.9	1.0
R410A	0.0	0	165	15.0	975	0.37	976	289.7	0.44	6.0	10.4	3.49	698	-4.8	-2.4
R410A	0.0	0	166	14.7	975	0.22	975	256.6	0.28	5.4	9.7	3.46	452	-0.1	-1.7
R410A	0.0	0	166	14.8	974	0.53	975	322.3	0.59	6.2	9.8	4.22	958	0.5	1.2
R410A	0.0	0	166	14.9	975	0.45	976	304.7	0.51	6.0	9.9	3.87	829	0.2	0.7
R410A	0.0	0	194	15.1	973	0.45	974	306.3	0.51	5.9	9.4	4.36	1194	-1.6	2.4
R410A	0.0	0	194	15.0	974	0.45	975	306.3	0.50	5.9	9.6	4.09	1135	-7.6	-2.5
R410A	0.0	0	195	15.1	969	0.33	969	281.0	0.39	5.4	9.4	3.80	874	-2.0	-1.8
R410A	0.0	0	195	14.7	974	0.32	974	279.0	0.38	5.6	9.5	3.83	828	-0.6	-4.0
R410A	0.0	0	195	14.9	981	0.33	982	279.8	0.38	5.8	10.1	3.49	865	-9.4	-0.6
R410A	0.0	0	196	15.2	975	0.33	975	280.0	0.38	5.6	9.6	3.81	879	-1.4	0.2
R410A	0.0	0	198	14.8	973	0.44	974	303.3	0.49	5.9	9.4	4.32	1130	-0.2	0.3
R410A	0.0	0	199	15.1	977	0.38	977	290.4	0.43	5.9	9.6	4.05	991	0.8	0.5
R410A	0.0	0	199	15.0	973	0.44	974	303.3	0.49	5.9	9.4	4.33	1130	0.0	0.2
R410A	0.0	0	200	15.0	979	0.20	979	252.0	0.25	5.4	9.4	3.79	558	0.1	-2.0
R410A-POE*	3.0	0	99	15.4	968	0.52	968	315.4	0.63	6.6	9.3	5.90	1379	64.4	199.0
R410A-POE*	3.1	0	125	15.0	963	0.66	964	344.3	0.74	6.9	10.1	5.18	1926	31.9	187.9
R410A-POE*	3.1	0	126	15.8	974	0.53	974	317.3	0.62	6.8	9.4	6.25	1653	66.7	157.8
R410A-POE*	3.0	0	126	15.4	965	0.65	965	342.7	0.73	6.9	9.6	6.29	2081	60.3	211.1
R410A-POE*	3.0	0	126	14.8	975	0.53	976	316.3	0.61	6.8	9.3	6.12	1572	64.3	147.0
R410A-POE*	3.0	0	163	15.1	984	0.52	985	315.8	0.59	7.0	9.6	6.02	1718	43.7	81.9
R410A-POE*	3.0	0	163	15.2	969	0.46	970	301.2	0.52	6.3	9.0	5.71	1531	45.5	81.0
R410A-POE	2.4	0	100	14.8	973	0.27	974	260.3	0.37	6.1	10.3	3.56	366	12.7	12.4
R410A-POE	2.4	0	100	15.0	974	0.45	975	299.5	0.55	6.7	9.8	5.03	632	46.1	44.5
R410A-POE	2.4	0	100	14.9	973	0.36	973	280.5	0.46	6.4	9.9	4.32	512	31.5	30.4
R410A-POE	2.4	0	101	14.7	975	0.58	976	328.5	0.68	7.2	9.8	5.88	736	60.1	56.8
R410A-POE	2.4	0	101	15.1	974	0.44	974	298.3	0.55	6.7	10.0	4.59	571	33.5	31.3
R410A-POE	2.4	0	101	14.7	973	0.45	973	299.1	0.55	6.7	9.6	5.07	638	47.5	46.5
R410A-POE	2.4	0	127	14.8	979	0.27	979	261.1	0.35	6.2	9.8	4.14	547	27.6	32.7
R410A-POE	2.4	0	128	15.0	974	0.42	974	292.3	0.49	6.3	9.1	5.65	876	63.3	54.9

Fluid	OMF [wt.%]	NP _{conc} [wt.%]	\dot{m} [kg/m ² -s]	\ddot{q}_{avg} [kW/m ²]	P _{ref,avg} [kPa]	x _{in} [-]	P _{ref,in} [kPa]	h _{in} [kJ/kg]	x _{avg} [-]	T _{bub} [°C]	T _{s,avg} [°C]	HTC [kW/m ² -K]	ΔP/L [Pa/m]	HTF [%]	PDF [%]
R410A-POE	2.4	0	128	14.9	975	0.59	975	328.8	0.66	7.2	9.7	5.94	1131	54.8	72.0
R410A-POE	2.4	0	128	15.0	975	0.59	976	328.7	0.66	7.2	9.8	5.97	1135	55.6	72.6
R410A-POE	2.4	0	129	15.0	994	0.60	994	332.6	0.68	7.9	10.4	6.11	1096	58.0	65.8
R410A-POE	2.4	0	129	14.6	976	0.54	976	319.9	0.62	6.8	9.2	6.58	1078	75.1	67.8
R410A-POE	2.4	0	129	14.7	975	0.48	975	306.8	0.56	6.8	9.4	5.83	1065	61.1	74.1
R410A-POE	2.4	0	130	14.9	977	0.66	977	344.3	0.74	7.3	9.5	7.38	1208	88.0	80.7
R410A-POE	2.4	0	163	15.1	975	0.41	975	291.6	0.47	6.5	9.3	5.58	1203	48.1	55.3
R410A-POE	2.4	0	164	14.8	977	0.41	978	291.0	0.47	6.6	9.3	5.45	1153	45.3	50.3
R410A-POE	2.4	0	164	14.9	974	0.47	974	303.3	0.53	6.7	9.2	6.03	1360	52.8	58.7
R410A-POE	2.4	0	164	14.7	976	0.19	976	244.1	0.25	5.9	9.5	4.11	664	18.6	62.0
R410A-POE	2.4	0	164	14.9	973	0.52	974	315.0	0.58	6.8	9.2	6.37	1498	52.5	59.5
R410A-POE	2.4	0	164	15.1	978	0.32	978	271.7	0.38	6.3	9.4	4.89	949	37.9	51.9
R410A-POE	2.4	0	197	14.9	975	0.43	975	296.4	0.49	6.6	9.2	5.71	1481	32.7	32.6
R410A-POE	2.4	0	197	14.9	976	0.24	976	254.8	0.29	6.0	9.3	4.48	897	19.4	34.7
R410A-POE	2.4	0	198	14.9	976	0.32	976	271.5	0.37	6.2	9.3	4.92	1132	28.3	33.8
R410A-ZnO NL	2.4	20	101	15.2	978	0.57	978	324.4	0.67	7.1	11.6	3.39	687	-7.0	46.9
R410A-ZnO NL	2.4	20	102	15.0	969	0.35	969	277.2	0.45	6.0	12.3	2.40	378	-26.4	-1.4
R410A-ZnO NL	2.4	20	103	15.3	974	0.42	974	293.3	0.52	6.4	12.7	2.45	457	-27.8	7.8
R410A-ZnO NL	2.4	20	127	15.4	968	0.28	968	262.9	0.36	5.7	11.9	2.52	462	-22.5	7.8
R410A-ZnO NL	2.4	20	128	15.0	975	0.42	975	293.2	0.50	6.4	11.3	3.09	737	-11.0	29.5
R410A-ZnO NL	2.4	20	129	15.3	972	0.59	973	329.2	0.67	6.9	10.8	3.97	1102	3.1	67.4
R410A-ZnO NL	2.4	20	130	14.9	975	0.50	976	309.6	0.57	6.6	11.2	3.32	851	-9.0	37.4
R410A-ZnO NL	2.4	20	164	15.2	975	0.51	975	313.2	0.58	6.6	10.8	3.71	1333	-10.5	43.5
R410A-ZnO NL	2.4	20	164	15.0	981	0.22	981	250.0	0.28	5.9	11.3	2.78	638	-19.6	39.6
R410A-ZnO NL	2.4	20	165	15.1	973	0.43	974	294.5	0.49	6.3	10.9	3.28	1076	-13.8	35.3
R410A-ZnO NL	2.4	20	165	15.2	973	0.33	973	275.0	0.40	6.0	11.1	3.01	875	-16.0	34.3
R410A-ZnO NL	2.4	20	197	15.2	978	0.26	979	258.6	0.31	5.9	11.1	2.93	919	-22.0	29.7
R410A-ZnO NL	2.4	20	197	15.2	977	0.43	977	294.7	0.48	6.4	10.8	3.45	1419	-19.2	29.0
R410A-ZnO NL	2.4	20	198	15.2	974	0.33	974	274.8	0.39	6.0	10.9	3.12	1129	-19.5	27.7
R410A-Al ₂ O ₃ NL	2.4	20	100	15.7	973	0.44	973	296.6	0.54	6.4	13.5	2.23	471	-34.9	8.6
R410A-Al ₂ O ₃ NL	2.4	20	100	15.3	972	0.27	972	260.5	0.37	5.8	12.7	2.22	338	-29.7	2.9
R410A-Al ₂ O ₃ NL	2.4	20	101	15.3	973	0.34	973	277.1	0.45	6.0	13.1	2.20	398	-32.5	3.6
R410A-Al ₂ O ₃ NL	2.4	20	101	16.0	981	0.57	981	324.6	0.67	7.1	12.2	3.27	589	-10.5	25.8
R410A-Al ₂ O ₃ NL	2.4	20	127	15.0	971	0.49	971	308.5	0.57	6.4	11.3	3.09	744	-15.4	20.3
R410A-Al ₂ O ₃ NL	2.4	20	127	15.2	971	0.41	972	290.5	0.49	6.1	11.0	3.18	721	-7.8	28.8
R410A-Al ₂ O ₃ NL	2.4	20	127	15.3	968	0.29	968	264.3	0.37	5.6	11.1	2.82	561	-13.2	28.6
R410A-Al ₂ O ₃ NL	2.4	20	128	15.5	975	0.28	975	263.4	0.36	5.8	11.5	2.77	547	-14.9	27.1
R410A-Al ₂ O ₃ NL	2.4	20	129	15.3	977	0.48	977	305.5	0.56	6.5	11.9	2.92	779	-19.2	27.6
R410A-Al ₂ O ₃ NL	2.4	20	129	15.5	979	0.63	979	337.8	0.71	7.2	10.5	4.85	1004	24.2	50.7
R410A-Al ₂ O ₃ NL	2.4	20	132	14.9	962	0.59	963	330.3	0.67	6.4	9.6	4.88	1054	26.8	59.8
R410A-Al ₂ O ₃ NL	2.4	20	132	15.2	976	0.52	976	314.6	0.60	6.6	11.0	3.54	912	-4.6	44.3

Fluid	OMF [wt.%]	NP_{conc} [wt.%]	\dot{m} [kg/m ² -s]	\ddot{q}_{avg} [kW/m ²]	$P_{ref,avg}$ [kPa]	x_{in} [-]	$P_{ref,in}$ [kPa]	h_{in} [kJ/kg]	x_{avg} [-]	T_{bub} [°C]	$T_{s,avg}$ [°C]	HTC [kW/m ² -K]	$\Delta P/L$ [Pa/m]	HTF [%]	PDF [%]
R410A-Al2O3 NL	2.4	20	160	15.0	968	0.23	968	251.6	0.29	5.4	9.8	3.42	611	-1.4	28.6
R410A-Al2O3 NL	2.4	20	164	15.2	973	0.34	973	275.3	0.40	5.9	9.9	3.83	839	6.9	28.0
R410A-Al2O3 NL	2.4	20	166	15.1	973	0.50	973	311.2	0.56	6.4	9.9	4.47	1254	9.1	37.4
R410A-Al2O3 NL	2.4	20	167	15.1	975	0.41	975	292.0	0.47	6.2	10.1	3.91	1047	3.7	35.1
R410A-Al2O3 NL	2.4	20	196	15.1	975	0.26	975	258.7	0.31	5.7	10.3	3.29	853	-12.5	20.0
R410A-Al2O3 NL	2.4	20	203	15.1	975	0.32	976	273.1	0.38	5.9	10.1	3.64	1134	-5.5	31.6
R410A-Al2O3 NL	2.4	20	204	15.1	978	0.41	978	291.3	0.46	6.3	10.1	4.00	1380	-4.0	30.5

* R410A-POE oil injection-extraction test

Appendix-D

Single-Phase Flow Experimental Data Set

The data set reported below represents the series of single-phase flow heat transfer tests conducted during the experimental campaign. At the beginning of each test series, the table lists the fluid tested. For each test, the conditions of the test section are provided, together with the calculated heat transfer coefficient, HTC_{exp} . The last column of the table provides the predicted, HTC_{cht} using equation (44).

#	Fluid	OMF [wt.%]	NP_{conc} [wt.%]	\dot{m} [kg/m ² -s]	Re [-]	\dot{q}_{avg} [kW/m ²]	P_{in} [kPa]	h_{in} [kJ/kg]	$T_{ref,in}$ [°C]	$T_{ref,out}$ [°C]	$T_{ref,avg}$ [°C]	$T_{s,avg}$ [°C]
1	R410A	0	0	198	14889	8.5	1460	209.7	6.0	14.3	10.1	21.2
2	R410A	0	0	199	16331	8.7	1744	209.6	6.1	14.0	10.1	21.0
3	R410A	0	0	207	15303	9.0	1406	207.8	5.9	14.1	10.0	20.4
4	R410A	0	0	208	15282	8.7	1401	207.8	5.9	13.8	9.9	20.1
5	R410A	0	0	208	15499	8.8	1437	209.1	5.7	13.8	9.8	20.6
6	R410A	0	0	209	15485	8.2	1422	209.2	5.7	13.3	9.5	20.0
7	R410A	0	0	209	16943	8.5	1706	209.2	5.8	13.3	9.5	20.0
8	R410A	0	0	209	15786	8.8	1471	209.2	5.8	13.4	9.6	18.7
9	R410A-POE	3	0	209	13107	8.8	1499	201.6	5.8	13.8	9.8	22.4
10	R410A-ZNO NL	3	14	208	12842	8.7	1486	202.8	5.7	13.4	9.6	23.1
11	R410A-ZNO NL	3	14	241	14713	8.5	1455	202.7	5.6	12.0	8.8	21.7
12	R410A-Al2O3 NL	3	20	207	13884	8.6	1741	203.0	5.7	13.6	9.7	22.8
13	R410A-Al2O3 NL	3	20	240	15660	8.4	1665	203.1	5.8	12.3	9.1	20.2

#	Fluid	HTC_{exp} [kW/m ² -K]	HTC_{cht} [kW/m ² -K] modified Buongiorno model	$HTC_{exp,Gnielinski}$ [kW/m ² -K]
1	R410A	0.77	0.61	0.69
2	R410A	0.80	0.62	0.71
3	R410A	0.82	0.63	0.71
4	R410A	0.79	0.63	0.71
5	R410A	0.81	0.64	0.71
6	R410A	0.78	0.64	0.72
7	R410A	0.81	0.65	0.74
8	R410A	0.97	0.64	0.72
9	R410A-POE	0.69	0.59	0.66
10	R410A-ZNO NL	0.64	0.59	0.66
11	R410A-ZNO NL	0.66	0.66	0.75
12	R410A-Al2O3 NL	0.66	0.59	0.68
13	R410A-Al2O3 NL	0.75	0.67	0.76

Appendix-E

Data Reduction in EES

The Engineering Equation Solver (EES) code reported below was used for the data reduction. At the end of the code, inputs (experimentally recorded raw data) are provided for one sample two-phase flow test of R410A at $x_{avg}=0.37$ and $\dot{m}=165 \text{ kg/m}^2\text{-s}$, and the resulting output variables obtained after data reduction calculations are reported later. The calculated *HTF* and *PDF* in the output variables were 0%, considering their propagated uncertainty, and represented the R410A baseline tests in absence of lubricants in Figure 23 and Figure 24. The calculated *HTC* in the output variable was plotted in Figure 51 (b) and Figure 52 (a). The calculated delPperL , $\Delta P/L$, was plotted in Figure 29 (b). The results of the sample two-phase flow test of R410A test at $x_{avg}=0.37$ and $\dot{m}=165 \text{ kg/m}^2\text{-s}$ results are also reported in Appendix-C.

EES code for data reduction

```
"Data for Tube Calorimeter"
R$='R410A'

D_1=(3/8)*convert(in,m)    "diamter at tube ID"
L_ts=2.26*convert(ft,m)    "test section length"

MF=(m_dot_ref*convert(lbm/hr,kg/s))*4/(PI*D_1*D_1)

p_r[1]=p_in_preheater*convert(psia,kPa)

"PrePre-Heater or Preheater-0-----"
"The condenser was converted to perform as a pre-preheater (or preheater-0) after 8-24-2018, i.e. it was in
between the Coriolis MFM and the preheater"
T_r_0=converttemp('F', 'C', T_in_preheater0)
{h_r_0=enthalpy(R$, P=p_r[1],T=T_r_0) "here is single phase or subcooled refrigerant condition"}
h_r_0=(enthalpy(R$, P=p_r[1],T=T_r_0))*(1-OMF)+oilspecificenthalpy(T_r_0)*OMF "here is single phase or
subcooled refrigerant condition"
h_r_1_check=h_r_0+Q_condenser/(m_dot_ref*convert(lbm/hr,kg/s))
```

density_ref_sat=**density**(R\$,T=T_r_0,P=p_r[1]) "this is used in excel file to compare the density calculated with Coriolis MFM to estimate the OMF"

"Pre-Heater or Preheater-1-----"

T_r[1]=**converttemp**('F', 'C', T_in_preheater)

{h_r[1]=**enthalpy**(R\$, P=p_r[1],T=T_r[1]) "here is single phase or subcooled refrigerant condition"}

h_r[1]=(**enthalpy**(R\$, P=p_r[1],T=T_r[1]))*(1-OMF)+**oilspecificenthalpy**(T_r[1])*OMF "here is single phase or subcooled refrigerant condition"

T_ETW_average_preheater=(**converttemp**('F', 'C', T_ETW_in_preheater)+**converttemp**('F', 'C', T_ETW_out_preheater))/2

cp_ETW_preheater=**cp**(EG,T=T_ETW_average_preheater,C=35 [%])

Q_preheaterOnly=(m_dot_ETW_preheater***convert**(lbm/hr,kg/s))*cp_ETW_preheater*(**converttemp**('F', 'C', T_ETW_in_preheater)-**converttemp**('F', 'C', T_ETW_out_preheater))

delT_potential=Tambient-(T_out_preheater+T_testsection_in)/2

Q_loss_after_preheater=(-1.38577+0.02598*m_dot_ref+0.8137*delT_potential-0.00009*m_dot_ref*m_dot_ref-0.002362*m_dot_ref*delT_potential)***convert**(J/s,kJ/s)

"qGainAfterPreheater= Q_loss_after_preheater"

Q_oilInjected=**q_oilinjected_find**(T_testsection_in,T_OilSyringePump,rho_OilSyringePump,m_OilSyringePump)

Q_preheater=Q_preheaterOnly+Q_loss_after_preheater+Q_oilInjected

h_r[2]=h_r[1]+Q_preheater/(m_dot_ref***convert**(lbm/hr,kg/s))

p_r[2]=p_in_testSection***convert**(psia,kPa) "pressure at inlet of test section"

{x_in=**quality**(R\$, h=h_r[2], P=p_r[2])}

x_in=(h_r[2]-OMF***oilspecificenthalpy**(**converttemp**('F', 'C', T_testsection_in)))-(1-OMF)*(**enthalpy**(R\$,P=p_r[2],x=0))/(**enthalpy**(R\$,P=p_r[2],x=1)-**Enthalpy**(R\$,P=p_r[2],x=0))

"quality from eq 7, Hu, Haitao, Guoliang Ding, Wenjian Wei, Zhence Wang, and Kaijian Wang. Heat transfer characteristics of R410A-oil mixture flow boiling inside a 7 mm straight smooth tube. Experimental Thermal and Fluid Science 32, no. 3 (2008): 857-869"

"-----"

h_r_prePreheater_out=h_r[1]+(Q_preheaterOnly/2)/(m_dot_ref***convert**(lbm/hr,kg/s))

T_r_prePreheater_out=**converttemp**('C', 'F', **temperature**(R\$,P=p_r[1],h=h_r_prePreheater_out))

T_subcool_prePreheater_out=**converttemp**('C', 'F', **temperature**(R\$,P=p_r[1],x=0))-T_r_prePreheater_out

T_subcool_Preheater_in_current=**converttemp**('C', 'F', **temperature**(R\$,P=p_r[1],x=0))-T_in_preheater

"Test Section-ts-----"

h_r[3]=h_r[2]+Q_totalheater/(m_dot_ref***convert**(lbm/hr,kg/s))

p_r[3]=p_r[2]+delP_testSection***convert**(psia,kPa) "pressure at outlet of test section"

{x_out=**quality**(R\$, h=h_r[3], P=p_r[3])}

x_out=(h_r[3]-OMF***oilspecificenthalpy**(**converttemp**('F', 'C', T_testsection_in)))-(1-OMF)*(**enthalpy**(R\$,P=p_r[3],x=0))/(**enthalpy**(R\$,P=p_r[3],x=1)-**Enthalpy**(R\$,P=p_r[3],x=0))

"quality from eq 7, Hu, Haitao, Guoliang Ding, Wenjian Wei, Zhence Wang, and Kaijian Wang. Heat transfer characteristics of R410A-oil mixture flow boiling inside a 7 mm straight smooth tube. Experimental Thermal and Fluid Science 32, no. 3 (2008): 857-869"

$$x_{avg}=(x_{in}+x_{out})/2$$

$$\Delta x=(x_{out}-x_{in})$$

"-----"

"Following is the Heat Transfer analysis in the copper slab-----"

$$r_1=((3/8)*0.5)*\text{convert}(\text{in},\text{m}) \quad \text{"radius at tube ID"}$$

$$r_2=((1/2)*0.5)*\text{convert}(\text{in},\text{m}) \quad \text{"radius at tube OD"}$$

$$L_{TC}=(0.3125)*\text{convert}(\text{in},\text{m}) \quad \text{"distance of TC in level3 or level4 from tube OD"}$$

$$s_{perimeter}=(0.361367)*\text{convert}(\text{in},\text{m}) \quad \text{"s_perimeter is surface perimeter of refrigerant tube OD in contact with only one copper plate (either top plate or bottom 1inchx1inch copper plate)"}$$

$$L=(4)*\text{convert}(\text{in},\text{m}) \quad \text{"heat transfer distance between the thermocouples in level1 and level2, and thermocouples in level5 and level6"}$$

$$k=0.401 \quad \text{"[kW/m-C], thermal conductivity of copper"}$$

$$\{k=\text{conductivity}(\text{Copper}, T=((NL_level1_T3+NL_level2_T3+NL_level6_T3+NL_level5_T3)/4))/1000\}$$

$$\Delta T_{topSlab_1}=\text{converttemp}('F', 'C', NL_level1_T1)-\text{converttemp}('F', 'C', NL_level2_T1)$$

$$\Delta T_{topSlab_2}=\text{converttemp}('F', 'C', NL_level1_T2)-\text{converttemp}('F', 'C', NL_level2_T2)$$

$$\Delta T_{topSlab_3}=\text{converttemp}('F', 'C', NL_level1_T3)-\text{converttemp}('F', 'C', NL_level2_T3)$$

$$\Delta T_{topSlab_4}=\text{converttemp}('F', 'C', NL_level1_T4)-\text{converttemp}('F', 'C', NL_level2_T4)$$

$$\Delta T_{topSlab_5}=\text{converttemp}('F', 'C', NL_level1_T5)-\text{converttemp}('F', 'C', NL_level2_T5)$$

$$\Delta T_{bottomSlab_1}=\text{converttemp}('F', 'C', NL_level6_T1)-\text{converttemp}('F', 'C', NL_level5_T1)$$

$$\Delta T_{bottomSlab_2}=\text{converttemp}('F', 'C', NL_level6_T2)-\text{converttemp}('F', 'C', NL_level5_T2)$$

$$\Delta T_{bottomSlab_3}=\text{converttemp}('F', 'C', NL_level6_T3)-\text{converttemp}('F', 'C', NL_level5_T3)$$

$$\Delta T_{bottomSlab_4}=\text{converttemp}('F', 'C', NL_level6_T4)-\text{converttemp}('F', 'C', NL_level5_T4)$$

$$\Delta T_{bottomSlab_5}=\text{converttemp}('F', 'C', NL_level6_T5)-\text{converttemp}('F', 'C', NL_level5_T5)$$

"below R is the representative resistance correction factor f to account for the thermocouple contact resistance and change of thermal paste conductivity with temperature"

$$T_{avg_copperSlab}=(NL_level1_T3+NL_level2_T3+NL_level6_T3+NL_level5_T3)/4$$

$$R=-0.0032*T_{avg_copperSlab}+0.1412$$

$$\text{Resistance_correction_factor}=R$$

$$\text{HeatFlux_topPlate1}=\Delta T_{topSlab_1}/(L/k*(1+R))$$

$$\text{HeatFlux_topPlate2}=\Delta T_{topSlab_2}/(L/k*(1+R))$$

$$\text{HeatFlux_topPlate3}=\Delta T_{topSlab_3}/(L/k*(1+R))$$

$$\text{HeatFlux_topPlate4}=\Delta T_{topSlab_4}/(L/k*(1+R))$$

$$\text{HeatFlux_topPlate5}=\Delta T_{topSlab_5}/(L/k*(1+R))$$

$$\text{HeatFlux_bottomPlate1}=\Delta T_{bottomSlab_1}/(L/k*(1+R))$$

$$\text{HeatFlux_bottomPlate2}=\Delta T_{bottomSlab_2}/(L/k*(1+R))$$

$$\text{HeatFlux_bottomPlate3}=\Delta T_{bottomSlab_3}/(L/k*(1+R))$$


```

HeatFlux_bottomPlate4=delT_bottomSlab_4/(L/k*(1+R))
HeatFlux_bottomPlate5=delT_bottomSlab_5/(L/k*(1+R))

"-----"
"area calculations from LabView"
Area_topPlate1=0.002232858
Area_topPlate2=0.001461691 "L_top1*1*convert(in,m)"
Area_topPlate3=0.001461691
Area_topPlate4=0.001461691 "L_top2*1*convert(in,m)"
Area_topPlate5=0.001461691
Area_topPlate6=0.001461691 "L_top3*1*convert(in,m)"
Area_topPlate7=0.001461691
Area_topPlate8=0.001461691 "L_top4*1*convert(in,m)"
Area_topPlate9=0.001461691
Area_topPlate10=0.001461691 "L_top5*1*convert(in,m)"
Area_topPlate11=0.002192536
Area_bottomPlate1=0.002086689
Area_bottomPlate2=0.001471771"L_bottom1*1*convert(in,m)"
Area_bottomPlate3=0.001471771
Area_bottomPlate4=0.001466731"L_bottom2*1*convert(in,m)"
Area_bottomPlate5=0.001461691
Area_bottomPlate6=0.001582658"L_bottom3*1*convert(in,m)"
Area_bottomPlate7=0.001703626
Area_bottomPlate8=0.001466731"L_bottom4*1*convert(in,m)"
Area_bottomPlate9=0.001229837
Area_bottomPlate10=0.001229837"L_bottom5*1*convert(in,m)"
Area_bottomPlate11=0.002449591
"-----"
"-----Following are the distances of thermocouples in TC level-1 and level-2 of top copper slab-----"
D_topTC11=(0+4.59375)/2*convert(in,m)
D_topTC1=4.59375*convert(in,m)
D_topTC2=9.125*convert(in,m)
D_topTC3=13.65625*convert(in,m)
D_topTC4=18.1875*convert(in,m)
D_topTC5=22.71875*convert(in,m)
D_topTC55=(27.25+22.71875)/2*convert(in,m)
"-----"
"-----Following are the distances of thermocouples in TC level-5 and level-6 of bottom copper slab-----"
D_bottomTC11=(0+4.375)/2*convert(in,m)
D_bottomTC1=4.375*convert(in,m)
D_bottomTC2=8.9375*convert(in,m)
D_bottomTC3=13.46875*convert(in,m)
D_bottomTC4=18.75*convert(in,m)
D_bottomTC5=22.5625*convert(in,m)
D_bottomTC55=(27.3125+22.5625)/2*convert(in,m)
"-----"
"-----"
"-----Following are the distances of thermocouples in TC level-3 of top copper slab-----"
"x1=0.375 ft "
"x2=0.753 ft "
"x3=1.128 ft "
"x4=1.570 ft "
"x5=1.883 ft "

```

```

"-----"
"-----"
"-----Following are the distances of thermocouples in TC level-4 of bottom copper slab-----"
"x11=0.313 ft "
"x12=0.690 ft "
"x13=1.068 ft "
"x14=1.443 ft "
"x15=1.883 ft "
"-----"

```

---Discretizing heat fluxes (HF)---

```

HF_TopHeater_1=HeatFlux_topPlate1+(HeatFlux_topPlate1-HeatFlux_topPlate2)*((D_topTC11-
D_topTC1)/(D_topTC1-D_topTC2))
HF_TopHeater_2=HeatFlux_topPlate1
HF_TopHeater_3=(HeatFlux_topPlate1+HeatFlux_topPlate2)/2
HF_TopHeater_4=HeatFlux_topPlate2
HF_TopHeater_5=(HeatFlux_topPlate2+HeatFlux_topPlate3)/2
HF_TopHeater_6=HeatFlux_topPlate3
HF_TopHeater_7=(HeatFlux_topPlate3+HeatFlux_topPlate4)/2
HF_TopHeater_8=HeatFlux_topPlate4
HF_TopHeater_9=(HeatFlux_topPlate4+HeatFlux_topPlate5)/2
HF_TopHeater_10=HeatFlux_topPlate5
HF_TopHeater_11=HeatFlux_topPlate5+(HeatFlux_topPlate5-HeatFlux_topPlate4)*((D_topTC55-
D_topTC5)/(D_topTC5-D_topTC4))

```

```

HF_bottomHeater_1=HeatFlux_bottomPlate1+(HeatFlux_bottomPlate1-
HeatFlux_bottomPlate2)*((D_bottomTC11-D_bottomTC1)/(D_bottomTC1-D_bottomTC2))
HF_bottomHeater_2=HeatFlux_bottomPlate1
HF_bottomHeater_3=(HeatFlux_bottomPlate1+HeatFlux_bottomPlate2)/2
HF_bottomHeater_4=HeatFlux_bottomPlate2
HF_bottomHeater_5=(HeatFlux_bottomPlate2+HeatFlux_bottomPlate3)/2
HF_bottomHeater_6=HeatFlux_bottomPlate3
HF_bottomHeater_7=(HeatFlux_bottomPlate3+HeatFlux_bottomPlate4)/2
HF_bottomHeater_8=HeatFlux_bottomPlate4
HF_bottomHeater_9=(HeatFlux_bottomPlate4+HeatFlux_bottomPlate5)/2
HF_bottomHeater_10=HeatFlux_bottomPlate5
HF_bottomHeater_11=HeatFlux_bottomPlate5+(HeatFlux_bottomPlate5-
HeatFlux_bottomPlate4)*((D_bottomTC55-D_bottomTC5)/(D_bottomTC5-
D_bottomTC4))

```

---Discretized heat-Q (kW) in each 11 segments---

```

Q_TopHeater_1=HF_TopHeater_1*Area_topPlate1
Q_TopHeater_2=HF_TopHeater_2*Area_topPlate2
Q_TopHeater_3=HF_TopHeater_3*Area_topPlate3
Q_TopHeater_4=HF_TopHeater_4*Area_topPlate4
Q_TopHeater_5=HF_TopHeater_5*Area_topPlate5
Q_TopHeater_6=HF_TopHeater_6*Area_topPlate6
Q_TopHeater_7=HF_TopHeater_7*Area_topPlate7
Q_TopHeater_8=HF_TopHeater_8*Area_topPlate8
Q_TopHeater_9=HF_TopHeater_9*Area_topPlate9
Q_TopHeater_10=HF_TopHeater_10*Area_topPlate10

```

$Q_{\text{TopHeater}_{11}} = HF_{\text{TopHeater}_{11}} * \text{Area}_{\text{topPlate}11}$

$Q_{\text{bottomHeater}_{1}} = HF_{\text{bottomHeater}_{1}} * \text{Area}_{\text{bottomPlate}1}$

$Q_{\text{bottomHeater}_{2}} = HF_{\text{bottomHeater}_{2}} * \text{Area}_{\text{bottomPlate}2}$

$Q_{\text{bottomHeater}_{3}} = HF_{\text{bottomHeater}_{3}} * \text{Area}_{\text{bottomPlate}3}$

$Q_{\text{bottomHeater}_{4}} = HF_{\text{bottomHeater}_{4}} * \text{Area}_{\text{bottomPlate}4}$

$Q_{\text{bottomHeater}_{5}} = HF_{\text{bottomHeater}_{5}} * \text{Area}_{\text{bottomPlate}5}$

$Q_{\text{bottomHeater}_{6}} = HF_{\text{bottomHeater}_{6}} * \text{Area}_{\text{bottomPlate}6}$

$Q_{\text{bottomHeater}_{7}} = HF_{\text{bottomHeater}_{7}} * \text{Area}_{\text{bottomPlate}7}$

$Q_{\text{bottomHeater}_{8}} = HF_{\text{bottomHeater}_{8}} * \text{Area}_{\text{bottomPlate}8}$

$Q_{\text{bottomHeater}_{9}} = HF_{\text{bottomHeater}_{9}} * \text{Area}_{\text{bottomPlate}9}$

$Q_{\text{bottomHeater}_{10}} = HF_{\text{bottomHeater}_{10}} * \text{Area}_{\text{bottomPlate}10}$

$Q_{\text{bottomHeater}_{11}} = HF_{\text{bottomHeater}_{11}} * \text{Area}_{\text{bottomPlate}11}$

$Q_{\text{totalheater}} = Q_{\text{topHeater}_{1}} + Q_{\text{topHeater}_{2}} + Q_{\text{topHeater}_{3}} + Q_{\text{topHeater}_{4}} + Q_{\text{topHeater}_{5}} + Q_{\text{topHeater}_{6}} + Q_{\text{topHeater}_{7}} + Q_{\text{topHeater}_{8}} + Q_{\text{topHeater}_{9}} + Q_{\text{topHeater}_{10}} + Q_{\text{topHeater}_{11}} + Q_{\text{bottomHeater}_{1}} + Q_{\text{bottomHeater}_{2}} + Q_{\text{bottomHeater}_{3}} + Q_{\text{bottomHeater}_{4}} + Q_{\text{bottomHeater}_{5}} + Q_{\text{bottomHeater}_{6}} + Q_{\text{bottomHeater}_{7}} + Q_{\text{bottomHeater}_{8}} + Q_{\text{bottomHeater}_{9}} + Q_{\text{bottomHeater}_{10}} + Q_{\text{bottomHeater}_{11}}$

"-----"

"-----Surface temperature at tube ID-----"

"Following are the length of the discretized small sections of the tube, normal to which the discretized heat transfer takes place"

$L_{\text{top}1} = 2.2656 * \text{convert}(\text{in}, \text{m})$

$L_{\text{top}2} = 2.2656 * \text{convert}(\text{in}, \text{m})$

$L_{\text{top}3} = 2.2656 * \text{convert}(\text{in}, \text{m})$

$L_{\text{top}4} = 2.2656 * \text{convert}(\text{in}, \text{m})$

$L_{\text{top}5} = 2.2656 * \text{convert}(\text{in}, \text{m})$

$L_{\text{bottom}1} = 2.28125 * \text{convert}(\text{in}, \text{m})$

$L_{\text{bottom}2} = 2.2734375 * \text{convert}(\text{in}, \text{m})$

$L_{\text{bottom}3} = 2.453125 * \text{convert}(\text{in}, \text{m})$

$L_{\text{bottom}4} = 2.640625 * \text{convert}(\text{in}, \text{m})$

$L_{\text{bottom}5} = 2.27344 * \text{convert}(\text{in}, \text{m})$

$L_{\text{bottom}6} = 1.90625 * \text{convert}(\text{in}, \text{m})$

" $R_{\text{thermalpaste}}$ [C/kW] is the thermal resistance of thermal paste at level 3 and level4, and between the junction of ref copper tube OD and copper plate"

" $R_{\text{mid_contact}}$ [C/kW] is the TC contact resistance at levelMid"

"Cengel and Ghajar. Heat and Mass Transfer Fundamentals and Application, 4th edition. Reports in Table 3-2 that for copper to copper contact in air the contact resistance is $R_{\text{c}} = (1/h_{\text{c}}) = 0.00699 \text{ m}^2\text{-K/kW}$ However we have a paste of thermal grease between the copper to copper contact, and we assume that this reduces the presence of air and thus reduces the contact resistance at the copper to copper contact significantly. Thus we consider the contact resistance to be zero in the analysis"

$R_{\text{top_thermalpaste}1} = r_{\text{contacttop}}(1, \text{HBFlag})$ "contact resistance at one location"

$R_{\text{top_thermalpaste}2} = r_{\text{contacttop}}(2, \text{HBFlag})$

$R_{\text{top_thermalpaste}3} = r_{\text{contacttop}}(3, \text{HBFlag})$

$R_{\text{top_thermalpaste}4} = r_{\text{contacttop}}(4, \text{HBFlag})$

$R_{\text{top_thermalpaste}5} = r_{\text{contacttop}}(5, \text{HBFlag})$

$R_{\text{mid_contact}1} = r_{\text{contactmid}}(1, \text{HBFlag})$

```

R_mid_contact2=r_contactmid(2,HBFlag)
R_mid_contact3=r_contactmid(3,HBFlag)
R_mid_contact4=r_contactmid(4,HBFlag)
R_mid_contact5=r_contactmid(5,HBFlag)

R_bottom_thermalpaste1=r_contactbottom(1,HBFlag)
R_bottom_thermalpaste2=r_contactbottom(2,HBFlag)
R_bottom_thermalpaste3=r_contactbottom(3,HBFlag)
R_bottom_thermalpaste4=r_contactbottom(4,HBFlag)
R_bottom_thermalpaste5=r_contactbottom(5,HBFlag)

Tsurface_top_ID_1=converttemp('F', 'C', NL_level3_T1)-
Q_TopHeater_2*(2*ln(r_2/r_1)/(2*PI*L_top1*k)+R_top_thermalpaste1+L_TC/(k*s_perimeter*L_top1))
Tsurface_top_ID_2=converttemp('F', 'C', NL_level3_T2)-
Q_TopHeater_4*(2*ln(r_2/r_1)/(2*PI*L_top2*k)+R_top_thermalpaste2+L_TC/(k*s_perimeter*L_top2))
Tsurface_top_ID_3=converttemp('F', 'C', NL_level3_T3)-
Q_TopHeater_6*(2*ln(r_2/r_1)/(2*PI*L_top3*k)+R_top_thermalpaste3+L_TC/(k*s_perimeter*L_top3))
Tsurface_top_ID_4=converttemp('F', 'C', NL_level3_T4)-
Q_TopHeater_8*(2*ln(r_2/r_1)/(2*PI*L_top4*k)+R_top_thermalpaste4+L_TC/(k*s_perimeter*L_top4))
Tsurface_top_ID_5=converttemp('F', 'C', NL_level3_T5)-
Q_TopHeater_10*(2*ln(r_2/r_1)/(2*PI*L_top5*k)+R_top_thermalpaste5+L_TC/(k*s_perimeter*L_top5))

Tsurface_bottom_ID_1=converttemp('F', 'C', NL_level4_T1)-
Q_bottomHeater_2*(2*ln(r_2/r_1)/(2*PI*L_bottom1*k)+R_bottom_thermalpaste1+L_TC/(k*s_perimeter*L_bottom1))
Tsurface_bottom_ID_2=converttemp('F', 'C', NL_level4_T2)-
Q_bottomHeater_4*(2*ln(r_2/r_1)/(2*PI*L_bottom2*k)+R_bottom_thermalpaste2+L_TC/(k*s_perimeter*L_bottom2))
Tsurface_bottom_ID_3=converttemp('F', 'C', NL_level4_T3)-
Q_bottomHeater_6*(2*ln(r_2/r_1)/(2*PI*L_bottom3*k)+R_bottom_thermalpaste3+L_TC/(k*s_perimeter*L_bottom3))
Tsurface_bottom_ID_4=converttemp('F', 'C', NL_level4_T4)-
((Q_bottomHeater_7+Q_bottomHeater_8)/2)*(2*ln(r_2/r_1)/(2*PI*L_bottom44*k)+R_bottom_thermalpaste4+
L_TC/(k*s_perimeter*L_bottom44))
Tsurface_bottom_ID_5=converttemp('F', 'C', NL_level4_T5)-
Q_bottomHeater_10*(2*ln(r_2/r_1)/(2*PI*L_bottom5*k)+R_bottom_thermalpaste5+L_TC/(k*s_perimeter*L_bottom5))

Tsurface_mid_ID_1=Tsurface_mid_ID_2 "converttemp('F', 'C', NL_levelMid_T1)-
Q_midHeater_2*(ln(r_2/r_1)/(2*PI*L_top1*k)+R_mid_contact1) Note: The thermocouple NL_levelMid_T1
could have error, hence is eliminated"
Tsurface_mid_ID_2=converttemp('F', 'C', NL_levelMid_T2)-
Q_midHeater_4*(ln(r_2/r_1)/(2*PI*L_top2*k)+R_mid_contact2)
Tsurface_mid_ID_3=converttemp('F', 'C', NL_levelMid_T3)-
Q_midHeater_6*(ln(r_2/r_1)/(2*PI*L_top3*k)+R_mid_contact3)
Tsurface_mid_ID_4=converttemp('F', 'C', NL_levelMid_T4)-
Q_midHeater_8*(ln(r_2/r_1)/(2*PI*L_top4*k)+R_mid_contact4)
Tsurface_mid_ID_5=converttemp('F', 'C', NL_levelMid_T5)-
Q_midHeater_10*(ln(r_2/r_1)/(2*PI*L_top5*k)+R_mid_contact5)

T_surface_avg=(Tsurface_top_ID_1+Tsurface_top_ID_2+Tsurface_top_ID_3+Tsurface_top_ID_4+Tsurface_top_ID_5+
Tsurface_bottom_ID_1+Tsurface_bottom_ID_2+Tsurface_bottom_ID_3+Tsurface_bottom_ID_4+Tsurface

```

```

bottom_ID_5+Tsurface_mid_ID_1+Tsurface_mid_ID_2+Tsurface_mid_ID_3+Tsurface_mid_ID_4+Tsurface_mid_ID_5)/15
"-----"
Q_midHeater_2=Q_TopHeater_2+Q_bottomHeater_2*(L_top1/L_bottom1)
Q_midHeater_4=Q_TopHeater_4+Q_bottomHeater_4*(L_top2/L_bottom2)
Q_midHeater_6=Q_TopHeater_6+Q_bottomHeater_6*(L_top3/L_bottom3)
Q_midHeater_8=Q_TopHeater_8+Q_bottomHeater_8*(L_top4/L_bottom4)
Q_midHeater_10=Q_TopHeater_10+Q_bottomHeater_10*(L_top5/L_bottom5)
"-----"

"-----HeatFlux at tube ID-----"
HF_TopTubeID1=Q_TopHeater_2/((2*PI*r_1*L_top1)/2)
HF_TopTubeID2=Q_TopHeater_4/((2*PI*r_1*L_top2)/2)
HF_TopTubeID3=Q_TopHeater_6/((2*PI*r_1*L_top3)/2)
HF_TopTubeID4=Q_TopHeater_8/((2*PI*r_1*L_top4)/2)
HF_TopTubeID5=Q_TopHeater_10/((2*PI*r_1*L_top5)/2)

HF_BottomTubeID1=Q_bottomHeater_2/((2*PI*r_1*L_bottom1)/2)
HF_BottomTubeID2=Q_bottomHeater_4/((2*PI*r_1*L_bottom2)/2)
HF_BottomTubeID3=Q_bottomHeater_6/((2*PI*r_1*L_bottom3)/2)
HF_BottomTubeID4=((Q_bottomHeater_7+Q_bottomHeater_8)/2)/((2*PI*r_1*L_bottom44)/2)
HF_BottomTubeID5=Q_bottomHeater_10/((2*PI*r_1*L_bottom5)/2)

HF_midTubeID1=(HF_TopTubeID1+HF_BottomTubeID1*(L_top1/L_bottom1))/2
HF_midTubeID2=(HF_TopTubeID2+HF_BottomTubeID2*(L_top2/L_bottom2))/2
HF_midTubeID3=(HF_TopTubeID3+HF_BottomTubeID3*(L_top3/L_bottom3))/2
HF_midTubeID4=(HF_TopTubeID4+HF_BottomTubeID4*(L_top4/L_bottom44))/2
HF_midTubeID5=(HF_TopTubeID5+HF_BottomTubeID5*(L_top5/L_bottom5))/2

HF_testsection_avg=(HF_TopTubeID1+HF_TopTubeID2+HF_TopTubeID3+HF_TopTubeID4+HF_TopTubeID5+HF_BottomTubeID1+HF_BottomTubeID2+HF_BottomTubeID3+HF_BottomTubeID4+HF_BottomTubeID5+HF_midTubeID1+HF_midTubeID2+HF_midTubeID3+HF_midTubeID4+HF_midTubeID5)/15
"-----"

"-----evaluation of T_saturation-----"
"see on top of the ees code for the function written for tsat"
T_sat_testSection=tsat((p_r[2]+p_r[3])/2,x_avg,R$,HBFlag,((T_testsection_out+T_testsection_in)/2),ref_Tsat_correction,OMF)
T_sat_testSection_in=tsat(p_r[2],x_in,R$,HBFlag,T_testsection_in,ref_Tsat_correction,OMF)
T_sat_testSection_out=tsat(p_r[3],x_out,R$,HBFlag,T_testsection_out,ref_Tsat_correction,OMF)
{T_sat_testSection_in=Temperature(R$,P=p_r[2],x=x_in)}

T_sat_level3_1=tsat((((27.125*convert(in,m)-L_TC_level3_1)/(27.125*convert(in,m)))*(p_r[3]-p_r[2])+p_r[2]),(((27.125*convert(in,m)-L_TC_level3_1)/(27.125*convert(in,m)))*(x_out-x_in)+x_in),R$,HBFlag,(((27.125*convert(in,m)-L_TC_level3_1)/(27.125*convert(in,m)))*(T_testsection_out-T_testsection_in)+T_testsection_in),ref_Tsat_correction,OMF)
T_sat_level3_2=tsat((((27.125*convert(in,m)-L_TC_level3_2)/(27.125*convert(in,m)))*(p_r[3]-p_r[2])+p_r[2]),(((27.125*convert(in,m)-L_TC_level3_2)/(27.125*convert(in,m)))*(x_out-x_in)+x_in),R$,HBFlag,(((27.125*convert(in,m)-L_TC_level3_1)/(27.125*convert(in,m)))*(T_testsection_out-T_testsection_in)+T_testsection_in),ref_Tsat_correction,OMF)
T_sat_level3_3=tsat((((27.125*convert(in,m)-L_TC_level3_3)/(27.125*convert(in,m)))*(p_r[3]-p_r[2])+p_r[2]),(((27.125*convert(in,m)-L_TC_level3_3)/(27.125*convert(in,m)))*(x_out-

```

```

x_in)+x_in),R$,HBFlag,(((27.125*convert(in,m)-L_TC_level3_1)/(27.125*convert(in,m)))*(T_testsection_out-
T_testsection_in)+T_testsection_in),ref_Tsat_correction,OMF)
T_sat_level3_4=tsat((((27.125*convert(in,m)-L_TC_level3_4)/(27.125*convert(in,m)))*(p_r[3]-
p_r[2])+p_r[2]),(((27.125*convert(in,m)-L_TC_level3_4)/(27.125*convert(in,m)))*(x_out-
x_in)+x_in),R$,HBFlag,(((27.125*convert(in,m)-L_TC_level3_1)/(27.125*convert(in,m)))*(T_testsection_out-
T_testsection_in)+T_testsection_in),ref_Tsat_correction,OMF)
T_sat_level3_5=tsat((((27.125*convert(in,m)-L_TC_level3_5)/(27.125*convert(in,m)))*(p_r[3]-
p_r[2])+p_r[2]),(((27.125*convert(in,m)-L_TC_level3_5)/(27.125*convert(in,m)))*(x_out-
x_in)+x_in),R$,HBFlag,(((27.125*convert(in,m)-L_TC_level3_1)/(27.125*convert(in,m)))*(T_testsection_out-
T_testsection_in)+T_testsection_in),ref_Tsat_correction,OMF)

```

"T_sat_level3 or Tsat at level_3 are same for level_mid"

```

T_sat_level4_1=tsat((((27.125*convert(in,m)-L_TC_level4_1)/(27.125*convert(in,m)))*(p_r[3]-
p_r[2])+p_r[2]),(((27.125*convert(in,m)-L_TC_level4_1)/(27.125*convert(in,m)))*(x_out-
x_in)+x_in),R$,HBFlag,(((27.125*convert(in,m)-L_TC_level3_1)/(27.125*convert(in,m)))*(T_testsection_out-
T_testsection_in)+T_testsection_in),ref_Tsat_correction,OMF)
T_sat_level4_2=tsat((((27.125*convert(in,m)-L_TC_level4_2)/(27.125*convert(in,m)))*(p_r[3]-
p_r[2])+p_r[2]),(((27.125*convert(in,m)-L_TC_level4_2)/(27.125*convert(in,m)))*(x_out-
x_in)+x_in),R$,HBFlag,(((27.125*convert(in,m)-L_TC_level3_1)/(27.125*convert(in,m)))*(T_testsection_out-
T_testsection_in)+T_testsection_in),ref_Tsat_correction,OMF)
T_sat_level4_3=tsat((((27.125*convert(in,m)-L_TC_level4_3)/(27.125*convert(in,m)))*(p_r[3]-
p_r[2])+p_r[2]),(((27.125*convert(in,m)-L_TC_level4_3)/(27.125*convert(in,m)))*(x_out-
x_in)+x_in),R$,HBFlag,(((27.125*convert(in,m)-L_TC_level3_1)/(27.125*convert(in,m)))*(T_testsection_out-
T_testsection_in)+T_testsection_in),ref_Tsat_correction,OMF)
T_sat_level4_4=tsat((((27.125*convert(in,m)-L_TC_level4_4)/(27.125*convert(in,m)))*(p_r[3]-
p_r[2])+p_r[2]),(((27.125*convert(in,m)-L_TC_level4_4)/(27.125*convert(in,m)))*(x_out-
x_in)+x_in),R$,HBFlag,(((27.125*convert(in,m)-L_TC_level3_1)/(27.125*convert(in,m)))*(T_testsection_out-
T_testsection_in)+T_testsection_in),ref_Tsat_correction,OMF)
T_sat_level4_5=tsat((((27.125*convert(in,m)-L_TC_level4_5)/(27.125*convert(in,m)))*(p_r[3]-
p_r[2])+p_r[2]),(((27.125*convert(in,m)-L_TC_level4_5)/(27.125*convert(in,m)))*(x_out-
x_in)+x_in),R$,HBFlag,(((27.125*convert(in,m)-L_TC_level3_1)/(27.125*convert(in,m)))*(T_testsection_out-
T_testsection_in)+T_testsection_in),ref_Tsat_correction,OMF)

```

"-----Following are the distances of thermocouples in TC level-3 and level-mid -----"

```

L_TC_level3_1=4.5*convert(in,m)
L_TC_level3_2=9.03125*convert(in,m)
L_TC_level3_3=13.53125*convert(in,m)
L_TC_level3_4=18.84375*convert(in,m)
L_TC_level3_5=22.59375*convert(in,m)

```

"-----"

"-----Following are the distances of thermocouples in TC level-4-----"

```

L_TC_level4_1=3.75*convert(in,m)
L_TC_level4_2=8.28125*convert(in,m)
L_TC_level4_3=12.8125*convert(in,m)
L_TC_level4_4=17.3125*convert(in,m)
L_TC_level4_5=22.59375*convert(in,m)

```

"-----"

"-----HTC calculations-----"

"HTC based on all overall averages"

```

HTC_avg=HF_testsection_avg/(T_surface_avg-T_sat_testSection)

```

"local_HTCs"

HTC_level3_1=HF_TopTubelD1/(Tsurface_top_ID_1-T_sat_level3_1)
HTC_level3_2=HF_TopTubelD2/(Tsurface_top_ID_2-T_sat_level3_2)
HTC_level3_3=HF_TopTubelD3/(Tsurface_top_ID_3-T_sat_level3_3)
HTC_level3_4=HF_TopTubelD4/(Tsurface_top_ID_4-T_sat_level3_4)
HTC_level3_5=HF_TopTubelD5/(Tsurface_top_ID_5-T_sat_level3_5)

HTC_levelMid_1=HF_midTubelD1/(Tsurface_mid_ID_1-T_sat_level3_1)
HTC_levelMid_2=HF_midTubelD2/(Tsurface_mid_ID_2-T_sat_level3_2)
HTC_levelMid_3=HF_midTubelD3/(Tsurface_mid_ID_3-T_sat_level3_3)
HTC_levelMid_4=HF_midTubelD4/(Tsurface_mid_ID_4-T_sat_level3_4)
HTC_levelMid_5=HF_midTubelD5/(Tsurface_mid_ID_5-T_sat_level3_5)

HTC_level4_1=HF_BottomTubelD1/(Tsurface_bottom_ID_1-T_sat_level4_1)
HTC_level4_2=HF_BottomTubelD2/(Tsurface_bottom_ID_2-T_sat_level4_2)
HTC_level4_3=HF_BottomTubelD3/(Tsurface_bottom_ID_3-T_sat_level4_3)
HTC_level4_4=HF_BottomTubelD4/(Tsurface_bottom_ID_4-T_sat_level4_4)
HTC_level4_5=HF_BottomTubelD5/(Tsurface_bottom_ID_5-T_sat_level4_5)

HTC_avg_of_locals=(HTC_level3_1+HTC_level3_2+HTC_level3_3+HTC_level3_4+HTC_level3_5+HTC_level4_1+HTC_level4_2+HTC_level4_3+HTC_level4_4+HTC_level4_5+HTC_levelMid_1+HTC_levelMid_2+HTC_levelMid_3+HTC_levelMid_4+HTC_levelMid_5)/15

HTC_o=**htc_oo**(MF,x_avg)

HTF=(((HTC_avg_of_locals-HTC_o)*100)/HTC_o)***abs(phase_condition**(HBFlag)-1)

"-----"

"-----delP/length-----"

delPperL=delP_testSection*convert(psia,Pa)/(33*convert(in,m))

"33 inch. is the distance between the ports where differential pressure is measured"

delPperL_o=**delpperl_oo**(MF,x_avg)

PDF=(((delPperL-delPperL_o)*100)/delPperL_o)***abs(phase_condition**(HBFlag)-1)

"-----"

"-----Energy Balance-----"

T_ETW_average_condenser=(converttemp('F', 'C', T_ETW_in_condenser)+converttemp('F', 'C', T_ETW_out_condenser))/2

cp_ETW_condenser=**cp**(EG,T=T_ETW_average_condenser,C=35 [%])

Q_condenser=(m_dot_ETW_preheater*convert(lbm/hr,kg/s))*cp_ETW_condenser*(converttemp('F', 'C', T_ETW_out_preheater)-converttemp('F', 'C', T_ETW_out_condenser))-(0.0146*T_ETW_out_preheater - 0.8133)

"(0.0146*T_ETW_out_preheater - 0.8133) is a correction so it matches Q_preheater0_refSide values"

"Here T_ETW_out_preheater is a calibrated TC and T_ETW_in_condenser is not a calibrated TC, also T_ETW_out_preheater is on the same ETW line after T_ETW_out_preheater, hence T_ETW_in_condenser is replaced by T_ETW_out_preheater"

Q_testsection_refSide=m_dot_ref***convert**(lbm/hr,kg/s)*cp_testsection_ref(R\$,T_testsection_out,T_testsection_in,p_r[2],HBFlag)*(**converttemp**('F', 'C', T_testsection_out)-**converttemp**('F', 'C', T_testsection_in))***phase_condition**(HBFlag)

HeatBalance_testsection=(Q_testsection_refSide-

Q_totalheater)*100/((Q_testsection_refSide+Q_totalheater)*0.5)***phase_condition**(HBFlag)

"-----"

"-----"

"Note: The functions should go above the main EES code, here the functions are presented after the main EES code for easy readability"

Function tsat(Press,Quality,R\$,FlagHB,TC_measured,ref_Tsat_correction2,OMF2)

"FlagHB=1, this flag will be 1 for heat balance test or single flow tests through the test section"

"FlagHB=0, this flag will be 0 for two phase flow tests"

{old coefficients

A0=6.3801E-03

A1=-4.0375E-04

A2=-3.4902E-05

aa0=-2394.50

bb0=15.51

}

"coefficients derived after 2-19-2019 to include all pure R410A data to get A0, A1, and A2, and all POE data to get aa0 and bb0"

A0=6.3860E-03

A1=-4.0482E-04

A2=-3.4596E-05

aa0=-2394.50

bb0=15.496478

OMF_local=OMF2/(1-Quality)

aa=aa0+182.52*OMF_local-724.21*(OMF_local^2)+3868*(OMF_local^3)-5268.9*(OMF_local^4)

bb=bb0-0.72212*OMF_local+2.3914*(OMF_local^2)-13.779*(OMF_local^3)+17.066*(OMF_local^4)

"evaluation of saturation temperature with oil as presented in Sawant 'Effect of Lubricant on R410A Horizontal Flow Boiling'. "

"and coefficient of eq to calculate a and b as per Thome, J., R., 1995, 'Comprehensive Thermodynamic Approach to Modeling Refrigerant-Lubricating Oil Mixtures,' HVAC&R Research, Vol. 1, No. 2, pp. 110-125"

{

If (Quality<0) Then

T_sat=temperature(R\$,P=Press,x=0)

Else

If (OMF2>0) Then

T_sat=(aa/(ln(Press)-bb+(A2/A1)*Quality))-273.15+ref_Tsat_correction2

Else

"T_sat=temperature(R\$,P=Press,x=Quality)"

T_sat=(1/(A0+A1*ln(Press)+A2*Quality))-273.15+ref_Tsat_correction2

Endif

Endif

}

If (Quality<0) Then

T_sat=**temperature**(R\$,P=Press,x=0)

Endif

If ((Quality>=0) AND (OMF2>0)) Then

T_sat=(aa/(ln(Press)-bb+(A2/A1)*Quality))-273.15+ref_Tsat_correction2

Endif

If ((Quality>=0) AND (OMF2=0)) Then


```

    "T_sat=temperature(R$,P=Press,x=Quality)"
    T_sat=(1/(A0+A1*ln(Press)+A2*Quality))-273.15+ref_Tsat_correction2
Endif

If (FlagHB=0) Then
    tsat=T_sat
Endif
If (FlagHB=1) Then
    tsat=converttemp('F', 'C', TC_measured)
Endif
If (FlagHB=2) Then
    tsat=T_sat
Endif
If (FlagHB=12) Then
    tsat=converttemp('F', 'C', TC_measured)
Endif

End
"-----"
Function q_oilinjected_find(T_testsection_in2,T_OilSyringePump2,rho_OilSyringePump2,m_OilSyringePump2)
If (m_OilSyringePump2<=0) Then
    q_oilinjected_find=0
Else
    cp_OilSyringePump =
    4.186*(0.388+0.00045*T_OilSyringePump2)/sqrt((rho_OilSyringePump2*convert(g/ml,kg/m3))/density(Water,
    T=converttemp('F', 'C', T_OilSyringePump2),x=0))
    "source: Thome, J. R. 1995. Comprehensive thermodynamic approach to modeling refrigerant-lubricating
    oil mixtures. HVAC&R Research 1(2): 110-125"
    q_oilinjected_find=(m_OilSyringePump2*convert(lbm/hr,kg/s))*cp_OilSyringePump*(converttemp('F', 'C',
    T_OilSyringePump2)-converttemp('F', 'C', T_testsection_in2))
Endif
End
"-----"
Function cp_testsection_ref(R$,T_testsection_out3,T_testsection_in3,P_testsection,FlagHB2)
If (FlagHB2=0) Then
    cp_testsection_ref=cp(R$,T=((converttemp('F', 'C', T_testsection_out3)+converttemp('F', 'C',
    T_testsection_in3))*0.5),x=0)
Endif
If (FlagHB2=2) Then
    cp_testsection_ref=cp(R$,T=((converttemp('F', 'C', T_testsection_out3)+converttemp('F', 'C',
    T_testsection_in3))*0.5),x=0) "case of two phase flow tests but in new test section TS-2"
Endif
If (FlagHB2=1) Then
    cp_testsection_ref=cp(R$,T=((converttemp('F', 'C', T_testsection_out3)+converttemp('F', 'C',
    T_testsection_in3))*0.5),P=P_testsection)
Endif
If (FlagHB2=12) Then
    cp_testsection_ref=cp(R$,T=((converttemp('F', 'C', T_testsection_out3)+converttemp('F', 'C',
    T_testsection_in3))*0.5),P=P_testsection) "case of single phase flow in TS-2"
Endif
End
"-----"
Function r_contactop(location,FlagHB2)

```

```

"contact resistance of tube in groove of 'TOP' copper block"
If (FlagHB2=0) OR (FlagHB2=1) Then
  If (location=1) Then
    r_contacttop=130+50+40 "275" "-10"
  Endif
  If (location=2) Then
    r_contacttop=5+50+40 "0" "-10"
  Endif
  If (location=3) Then
    r_contacttop=45+50+40 "0" "-10"
  Endif
  If (location=4) Then
    r_contacttop=5+50+40 "25" "-10"
  Endif
  If (location=5) Then
    r_contacttop=135+50+40 "125" "-10"
  Endif
Endif
If (FlagHB2=2) OR (FlagHB2=12) Then
  "case of two-phase or single-phase flow tests but in new test section TS-2"
  If (location=1) Then
    r_contacttop=55+50+40 "150" "-10"
  Endif
  If (location=2) Then
    r_contacttop=-55+50+40 "-170" "-10"
  Endif
  If (location=3) Then
    r_contacttop=-55+50+40 "-145" "-10"
  Endif
  If (location=4) Then
    r_contacttop=-55+50+40 "-170" "-10"
  Endif
  If (location=5) Then
    r_contacttop=135+50+40 "120" "-10"
  Endif
Endif
End
"-----"
Function r_contactmid(location,FlagHB2)
  "contact resistance of TC on tube in middle"
  If (FlagHB2=0) OR (FlagHB2=1) Then
    If (location=1) Then
      r_contactmid=-65+50-20 "0" "-150"
    Endif
    If (location=2) Then
      r_contactmid=-65+50-20 "-20" "-150"
    Endif
    If (location=3) Then
      r_contactmid=-35+50-20 "0" "-150"
    Endif
    If (location=4) Then
      r_contactmid=0+50-20 "0" "-150"
    Endif
  Endif

```

```

If (location=5) Then
  r_contactmid=-45+50-20 "-125" "-150"
Endif
Endif
If (FlagHB2=2) OR (FlagHB2=12) Then
  "case of two-phase or single-phase flow tests but in new test section TS-2"
  If (location=1) Then
    r_contactmid=-30+50-20 "-50" "-25"
  Endif
  If (location=2) Then
    r_contactmid=-40+50-20 "-70" "-25"
  Endif
  If (location=3) Then
    r_contactmid=-20+50-20 "-50" "-25"
  Endif
  If (location=4) Then
    r_contactmid=0+50-20 "-10" "-25"
  Endif
  If (location=5) Then
    r_contactmid=-25+50-20 "-100" "-25"
  Endif
Endif
End
"-----"
Function r_contactbottom(location,FlagHB2)
  "contact resistance of tube in groove of 'Bottom' copper block"
  If (FlagHB2=0) OR (FlagHB2=1) Then
    If (location=1) Then
      r_contactbottom=-85+50 "-135" "-150"
    Endif
    If (location=2) Then
      r_contactbottom=-65+50 "0" "-150"
    Endif
    If (location=3) Then
      r_contactbottom=-65+50 "-50" "-150"
    Endif
    If (location=4) Then
      r_contactbottom=-45+50 "0" "-150"
    Endif
    If (location=5) Then
      r_contactbottom=-65+50 "-150" "-150"
    Endif
  Endif
  If (FlagHB2=2) OR (FlagHB2=12) Then
    "case of two-phase or single-phase flow tests but in new test section TS-2"
    If (location=1) Then
      r_contactbottom=-45+50 "-155" "-25"
    Endif
    If (location=2) Then
      r_contactbottom=10+50 "-120" "-25"
    Endif
    If (location=3) Then
      r_contactbottom=45+50 "-20" "-25"
  
```

```

Endif
If (location=4) Then
    r_contactbottom=65+50 "-20" "-25"
Endif
If (location=5) Then
    r_contactbottom=15+50 "-150" "-25"
Endif
Endif
End
"-----"
Function testsectionnumber(FlagHB2)
    If (FlagHB2=0) OR (FlagHB2=1) Then
        testsectionnumber=1 "old new test section TS-1"
    Endif
    If (FlagHB2=2) OR (FlagHB2=12) Then
        testsectionnumber=2 "case of two-phase or single-phase flow tests but in new test section TS-2"
    Endif
End
"-----"
Function phase_condition(FlagHB2)
    If (FlagHB2=0) OR (FlagHB2=2) Then
        phase_condition=0 "case of two-phase flow tests"
    Endif
    If (FlagHB2=1) OR (FlagHB2=12) Then
        phase_condition=1 "case of single-phase flow tests"
    Endif
End
"-----"
Function oilspecificenthalpy(temp)
    "calculate pure oil specific enthalpy, kJ/kg"
    "source: Lottin, O., Guillemet, P. and Lebreton, J.-M. 2003. "
    "Effects of synthetic oil in a compression refrigeration system using R410A. Part I: modelling of the whole
    system"
    " and analysis of its response to an increase in the amount of circulating oil. International Journal of
    Refrigeration 26(7): 772-782"

    temp_ref = 15.56 [C]

    rho_water =density(Water,T=temp_ref,x=0)

    rho_oil = (1.22846-0.000868290*(temp + 273.15) +0.000000178598*((temp + 273.15)^2)) * 1000
    "oil density from Honeywell confidential document (EMKARATE POE RL32-3MAF)"

    oilspecificenthalpy = 4.186 * (0.4024*temp+0.000405*temp*temp) / sqrt(rho_oil / rho_water)
End
"-----"
Function htc_oo(MF, x)
    "MF is mass flux, x is ref vapor quality"
    If (MF < 114) Then "For MF=101"
        a3 = -10.521
        a2 = 17.286
        a1 = -7.5801
        a0 = 4.1343
    Endif

```

```

Endif
If (MF >= 114) AND (MF < 145) Then "For MF=128"
  a3 = -16.907
  a2 = 27.742
  a1 = -12.777
  a0 = 5.0416
Endif
If (MF >= 145) AND (MF < 178) Then "For MF=164"
  a3 = 0
  a2 = 7.2608
  a1 = -3.9079
  a0 = 3.9872
Endif
If (MF >= 178) Then "For MF=198"
  a3 = 0
  a2 = 15.719
  a1 = -9.3533
  a0 = 5.1434
Endif
htc_oo = a3 * x * x * x + a2 * x * x + a1 * x + a0
End
"-----"
Function delpperl_oo(MF, x)
  "MF is mass flux, x is ref vapor quality"
  If (MF < 114) Then "For MF=101"
    a3 = 0
    a2 = -1127.9
    a1 = 1636.3
    a0 = -122.02
  Endif
  If (MF >= 114) AND (MF < 145) Then "For MF=128"
    a3 = 0
    a2 = -1584.8
    a1 = 2377.2
    a0 = -222.24
  Endif
  If (MF >= 145) AND (MF < 178) Then "For MF=164"
    a3 = 0
    a2 = -309.03
    a1 = 1847.7
    a0 = -32.379
  Endif
  If (MF >= 178) Then "For MF=198"
    a3 = 0
    a2 = 131.98
    a1 = 2215.2
    a0 = 11.975
  Endif
  delpperl_oo = a3 * x * x * x + a2 * x * x + a1 * x + a0
End

```

Sample Input Variables

Tambient=74.58 [F] "ambient temperature, used to calculate heat losses to ambient"
m_dot_ETW_preheater=518.3 [lbm/hr] "mass flow rate of ethylene-glycol mixture through preheater"
T_ETW_in_preheater=73.19 [F] "T_inlet of ethylene-glycol mixture through second-stage-preheater"
T_ETW_out_preheater=67.2 [F] "T_outlet of ethylene-glycol mixture through second-stage-preheater"
T_ETW_in_condenser=67.74 [F] "T_inlet of ethylene-glycol mixture through first-stage-preheater"
T_ETW_out_condenser=64.3 [F] "T_outlet of ethylene-glycol mixture through first-stage-preheater"
m_dot_ref=93.07 [lbm/hr] "mass flow rate of refrigerant"
p_in_preheater=143.7 [psia] "Refrigerant pressure at second-stage-preheater inlet for enthalpy calculation"
T_in_preheater0=17.01 [F] "Refrigerant temperature at first-stage-preheater inlet"
T_in_preheater=39.89 [F] "Liquid Refrigerant temperature at second-stage-preheater inlet for enthalpy calculation"
T_out_preheater=42.85 [F] "Refrigerant temperature at second-stage-preheater outlet"
p_in_testSection=141.3 [psia] "Refrigerant pressure at test section inlet"
T_testsection_in=41.99 [F] "Refrigerant temperature at test section inlet using inline thermocouple"
T_testsection_out=42.27 [F] "Refrigerant temperature at test section outlet using inline thermocouple"
delP_testSection=0.0763 [psia] "pressure drop across test section, delP"
m_OilSyringePump=0 [lbm/hr] "mass flow rate of oil injected into the test section"
rho_OilSyringePump=0 [g/ml] "density of oil injected into the test section"
T_OilSyringePump=74.33 [F] "Temp of injected oil/lubricant/nanolubricant"
HBFlag=0 "HBFlag=1 for heat balance test or single flow tests through the test section, HBFlag=0 for two phase flow tests"
OMF=0 [wt/wt] "Oil Mass Fraction"
ref_Tsat_correction=0 [C] "correction to saturated temperature"
"Following are the temperatures measured with T-type welded thermocouple, the thermocouples were attached on copper blocks and outside the refrigerant copper tube, see Figure 8 of dissertation for more details"
NL_level1_T1=62.77 [F]
NL_level1_T2=63.59 [F]
NL_level1_T3=63.63 [F]
NL_level1_T4=63.16 [F]
NL_level1_T5=62.65 [F]
NL_level2_T1=59.11 [F]
NL_level2_T2=59.36 [F]
NL_level2_T3=59.6 [F]
NL_level2_T4=59 [F]
NL_level2_T5=59.02 [F]
NL_level3_T1=56.38 [F]
NL_level3_T2=55.15 [F]
NL_level3_T3=55.54 [F]
NL_level3_T4=54.68 [F]
NL_level3_T5=56.4 [F]
NL_levelMid_T1=51.12 [F]
NL_levelMid_T2=48.53 [F]
NL_levelMid_T3=49.6 [F]
NL_levelMid_T4=50.5 [F]
NL_levelMid_T5=50.14 [F]
NL_level4_T1=49.29 [F]
NL_level4_T2=49.4 [F]
NL_level4_T3=49.26 [F]
NL_level4_T4=49.11 [F]
NL_level4_T5=49.67 [F]
NL_level5_T1=53.7 [F]
NL_level5_T2=54.36 [F]
NL_level5_T3=54.69 [F]
NL_level5_T4=54.41 [F]
NL_level5_T5=53.84 [F]

NL_level6_T1=57.68 [F]
NL_level6_T2=58.06 [F]
NL_level6_T3=58.47 [F]
NL_level6_T4=58.34 [F]
NL_level6_T5=57.63 [F]

Output Variables

x_avg=0.3704 [-] "average vapor quality"
x_in=0.3084 [-] "vapor quality at inlet of test section"
x_out=0.4325 [-] "vapor quality at outlet of test section"
MF=164.6 [kg/m2-s] "Mass Flux"
HF_testsection_avg=15.07 [kW/m2] "Heat Flux"
T_sat_testSection=5.615 [C] "average saturation temp of test section"
T_sat_testSection_in=5.44 [C] "saturation temp at inlet of test section"
T_sat_testSection_out=5.791 [C] "saturation temp at outlet of test section"
T_surface_avg=9.948 [C] "average surface temp of test section tube wall"
HTC_avg_of_locals=3.529 [kW/m2-C] "heat transfer coefficient, HTC"
HTC_o=3.536 [kW/m2-C] "HTC_o"
HTF=-0.19 [-] "Heat Transfer Factor"
delPperL=627.6 [Pa/m] "pressure drop per unit length, delP/L_o"
delPperL_o=609.7 [Pa/m] "delP/L_o"
PDF=2.946 [-] "Pressure Drop Factor"

Appendix-F

Uncertainty Calculation in EES

The error analysis outlined by Taylor and Kuyatt (1994) was used for calculating the experimental uncertainties in the EES software. Following example shows sample calculated uncertainties for EES output variables of local heat flux, mass flux, local wall temperature, average vapor quality, local heat transfer coefficient, and pressure drop per unit length for a two-phase flow test.

Unit Settings: SI C kPa kJ mass deg

Variable±Uncertainty

Partial derivative

% of uncertainty

Heat Flux

$HF_{TopTubelD3} = 15.76 \pm 1.511 \text{ [kW/m}^2\text{]}$

$Area_{topPlate6} = 0.001462 \pm 0.00000126 \text{ [m}^2\text{]}$

$L = 0.1016 \pm 0.004 \text{ [m]}$

$L_{top3} = 0.05755 \pm 0.003 \text{ [m]}$

$NL_{level1,T3} = 63.63 \pm 0.2 \text{ [F]}$

$NL_{level2,T3} = 59.6 \pm 0.2 \text{ [F]}$

$\partial HF_{TopTubelD3} / \partial Area_{topPlate6} = 10780$

$\partial HF_{TopTubelD3} / \partial L = -155.1$

$\partial HF_{TopTubelD3} / \partial L_{top3} = -274$

$\partial HF_{TopTubelD3} / \partial NL_{level1,T3} = 3.923$

$\partial HF_{TopTubelD3} / \partial NL_{level2,T3} = -3.897$

0.01 %

16.86 %

29.58 %

26.95 %

26.59 %

Mass Flux

$MF = 164.6 \pm 0.06583 \text{ [kg/m}^2\text{-s]}$

$\dot{m}_{ref} = 93.07 \pm 0.03723 \text{ [lbm/hr]}$

$\partial MF / \partial \dot{m}_{ref} = 1.768$

100.00 %

Surface temperature of inner wall of copper tube

$T_{surface,top,ID,3} = 12.52 \pm 0.2284 \text{ [C]}$

$L = 0.1016 \pm 0.004 \text{ [m]}$

$L_{TC} = 0.007938 \pm 0.003 \text{ [m]}$

$L_{top3} = 0.05755 \pm 0.003 \text{ [m]}$

$NL_{level1,T3} = 63.63 \pm 0.2 \text{ [F]}$

$NL_{level2,T3} = 59.6 \pm 0.2 \text{ [F]}$

$NL_{level3,T3} = 55.54 \pm 0.2 \text{ [F]}$

$\partial T_{surface,top,ID,3} / \partial L = 5.536$

$\partial T_{surface,top,ID,3} / \partial L_{TC} = -64.05$

$\partial T_{surface,top,ID,3} / \partial L_{top3} = 9.777$

$\partial T_{surface,top,ID,3} / \partial NL_{level1,T3} = -0.14$

$\partial T_{surface,top,ID,3} / \partial NL_{level2,T3} = 0.139$

$\partial T_{surface,top,ID,3} / \partial NL_{level3,T3} = 0.5556$

0.94 %

70.76 %

1.65 %

1.50 %

1.48 %

23.66 %

Average vapor quality of the test section

$X_{avg} = 0.3704 \pm 0.01509$

$L = 0.1016 \pm 0.004 \text{ [m]}$

$\dot{m}_{ref} = 93.07 \pm 0.03723 \text{ [lbm/hr]}$

$NL_{level1,T3} = 63.63 \pm 0.2 \text{ [F]}$

$NL_{level2,T3} = 59.6 \pm 0.2 \text{ [F]}$

$P_{in,testSection} = 141.3 \pm 0.1554 \text{ [psia]}$

$T_{ETW,in,preheater} = 73.19 \pm 0.2 \text{ [F]}$

$T_{ETW,out,preheater} = 67.2 \pm 0.2 \text{ [F]}$

$T_{in,preheater} = 39.89 \pm 0.2 \text{ [F]}$

$\partial X_{avg} / \partial L = -0.6114$

$\partial X_{avg} / \partial \dot{m}_{ref} = -0.004158$

$\partial X_{avg} / \partial NL_{level1,T3} = 0.001397$

$\partial X_{avg} / \partial NL_{level2,T3} = -0.001293$

$\partial X_{avg} / \partial P_{in,testSection} = -0.001166$

$\partial X_{avg} / \partial T_{ETW,in,preheater} = 0.05261$

$\partial X_{avg} / \partial T_{ETW,out,preheater} = -0.05245$

$\partial X_{avg} / \partial T_{in,preheater} = 0.00401$

2.63 %

0.01 %

0.03 %

0.03 %

0.01 %

48.66 %

48.34 %

0.28 %

Heat Transfer Coefficient

$HTC_{level3,3} = 2.249 \pm 0.2463 \text{ [kW/m}^2\text{-C]}$

$Area_{topPlate6} = 0.001462 \pm 0.00000126 \text{ [m}^2\text{]}$

$L = 0.1016 \pm 0.004 \text{ [m]}$

$L_{TC} = 0.007938 \pm 0.003 \text{ [m]}$

$L_{top3} = 0.05755 \pm 0.003 \text{ [m]}$

$NL_{level1,T3} = 63.63 \pm 0.2 \text{ [F]}$

$NL_{level2,T3} = 59.6 \pm 0.2 \text{ [F]}$

$NL_{level3,T3} = 55.54 \pm 0.2 \text{ [F]}$

$T_{sat,level3,3} = 5.511 \pm 0.11 \text{ [C]}$

$\partial HTC_{level3,3} / \partial Area_{topPlate6} = 1662$

$\partial HTC_{level3,3} / \partial L = -23.93$

$\partial HTC_{level3,3} / \partial L_{TC} = 20.57$

$\partial HTC_{level3,3} / \partial L_{top3} = -42.26$

$\partial HTC_{level3,3} / \partial NL_{level1,T3} = 0.605$

$\partial HTC_{level3,3} / \partial NL_{level2,T3} = -0.6009$

$\partial HTC_{level3,3} / \partial NL_{level3,T3} = -0.1784$

$\partial HTC_{level3,3} / \partial T_{sat,level3,3} = 0.3212$

0.01 %

15.10 %

6.28 %

26.50 %

24.14 %

23.81 %

2.10 %

2.06 %

Pressure drop per unit length

$\partial P_{perL} = 627.6 \pm 0.4393 \text{ [Pa/m]}$

$\partial P_{testSection} = 0.0763 \pm 0.00005341 \text{ [psia]}$

$\partial \partial P_{perL} / \partial \partial P_{testSection} = 8226$

100.00 %

Appendix-G

Modified Buongiorno Model Script in C++

The C++ script reported below presents the Buongiorno (2006) model to evaluate the convective heat transfer coefficient for nanofluids. The code has the new Newton-Raphson procedure to evaluate the mass balance of nanoparticles while accounting for the distribution of nanoparticles in the laminar sublayer and the turbulent core. The code also has the equations for calculating the diffusion time of nanoparticles under the influence of different slip mechanisms. The presented script in this appendix is just one subroutine of an in-house C++ code to simulate the in-tube flow boiling of refrigerant-lubricant mixtures. Readers are suggested to follow the dissertation work by Bigi (2018) to understand the complete in-house program.

```
double Buongiorno2006_4b(double nRad, int index_Nbt, ofstream &Buongiorno_output_file, string fluid, double
    A0, double A1, double A2, double a0, double b0, string oil, string nano_mater, string nano_shape, double
    D_nano, double ff, double OMF, double NMF, double n_np_Seg, double m_dot_fluid, double p_in, double
    h_in, double t_in, double x_in, double rho_in, double v_in, double cp_in, double mu_in, double k_in,
    double sigma_in, double t_sat_f, double h_f, double rho_f, double v_f, double cp_f, double mu_f, double
    k_f, double sigma_f, double t_sat_g, double h_g, double rho_g, double v_g, double cp_g, double mu_g,
    double k_g, double sigma_g, double h_fg, double dh_x, double t_sat, double w_local, double Dh, double
    De, double SectA, double lengthSeg, double t_wall, double G_flux, double q_flux, double delta_f, double
    delPperL, double &N_bt, double &phi, double &delta_v, double &phi_v, double &phi_i, double
    &N_nanoLSLperL, double &NMF_v, double number_in)
{
    //use: calculate single phase convective heat transfer in nanofluids
    //
    //source: Buongiorno, J. (2006). Convective transport in nanofluids, Transactions of the ASME (128):
    240-250
    //
    //author: Andrea Bigi
    //date: 10/2017
    //modified: Pratik Deokar
    //-----

    //local variables

    //inventory
    double epsilon;           //void fraction,
    double VolSeg;           //segment volume, m3
    double OilSeg;           //oil mass per segment, kg
```

```

double OilNanoSeg; //nanooil mass per segment, kg
double NanoSeg; //nanoparticles mass per segment, kg
double RefSeg; //total refrigerant mass per segment, kg
double RefSegLIQ; //liquid refrigerant mass per segment, kg
double RefSegVAP; //vapor refrigerant mass per segment, kg
double NanoRad; //nanoparticles mass, inside each radius of the laminar sublayer, kg
double V_nano; //nanoparticle volume, m3
double N_nano_Seg; //number of nanoparticles inside the segment, -
double Kn; //Knudsen number
double lambda; //molecule mean free path, m
double alpha; //thermal diffusivity, m2/s
double Re_fo; //Reynolds number, fluid only, -
double Pe_r; //rotational Peclet number, -
double C, n; //friction factor coefficients
double k_B = 1.38064852e-23; //Boltzmann constant, J/K
double D_B; //Brownian diffusion coefficient, m2/s
double V_T; //thermophoretic diffusion coefficient, m2/s
//double N_bt; //ratio of Brownian and thermophoretic diffusivities
double grad_T; //film temperature gradient, K
double tau_p; //nanoparticle relaxation time, s
double beta; //thermophoresis coefficient / proportionality factor
double beta_oil; //thermophoresis coefficient / proportionality factor for oil
double beta_ref; //thermophoresis coefficient / proportionality factor for refrigerant
double gradT; //temperature gradient, K/m
double Vel_eo; //turbulent eddies velocity, m/s
double Vel_e; //nanoparticle/fluid slip velocity due to turbulent eddies, m/s
double Vel_t; //thermophoresis velocity, m/s
double Vel_Brown; //Brownian velocity, m/s
double Vel_g; //gravity velocity, m/s
double t_inert; //time for inertial diffusion, s
double t_Brown; //time for Brownian diffusion, s
double t_thermoph; //time for Thermophoretic diffusion, s
double t_grav; //time for gravity influenced diffusion, s
double delta_u_inert; //inertial slip velocity, m/s
double delta_u_Brown; //Brownian motion slip velocity, m/s
double delta_u_thermoph; //thermophoresis slip velocity, m/s
double delta_u_grav; //gravitational slip velocity, m/s
double F_rotat; //rotational force
double F_Brown; //Brownian force
double F_thermoph; //Thermophoretic force
double F_grav; //gravity force
double F_inert; //inertia force
double gamma; //shear rate
double tau_w; //shear stress at the wall, Pa
//double ff; //friction factor
double u_ave; //mean axial velocity or bulk velocity, m/s
double u_f; //liquid layer velocity, m/s
double u_i; //liquid-vapor interface velocity, m/s
double phi_v_guess; //volume fraction initial guess
//double phi_v; //average nanoparticle volume fraction in laminar sublayer
//double delta_v; //thickness of the laminar sublayer, m
double delta_v_plus; //non-dimensional thickness of the laminar sublayer
double NMF_v_guess; //mass fraction initial guess
//double NMF_v; //nanoparticle mass fraction in refrigerant and oil, in laminar sublayer
double NMF_v_oil; //nanoparticle mass fraction in oil, in laminar sublayer

//properties
double rho_nano; //nanoparticle density, kg/m3
double k_nano; //nanoparticle thermal conductivity, W/m-K
double cp_nano; //nanoparticle specific heat, kJ/kg-K

double t_v; //temperature in laminar sublayer, C

```

```

double mu_v;           //dynamic viscosity in laminar sublayer, Pa*s
double rho_v;
double cp_v;
double k_v;
double mu_b;          //dynamic viscosity in turbulent sublayer, Pa*s
double rho_b;
double cp_b;
double k_b;
double sigma_b;

//pure refrigerant saturation properties used to recalculate nanolubricant-refrigerant mixture
double mu_f_pure;
double rho_f_pure;    //density of pure refrigerant, kg/m3
double cp_f_pure;
double k_f_pure;
double rho_f_N;      //density of refrigerant-oil mixture, kg/m3
double k_f_N;

double NMF_b;        //nanoparticle mass fraction in oil and refrigerant
double Pr_v;
double Pr_b;
double Re_b;
double Nu_b;         //Nusselt bulk
double t_wall_new;
double S_p;
double r_vt;         //laminar-turbulent interface radius, m
double u_f_star;
double y_plus_i;
int count;           //convergence counter
int count_NMF;       //NMF convergence counter
int iter;            //number of iterations

double tau_i;        //interfacial shear stress, Pa
double tau_vt;       //laminar-turbulent interface shear stress, Pa
double t_i;          //liquid-vapor interface temperature, C
double u_vt;         //laminar-turbulent interface velocity, m/s
double r_i;          //interfacial radius, m
double q_v[100];     //laminar sublayer heat flux, W/m2
double HH;           //heat transfer parameter
double htc_[100];
double htc_rv;
double htc_radial;
double rho_f_N_v_Rad[100];
double NanoOilRefRad; //liquid refrigerant and nanooil mass, inside each radius of the laminar
sublayer, kg
double OilRad;       //oil mass, inside each radius of the laminar sublayer, kg
double OilNanoRad;  //nanooil mass, inside each radius of the laminar sublayer, kg
double DpSeg_tot_;  //segment delta pressure, Pa

int j;

//output variables
double htc;           //heat transfer coefficient, W/m2-C

//*****added by Pratik*****
double AR;           //aspect ratio of nanoparticle,

int count_phi_i;    //phi_i convergence counter
double NMF_i;       //NMF at laminar sublayer and turbulent layer interface, also NMF of the turbulent layer,
bounded by delta_f and delta_v
//double phi_i;     //phi at laminar sublayer and turbulent layer interface, also NMF of the turbulent layer,
bounded by delta_f and delta_v

```

```

double phi_i_iter; //phi_i at next iteration
double mass_np_inventory; //[kg] mass of the nanoparticles in liquid oil+ref, calculated from inventory
subroutine
double massLSL_np; //[kg] mass of the nanoparticles in laminar sublayer
double massTL_np; //[kg] mass of the nanoparticles in turbulent layer
double mass_np_total; //[kg] mass of the nanoparticles in laminar sublayer and turbulent layer bounded
by film thickness
double D_mass_np; //derivative of (mass_np_inventory-massLSL_np-massTL_np) w.r.t phi_i
double D_mass_np_inventory; //derivative of (mass_np_inventory) w.r.t phi_i
double D_massLSL_np; //derivative of (massLSL_np) w.r.t phi_i
double D_massTL_np; //derivative of (massTL_np) w.r.t phi_i
double PercentAreaLSL; //[m2] area of the laminar sublayer, bounded by wall of tube and delta_v
double PercentAreaTL; //[m2] area of the turbulent layer, bounded by delta_f and delta_v
double OilMassLSL; //[kg] mass of oil in laminar sublayer, bounded by wall of tube and delta_v
double OilMassTL; //[kg] mass of oil in turbulent layer, bounded by delta_f and delta_v
double NMF_check; //NMF that should be same as the input NMF if all the calculations are correct
double massBalancePercent;
double phiBalancePercent;
double LogFunction;
//double N_nanoLSLperL; //[#/m] number of nanoparticles in laminar sublayer per unit length
double N_nanoTLperL; //[#/m] number of nanoparticles in turbulent layer per unit length
double N_nano_i_perL; //[#/m] (approximated) number of nanoparticles at the interface of laminar
sublayer and turbulent layer
double N_nano_total; //[#/m] total number of nanoparticles per unit length

double M_base; //mass of oil and refrigerant mixture per unit length [kg/m]
double AA; //variable in laminar sublayer nanoparticle mass equation
double AA2; //variable in laminar sublayer nanoparticle mass equation
double BB; //variable in laminar sublayer nanoparticle mass equation
double CC; //variable in laminar sublayer nanoparticle mass equation

double u_liquid; //liquid mean phase velocity
double ff_DW; //Darcy-Weisbach friction factor

double V_c; // diffusivity due to particle interaction due to change in nanoparticle gradient [m2/s]
double V_mu; // diffusivity due to spatial variation of viscosity [m2/s]
double Kc; //proportionality constant of order unity
double Kmu; //proportionality constant of order unity
double t_collision; //diffusion time [s], the time a particle takes to diffuse a length equivalent to its diameter
under the influence of V_c
double t_viscosity; //diffusion time [s], the time a particle takes to diffuse a length equivalent to its
diameter under the influence of V_mu

double D_tB; //Brownian translational diffusion coefficient by Yuan Lin Yu_2018
double gamma_tL; //translational friction coefficient parallel to the long axis
double gamma_tS; //translational friction coefficient perpendicular to the long axis

double mu_v_allLub; //dynamic viscosity of pure oil or nanolubricant in absence of refrigerant, Pa-s
double l_e; //lubricant excess layer, m
double w_local_v; //w_local in laminar sublayer

//*****

//flow

count = 0;
count_NMF = 0;
iter = 50;
count_phi_i = 0;

if (NMF == 0)
{

```

```

        rho_nano = 0;
        k_nano = 0;
        cp_nano = 0;
    }

    rho_f_pure = PropsSI("D", "P", p_in * 1000, "Q", 0, fluid);
    k_f_pure = PropsSI("L", "P", p_in * 1000, "Q", 0, fluid);
    cp_f_pure = PropsSI("C", "P", p_in * 1000, "Q", 0, fluid) / 1000;
    mu_f_pure = PropsSI("V", "P", p_in * 1000, "Q", 0, fluid);

    k_f_N = OilMixtureConductivity(t_in, w_local, k_f_pure);

    ////////////////////////////////////////////////////////////////////segment inventory, based on section area////////////////////////////////////////////////////////////////// //****added by Pratik
05/11/2018
    epsilon = RouhaniAxelsson(fluid, G_flux, sigma_f, rho_g, rho_f, x_in);
    //****added by Pratik 05/11/2018
    Inventory(fluid, nano_mater, D_nano, SectA, lengthSeg, epsilon, w_local, NMF, rho_g, rho_f,
    //****added by Pratik 05/11/2018
    VolSeg, RefSegLIQ, RefSegVAP, RefSeg, OilNanoSeg, NanoSeg, OilSeg, V_nano,
N_nano_Seg); //****added by Pratik 05/11/2018
    V_nano = M_PI / 6 * pow(D_nano*1e-9, 3);

    if (nano_mater == "Al2O3")
    {
        AR = 1;
        V_nano = M_PI / 6 * pow(D_nano*1e-9, 3);
    }
    else if (nano_mater == "ZnO")
    {
        AR = 3;
        V_nano = M_PI / 6 * pow(D_nano*1e-9, 3)*(AR / 2); //volume of a prolate spheroid
    }

    mass_np_inventory = NanoSeg; //mass of the nanoparticles in liquid oil+ref, calculated from inventory
    subroutine

    //initialize
    NMF_i = NMF;
    NMF_v = NMF;
    rho_nano = NanoDensity(nano_mater);
    phi_i = V_nano / ((RefSegLIQ / rho_f_pure) + (OilSeg / OilDensity(t_in)));
    //phi_i = NMF / (NMF + (1 - NMF)*rho_nano / rho_f);
    phi_v = phi_i; // NMF / (NMF + (1 - NMF)*rho_nano / rho_f);
    phi = NMF / (NMF + (1 - NMF)*rho_nano / rho_f);

    //Loop to find the correct phi_i laminar sublayer interface
    while (TRUE && count_phi_i < 100)
    {
        //calculate bulk properties for the case with water and nanoparticles
        if (OMF == 0 && NMF > 0)
        {
            //calculation of the saturated properties before nanoparticles (NMF = 0)
            CalcProps(fluid, A0, A1, A2, a0, b0, oil, nano_mater, nano_shape, D_nano, 0, 0,
            m_dot_fluid, p_in, h_in, t_in, x_in, rho_in, v_in, cp_in, mu_in, k_in, sigma_in, t_sat_f,
            h_f, rho_f, v_f, cp_f, mu_f, k_f, sigma_f, t_sat_g, h_g, rho_g, v_g, cp_g, mu_g, k_g,
            sigma_g, h_fg, dh_x, t_sat, w_local);

            rho_nano = 3880; // NanoDensity(nano_mater); //3880;
            k_nano = NanoConductivity(nano_mater, t_in); //36; 40
            cp_nano = NanoSpecificHeat(nano_mater, t_in) * 1000;

            //calculation of the volume concentration in water

```



```

phi = NMF / (NMF + (1 - NMF)*rho_nano / rho_f);

rho_b = phi*rho_nano + (1 - phi)*rho_f;           //Buongiorno
mu_b = mu_f*(1 + 39.11*phi + 533.9*pow(phi, 2)); //Buongiorno
k_b = k_f*(1 + 7.47*phi);                         //Buongiorno
cp_b = phi*cp_nano + (1 - phi)*cp_f * 1000;      //Buongiorno
sigma_b = sigma_f;

//calculation of the volume concentration in water
phi_v = NMF_v / (NMF_v + (1 - NMF_v)*rho_nano / rho_f);

rho_v = phi_v*rho_nano + (1 - phi_v)*rho_f;       //Buongiorno
mu_v = mu_f*(1 + 39.11*phi_v + 533.9*pow(phi_v, 2)); //Buongiorno
k_v = k_f*(1 + 7.47*phi_v);                       //Buongiorno
cp_v = phi_v*cp_nano + (1 - phi_v)*cp_f;         //Buongiorno
}
////calculate bulk properties for the case with nanolubricant and refrigerant
else
{
//calculation of the saturated properties before nanoparticles (NMF = 0)
CalcProps(fluid, A0, A1, A2, a0, b0, oil, nano_mater, nano_shape, D_nano, OMF, 0,
m_dot_fluid, p_in, h_in, t_in, x_in, rho_in, v_in, cp_in, mu_in, k_in, sigma_in, t_sat_f,
h_f, rho_f, v_f, cp_f, mu_f, k_f, sigma_f, t_sat_g, h_g, rho_g, v_g, cp_g, mu_g, k_g,
sigma_g, h_fg, dh_x, t_sat, w_local);

//calculation of inlet fluid bulk properties
if (NMF_i > 0)
{
//Turbulent layer properties
CalcProps(fluid, A0, A1, A2, a0, b0, oil, nano_mater, nano_shape, D_nano,
OMF, NMF_i, m_dot_fluid, p_in, h_in, t_in, x_in, rho_in, v_in, cp_in, mu_in,
k_in, sigma_in, t_sat_f, h_f, rho_b, v_f, cp_b, mu_b, k_b, sigma_b, t_sat_g,
h_g, rho_g, v_g, cp_g, mu_g, k_g, sigma_g, h_fg, dh_x, t_sat, w_local);

//laminar Sublayer properties
CalcProps(fluid, A0, A1, A2, a0, b0, oil, nano_mater, nano_shape, D_nano,
OMF, NMF_v, m_dot_fluid, p_in, h_in, t_in, x_in, rho_in, v_in, cp_in, mu_in,
k_in, sigma_in, t_sat_f, h_f, rho_v, v_f, cp_v, mu_v, k_v, sigma_f, t_sat_g,
h_g, rho_g, v_g, cp_g, mu_g, k_g, sigma_g, h_fg, dh_x, t_sat, w_local);

rho_nano = NanoDensity(nano_mater);           //3880;
k_nano = NanoConductivity(nano_mater, t_in); //36; 40
cp_nano = NanoSpecificHeat(nano_mater, t_in) * 1000;

}
else
{
rho_b = rho_f;
cp_b = cp_f;
mu_b = mu_f;
k_b = k_f;
rho_v = rho_f;
cp_v = cp_f;
mu_v = mu_f;
k_v = k_f;
}

cp_b = cp_b * 1000;
cp_v = cp_v * 1000;
}

```

```

//*****Beta calculation*****
if (fluid == "water")
{
    //McNab&Meisen, suggested by Buongiorno
    beta = 0.26*(k_f_pure / (2 * k_f_pure + k_nano));

    //alternative correlation for beta - (IJHMT - 2015 - Michaelides - Brownian movement
    and thermophoresis of nanoparticles in liquids)
    //beta = 1227 * pow(D_nano / 2 / 1, -1.434);           //water
}
else if (fluid != "water" && OMF == 0)
{
    //alternative correlation for beta - (IJHMT - 2015 - Michaelides - Brownian movement
    and thermophoresis of nanoparticles in liquids)
    beta = 6270 * pow(D_nano / 2 / 1, -1.819);           //R134a
}
else if (fluid != "water" && OMF > 0)
{
    //alternative correlation for beta - (IJHMT - 2015 - Michaelides - Brownian movement
    and thermophoresis of nanoparticles in liquids)
    beta_oil = 7.1026*pow(D_nano / 2 / 1, -1.579);           //engine oil
    beta_ref = 6270 * pow(D_nano / 2 / 1, -1.819);           //R134a

    //weighted beta for oil-refrigerant mixture           //Bigi
    beta = beta_oil * w_local + beta_ref * (1 - w_local);
}

//added for sensitivity analysis on Nbt
beta = beta / pow(10, 3 * index_Nbt);
//*****

u_ave = m_dot_fluid / (rho_b * SectA);
Re_b = rho_b * u_ave * Dh / mu_b;

C = 0.184;
n = 0.2;

tau_w = ff / 8 * rho_v * pow(u_ave, 2);

if (fluid == "water")
{
    delta_v_plus = 15.5; // 8.7 15.5; //Buongiorno used 15.5 for his validation
}
else
{
    delta_v_plus = u_ave / (sqrt(tau_w / rho_v));/**Added by Pratik, 3.7 is multiplied to
    round the delta_v_plus to 10.5
}

delta_v = delta_v_plus*(mu_v / rho_v / sqrt(tau_w / rho_v)); //mu_b or mu_v ??? according to
Hewitt, Annular Two-Phase Flow, pag.126,

//I think this form is correct, rather than: delta_v_plus*(mu_b / rho_b / sqrt(tau_w / rho_b))

if (delta_v > 0.98*delta_f) //if condition added by Pratik on 4-14-2019
{
    delta_v = 0.98*delta_f;
}

D_B = k_B*(t_sat_f + 273.15) / (3 * M_PI*mu_v*D_nano*1e-9); //function of laminar properties
(from email correspondence with Dr Buongiorno)

```



```

//*****added by Pratik 03-22-2018*****
if (nano_mater == "Al2O3")
{
    AR = 1;
    D_B = k_B*(t_sat_f + 273.15) / (3 * M_PI*mu_v*D_nano*1e-9);
}
else if (nano_mater == "ZnO")
{
    AR = 3;
    //aspect ration as defined by Dr. Cremaschi in his proposal, Kedzierski_2017 image on
    ZnO shows the AR should be about 3.6, ***added by Pratik

    D_B = (k_B*(t_sat_f + 273.15) / (3 * M_PI*mu_v*(D_nano*pow(AR, 0.666))*1e-
    9))*log(AR) - 0.662 + 0.917*(1 / AR) - 0.05*pow((1 / AR), 2));
    //added by Pratik, source: Savithiri et al. (2011)

}
//*****
grad_T = q_flux*delta_v / k_v;
//function of laminar properties (from email correspondence with Dr Buongiorno)
V_T = beta*mu_v*grad_T / (rho_v*(t_sat_f + 273.15)); //function of laminar properties (from
email correspondence with Dr Buongiorno)
N_bt = D_B / V_T;

/*
//AA2 = (rho_f / rho_nano)/exp(-1 / N_bt);
//AA = AA2 / phi_i;
//BB = 1 - (rho_f / rho_nano);
//CC = 1 / (N_bt*delta_v);
//M_base = M_PI*(Dh-delta_f)*rho_f; //this is approximation to avoid intergrating in radial co-
ordinate, the film is considered thin without curvature effect.

// mass_np_inventory; //mass of the nanoparticles in liquid oil+ref, calculated from inventory
subroutine
// massLSL_np; //mass of the nanoparticles in laminar sublayer
// massTL_np; //mass of the nanoparticles in turbulent layer
// mass_np_total; //mass of the nanoparticles in laminar sublayer and turbulent layer bounded
by film thickness
// D_mass_np; //derivative of (mass_np_inventory-massLSL_np-massTL_np) w.r.t phi_i
// D_mass_np_inventory; //derivative of (mass_np_inventory) w.r.t phi_i
// D_massLSL_np; //derivative of (massLSL_np) w.r.t phi_i
// D_massTL_np; //derivative of (massTL_np) w.r.t phi_i
*/

PercentAreaLSL = (pow(Dh, 2) - pow((Dh - 2 * delta_v), 2)) / (pow(Dh, 2) - pow((Dh - 2 * delta_f),
2));
PercentAreaTL = (pow((Dh - 2 * delta_v), 2) - pow((Dh - 2 * delta_f), 2)) / (pow(Dh, 2) - pow((Dh
- 2 * delta_f), 2));
OilMassLSL = OilSeg*PercentAreaLSL;
OilMassTL = OilSeg*PercentAreaTL;

massTL_np = M_PI*(Dh - delta_f)*rho_nano*(delta_f - delta_v)*phi_i / (1 - phi_i);
LogFunction = (1 - phi_i) / (1 - phi_i*exp(-1 / N_bt));
massLSL_np = -1 * M_PI*(Dh - delta_f)*rho_nano*N_bt*delta_v*log(LogFunction);
mass_np_total = massLSL_np + massTL_np;

D_mass_np_inventory = 0; //as mass_np_inventory is a constant
D_massTL_np = M_PI*(Dh - delta_f)*rho_nano*(delta_f - delta_v) / pow((1-phi_i), 2);
D_massLSL_np = (M_PI*(Dh - delta_f)*rho_nano*N_bt*delta_v / (1 - phi_i))*(exp(-1 / N_bt) - 1) /
(phi_i*exp(-1 / N_bt) - 1);

```

```

D_mass_np = D_mass_np_inventory - D_massLSL_np - D_massTL_np;

phi_i_iter = phi_i - (mass_np_inventory - mass_np_total) / D_mass_np;

//The Newton-Raphson Method

phiBalancePercent = ((abs(phi_i - phi_i_iter)) * 100 / phi_i);
if (phiBalancePercent < 0.005)
{
    phi_i = phi_i_iter;
    phi_v = phi_i * N_bt * (1 - exp(-1 / N_bt));
    NMF_i = massTL_np / OilMassTL; //(phi_i * rho_nano / rho_f) / (1 - phi_i + phi_i *
    rho_nano / rho_f);
    NMF_v = massLSL_np / OilMassLSL; //(phi_v * rho_nano / rho_f) / (1 - phi_v + phi_v *
    rho_nano / rho_f);
    //NMF_v = (phi_v * rho_nano / rho_f) / (1 - phi_v + phi_v * rho_nano / rho_f);
    //***Pratik added on 5/25/2018, this is a correct way to get NMF_V for fluid properties
    to stay consistent with Buongiorno

    if (NMF == 0)
    {
        break;
    }
    break;
}
else
{

    phi_i = phi_i_iter;

    count_phi_i++;
    phi_v = phi_i * N_bt * (1 - exp(-1 / N_bt));
    NMF_i = massTL_np / OilMassTL; //(phi_i * rho_nano / rho_f) / (1 - phi_i + phi_i *
    rho_nano / rho_f);
    NMF_v = massLSL_np / OilMassLSL; //(phi_v * rho_nano / rho_f) / (1 - phi_v + phi_v *
    rho_nano / rho_f);

    //NMF_v = (phi_v * rho_nano / rho_f) / (1 - phi_v + phi_v * rho_nano / rho_f); //***Pratik
    added on 5/25/2018, this is a correct way to get NMF_V for fluid properties to stay
    consistent with Buongiorno
    //The original flaw of this model is that the NMF_v (nanoparticle conc in oil and ref) and
    used to get fluid properties using CalcProps().
    //But CalcProps() needs NMF (nanoparticle conc in oil only as input), this correction
    was noticed on 3/28/2019
    //this should change the HTC results insignificantly as NMF_v is very very small to
    cause significant effect

    if (NMF_i >= 1)
    {
        NMF_i = 0.99; //(NMF_i should not be greater than 1, currently if it is not
        followed then it is forced to be 1)
    }

    if (NMF_v >= 1)
    {
        NMF_v = 0.99;
    }

    if (NMF == 0)
    {
        break;
    }
}

```

```

    }
}

NMF_check = mass_np_total / OilNanoSeg;

N_nanoLSLperL = massLSL_np / (rho_nano*V_nano) / lengthSeg;
N_nanoTLperL = massTL_np / (rho_nano*V_nano) / lengthSeg;
N_nano_i_perL = N_nanoTLperL*D_nano / (delta_f - delta_v);

N_nano_total = N_nanoLSLperL + N_nanoTLperL;

//(vii)
r_vt = De / 2 - delta_v;

//*****original code Andrea (t_wall changes)*****

//here T_wall does not stays as input, but changes (increases)
t_wall_new = t_wall;

while (TRUE && count < iter)
{
    t_v = (t_wall_new + t_sat_f) / 2;

    //for water, from Buongiorno
    if (OMF == 0 && NMF > 0)
    {
        rho_f = PropsSI("D", "T", t_v + 273.15, "Q", 0, fluid);
        mu_f = PropsSI("V", "T", t_v + 273.15, "Q", 0, fluid);
        k_f = PropsSI("L", "T", t_v + 273.15, "Q", 0, fluid);
        cp_f = PropsSI("C", "T", t_v + 273.15, "Q", 0, fluid);
        cp_nano = NanoSpecificHeat(nano_mater, t_v) * 1000;

        rho_v = phi_v*rho_nano + (1 - phi_v)*rho_f;           //Buongiorno
        mu_v = mu_f*(1 + 39.11*phi_v + 533.9*pow(phi_v, 2)); //Buongiorno
        k_v = k_f*(1 + 7.47*phi_v);                          //Buongiorno
        cp_v = phi_v*cp_nano + (1 - phi_v)*cp_f;            //Buongiorno
    }
    ////for nanolubricants
    else
    {
        p_in = PropsSI("P", "T", t_v + 273.15, "Q", 0, fluid) / 1000; ////! check that tsat changes
        when props are calculated

        CalcProps(fluid, A0, A1, A2, a0, b0, oil, nano_mater, nano_shape, D_nano, OMF, 0,
        m_dot_fluid, p_in, h_in, t_in, x_in, rho_in, v_in, cp_in, mu_in, k_in, sigma_in, t_v, h_f,
        rho_f, v_f, cp_f, mu_f, k_f, sigma_f, t_sat_g, h_g, rho_g, v_g, cp_g, mu_g, k_g,
        sigma_g, h_fg, dh_x, t_sat, w_local);

        if (NMF_v > 0)
        {
            CalcProps(fluid, A0, A1, A2, a0, b0, oil, nano_mater, nano_shape, D_nano,
            OMF, NMF_v, m_dot_fluid, p_in, h_in, t_in, x_in, rho_in, v_in, cp_in, mu_in,
            k_in, sigma_in, t_v, h_f, rho_v, v_f, cp_v, mu_v, k_v, sigma_f, t_sat_g, h_g,
            rho_g, v_g, cp_g, mu_g, k_g, sigma_g, h_fg, dh_x, t_sat, w_local);
        }
        else
        {
            rho_v = rho_f;
            cp_v = cp_f;
            mu_v = mu_f;
        }
    }
}

```

```

        k_v = k_f;
    }

    cp_v = cp_v * 1000;
}

Pr_v = mu_v*cp_v / k_v;
Pr_b = mu_b*cp_b / k_b;
u_ave = m_dot_fluid / (rho_b * SectA); //this was added over here on 4-2-2019
Re_b = rho_b * u_ave * Dh / mu_b; //this was added over here on 4-2-2019

//tau_w = ff / 8 * rho_b * pow(u_ave, 2); //this was added over here on 4-2-2019
tau_w = ff / 8 * rho_v * pow(u_ave, 2);
delta_v_plus = u_ave / (sqrt(tau_w / rho_v)); //this was added over here on 4-2-2019

//following radial analysis section is commented out by Pratik
//{ radial analysis section}

if (Re_b < 2300)
{
    Nu_b = 4.36; //Nusselt number for laminar flow at constant heat flux
}
else
{
    //Nu_b = (ff / 8 * Re_b * Pr_b) / (1 + delta_v_plus*sqrt(ff / 8)*(Pr_v - 1));
//Buongiorno, eq. 47
    Nu_b = (ff / 8 * (Re_b - 1000) * Pr_b) / (1 + delta_v_plus*sqrt(ff / 8)*(pow(Pr_v, 2.0 /
3.0) - 1)); //Buongiorno, eq. 50
}

//(ix)
htc = Nu_b*k_b / Dh;
t_wall = t_sat_f + q_flux / htc; //Newton's law of cooling

if (abs(t_wall_new - t_wall) < 0.01)
{
    break;
}
else
{
    t_wall_new = (t_wall_new + t_wall) / 2; //t_wall;
    count++;
}

}

//*****original code Andrea – section end*****

//*****Slip mechanisms and diffusion time analysis in laminar sublayer (added by Pratik)*****

if (nano_mater == "Al2O3")
{
    //for spherical partilce size range 100 miro-meter to 675 miro-meter at phi=0.55 the best
    prediction were Kc/Kmu=0.66 where Kc=0.41 abd Kmu=0.62
    Kc = 0.41;
    Kmu = 0.62;
}
else if (nano_mater == "ZnO")
{
    //for ZnO the aspect ration is 3 as defined by Dr. Cremaschi in his proposal, Kedzierski_2017
    image on ZnO shows the AR should be about 3.6
    //hence peanut shaped ZnO should have more interaction with each other than spherical Al2O3

```

```

//Assume for ZnO Kc is doubled
Kc = 0.41 * 2;

//Assume Kmu stays unchanged
Kmu = 0.62;
}

V_c = Kc*pow(D_nano*1e-9, 2)*phi_v*u_ave / delta_v; // diffusivity due to particle interaction due to
chane in nanoparticle gradient [m2/s]
V_mu = Kmu*pow(D_nano*1e-9, 2)*(u_ave / delta_v)*(phi_v*phi_v / mu_v)*(mu_b - mu_v) / (phi_i -
phi_v); // diffusivity due to spacial vairation of viscosity [m2/s]

if (NMF == 0)
{
    t_Brown = 0;
    t_thermoph = 0;
    t_collision = 0;
    t_viscosity = 0;
}
else
{
    t_Brown = pow(D_nano*1e-9, 2) / D_B; //time for Brownian diffusion
    t_thermoph = pow(D_nano*1e-9, 2) / V_T; //time for Thermophoretic diffusion
    t_collision = pow(D_nano*1e-9, 2) / V_c; //time for Shear induced diffusion
    t_viscosity = pow(D_nano*1e-9, 2) / V_mu; //time for Viscosity gradient induced diffusion
}

//*****//
if (count == iter)
{
    Buongiorno_output_file << "This test did not converge." << endl;
}
else
{
    Buongiorno_output_file << G_flux << "," << q_flux << "," << phi_i << "," << N_bt << "," << phi_v
<< "," << ff << "," << tau_w << "," << D_B << "," << grad_T << "," << V_T << "," << delta_v << ","
<< u_ave << "," << t_wall << "," << Re_b << "," << Pr_b << "," << Pr_v << "," << Nu_b << "," <<
htc << "," << rho_b << "," << cp_b << "," << mu_b << "," << k_b << "," << rho_v << "," << cp_v <<
"," << mu_v << "," << k_v << "," << NMF_i << "," << NMF_v << "," << mass_np_inventory << ","
<< NMF_check << "," << delta_v_plus << "," << delta_f << "," << N_nanoLSLperL << "," <<
N_nanoTLperL << "," << N_nano_i_perL << "," << V_c << "," << V_mu << "," << t_Brown << ","
<< t_thermoph << "," << t_collision << "," << t_viscosity << "," << p_in << "," << t_v << endl;
}
}

return htc;
}
}

```

Appendix-H

Two-Phase Flow Model Prediction Data

The data set in the table below reports the prediction of the superposition model of saturated two-phase flow boiling of R410A with POE and nanolubricants in a smooth tube. The table reports the evaluated nucleate boiling heat transfer coefficients, HTC_{nb} using equation (75), single phase convective heat transfer coefficients, HTC_{cht} using equation (44), suppression factors, S using equation (77), superposition model prediction, HTC_p using equation (76), experimentally measured HTC_{exp} , and the desired two-phase convective multiplier, \bar{F} using equation (79), and the two-phase convective multiplier, F using equation (78).

Fluid	OMF [wt.%]	NP_{conc} [wt.%]	\dot{m} [kg/m ² -s]	\dot{q}_{avg} [kW/m ²]	x_{avg} [-]	T_{bub} [°C]	HTC_{nb} [kW/m ² -K]	HTC_{cht} [kW/m ² -K]	S	HTC_p [kW/m ² -K]	HTC_{exp} [kW/m ² -K]	\bar{F}	F
R410A	0.0	0	102	14.8	0.25	5.3	2.01	0.34	0.77	2.83	3.10	4.64	3.84
R410A	0.0	0	102	14.8	0.26	4.6	2.02	0.34	0.77	2.86	3.10	4.59	3.88
R410A	0.0	0	101	14.9	0.32	5.4	2.01	0.33	0.78	2.90	3.14	4.73	4.00
R410A	0.0	0	101	15.2	0.40	6.5	2.00	0.33	0.79	2.98	3.24	4.93	4.17
R410A	0.0	0	104	14.8	0.40	5.7	2.01	0.34	0.79	3.02	3.18	4.67	4.19
R410A	0.0	0	102	14.8	0.43	5.0	2.02	0.34	0.80	3.04	3.18	4.66	4.24
R410A	0.0	0	101	15.2	0.51	6.1	2.01	0.33	0.82	3.12	3.37	5.16	4.43
R410A	0.0	0	100	14.9	0.53	5.8	2.01	0.33	0.83	3.13	3.78	6.45	4.46
R410A	0.0	0	100	14.4	0.61	6.0	2.01	0.33	0.85	3.25	3.38	5.07	4.67
R410A	0.0	0	100	14.9	0.65	6.5	2.01	0.33	0.86	3.30	3.47	5.29	4.76
R410A	0.0	0	101	15.1	0.73	7.4	2.00	0.33	0.88	3.43	3.59	5.48	4.98
R410A	0.0	0	100	15.0	0.75	6.7	2.00	0.33	0.89	3.45	3.56	5.38	5.05
R410A	0.0	0	100	15.3	0.75	6.4	2.00	0.33	0.89	3.46	3.12	4.04	5.06
R410A	0.0	0	127	15.0	0.24	6.0	2.01	0.41	0.72	3.00	3.26	4.46	3.82
R410A	0.0	0	127	14.9	0.26	5.3	2.01	0.41	0.72	3.03	3.27	4.46	3.86
R410A	0.0	0	128	15.1	0.27	4.7	2.02	0.41	0.72	3.06	3.32	4.54	3.90
R410A	0.0	0	128	21.3	0.28	6.0	2.01	0.41	0.72	3.04	3.89	6.00	3.91
R410A	0.0	0	132	21.1	0.31	6.3	2.01	0.42	0.72	3.11	3.96	6.02	3.99
R410A	0.0	0	125	15.1	0.35	5.6	2.01	0.40	0.74	3.14	3.25	4.36	4.08
R410A	0.0	0	128	21.3	0.40	6.3	2.01	0.41	0.75	3.19	4.01	6.17	4.17
R410A	0.0	0	128	15.0	0.41	5.7	2.01	0.41	0.75	3.24	3.72	5.37	4.21
R410A	0.0	0	128	14.9	0.41	5.7	2.01	0.41	0.75	3.24	3.73	5.40	4.21
R410A	0.0	0	128	15.0	0.42	5.8	2.01	0.41	0.75	3.24	3.33	4.43	4.22
R410A	0.0	0	128	15.0	0.42	5.4	2.01	0.41	0.75	3.25	3.70	5.31	4.23
R410A	0.0	0	128	15.2	0.51	6.3	2.01	0.41	0.78	3.37	3.37	4.42	4.41
R410A	0.0	0	129	15.1	0.51	6.2	2.01	0.41	0.77	3.38	3.34	4.32	4.42
R410A	0.0	0	129	15.1	0.51	6.1	2.01	0.41	0.77	3.38	3.44	4.57	4.42
R410A	0.0	0	126	15.1	0.51	6.3	2.01	0.41	0.78	3.36	3.38	4.48	4.43

Fluid	OMF [wt.%]	NP_{conc} [wt.%]	\dot{m} [kg/m ² -s]	\dot{q}_{avg} [kW/m ²]	x_{avg} [-]	T_{bub} [°C]	HTC_{nb} [kW/m ² -K]	HTC_{cht} [kW/m ² -K]	S	HTC_p [kW/m ² -K]	HTC_{exp} [kW/m ² -K]	\bar{F}	F
R410A	0.0	0	128	15.0	0.52	6.9	2.00	0.41	0.78	3.38	3.52	4.77	4.43
R410A	0.0	0	131	14.9	0.54	6.2	2.01	0.42	0.78	3.44	3.45	4.51	4.49
R410A	0.0	0	128	15.1	0.54	6.0	2.01	0.41	0.79	3.42	3.56	4.83	4.49
R410A	0.0	0	130	15.1	0.54	6.2	2.01	0.42	0.78	3.45	3.43	4.46	4.50
R410A	0.0	0	127	14.9	0.56	5.4	2.01	0.41	0.80	3.45	3.57	4.85	4.55
R410A	0.0	0	127	14.9	0.58	6.2	2.01	0.41	0.80	3.48	3.67	5.05	4.59
R410A	0.0	0	129	15.1	0.58	6.1	2.01	0.41	0.80	3.50	3.75	5.20	4.59
R410A	0.0	0	128	15.0	0.59	6.1	2.01	0.41	0.80	3.50	4.04	5.94	4.61
R410A	0.0	0	128	14.3	0.59	6.3	2.01	0.41	0.80	3.51	3.66	4.98	4.62
R410A	0.0	0	127	14.8	0.60	6.3	2.01	0.41	0.81	3.51	3.67	5.02	4.63
R410A	0.0	0	128	15.2	0.64	6.5	2.01	0.41	0.82	3.58	3.85	5.36	4.72
R410A	0.0	0	129	20.8	0.70	8.1	1.99	0.41	0.84	3.69	4.51	6.92	4.90
R410A	0.0	0	128	15.0	0.72	6.4	2.01	0.41	0.85	3.74	4.01	5.62	4.96
R410A	0.0	0	128	15.1	0.72	6.8	2.00	0.41	0.85	3.74	3.93	5.42	4.96
R410A	0.0	0	127	14.7	0.72	6.6	2.00	0.41	0.85	3.73	3.91	5.39	4.97
R410A	0.0	0	128	14.9	0.73	7.4	2.00	0.41	0.86	3.77	3.97	5.50	5.00
R410A	0.0	0	128	21.3	0.74	7.1	2.00	0.41	0.86	3.76	4.56	6.99	5.02
R410A	0.0	0	127	14.9	0.76	6.8	2.00	0.41	0.87	3.82	3.92	5.36	5.10
R410A	0.0	0	127	14.9	0.76	6.7	2.00	0.41	0.87	3.82	4.15	5.91	5.10
R410A	0.0	0	166	14.7	0.28	5.4	2.01	0.51	0.66	3.33	3.46	4.18	3.92
R410A	0.0	0	165	15.1	0.37	5.6	2.01	0.51	0.68	3.46	3.53	4.25	4.12
R410A	0.0	0	164	15.0	0.41	5.8	2.01	0.51	0.69	3.52	3.56	4.27	4.20
R410A	0.0	0	164	15.1	0.41	5.8	2.01	0.51	0.69	3.52	3.54	4.25	4.21
R410A	0.0	0	165	15.2	0.43	5.8	2.01	0.51	0.70	3.57	3.69	4.50	4.26
R410A	0.0	0	165	15.0	0.44	6.0	2.01	0.51	0.70	3.57	3.49	4.10	4.26
R410A	0.0	0	164	15.2	0.46	5.9	2.01	0.51	0.70	3.60	3.36	3.84	4.30
R410A	0.0	0	164	15.1	0.46	5.8	2.01	0.51	0.71	3.60	3.87	4.84	4.31
R410A	0.0	0	162	15.1	0.50	6.8	2.00	0.50	0.72	3.65	3.83	4.75	4.39

Fluid	OMF [wt.%]	NP_{conc} [wt.%]	\dot{m} [kg/m ² -s]	\dot{q}_{avg} [kW/m ²]	x_{avg} [-]	T_{bub} [°C]	HTC_{nb} [kW/m ² -K]	HTC_{cht} [kW/m ² -K]	S	HTC_p [kW/m ² -K]	HTC_{exp} [kW/m ² -K]	\bar{F}	F
R410A	0.0	0	166	14.9	0.51	6.0	2.01	0.51	0.72	3.70	3.87	4.75	4.41
R410A	0.0	0	164	14.7	0.52	5.7	2.01	0.51	0.73	3.71	3.85	4.72	4.44
R410A	0.0	0	162	14.7	0.53	5.3	2.01	0.50	0.73	3.71	3.90	4.85	4.47
R410A	0.0	0	162	14.9	0.56	6.1	2.01	0.50	0.74	3.76	4.32	5.65	4.54
R410A	0.0	0	163	14.9	0.59	6.2	2.01	0.51	0.75	3.83	4.13	5.19	4.60
R410A	0.0	0	166	14.8	0.59	6.2	2.01	0.51	0.75	3.86	4.22	5.31	4.60
R410A	0.0	0	163	15.0	0.59	6.3	2.01	0.50	0.75	3.85	4.43	5.77	4.62
R410A	0.0	0	164	15.1	0.60	6.3	2.01	0.51	0.76	3.86	4.16	5.22	4.63
R410A	0.0	0	164	15.0	0.61	6.1	2.01	0.51	0.76	3.88	3.95	4.78	4.65
R410A	0.0	0	200	15.0	0.25	5.4	2.01	0.60	0.60	3.50	3.79	4.33	3.84
R410A	0.0	0	214	16.3	0.26	5.2	2.01	0.63	0.58	3.63	3.53	3.72	3.88
R410A	0.0	0	203	14.7	0.33	5.6	2.01	0.60	0.62	3.68	3.59	3.90	4.04
R410A	0.0	0	204	15.0	0.33	5.6	2.01	0.61	0.61	3.68	3.64	3.97	4.04
R410A	0.0	0	195	14.7	0.38	5.6	2.01	0.59	0.64	3.70	3.83	4.35	4.13
R410A	0.0	0	195	14.9	0.38	5.8	2.01	0.59	0.64	3.70	3.49	3.78	4.14
R410A	0.0	0	196	15.1	0.38	5.6	2.01	0.59	0.64	3.72	3.81	4.30	4.14
R410A	0.0	0	195	15.1	0.39	5.4	2.01	0.58	0.64	3.72	3.80	4.30	4.16
R410A	0.0	0	199	15.1	0.43	5.9	2.01	0.60	0.65	3.82	4.05	4.63	4.24
R410A	0.0	0	198	14.8	0.49	5.9	2.01	0.59	0.67	3.93	4.32	5.03	4.38
R410A	0.0	0	199	15.0	0.49	5.9	2.01	0.60	0.67	3.95	4.33	5.02	4.38
R410A	0.0	0	194	15.0	0.50	5.9	2.01	0.58	0.68	3.93	4.09	4.68	4.41
R410A	0.0	0	193	15.0	0.51	5.9	2.01	0.58	0.68	3.93	4.36	5.15	4.41
R410A	0.0	0	188	23.5	0.53	5.9	2.01	0.57	0.70	3.93	4.87	6.13	4.47
R410A-POE	2.4	0	100	14.9	0.38	6.1	0.64	0.30	0.55	4.11	3.56	10.77	12.61
R410A-POE	2.4	0	100	14.9	0.47	6.4	0.44	0.30	0.57	4.42	4.32	13.72	14.08
R410A-POE	2.4	0	100	15.2	0.56	6.7	0.34	0.29	0.59	4.80	4.59	15.04	15.77
R410A-POE	2.4	0	101	14.7	0.56	6.7	0.31	0.29	0.59	4.78	5.07	16.74	15.77
R410A-POE	2.4	0	100	15.1	0.57	6.7	0.31	0.29	0.60	4.78	5.03	16.81	15.94

Fluid	OMF [wt.%]	NP_{conc} [wt.%]	\dot{m} [kg/m ² -s]	\dot{q}_{avg} [kW/m ²]	x_{avg} [-]	T_{bub} [°C]	HTC_{nb} [kW/m ² -K]	HTC_{cht} [kW/m ² -K]	S	HTC_p [kW/m ² -K]	HTC_{exp} [kW/m ² -K]	\bar{F}	F
R410A-POE	2.4	0	99	15.3	0.65	6.6	0.15	0.27	0.63	5.59	5.90	21.78	20.61
R410A-POE	2.4	0	100	14.7	0.70	7.2	0.17	0.28	0.66	5.64	5.88	20.79	19.93
R410A-POE	2.4	0	127	14.8	0.36	6.2	0.58	0.37	0.49	4.58	4.14	10.32	11.49
R410A-POE	2.4	0	127	14.9	0.51	6.3	0.30	0.37	0.53	5.14	5.65	14.99	13.59
R410A-POE	2.4	0	129	14.7	0.57	6.8	0.26	0.36	0.56	5.53	5.83	15.58	14.77
R410A-POE	2.4	0	126	14.7	0.63	6.8	0.15	0.34	0.58	6.21	6.12	17.68	17.96
R410A-POE	2.4	0	129	14.6	0.64	6.8	0.18	0.36	0.58	5.91	6.58	18.05	16.18
R410A-POE	2.4	0	125	15.7	0.64	6.8	0.15	0.34	0.58	6.32	6.25	18.23	18.43
R410A-POE	2.4	0	128	14.9	0.68	7.2	0.19	0.35	0.61	6.26	5.94	16.58	17.48
R410A-POE	2.4	0	128	15.0	0.68	7.2	0.19	0.35	0.61	6.27	5.97	16.66	17.49
R410A-POE	2.4	0	129	15.0	0.70	7.9	0.17	0.35	0.62	6.43	6.11	17.11	18.02
R410A-POE	2.4	0	130	14.8	0.75	7.3	0.11	0.34	0.66	6.97	7.38	21.24	20.05
R410A-POE	2.4	0	126	15.3	0.76	6.9	0.10	0.32	0.67	7.38	6.29	19.71	23.18
R410A-POE	2.4	0	164	14.7	0.26	5.9	0.69	0.47	0.44	4.62	4.11	8.11	9.20
R410A-POE	2.4	0	164	15.1	0.39	6.3	0.48	0.46	0.47	5.08	4.89	10.07	10.47
R410A-POE	2.4	0	164	14.8	0.48	6.6	0.35	0.46	0.49	5.44	5.45	11.59	11.56
R410A-POE	2.4	0	163	15.1	0.49	6.5	0.35	0.46	0.50	5.46	5.58	11.88	11.63
R410A-POE	2.4	0	164	14.9	0.54	6.7	0.28	0.45	0.52	5.73	6.03	13.06	12.38
R410A-POE	2.4	0	163	15.2	0.55	6.3	0.21	0.44	0.51	6.04	5.71	12.76	13.53
R410A-POE	2.4	0	164	14.9	0.60	6.8	0.23	0.45	0.54	6.04	6.37	14.01	13.28
R410A-POE	2.4	0	163	15.0	0.61	7.0	0.17	0.43	0.54	6.46	6.02	13.80	14.81
R410A-POE	2.4	0	197	14.9	0.30	6.0	0.60	0.54	0.44	4.82	4.48	7.74	8.35
R410A-POE	2.4	0	198	14.9	0.38	6.2	0.48	0.54	0.46	5.07	4.92	8.68	8.97
R410A-POE	2.4	0	197	14.9	0.50	6.6	0.33	0.53	0.50	5.51	5.71	10.46	10.08
R410A-ZnO NL	2.4	20	102	15.1	0.46	6.0	0.79	0.28	0.74	2.68	2.40	6.47	7.46
R410A-ZnO NL	2.4	20	103	15.4	0.54	6.4	0.67	0.27	0.74	2.90	2.45	7.12	8.77
R410A-ZnO NL	2.4	20	101	15.3	0.68	7.1	0.38	0.24	0.78	3.24	3.39	12.73	12.11
R410A-ZnO NL	2.4	20	127	15.4	0.37	5.7	0.90	0.35	0.73	2.59	2.52	5.25	5.44

Fluid	OMF [wt.%]	NP_{conc} [wt.%]	\dot{m} [kg/m ² -s]	\dot{q}_{avg} [kW/m ²]	x_{avg} [-]	T_{bub} [°C]	HTC_{nb} [kW/m ² -K]	HTC_{cht} [kW/m ² -K]	S	HTC_p [kW/m ² -K]	HTC_{exp} [kW/m ² -K]	\bar{F}	F
R410A-ZnO NL	2.4	20	131	15.1	0.48	6.2	0.60	0.35	0.71	2.92	2.95	7.13	7.05
R410A-ZnO NL	2.4	20	128	15.1	0.51	6.4	0.57	0.34	0.72	3.00	3.09	7.84	7.58
R410A-ZnO NL	2.4	20	130	14.9	0.59	6.6	0.46	0.34	0.73	3.27	3.32	8.86	8.71
R410A-ZnO NL	2.4	20	129	15.3	0.68	6.9	0.35	0.32	0.76	3.61	3.97	11.73	10.62
R410A-ZnO NL	2.4	20	128	15.1	0.69	6.8	0.36	0.31	0.76	3.62	3.71	11.07	10.77
R410A-ZnO NL	2.4	20	164	15.1	0.29	5.9	0.93	0.46	0.63	3.08	2.78	4.78	5.43
R410A-ZnO NL	2.4	20	165	15.3	0.41	6.0	0.70	0.44	0.69	2.90	3.01	5.70	5.45
R410A-ZnO NL	2.4	20	164	15.1	0.49	6.2	0.48	0.43	0.70	2.98	3.72	7.86	6.15
R410A-ZnO NL	2.4	20	165	15.2	0.50	6.3	0.52	0.43	0.70	3.08	3.28	6.77	6.29
R410A-ZnO NL	2.4	20	164	15.2	0.59	6.6	0.43	0.42	0.72	3.39	3.71	8.16	7.41
R410A-ZnO NL	2.4	20	197	15.3	0.32	5.9	0.85	0.53	0.60	3.35	2.93	4.53	5.32
R410A-ZnO NL	2.4	20	198	15.3	0.39	6.0	0.60	0.53	0.62	3.29	3.69	6.27	5.52
R410A-ZnO NL	2.4	20	198	15.2	0.40	6.0	0.69	0.53	0.63	3.35	3.12	5.10	5.54
R410A-ZnO NL	2.4	20	197	15.2	0.49	6.4	0.51	0.50	0.70	3.00	3.45	6.11	5.23
R410A-ZnO NL	2.4	20	198	15.2	0.49	6.4	0.49	0.51	0.70	2.99	3.58	6.39	5.22
R410A-ZnO NL	2.4	20	197	15.2	0.50	6.4	0.47	0.50	0.70	2.98	3.70	6.68	5.25
R410A-Al ₂ O ₃ NL	2.4	20	100	15.3	0.38	5.8	1.01	0.28	0.73	2.68	2.22	5.27	6.88
R410A-Al ₂ O ₃ NL	2.4	20	101	15.3	0.46	6.0	1.00	0.30	0.72	3.20	2.20	4.95	8.30
R410A-Al ₂ O ₃ NL	2.4	20	100	15.7	0.56	6.4	0.90	0.29	0.73	3.61	2.23	5.39	10.09
R410A-Al ₂ O ₃ NL	2.4	20	101	16.0	0.69	7.1	0.89	0.28	0.76	4.45	3.27	9.22	13.39
R410A-Al ₂ O ₃ NL	2.4	20	127	15.5	0.38	5.8	0.83	0.36	0.70	2.76	2.77	6.13	6.11
R410A-Al ₂ O ₃ NL	2.4	20	127	15.3	0.38	5.6	0.80	0.35	0.70	2.76	2.82	6.39	6.20
R410A-Al ₂ O ₃ NL	2.4	20	127	15.1	0.50	6.2	0.71	0.34	0.69	3.25	3.09	7.57	8.04
R410A-Al ₂ O ₃ NL	2.4	20	127	15.1	0.50	6.1	0.80	0.34	0.69	3.35	3.18	7.68	8.17
R410A-Al ₂ O ₃ NL	2.4	20	127	15.0	0.59	6.4	0.84	0.36	0.71	4.05	3.09	6.92	9.60
R410A-Al ₂ O ₃ NL	2.4	20	132	15.2	0.61	6.6	0.86	0.37	0.71	4.27	3.54	7.87	9.86
R410A-Al ₂ O ₃ NL	2.4	20	129	14.6	0.62	6.5	1.02	0.36	0.72	4.42	4.79	11.23	10.19
R410A-Al ₂ O ₃ NL	2.4	20	131	14.9	0.69	6.4	1.24	0.36	0.74	5.06	4.88	11.00	11.50

Fluid	OMF [wt.%]	NP_{conc} [wt.%]	\dot{m} [kg/m ² -s]	\dot{q}_{avg} [kW/m ²]	x_{avg} [-]	T_{bub} [°C]	HTC_{nb} [kW/m ² -K]	HTC_{cht} [kW/m ² -K]	S	HTC_p [kW/m ² -K]	HTC_{exp} [kW/m ² -K]	\bar{F}	F
R410A-Al2O3 NL	2.4	20	129	15.5	0.72	7.2	1.30	0.35	0.75	5.45	4.85	11.03	12.76
R410A-Al2O3 NL	2.4	20	160	14.9	0.30	5.4	0.74	0.45	0.61	3.13	3.42	6.58	5.95
R410A-Al2O3 NL	2.4	20	164	15.2	0.41	5.9	0.56	0.44	0.66	3.04	3.83	7.80	6.02
R410A-Al2O3 NL	2.4	20	167	15.1	0.49	6.2	0.49	0.44	0.67	3.25	3.91	8.14	6.64
R410A-Al2O3 NL	2.4	20	166	15.0	0.58	6.4	0.64	0.43	0.69	3.77	4.47	9.46	7.82
R410A-Al2O3 NL	2.4	20	196	15.1	0.32	5.7	0.75	0.53	0.58	3.48	3.29	5.35	5.72
R410A-Al2O3 NL	2.4	20	203	15.1	0.39	5.9	0.61	0.54	0.60	3.54	3.64	6.05	5.87
R410A-Al2O3 NL	2.4	20	198	15.0	0.40	6.0	0.58	0.53	0.60	3.51	3.73	6.38	5.96
R410A-Al2O3 NL	2.4	20	204	15.0	0.47	6.3	0.48	0.53	0.65	3.38	4.00	6.95	5.79
R410A-Al2O3 NL	2.4	20	203	15.2	0.48	6.3	0.45	0.52	0.66	3.31	4.38	7.78	5.76